ANL-7753

Argonne National Laboratory

REACTOR DEVELOPMENT PROGRAM PROGRESS REPORT

October 1970

Printed in the United States of America
Available from
National Technical Information Service
U.S. Department of Commerce
Springfield, Virginia 22151
Price: Printed Copy $3.00; Microfiche $0.65

ANL-7753
Reactor Technology

ARGONNE NATIONAL LABORATORY
9700 South Cass Avenue
Argonne, Illinois 60439

REACTOR DEVELOPMENT PROGRAM PROGRESS REPORT

October 1970

Robert B. Duffield, Laboratory Director
Robert V. Laney, Associate Laboratory Director

Division	Director
Applied Physics	R. Avery
Center for Environmental Studies	L. E. Link
Chemical Engineering	R. C. Vogel
EBR-II Project	M. Levenson
Engineering and Technology	S. A. Davis
Materials Science	P. G. Shewmon
Reactor Analysis and Safety	W. R. Simmons

Report coordinated by
M. Weber and V. G. Trice, Jr.

Issued November 24, 1970

FOREWORD

The Reactor Development Program Progress Report describes current activities, technical progress, and technical problems in the program at Argonne National Laboratory sponsored by the USAEC Division of Reactor Development and Technology. Organized in accordance with the AEC's budget and reporting classifications, the report is published monthly. Not all projects are reported every month, but a running account of each project is maintained in the series of reports.

The last six reports
in this series are:

March 1970	ANL-7679
April-May 1970	ANL-7688
June 1970	ANL-7705
July 1970	ANL-7726
August 1970	ANL-7737
September 1970	ANL-7742

REACTOR DEVELOPMENT PROGRAM

Highlights of Project Activities for October 1970

EBR-II

Regular operation of the reactor at 62.5 MWt began on September 25, with Run 46A. Through October 15, the reactor had operated for 1136 MWd in Runs 46A and 46B, bringing its cumulative operational total to 40,427 MWd. Performance of the reactor and plant, measured as part of the extensive program of nuclear, thermal, and hydraulic surveillance planned for the power increase, was as anticipated.

The digital data-acquisition system (DAS) passed its acceptance test by operating reliably 96.6% of the time during its 30-day test period. The results of rod-drop data from Run 46A processed with the DAS were in excellent agreement with the results obtained with the conventional method.

ZPR-3

Assembly 62, Second Step, is a stainless steel reflected critical assembly built in support of the EBR-II program. Thermoluminescent dosimeter gamma-ray mapping studies and neutron-spectrum measurements were made using the same methods as those for the earlier nickel reflected assembly. The worth of tantalum and of a simulated boron-poisoned safety rod in four stepped core positions was also determined.

Loading of Assembly 63 is now in progress.

ZPR-6

Studies of the time variation of the core temperature profiles in the large, plutonium-fueled Assembly 7 were made with 16 installed monitor thermocouples. With the reactor halves closed and cooling fans operating, nearly 2 hr must elapse before a temperature equilibrium is reached. A preliminary evaluation of the temperature coefficient of reactivity (-3.5 Ih/°C) was obtained for this loading.

ZPR-9

To support the development of calculational models to be used for large in-core perturbations, the reactivity effects of simulated open and closed loops were studied in the FTR-3 critical assembly. Worths of fueled and absorber rods were measured in the perturbed assemblies.

ZPPR

Cell integrity tests have been completed. Measurements on ZPPR Assembly 2, a two-zone demonstration benchmark reactor, have emphasized boron and tantalum control rod studies in the 2400-liter core. Preanalysis studies of pin fuel-element loadings in ZPPR-2 indicate that a full-core version of Assembly 2 containing only fuel pins in calandria cans would have a reduction of 1% in k, or a 6% increase in critical mass.

TABLE OF CONTENTS

TABLE OF CONTENTS

TABLE OF CONTENTS

189a No.	Reported This Month	189a Title	RDT Branch
02-157		LMFBR Fuel Materials Preparation--U/Pu Nitrates to Oxides	RT-FR
02-158	x	LMFBR Fuel Fabrication--Analyses and Continuous Processing	RT-FR
02-159		LMFBR Reprocessing--Plutonium Isolation	RT-FR
02-162	x	Thermophysical Properties of Reactor Fuels	RT-FR
02-164	x	Fuel-Coolant Interactions	NS-RD
02-165	x	Post-accident Heat Removal	NS-RD
02-166		Thermal-plume Dispersion Studies	NS-ES
02-173	x	Molten Metal Decladding of LMFBR Fuels	RT-FR
02-175		Physical and Chemical Studies--Molten Fuel, Cladding, and Coolant	RT-FR
02-178		ZPR-6 and -9 Operations and Maintenance	RT-PH
02-179	x	Fast Critical Facilities Experiments and Evaluation--Illinois	RT-PH
02-180		ZPPR and ZPR-3 Operations and Maintenance	RT-PH
02-181	x	Fast Critical Facilities Experiments and Evaluation--Idaho	RT-PH
02-182		LMFBR Fuel Management Studies	RT-FR
02-184		Mass/Energy Balance of the Great Lakes	NS-ES
02-185		Lake Circulation Model Development	NS-ES
02-186	x	1000-MWe Contract Management, Technical Review, and Evaluation	PE-LM
02-191		Disposal of EBWR Fuel	RD-AB
02-194		Surveillance and Failure Evaluation of Experimental Fuel Irradiations	RT-FM
02-195		Scram System Study	PE-LM
02-200		Conceptual Design Study of FFTF Vessel Head-cavity System	RE-CD
02-201		Utilization of EBR-II in the Development of Sodium Technology	RT-CC
02-509		Sodium Chemistry and Radioactive Contaminant Behavior	RT-CC
02-526		In-pile Stainless Steel Swelling and Mechanical Behavior	RT-FM
02-528	x	Plant Dynamics and Control Analysis	PE-IC
02-530	x	Operation of Data Acquisition System (DAS)	PE-IC

I. LIQUID METAL FAST BREEDER REACTORS

A. Physics Development

1. Theoretical Reactor Physics

a. General Fast Reactor Physics (189a 02-009)

(i) Testing and Improvement of Fuel Cycle Analysis

Last Reported: ANL-7705, pp. 3-5 (June 1970).

(a) Time Step Subinterval Length Required for REBUS (J. Hoover and D. A. Meneley)

As part of a continuing effort to develop efficient but reliable computational schemes for fuel-cycle analysis, the effect of increasing the length of the time step between neutronics solutions was studied. In REBUS,* the burn time is divided into P subintervals; thus, there are P + 1 time nodes at which the neutronics solutions are done to obtain the system multiplication and the multigroup flux distribution. (See J. Hoover et al., for a discussion of the solution method.) The neutronics solutions are typically done by a two-dimensional finite-difference approximation. Because of the high cost of these neutronics solutions, significant economies could result by reducing P, the number of subintervals.

In this study, three 1000-MWe LMFBR's**,†,†† were analyzed. The cross sections were based on the Revised Category 1 file of ENDF/B, except that the higher ^{239}Pu capture-to-fission ratios were incorporated. Multigroup cross sections were obtained with the ultrafine group P1 option of the MC^2 code‡ using estimated core-averaged midcycle atom densities. The cross-section set consisisted of 26 half-lethargy-width groups from 10 MeV to 22.6 eV. For the fuel-cycle calculations, the 26-group set was collapsed to 13 groups for the General Electric Reference Reactor† and eight groups for the Babcock & Wilcox and the General Electric Advanced Designs††,‡ by linear flux weighting with the single spectrum obtained from the MC^2 code.

---

* J. Hoover et al., "Solution Techniques Used in the Fast Reactor Fuel Cycle Code REBUS," Reactor Physics Division Annual Report, July 1, 1968 to June 30, 1969, ANL-7610, pp. 471-480 (1969).

** P. M. Murphy et al., Conceptual Plant Design, System Descriptions and Cost for a 1000 MWe Sodium Cooled Fast Reactor, GEAP-5678 (1968).

† B. J. Goulding et al., 1000 MWe LMFBR Follow-on Study, BAW-1328 (1968).

†† P. M. Murphy et al., Comparison of Two Sodium-Cooled, 1000 MWe Fast Reactor Concepts, GEAP-5618 (1968).

‡ B. J. Toppel, A. L. Rago, and D. M. O'Shea, MC^2, A Code to Calculate Multigroup Cross Sections, ANL-7318, Argonne National Laboratory (June 1967).

Fuel-cycle calculations were done to obtain the equilibrium operating conditions of the reactor system. Fuel-cycle parameters were examined to assess the accuracy of the results obtained. Calculations were done with the burn step or operating interval divided into one or two subintervals. The results for each of the reactor designs are presented in Tables I.A.1, I.A.2, and I.A.3.

TABLE I.A.1. Fuel-cycle Results for General Electric Reference Design[a]

	2 Subintervals	1 Subinterval
Fissile Mass[b]		
Beginning of Cycle		
Core	1677.4	1677.9
Radial Blanket	213.8	213.9
Axial Blanket	185.4	185.3
End of Cycle		
Core	1603.0	1603.0
Radial Blanket	336.8	337.1
Axial Blanket	409.7	409.5
Breeding Ratio	1.368	1.378
Core Conversion Ratio	.8819	.8853
Cycle Time (full power days)	300	300
Supplied Fissile Mass		
Core Zone 1	363.5	363.7
Core Zone 2	251.6	251.7
Core Zone 3	168.0	168.0
Radial Blanket	14.2	14.2
Axial Blanket 1	11.1	11.1
Axial Blanket 2	5.6	5.6
Axial Blanket 3	3.7	3.7
Discharged Fissile Mass		
Core Zone 1	358.2	359.6
Core Zone 2	209.0	208.9
Core Zone 3	139.0	139.0
Radial Blanket	142.1	142.2
Axial Blanket 1	149.0	147.9
Axial Blanket 2	55.9	55.9
Axial Blanket 3	38.6	38.6

[a] P. M. Murphy et al., Conceptual Plant Design, System Descriptions and Cost for a 1000 MWe Sodium Cooled Fast Reactor, GEAP-5678 (1968).

[b] kg of $U^{235} + Pu^{239} + Pu^{241}$.

TABLE I.A.2. Fuel-cycle Results for Babcock and Wilcox Reference Design[a]

	2 Subintervals	1 Subinterval
Fissile Mass[b]		
Beginning of Cycle		
Core	1380.3	1380.5
Radial Blanket	116.4	116.6
Axial Blanket	136.9	136.4
End of Cycle		
Core	1371.5	1371.5
Radial Blanket	179.9	180.4
Axial Blanket	236.5	236.2
Breeding Ratio	1.343	1.358
Core Conversion Ratio	.9685	.9776
Cycle Time (full power days)	352	352
Supplied Fissile Mass		
Core Zone 1	275.8	275.8
Core Zone 2	259.8	259.8
Core Zone 3	384.6	384.6
Radial Blanket	16.2	16.2
Axial Blanket 1	6.3	6.3
Axial Blanket 2	5.5	5.5
Axial Blanket 3	7.1	7.1
Discharged Fissile Mass		
Core Zone 1	285.9	286.0
Core Zone 2	256.4	256.4
Core Zone 3	359.8	359.8
Radial Blanket	143.4	143.6
Axial Blanket 1	88.4	88.4
Axial Blanket 2	67.8	67.8
Axial Blanket 3	62.0	62.0

[a]B. J. Goulding et al., 1000 MWe LMFBR Follow-on Study, BAW-1328 (1968).
[b]kg of $U^{235} + Pu^{239} + Pu^{241}$.

TABLE I.A.3. Fuel-cycle Results for General Electric Advanced Design[a]

	2 Subintervals	1 Subinterval
Fissile Mass[b]		
Beginning of Cycle		
Core	724.9	725.4
Radial Blanket	172.2	172.5
Axial Blanket	76.9	76.9
End of Cycle		
Core	709.0	708.0
Radial Blanket	209.9	210.2
Axial Blanket	111.0	111.3
Breeding Ratio	1.345	1.352
Core Conversion Ratio	.9826	.9904
Cycle Time (full power days)	132	132
Supplied Fissile Mass		
Core Zone 1	78.2	78.2
Core Zone 2	89.5	89.5
Radial Blanket	3.6	3.6
Axial Blanket 1	1.8	1.8
Axial Blanket 2	1.4	1.4
Discharged Fissile Mass		
Core Zone 1	77.5	78.9
Core Zone 2	72.8	72.8
Radial Blanket	41.2	41.4
Axial Blanket 1	22.8	22.9
Axial Blanket 2	14.7	14.8

[a]P. M. Murphy et al., Comparison of Two Sodium-Cooled, 1000 MWe Fast Reactor Concepts, GEAP-5618 (1968).
[b]kg of $U^{235} + Pu^{239} + Pu^{241}$.

The agreement between the two cases for the fissile masses is quite good. The error is at most 0.5%. The cycle time or operating interval was calculated quite accurately with one subinterval. However, the breeding ratio and core-conversion ratio are consistently overestimated by approximately 1% with one subinterval.

To determine the accuracy of the detailed burnup, power and flux calculations the two-dimensional power distributions obtained with one subinterval and two subintervals were compared. The maximum error in the power distribution obtained with one subinterval is 0.5%. For illustrative purposes, the radial power distributions at the reactor midplane are shown in Table I.A.4 for the General Electric Advanced Design.

TABLE I.A.4. Radial Power Distribution at End of Cycle for General Electric Advanced Design[a]

Radial Position cm	Power Density[b]	
	2 Subintervals	1 Subinterval
3.67	8.688×10^{-7}	8.691×10^{-7}
11.02	8.644×10^{-7}	8.647×10^{-7}
18.37	8.556×10^{-7}	8.559×10^{-7}
25.72	8.424×10^{-7}	8.427×10^{-7}
33.07	8.251×10^{-7}	8.253×10^{-7}
40.41	8.035×10^{-7}	8.037×10^{-7}
47.72	7.779×10^{-7}	7.780×10^{-7}
55.11	7.482×10^{-7}	7.482×10^{-7}
62.46	7.141×10^{-7}	7.141×10^{-7}
69.81	6.751×10^{-7}	6.751×10^{-7}
76.52	7.707×10^{-7}	7.705×10^{-7}
82.61	7.077×10^{-7}	7.075×10^{-7}
88.69	6.299×10^{-7}	6.297×10^{-7}
94.78	5.401×10^{-7}	5.399×10^{-7}
100.87	4.425×10^{-7}	4.424×10^{-7}
106.03	1.616×10^{-7}	1.616×10^{-7}
110.28	1.268×10^{-7}	1.268×10^{-7}
114.52	9.892×10^{-8}	9.897×10^{-8}
118.56	5.755×10^{-8}	5.758×10^{-8}
122.39	4.506×10^{-8}	4.509×10^{-8}
126.21	3.523×10^{-8}	3.526×10^{-8}
129.88	2.054×10^{-8}	2.056×10^{-8}
133.39	1.636×10^{-8}	1.637×10^{-8}
136.90	1.326×10^{-8}	1.327×10^{-8}

[a] P. M. Murphy et al., Comparison of Two Sodium-Cooled, 1000 MWe Fast Reactor Concepts, GEAP-5618 (1968).

[b] Relative power density (W/cm^3) normalized to a total power of 1.0 W.

In conclusion, for conceptual design analysis with the REBUS System, one subinterval or two time nodes (beginning and end of cycle) can be used. The fissile mass and power distributions can be accurately obtained, and the breeding ratio and core-conversion ratio are overestimated by almost 1%.

(ii) Group Constant Averaging

Not previously reported.

(a) Effects of Energy-Angle Correlation in Inelastic Scattering on Fast Reactor Calculations (M. Segev)

The new MC^2 code will include energy-angle correlation in inelastic scattering to single levels. The inclusion was enabled by an algorithm developed to translate basic inelastic data from ENDF/B files to inelastic transfer matrices. The latter are needed in the multigroup as well as in the continuous slowing-down option of the new MC^2. The algorithm is highly accurate and yet of a much simpler logic than the one reported by O'Reilly and Lewis.*

Inclusion of the inelastic energy-angle correlation in the P_0 component of the Boltzmann equation has nonnegligible effects on fast infinite systems, as indicated by a study of the infinite mixtures by Okrent.** In these mixtures the neutron energy spectrum softens, the criticality factor drops by 0.3-0.5%, and the ratio of the uranium capture rate to the plutonium fission rate drops by 2-3% when inelastic energy-angle correlation is included.

Another algorithm for the P_0 inelastic matrices was developed. It accounts for energy-angle correlation by retaining only the first moment of the angular distribution resulting from a scattering to a single level. This algorithm is simple in logic and is twice as fast as the more rigorous algorithm. Although based on a simplifying assumption, it led to practically the same criticality factors, reaction rates, Doppler effects, and sodium-void effects, as did the more rigorous algorithm.

The energy-angle correlation in the P_1 inelastic matrices (finite systems) is being studied.

---

*B. D. O'Reilly and R. C. Lewis, The Calculation of Slowing-Down Transfer Matrices in the Spherical Harmonics Representation, NAA-SR-11530 (1966).

**D. Okrent, "Summary of Intercomparison Calculations Performed in Confjunction with Conference on Safety, Fuels, and Core Design in Large Fast Power Reactors," Proceedings of the Conference on Safety, Fuels, and Core Design in Large Fast Power Reactors, October 11-14, 1965, ANL-7120, pp. 3-23.

b. Fast Critical Experiments--Theoretical Support--Idaho (189a 02-010)

(i) Planning Support (R. G. Palmer)

(a) Preanalysis of ZPPR Assembly 2 (A. P. Olson)

Neutron cross sections for preanalysis of pin zones in ZPPR Assembly 2 are now available, as additions to a previously reported cross section library. (See Progress Report for April-May 1970, ANL-7688, p. 7.) The MC^2 code was used with ENDF/B (1968) data in a two-region cylindrical-equivalent cell to produce heterogeneously self-shielded cross sections. In addition to the cross sections generated assuming full-density sodium, others were obtained assuming complete sodium voiding. The CALHET-3 code was used to flux-volume-weight these neutron cross sections in order to account for spatial self-shielding.

Two-dimensional diffusion-theory calculations were made with the ARC System to study the effect of heterogeneity on k_{eff} for a reactor configuration similar to the current loading. (See Progress Report for July 1970, ANL-7726, pp. 11-16.) It was assumed that the entire inner and outer core zones, and the inner 15.24 cm of the axial blanket, were assembled from pins in calandria cans. Due to inventory limitations, the complete loading cannot be obtained in practice, but it makes a good reference case from a calculational viewpoint.

These pin calculations, assuming homogeneously self-shielded neutron cross sections, gave k = 0.9774. Going to heterogeneously self-shielded cross sections gave k = 0.9807, for an energy self-shielding effect of 0.34% $\Delta k/k$. The use of spatially weighted cross sections from CALHET-3 gave k = 0.9822, for a spatial self-shielding effect of 0.16% $\Delta k/k$. For comparison, this effect was predicted (by CALHET-3) to be 0.11 and 0.13% $\Delta k/k$ in the inner and outer core zones, respectively. Thus the total heterogeneity effect in the pin-zone version of Assembly 2 was calculated to be 0.50% $\Delta k/k$, as compared to 1.90% $\Delta k/k$ in the plate-zone version for which k = 0.9923. All the quoted k-values include a transport-effect correction of 0.35% (k). It is predicted that a full-core pin-zone version of Assembly 2 would have a reduction of 1.0% in k, or a 6.0% increase in critical mass.

Two-dimensional calculations of the prompt-neutron lifetime ℓ_p, the effective delayed-neutron fraction β_{eff}, and the conversion factor of inhours to percent reactivity gave $\ell_p = 5 \times 10^{-7}$ sec, $\beta_{eff} = 0.003226$, and Ih/%k = 997.9.

2. Experimental Reactor Physics

a. Fast Critical Experiments--Experimental Support--Idaho (189a 02-011)

(i) Neutron Spectroscopy (G. G. Simons)

Last Reported: ANL-7726, pp. 3-5 (July 1970).

The proton-recoil proportional-counter spectrometer is routinely used to measure fast-neutron spectra in the presence of gamma rays. Data required to evaluate the importance of gamma-ray source geometry and energy distribution relative to errors induced in neutron spectra from incorrect removal of gamma-ray background were obtained in conjunction with the ZPR-3 Assemblies 61 (see July Progress Report) and 62 neutron-spectrum measurements. In Assembly 62, relative background measurements were made with both hydrogen- and methane-filled counters in matrix positions 1-P-16 and 1-P-9 during reactor shutdown and with a point ^{60}Co source. Final results of this background study will be reported later.

To ensure consistent fast-neutron spectrum measurements at the Idaho and Illinois Sites, the two groups measured the spectrum at the ATSR in Illinois. Respective detectors, preamplifiers and pulse shaping circuitry were used by each group. The resulting neutron spectra are shown in Fig. I.A.1. The slight discrepancies in the two spectra have been traced to errors induced by improper gamma-ray background subtraction and not to different fast-neutron responses. This emphasizes the need for good gamma-ray pulse-shape identification techniques and correct gamma-ray background measurements and removal. A detailed report of this study is in preparation.

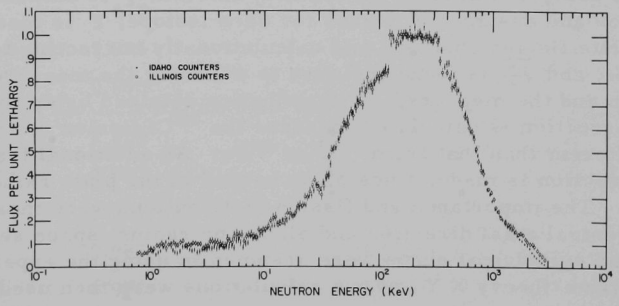

Fig. I.A.1. Comparison of Spectra Measured with Different Idaho and Illinois Detectors and Pulse Shaping Electronics. ANL Neg. No. ID-103-A11495.

(ii) Development of Experimental Techniques (S. G. Carpenter)

(a) β_{eff} Studies

Last Reported: ANL-7640, pp. 13-14 (Nov 1969).

Since no large errors were found in the relative values of β_{eff} for ^{235}U, ^{238}U, and ^{239}Pu in the earlier experiments, a further set of experiments were carried out to measure total β_{eff}. Two particularly simple cores were used: ZPR-3 Core 57 (ANL-7581, pp. 9-11) and Core 59 (ANL-7655, pp. 15-17). Core 57 contained predominantly ^{235}U and BeO with an iron reflector and Core 59 contained predominantly ^{239}Pu and carbon with a lead reflector.

The method used was to measure the reactivity effect (in dollars, since only the correct relative β_{eff} values are needed) of removing all the fissions in the reactor. Instead of using an equivalent $1/v$ absorber to replace the fissionable material (as done in a thermal-reactor experiment), the fission rate was measured as a function of position, and then the apparent reactivity effect of a neutron source (^{252}Cf) of the same magnitude was determined. These values were integrated over the reactor and set equal to $1/\beta_{eff}$. The result can be written as

$$\beta_{eff} = \frac{S\phi^*}{V\nu F\overline{\phi_F^*}},$$

where S is the source strength of the ^{252}Cf, V is the apparent reactivity of the source neutrons, ν is the average number of neutrons per fission, F is the total fission rate, $\overline{\phi_F^*}$ is the average importance of a fission neutron, and ϕ^* is the average importance of a source neutron at the position where V is measured. S is determined outside the reactor, V is determined using a calibrated (in dollars) autorod, ν is calculated from fission rates and assumed ν values for each isotope, F is measured using absolute fission counters and calculationally correcting to the in-plate values, and $\overline{\phi_F^*}$ is found (relative to ϕ^*) using the measured fission distribution and the measured ϕ^* distribution obtained using the source. A small correction is calculated, because the ^{252}Cf fission distribution is slightly different than that from ^{235}U or ^{239}Pu. An additional transport-theory correction is made, since $\overline{\phi_F^*}$ is needed in the plate rather than in the source. The importance and fission distributions were measured along the central axial direction and along one radius; space separability of fluxes and cylindrical shape were assumed in using the experimental data. Diffusion-theory X,Y and r,z calculations were then used to correct these results.

Table I.A.5 gives the various components which are combined to produce β_{eff}:

$$\beta_{eff} = \frac{S}{V\nu N F_{mc}} \cdot R_F \cdot R_I \cdot \frac{F_{mc}}{F_c}\left(\frac{F_c}{F_p} \cdot \frac{\phi^*_S}{\phi^*_F} \cdot \frac{\phi^*_{FS}}{\phi^*_{FP}} \cdot R_{FC} \cdot R_{IC}\right).$$

An estimated error is also given for each component. The experimental results are not greatly different from the calculated values, which are spherical diffusion-theory results using the input typical of that normally used when calculating reactivity effects. The values between the dotted lines are the calculated ratios, which correct the experimental values for (in order) in-counter to in-plate fission rates, difference in the fission spectrum between ^{252}Cf and ^{235}U or ^{239}Pu, in source to in-plate importance, assumed fission-space separability and cylindrical core, assumed importance-flux space separability, and the effects of the imperfect cylindrical-core boundary. The values above the first dotted line (except ν) are the measured values for the source strength (neutrons/sec), apparent reactivity, ν, atoms of ^{239}Pu or ^{235}U, fission rate per atom of ^{239}Pu or ^{235}U, peak-to-average fission rate, peak-to-average importance, and ratio of ^{239}Pu or ^{235}U fission rate to total fission rate.

TABLE I.A.5. β_{eff} Results

	Core 59 (^{239}Pu)	Core 57 (^{235}U)	Error Est
S	5.94×10^7	9.197×10^6	±1.0%
V	0.03938 $	0.06997 $	±1.0%
ν	2.950	2.490	±1.0%
N	1.913×10^{26}	2.165×10^{26}	±0.5%
F_{mc}	2.483×10^{-15}	7.850×10^{-15}	±2.0%
R_F	1.477	1.564	±2.0%
R_I	1.523	1.667	±1.5%
F_{mc}/F_c	0.986	0.948	±0.2%
F_c/F_p	1.059	1.013	±1.5%
ϕ^*_S/ϕ^*_F	0.997	1.005	±0.3%
ϕ^*_{FS}/ϕ^*_{FP}	0.971	0.949	±1.0%
R_{FC}	0.987	1.022	±1.0%
R_{IC}	0.972	1.026	±1.0%
β_{eff} (exp)	0.00233 ± 0.00010	0.0078 ± 0.0003	
β_{eff} (calc)	0.00230	0.0072	

The results do not indicate a large error in the normally calculated β_{eff} (1-8%). Further, the measured distributions of flux and adjoint flux compare well with the calculated values, so that the ratio of the product of the flux and importance to the denominator in the perturbation expression, used for calculating central reactivities, must be nearly correct. It does not seem probable that errors of the order of 30% can be attributed to the experimental values for central reactivities, even if they are quoted in Δk_e.

(b) Rod-drop Subcriticality Measurements

Last Reported: ANL-7632, p. 16 (Oct 1969).

The method of analyzing the power-history data referred to ANL-7632 has been further studied with the objective of evaluating the error in the derived reactivity in a more straightforward manner. Instead of searching for the source that produces a constant reactivity after the rod drop, the point-kinetic equations for the flux (or detector count-rate) are combined* in such a manner that a straight line is obtained relating two variables which do not have correlated errors and which have statistical errors large in one variable compared to the other. The best fit is then obtained directly and simply by the least-squares method with the statistical variation in the reactor power producing similar regular statistical errors in the fit. From the two constants for the fitted line and their errors, the final reactivity (and initial reactivity if required) and its error are determined. The reasonable approximation is made that $(\ell/CR)(dCR/dt) \ll \Delta k_e$.

The equation used is $CR(t) = a + bX(t)$, where $CR(t)$ is the instantaneous count rate

$$a = \frac{S_e \ell}{k_e A \left(1 - \frac{\Delta k_e}{k_e \beta_{eff}}\right)},$$

a constant after the rod movement if A, S_e, and ℓ are constants, A is a function of counter efficiency,

$$b = \frac{\ell}{k_e \left(1 - \frac{\Delta k_e}{k_e \beta_{eff}}\right)},$$

a constant after the rod movement, and

*S. G. Carpenter, Reactivity Measurements in the Advanced Epithermal Thorium (AETR) Critical Experiments, Nucl. Sci. Eng. 21, 429 (1965).

$$X(t) = \frac{1}{A} \sum_i a_i e^{-\lambda_i t} \left(A_0 C R_0 k_{e0} + \lambda_i \int_0^t k_e A C R e^{\lambda_i t} \, dt \right),$$

which can be solved from the count-rate history at each time point at which CR(t) is determined if $A = A_0$ and k_{e0} is estimated. (The result is so insensitive to k_{e0} that it can be set to one without significant loss in accuracy.) Then,

$$\Delta k_e / \beta_{eff} = (1 - 1/b)/(1 - \beta_{eff})$$

and

$$\Delta\left(\frac{\Delta k_e}{\beta_{eff}}\right) = \frac{\Delta b}{b^2(1 - \beta_{eff})}$$

if Δb is small compared to b.

b. Fast Critical Experiments--Experimental Support--Illinois (189a 02-013)

(i) Neutron Spectroscopy Measurements

Last Reported: ANL-7705, pp. 18-19 (June 1970).

(a) The Soft Photon Response of Proportional Counters for Neutron Spectroscopy (E. F. Bennett)

Proton-recoil proportional counters, when set to view the low-energy region of spectra (down to about 1 kV), will respond readily to any soft photon incident upon the tube. These photons convert (by predominantly Compton scattering in the stainless walls), and conversion electrons will ionize equivalent to low-energy recoil protons.

Pulse-shape discrimination against electrons is effective and is normally used in neutron-spectrum measurements. However, if the intensity of background is high, the detector may record predominantly electron-induced events and consequently neutron-signal-to-electron background will be poor. In an extreme case, the count-rate limitation of the electronics may be exceeded and no measurement is possible.

Any shielding to reduce the sensitivity to photon background is desirable, assuming that the extent of shielding does not also alter the neutron spectrum.

Alpha decay in fertile and fissile isotopes will introduce a very strong photon and electron component resulting from ionization during stopping of the alpha particles. Most of this component is readily absorbed

in the material itself, but a substantial emission will exist nevertheless. The upshot is that proportional counter measurements near alpha emitters may be affected by background, and in order to estimate the magnitude of this background and the effect of shielding, a simple experiment was done.

Successively thicker sleeves of gold and lead were wrapped around a hydrogen-gas-filled tube (2.54 cm in diameter and 7.5 cm long), which was contained in a block of depleted uranium. The counter was set to register all events in excess of about 1/2 kV. Results are shown below:

Extent of Shielding	Gamma Detection Rate, counts per min
None*	333,270
2 mils gold	96,626
4 mils gold	53,302
19 mils lead	44,316

The rapid decrease initially corresponds to photons with energy less than 100 kV. At the point where about 10 mils lead has been added, only a very slow subsequent additional reduction through shielding can be expected. Lead shielding, to this extent, will have no observable effect upon the neutron spectrum and is recommended in any experiment where chambers are placed in contact with uranium or plutonium metal.

c. Planning and Evaluation of FFTF Critical Assembly Experiments (A. Travelli) (189a 02-015)

Last Reported: ANL-7742, pp. 5-6 (Sept 1970).

(i) More Accurate Calculation of Infinite Dilution Worth of ^{10}B in FTR-3. Preliminary calculations of the infinite dilution worth of ^{10}B at the center of ZPR-3 Assembly 56B were reported on page 7 of the ANL-FFTF Critical Experiments Program Monthly Informal Technical Progress Report, which used the method of Dwark et al.,** to calculate self-shielding factors to be applied to experimental measurements of boron worth reported in the Progress Report for April-May 1969, ANL-7577 (pp. 19, 20, and 33). A more accurate treatment of the self-shielding effect in the same experiments is reported here.

The boron samples used in the worth measurements comprised a 0.2-in.-dia, 1.688-in.-long solid cylinder weighing 1.011 g; a 0.391-in.-OD, 0.020-in.-thick, 1.688-in.-long hollow cylinder weighing

*The counter wall thickness was 0.4 mm of stainless steel.

**J. Dwark, P. L. Hoffman, H. Hurwitz, Jr., and E. J. Clancy, Self-Shielding Factors for Infinitely Long Hollow Cylinders, KAPL-1262 (1955).

0.691 g; and a 0.391-OD, 0.010-in.-thick, 1.688-in.-long hollow cylinder weighing 0.406 g. The samples were 92.8 wt % boron, and the boron was 92.1 wt % ^{10}B.

To reduce the computation cost, self-shielding factors were calculated in spherical geometry rather than in two-dimensional rz-geometry. This required the definition of equivalent spherical annular samples. The three parameters--outer radius, inner radius, and density of ^{10}B--were adjusted for each spherical sample so that it was equivalent to one of the finite cylindrical samples in the sense that it contained the same mass of ^{10}B and had the same first two average chord moments. The radii of the spherical annulii and their density ratios with respect to the finite cylindrical samples are given in Table I.A.6.

TABLE I.A.6. Data on Equivalent Cylindrical and Spherical Samples

Sample	Outer Radius, cm	Inner Radius, cm	Height, cm	Density Ratio
1 Cylinder	0.25400	0	4.28752	1.0
Sphere	0.75945	0.699039	-	2.15111
2 Cylinder	0.49657	0.44577	4.28752	1.0
Sphere	1.08987	1.05926	-	1.45165
3 Cylinder	0.49657	0.47117	4.28752	1.0
Sphere	1.08987	1.07530	-	1.54306

The ratio f of the average flux within the spherical annular sample position with sample material present to that with the sample material not present was calculated for each of the 29 energy groups of the Argonne cross-section set 29004. (See Reactor Development Progress Report, December 1968, ANL-7527, pp. 9-10.) The average fluxes for each group with and without sample material present were obtained from spherical S-16 calculations using the SNARG-1D code.*

The perturbation worth for ^{10}B at the center of ZPR-3 Assembly 56B was computed in diffusion theory using the MACH-1 code.** As before, the perturbation-worth component associated with each group was then multiplied by the f calculated for that group, and the products were summed to give the computed perturbation worth corrected for self-shielding. This method assumes that the adjoint flux for each group over the sample volume and without the sample in place is almost the same when calculated in diffusion theory or in the S-16 approximation. It also assumes

*G. J. Duffy, H. Greenspan, S. D. Sparck, J. V. Zapatka, and M. K. Butler, SNARG-1D, A One-dimensional Discrete-ordinate Transport Theory Program for the CDC-3600, ANL-7221 (1966).

**D. A. Meneley, L. C. Kvitek, and D. M. O'Shea, MACH-1, A One-dimensional Diffusion Theory Package, ANL-7223 (June 1966).

that the leakage component of the sample worth is negligible. The self-shielding factor, F, for each sample was taken to be the ratio of the perturbation worth of ^{10}B with or without the self-shielding correction.

The five sample worth measurements were then corrected for self-shielding using the F factors. The resultant worth values were averaged with weights inversely proportional to the squares of the statistical deviations of the worth values corrected for self-shielding. These statistical deviations include the experimental statistical deviation and an estimate of the statistical deviation in F. The central worth of ^{10}B in ZPR-3 Assembly 56B is then found to be 6961 (Ih/kg ^{10}B). The relative statistical uncertainty of this result is estimated to be 1.5%. This value includes the rather large uncertainty due to the presence of heterogeneity in the core material that surrounded the various samples during the experiments. In addition, there may be small systematic errors due to the calibration of the autorod. (See ANL-7577, pp. 19,20, and 33.)

3. ZPR-6 and -9 Operations and Analysis

a. Fast Critical Facilities Experiments and Evaluation--Illinois (189a 02-179)

(i) Mockup Critical Experiments

Last Reported: ANL-7742, pp. 8-13 (Sept 1970).

(a) Reactivity Worths of Simulated FTR Loops (R. M. Fleischman, R. B. Pond, C. D. Swanson, and J. W. Daughtry)

The reactivity worths of simulated open and closed loops in FTR-3 have been measured. The purpose of these experiments is to provide data relative to large in-core perturbations of interest in the development of calculational models for use in fuel and test management of FTR.

Simulation of open- and closed-loop compositions required the use of drawer loading patterns not previously used in FTR-3. Atom densities of each drawer loading and smeared atom densities for open- and closed-loop clusters are given in Table I.A.7. Two of the six matrix positions used to make an open-loop cluster (zone F in Fig. I.A.2) contain regular outer-core composition and were not changed in the simulation of the loop. The materials in these drawers were, however, used in calculating the smeared atom densities of an open loop.

All reactor configurations achieved during the experiments and temperature corrected k_{ex} results are described in Fig. I.A.2 and Table I.A.8. Columns 2-4 of Table I.A.8 describe the changes in

TABLE I.A.7. As-built Atom Densities for Open and Closed Loops

Isotope or Element	Atom Densities, 10^{21} atoms/cm^3						
	Closed Loop			Open Loop			
	Type A	Type B	Avg[a]	Type B	Type C	Type D	Avg[b]
^{238}Pu	-	-	-	-	0.0006	-	0.0003
^{239}Pu	0.5631	-	0.1877	1.1774	0.8814	-	1.0276
^{240}Pu	0.0535	-	0.0178	0.1118	0.1167	-	0.1141
^{241}Pu	0.0044	-	0.0015	0.0092	0.0181	-	0.0136
^{242}Pu	0.0003	-	0.0001	0.0006	0.0019	-	0.0013
^{239}Pu + ^{241}Pu	0.5675	-	0.1892	1.1866	0.8995	-	1.0412
^{240}Pu + ^{242}Pu	0.0538	-	0.0179	0.1124	0.1186	-	0.1154
Pu	0.6273	-	0.2071	1.2990	1.0187	-	1.1569
^{235}U	0.0057	-	0.0019	0.0129	0.0065	0.0009	0.0097
^{238}U	2.4836	-	0.8279	6.0085	3.3172	0.8130	4.6547
U	2.4893	-	0.8298	6.0214	3.3237	0.8139	4.6644
Mo	0.0582	0.0244	0.0357	0.4304	0.2361	0.0164	0.3324
Na	9.1730	9.4957	9.3880	8.3733	10.470	12.567	9.5310
C	0.0732	0.0708	0.0716	1.0859	1.0710	1.0868	1.0778
O	-	-	-	7.7557	12.717	7.7557	10.236
Fe	27.192	26.297	26.595	18.976	16.742	19.301	17.634
Cr	7.8448	7.5866	7.6726	4.9973	3.3981	5.0909	4.1332
Ni	3.7432	3.6200	3.6610	2.3845	1.6215	2.4292	1.9722
Mn	0.5760	0.5571	0.5634	0.3670	0.2495	0.3738	0.3035

[a]In one closed loop there are two Type A drawers and four Type B drawers.
[b]In one open loop there are two Type A (outer core drawer), two Type B, one Type C, and one Type D drawers.

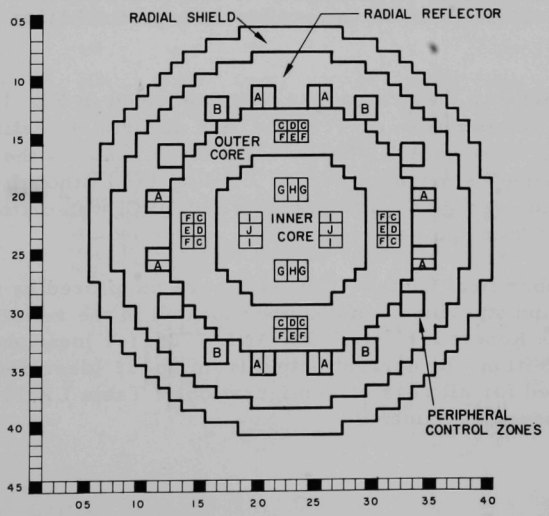

Fig. I.A.2
Reactor Zones Affected in Loop Experiments

TABLE I.A.8. Description of Reactor Configurations and k_{ex} Results for Loop Experiments

Loading No.	Zone[a]	Changes from Previous Loading: Composition Removed	Changes from Previous Loading: Composition Added	k_{ex}, 30°C, Ih	σ^b, Ih
114	Reference			+44.3	4.1
115	C	Outer Core	Open Loop B		
	D	Outer Core	Open Loop C		
	E	Outer Core	Open Loop D	-832.3	11.9
116	A	B_4C Control	Radial Reflector	-5.8	4.1
117	G	Inner Core	Closed Loop B		
	H	Inner Core	Closed Loop A	-1414	37
118	B	B_4C Control	Radial Reflector	-366.8	4.0
119	I	Inner Core	Closed Loop B		
	J	Inner Core	Closed Loop A	-1922	68

[a]See Fig. I.A.2 for description of reactor zones.

[b]Statistical uncertainty based on redundancy of measurements, not absolute accuracy. Includes ±4 Ih uncertainty in reproducibility of assembly.

reactor-zone compositions as they relate to zones described in Fig. I.A.2. All k_{ex} measurements, temperature corrections, and uncertainty estimates were carried out as described in ANL-7742. Table I.A.9 contains the details of the inverse-kinetics measurements. Loading 116, although slightly subcritical at an average core temperature of 30°C, was critical for the temperature at which k_{ex} was measured.

Subcritical neutron-flux data were monitored by four ^{235}U fission chambers and one boron ion chamber located in the reflector regions. (See Progress Report for July 1970, ANL-7726, for locations of these detectors.) In addition, the current output from Sp. 11 (described in ANL-7742) was recorded for all reactor configurations. Table I.A.10 lists the detector data for these experiments.

TABLE I.A.9. Details of Inverse Kinetics Rod Drop Measurements for Subcritical Reactor Configurations in Loop Experiments

Loading No.	Data Tape No.	Rods Dropped[a] Boron	Rods Dropped[a] Fuel	Chamber Used	Data Sampling Time (sec)	k_{ex}, T (Ih)	Temp. (°C)	k_{ex}, 30° (Ih)	$\overline{k_{ex}}$, 30° (Ih)
115	10/8/70 -1		1-10	Sp. 11	1/15	-861.1	32.7	-851.9	
	-2		1-10	Sp. 11	1/15	-839.6	31.0	-836.4	
	-3		1-10	Sp. 11	1/15	-832.0	30.0	-832.0	
	-4		1-10	Sp. 11	1/15	-801.4	27.8	-808.9	-832.3
117	10/13/70-1		1-10	Sp. 11	1/15	-1339	25.2	-1355	
	-2	1,2,4,5,7,8,10,11	3,5	Sp. 11	1/15	-1472	24.7	-1490	
	-3	2,5,8,11	4,9	Sp. 11	1/15	-1366	25.1	-1383	
	-4	2,4,6,8,10,12		Sp. 11	1/15	-1414	25.8	-1428	-1414
118	10/14/70-1	3,6,12		Sp. 11	1/15	-349.5	25.1	-366.4	
	-2	3,6,12		Sp. 11	1/15	-350.3	24.7	-367.2	
	-3	3,6,12		Sp. 11	1/15	-348.3	25.0	-366.5	
	-4	3,6,12		Sp. 11	1/15	-350.4	25.0	-367.1	-366.8
119	10/16/70-1	1-8, 10-12	2,3,5,6,7,9,10	Sp. 11	1/15	-1915	24.9	-1933	
	-2	1-8, 10-12	1-10	Sp. 11	1/15	-2014	25.1	-2030	
	-3		1-10	Sp. 11	1/15	-1754	25.1	-1772	
	-4	1-8, 10-12	1-10	Sp. 11	1/15	-1938	25.5	-1953	-1922

[a]See Progress Report for August 1970, ANL-7737, for location of control and safety rods.

TABLE I.A.10. Subcritical Neutron-flux Data for Loop Experiments

Loading No.	Fission Counters, counts/min[a] M32-32[b]	S13-13[b]	S13-33[b]	S27-19[b]	Current Chambers, amps M23-23[b]	Sp. 11[c]
115	76,313	62,383	106,698	53,775	0.5539×10^{-10}	0.3509×10^{-8}
116	-	-	-	-	0.823×10^{-7}	-
117	47,144	39,845	66,478	34,907	0.3120×10^{-10}	0.2361×10^{-8}
118	255,847	204,593	261,180	154,689	0.1331×10^{-9}	0.1069×10^{-7}
119	50,609	41,612	51,457	31,284	0.2364×10^{-10}	0.2136×10^{-8}

[a]Count rates are average of 10 one-min counts.
[b]See Progress Report for July 1970, ANL-7726, for description and location of flux-detection equipment.
[c]Four ^{10}B ion chambers in parallel suspended above stationary half columns 33-41 near the midplane.

(ii) Clean Critical Experiments (R. A. Lewis)

Last Reported: ANL-7742, pp. 6-8 (Sept 1970).

(a) Temperature Characteristics of ZPR-6 Assembly 7 (L. LeSage and E. Bohn)

Several thermocouples have been loaded into ZPR-6 Assembly 7 so that the temperatures of fuel plates located throughout the core may be monitored during operation. Each thermocouple has been attached to

the stainless steel cladding on the side of a fuel plate as indicated in Fig. I.A.3. The locations of 16 thermocouples currently in the core are listed in Table I.A.11. Eight of the thermocouples, located in drawers S26-23 and M26-23, provide an axial temperature profile, and four thermocouples (No. 5 through 8) provide a radial temperature profile.

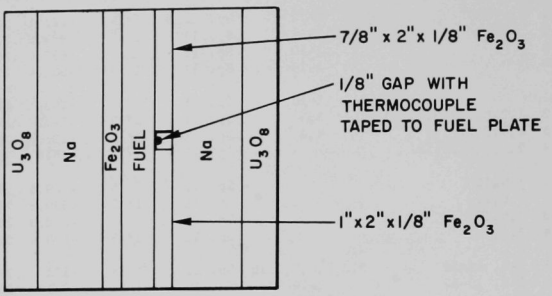

Fig. I.A.3. End View of Unit Cell with Thermocouple Attached to the Outside of a Fuel Plate

TABLE I.A.11. Locations of Thermocouples in ZPR-6 Assembly 7

Thermocouple No.	Drawer			Location in Drawer (distance from center of core, in.)
	Half[a]	Row	Column	
1	S	26	23	28
2	S	26	23	20
3	S	26	23	11
4	S	26	23	2
5	S	24	18	2
6	S	24	15	2
7	S	24	12	2
8	S	24	09	2
9	S	33	28	28
10	S	13	18	28
11	M	26	23	28
12	M	26	23	20
13	M	26	23	11
14	M	26	23	2
15	M	33	28	28
16	M	13	18	28

[a] S = stationary half, M = movable half.

Thermocouple readings were recorded at 10 min intervals during reactor operation on October 20, 1970. During operation, the reactor-cell air conditioning was on continuously and the reactor cooling fans ran at an intermediate speed (18 in. H_2O pressure across the core). Axial temperature profiles for various times during the operation are displayed in Fig. I.A.4. The axial profile is relatively flat at the beginning of operation (curve 1). With the halves together and cooling air entering the reactor matrix through the back of the movable half, the temperature drops rapidly at the rear of the movable half (curve 2). As cooling continues, the temperatures drop along the reactor axis and eventually (after about 2 hr of operation) establish an equilibrium profile (curve 4).

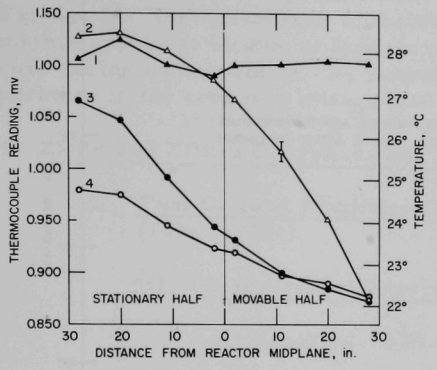

Fig. I.A.4

Axial Temperature Profiles Recorded during ZPR-6 Assembly 7 Reactor Operation on October 20, 1970. Curve 1, reactor halves together, cooling fans have been on for 4 min; curve 2, reactor critical, cooling fans have been on for 24 min; curve 3, cooling fans have been on for 1 hr 14 min; curve 4, cooling fans have been on for 3 hr 14 min.

The radial temperature profile at the reactor midplane was found to be nearly flat from core center to edge during operation. The average axial and radial temperatures during reactor operation are shown in Fig. I.A.5. Here it is seen that after the halves are closed, nearly 2 hr are required to reach a temperature equilibrium.

A preliminary value of the temperature coefficient of reactivity for Assembly 7 was obtained by inserting a control rod to yield an initial period corresponding to 4 Ih and recording the temperature increase (thermocouples 1, 4, 12, 13, and 14) and reactivity decrease over 20 min. The period was analyzed several times during the run by the Hürlimann-Schmid technique.* An increase in average temperature of 0.63°C and a reactivity decrease of 2.2 Ih were recorded, giving a temperature coefficient of reactivity of 3.5 Ih/°C.

An indication of the effect of temperature on the results of various reactivity calibration techniques may be deduced from data in Table I.A.12 which displays the comparison of the inverse kinetics and Hürlimann-Schmid period methods of reactivity measurement. With the reactor stable and a few inhours subcritical, a DP rod was driven into the core. The resulting reactivity change was analyzed by inverse kinetics during and immediately following the reactivity change and by the period

*T. Hürlimann and P. Schmid, Determination of the Stable Reactor Period in the Presence of a Neutron Source, Nucleonik 5, No. 6 (1963).

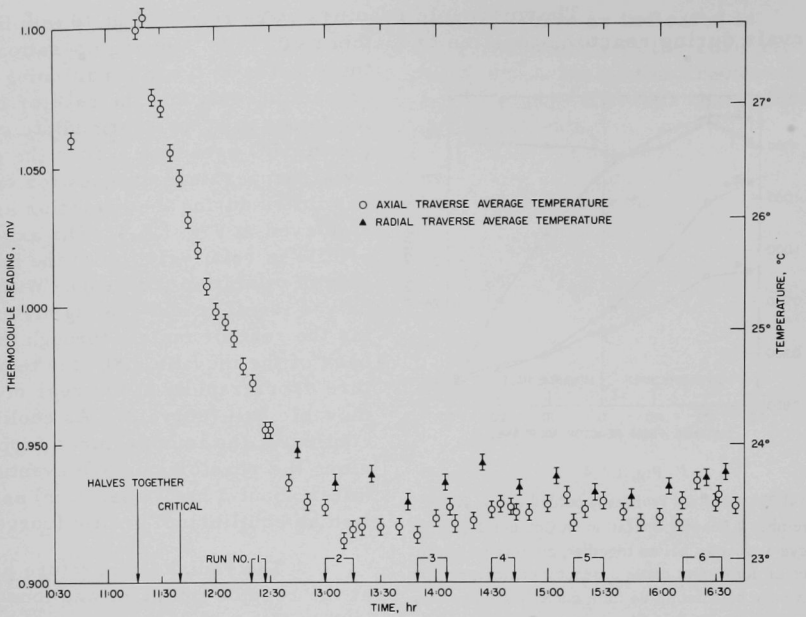

Fig. I.A.5. Average Axial and Radial Temperatures during ZPR-6 Assembly 7 Reactor Operation on October 20, 1970. Runs 1 through 6 refer to period-reactivity measurements during which the reactor power rose a factor of 15 over the reference power. At the end of each run, the reactor was returned to the reference power.

TABLE I.A.12. Comparison of Inverse Kinetics and Hürlimann-Schmid Methods of Reactivity Measurement in ZPR-6 Assembly 7

Run	Inverse Kinetics[a]		Hürlimann-Schmid Period[b]
	Initial Reactivity, Ih	Final Reactivity, Ih	Final Reactivity, Ih
1	-12.673	15.478	16.502
2	-14.328	8.323	8.628
			8.650
			8.694
3	-14.416	8.159	7.945
			7.936
			7.840
4	-14.185	8.233	8.108
			8.171
5	-14.081	8.180	7.960
			7.876
			7.966
6	-14.348	6.229	6.096
			6.035
			6.031

[a]Reactor was initially subcritical; a rod was inserted to give a final reactivity.
[b]As the reactor power rose, period measurements were obtained until the chamber current exceeded the range of the computer input devices.

method, a number of times, a few minutes after the reactivity change. The two methods agree to within 4% for all runs, the largest difference being obtained for Run 1 during which the reactor was still cooling down (see Fig. I.A.5). The differences in the final reactivities computed with each method appear to be due, at least in part, to temperature changes in the core during measurement. As indicated in Fig. I.A.5, the average temperature in the core may change by 0.25°C during a measurement.

4. ZPPR and ZPR-3 Operations and Analysis

a. Fast Critical Facilities Experiments and Evaluation--Idaho (189a 02-181)

(i) Clean Critical Experiments (P. I. Amundson)

Last Reported: ANL-7742, pp. 15-16 (Sept 1970).

(a) ZPPR Assembly 2 (R. E. Kaiser)

Operations have been resumed following cell-integrity tests. Some additional radial reactivity traverses were performed with tantalum and ^{10}B samples, and a new reference core was established with boron shim control and no fuel-spiked control rods. Work was then begun on a program of comprehensive measurements on the worths, interaction effects, and flux distortion of boron and tantalum control rods.

The reactivity traverses were performed by inverse-kinetics techniques, with the sample moving from full out to full in and back, in steps of 2.173 in. (one matrix-tube width). The stepwise motion provides sufficient data for an accurate evaluation of reactor drift, and the inverse-kinetics technique eliminates the need for a calibrated autorod. The samples used were ^{10}B and tantalum and were intended, along with previous measurements, to provide data for the program of control-rod studies now in progress.

A new reference core was established, with equal zone volumes, after the installation of shim-control rods had eliminated the need for spiked control rods. The interface diagram of this core is shown in Fig. I.A.6. The corrected critical mass has not yet been determined, though it should be very close to the same as the previously quoted values for the 50/50 core. The volume of the new version is 2400 liters.

An extensive program of experiments on control rods and control-rod materials has been started. Measurements performed to date include small sample radial reactivity traverses and central worths, and measurements of the worth of 6-in.-long plate and rod samples in an experimental drawer (reported in Progress Report for April-May 1970, ANL-7688). Both boron and tantalum samples were used.

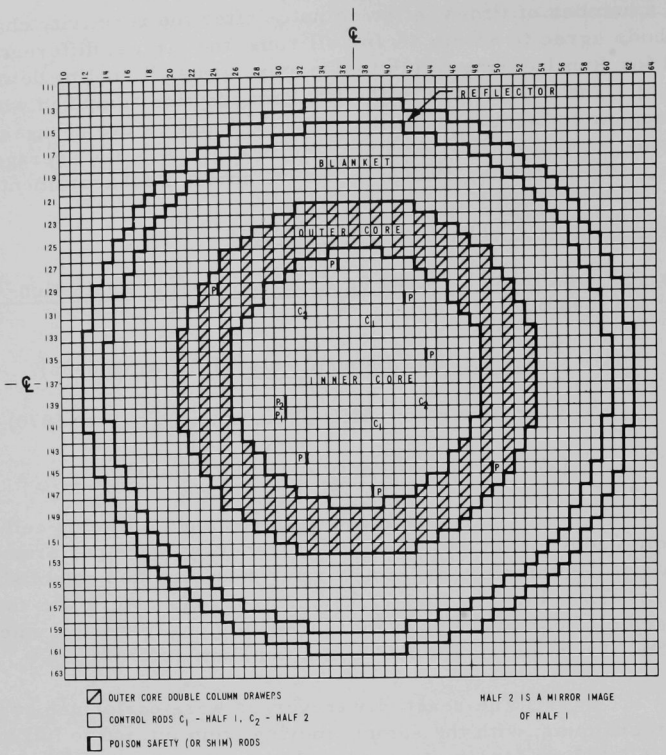

Fig. I.A.6. Reference Loading for Assembly 2 with Equal Zone Volumes and No Spiked Control Rods. ANL Neg. No. ID-103-A11520.

(ii) Mockup Critical Experiments (W. P. Keeney, R. O. Vosburgh, and D. Meneghetti)

Last Reported: ANL-7742, pp. 16-21 (Sept 1970).

(a) Experimental Status. The experimental program of Assembly 62, Second Step, has been completed. The final experiments conducted were gamma-dose measurements using thermoluminescent dosimeters, foil irradiations, and a supplementary tantalum worth and self-shielding measurement. After a sufficient waiting period to allow decay of core radiation, the fissile material was removed from the core region. Loading of partial driver and oxide-type core drawers for the initial configuration of Assembly 63 is now in progress.

(b) Experimental Results, Assembly 62, Second Step

(1) Thermoluminescent Dosimeter Measurements in Assemblies 61 and 62 (G. G. Simons)

Thermoluminescent dosimeter (TLD) dose mapping studies similar to those reported for ZPR-3 Assembly 60 (see Reactor Development Program Progress Report for April-May 1970, ANL-7688, pp. 35-42) were completed in ZPR-3 Assemblies 61 and 62. TLD dose heterogeneity measurements were also made across the core/reflector and reflector/blanket interfaces.

Both axial and radial dose traverses were completed throughout the two assemblies. Figure I.A.7 shows the result of the relative radial dose traverses along the P row. These curves are normalized to the dose near the core center.

The heterogeneity and boundary dose traverses across drawers 1-P-11/1-P-10 and 1-P-7/1-P-6, the core/reflector and reflector/blanket interfaces, are shown in Figs. I.A.8 and I.A.9. The centerline of the TLD marked as "Reference TLD," in drawer 1-P-10, was at a position approximately equivalent to the radial drawer position of the steel inserts used in the dose traverse measurements.

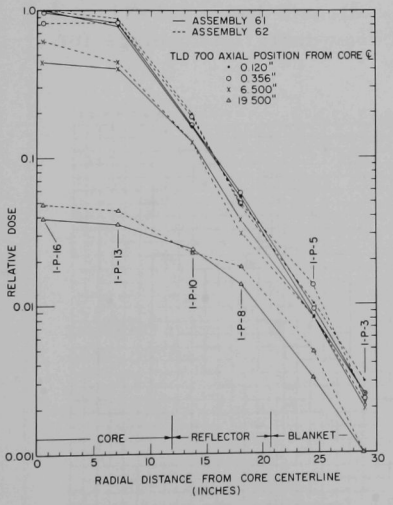

Fig. I.A.7. ZPR-3 Assemblies 61 and 62 TLD-700 Radial Traverses, P Row. ANL Neg. No. ID-103-A11502.

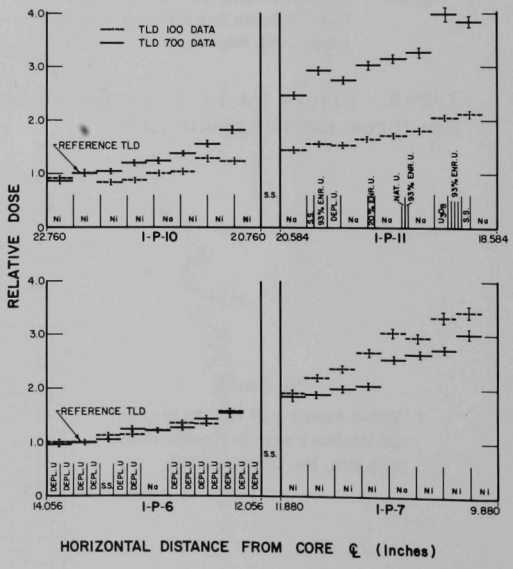

Fig. I.A.8. ZPR-3 Assembly 61 TLD Traverses across Core/Reflector and Reflector/Blanket Interfaces. ANL Neg. No. ID-103-A2104.

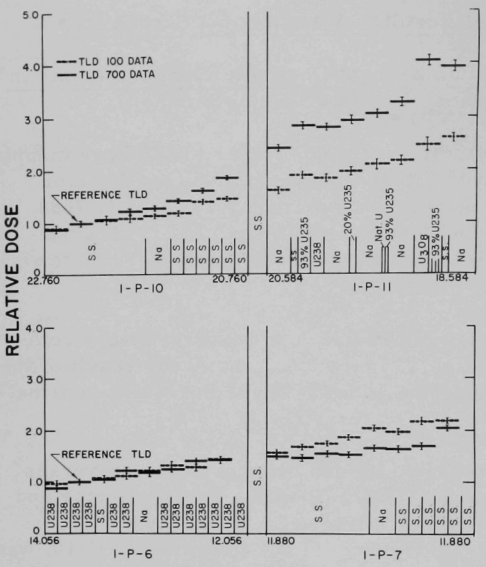

Fig. I.A.9. ZPR-3 Assembly 62 TLD Traverses across Core/Reflector and Reflector/Blanket Interfaces. ANL Neg. No. ID-103-A11501 Rev. 1.

Auxiliary experiments pertaining to TLD exposure from residual gamma rays and TLD encasement studies are presented in Sect. I.A.4.a(iv) below.

(2) Neutron Spectrum Measurement (G. G. Simons)

Three fast-neutron spectrum measurements were completed in ZPR-3 Assembly 62 (see Fig. I.A.10) using the proton-recoil proportional counter spectrometer. These data are graphed in Figs. I.A.11-I.A.13. A 3/8-in.-dia hydrogen and a 5/8-in.-dia methane-filled cylindrical counter, positioned with their centers of active volumes 1 in. from the core centerline, were used in partially voided drawers in matrix positions 1-P-16, 1-P-11, and 1-P-9. Figure I.A.14 shows the counter draw material loadings for the three matrix positions.

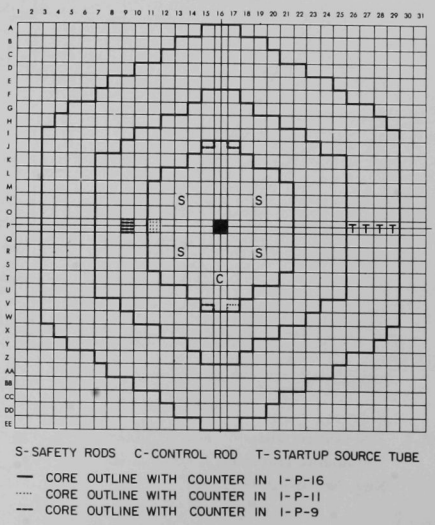

Fig. I.A.10

ZPR-3 Assembly 62 Loading Diagram for Neutron Spectrum Measurements. ANL Neg. No. ID-103-A2118.

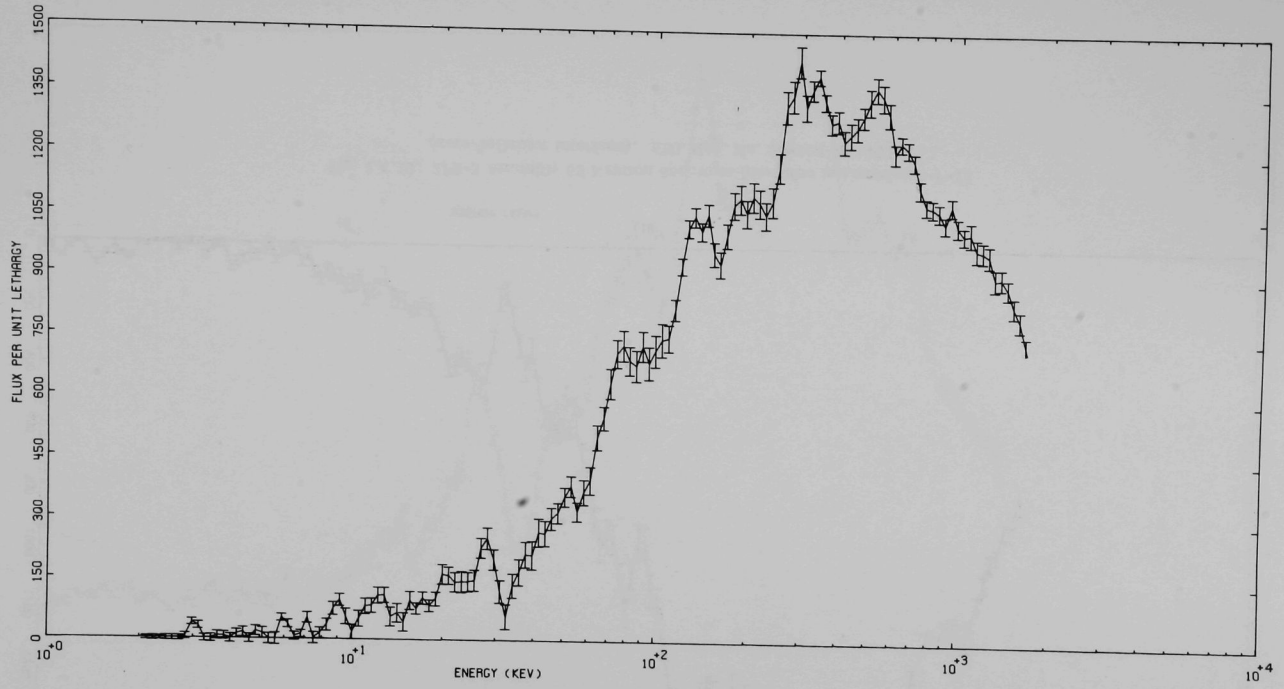

Fig. I.A.11. ZPR-3 Assembly 62 Neutron Spectrum Measured in Location 1-P-16 (core center). ANL Neg. No. ID-103-A2147 Rev. 1.

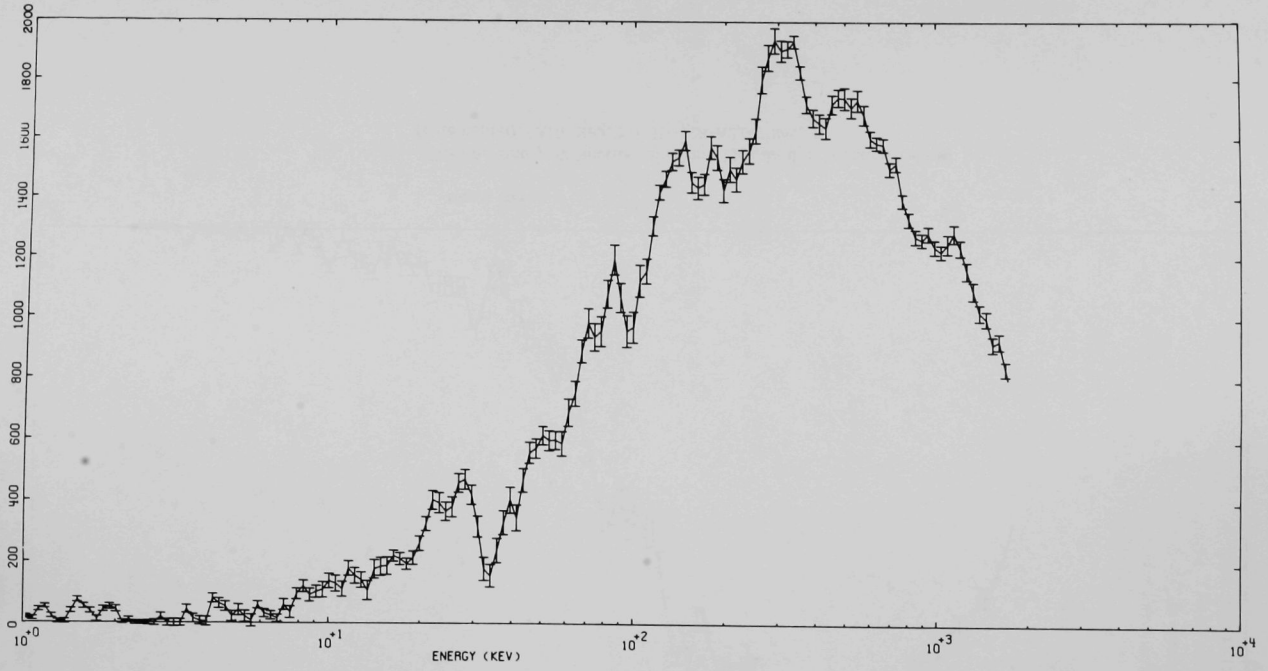

Fig. I.A.12. ZPR-3 Assembly 62 Neutron Spectrum Measured in Location 1-P-11 (core/reflector interface). ANL Neg. No. ID-103-A2145 Rev. 1.

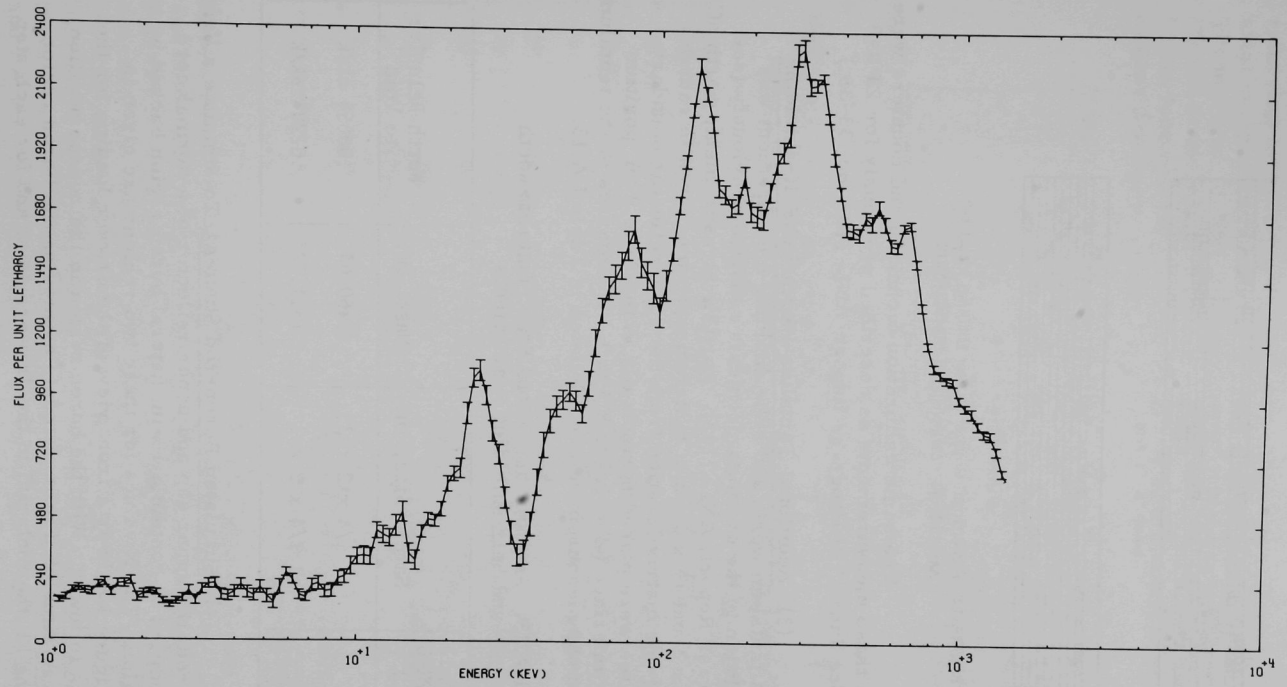

Fig. I.A.13. ZPR-3 Assembly 62 Neutron Spectrum Measured in Location 1-P-9 (reflector). ANL Neg. No. ID-103-A2144 Rev. 1.

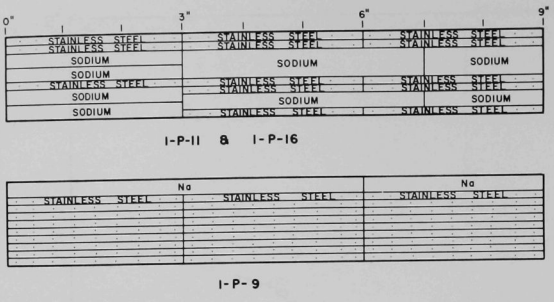

Fig. I.A.14. Proportional Counter Drawer Loadings for ZPR-3 Assembly 62. ANL Neg. No. ID-103-A2120.

The same calibration technique and counters were used to complete these measurements as described previously for ZPR-3 Assembly 61. (See June 1970 Progress Report, ANL-7705, pp. 33-35.)

(3) Additional Tantalum Worth and Self-shielding Measurement. A tantalum worth and self-shielding measurement was performed in addition to the two measurements reported previously (see September Progress Report, ANL-7742). For this measurement, worth of volumes 1/4 x 2 x 2 and $1\frac{1}{4}$ x 2 x 2 of tantalum were measured in radial position (1-P-12) one matrix location from the core-reflector boundary. The tantalum plates were placed horizontally in the 7- to 9-in. position from the reactor interface (Z = 6.5 to 8.5 in.). The masses of the tantalum and the results of the measurement are tabulated in Table I.A.13.

TABLE I.A.13. Assembly 62, Second Step, Tantalum-worth and Self-shielding Measurements

Position in 1-P-12 Relative to ZPR-3 Interface (in.)	Sample Size, in.	Mass, gm.	Worth Relative to Void
7 - 9	1/4 x 2 x 2	260.64	.0065% Δk/k
7 - 9	1 1/4 x 2 x 2	1311.72	.0220% Δk/k

(4) Simulated Boron-rod Studies. To simulate a boron-poisoned safety rod, the upper gap and upper reflector of a normal core drawer were modified to contain a 13-in. natural boron region backed by a rod follower region. The N values for these two regions are given in Table I.A.14. Figure I.A.15 is a front view of the drawer loading for the boron rod and its follower. With the boron region in the rod-up position, rod movement was simulated in increments by moving the boron region down, i.e., sliding all the material in the drawers down and for each step

removing lower reflector and adding follower material. There were four axial positions at which the worth of the simulated boron rod was measured. These were: (1) Rod full up, (2) rod inserted in the core region 2 in., (3) rod at the reactor interface, and (4) rod fully inserted in the core region. These four positions and the relative location of the core material in the drawer are shown in Fig. I.A.16.

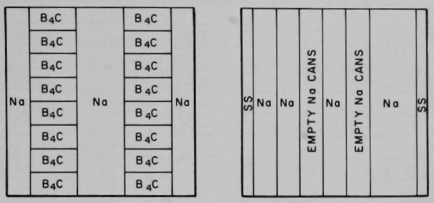

Fig. I.A.15

Front View of Boron Region and Follower Region of Simulated Boron Rod, Assembly 62. ANL Neg. No. ID-103-A2149.

TABLE I.A.14. Assembly 62, Second Step, Composition of Simulated Boron Rod Region and Rod Follower Region

(Units: 10^{24} atoms/cc)

Element	Boron Rod	Rod Follower
B-10	.007434	--
B-11	.031315	--
C	.010437	--
Na	.009117	.010742
Fe	.008696	.017828
Cr	.002163	.004435
Ni	.000947	.001941
Mn	.000090	.000185
Si	.000106	.000217

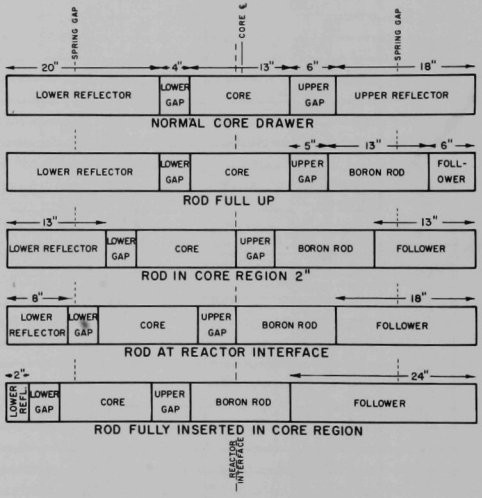

Fig. I.A.16. Relative Positions of Simulated Boron Rod to Core Regions, Assembly 62. ANL Neg. No. ID-103-A2148 Rev. 1.

The simulated boron-rod worths were measured in two matrix locations. In P-12, the worth of the boron rod in the full-up and at the reactor interface positions relative to normal configuration was measured. In addition, with the boron rod at the interface, edge core drawers were added to bring the system critical and axial reaction rate traverses were measured using ^{235}U, ^{238}U, and ^{10}B counters in the adjacent matrix (P-11) location to the boron rod. The results of the reaction-rate traverses in P-11 with the rod at the interface are given in Tables I.A.15 and I.A.16. In the second location, P-16, the worth of the boron rod at all

TABLE I.A.15. Assembly 62, Second Step, Axial ^{235}U and ^{238}U Counter Traverses Adjacent to Simulated Boron Rod in P-12. Simulated rod inserted to reactor interface.

Position (in.)	U-235 Rel. Count	U-235 Error	U-238 Rel. Count	U-238 Error
24.56	--	--	.0104	2.42
23.56	.7039	.78	--	--
21.56	.8260	.74	.0188	1.81
20.56	.8694	.73	--	--
19.56	.9154	.72	.0370	1.30
18.56	.9379	.72	--	--
17.56	.9588	.71	.0722	.94
16.56	.9833	.71	--	--
15.56	1.0143	.70	.1092	1.11
14.56	1.0568	.69	--	--
13.56	1.0948	.69	.1494	.96
12.56	1.1205	.69	.1793	.89
11.56	1.1541	.68	.2152	1.17
10.56	1.1529	.68	.2489	1.10
9.56	1.1423	.68	.3058	1.01
8.56	1.1351	.68	.3684	.95
7.56	1.0842	.69	.4659	.87
6.56	1.0184	.70	.6218	.79
5.56	.9505	.71	.7901	.74
4.56	.9611	.71	.8854	.71
3.56	.9844	.71	.9498	.70
2.56	.9895	.71	.9886	.69
1.56	1.0013	.70	1.0103	.69
- 0.53	1.0002	.70	.9997	.69
0	1.0000	--	1.0000	--
+ 0.50	.9899	.71	1.0027	.69
+ 1.50	.9757	.71	.9748	.70
+ 2.50	.9509	.71	.9429	.70
+ 3.50	.9307	.72	.8889	.71
+ 4.50	.9079	.72	.8148	.73
+ 5.50	.8958	.72	.7234	.76
+ 6.50	.9394	.72	.5516	.82
+ 7.50	1.0238	.70	.3982	.92
+ 8.50	1.0697	.69	.3034	1.02
+ 9.50	1.0901	.69	.2403	1.11
+10.50	1.1148	.69	.1895	.87
+11.50	1.1279	.68	.1504	.96
+12.50	1.1659	.68	.1210	1.06
+13.50	1.2193	.67	.0965	.83
+14.50	1.2542	.67	.0765	.92
+15.50	1.2381	.67	--	--
+16.50	1.2117	.67	.0470	1.16
+17.50	1.1749	.68	--	--
+18.50	1.1200	.69	.0297	1.45
+20.50	.9941	.71	.0178	1.86
+24.50	.6866	.78	.0070	2.94
+28.50	.3374	.99	.0024	4.99
+29.50	.2500	1.12	--	--
+30.50	.1615	1.34	--	--
+31.50	.1133	1.57	--	--

TABLE I.A.16. Assembly 62, Second Step, Axial ^{10}B Counter Traverse Adjacent to Simulated Boron Rod in P-12. Simulated rod inserted to reactor interface.

	Boron-Plated Side B-10 (N + G)		Blank Side B-10 (G)		Difference B-10 (N + G - G)	
Position (in.)	Rel. Count	Error	Rel. Count	Error	Rel. Count	Error
23.56	1.3974	.76	.0131	5.10	1.3842	.76
21.56	1.6011	.74	.0182	4.34	1.5829	.74
20.56	1.6798	.73	.0246	3.74	1.6550	.73
19.56	1.7076	.73	.0289	3.46	1.6786	.73
18.56	1.7217	.73	.0327	3.26	1.6889	.73
17.56	1.7391	.72	.0378	3.04	1.7012	.73
16.56	1.7508	.72	.0466	2.75	1.7041	.73
15.56	1.7770	.72	.0575	2.48	1.7193	.73
14.56	1.7979	.72	.0672	2.31	1.7304	.72
13.56	1.8273	.72	.0787	2.14	1.7483	.72
12.56	1.8427	.72	.0916	2.00	1.7508	.72
11.56	1.8407	.72	.1026	1.90	1.7378	.72
10.56	1.8360	.72	.1180	1.78	1.7176	.73
9.56	1.7934	.72	.1388	1.66	1.6541	.73
8.56	1.7052	.73	.1622	1.55	1.5426	.74
7.56	1.6225	.73	.1901	1.45	1.4319	.75
6.56	1.4628	.75	.2220	1.36	1.2402	.78
5.56	1.3310	.76	.2567	1.28	1.0738	.80
4.56	1.3160	.77	.2903	1.22	1.0250	.81
3.56	1.3182	.77	.3105	1.19	1.0071	.81
2.56	1.3265	.76	.3266	1.16	.9992	.82
1.56	1.3407	.76	.3301	1.16	1.0100	.81
- 0.53	1.3456	.76	.3307	1.16	1.0143	.81
0	1.3300	--	.3300	--	1.0000	--
+ 0.50	1.3311	.76	.3275	1.16	1.0031	.82
+ 1.50	1.3009	.77	.3250	1.17	.9753	.82
+ 2.50	1.2837	.77	.3075	1.19	.9756	.82
+ 3.50	1.2438	.77	.2871	1.22	.9561	.83
+ 4.50	1.2310	.78	.2636	1.27	.9669	.82
+ 5.50	1.2550	.77	.2396	1.32	1.0150	.81
+ 6.50	1.3630	.76	.1962	1.43	1.1662	.79
+ 7.50	1.5138	.74	.1641	1.54	1.3492	.76
+ 8.50	1.6151	.73	.1351	1.68	1.4796	.75
+ 9.50	1.7070	.73	.1203	1.77	1.5862	.74
+10.50	1.7895	.72	.0967	1.95	1.6925	.73
+11.50	1.8882	.71	.0876	2.04	1.8003	.72
+12.50	1.9898	.71	.0744	2.20	1.9151	.71
+13.50	2.1122	.70	.0615	2.41	2.0504	.70
+14.50	2.1888	.70	.0536	2.51	2.1350	.70
+15.50	2.2192	.69	.0442	2.82	2.1748	.70
+16.50	2.2116	.69	.0376	3.04	2.1738	.70
+17.50	2.1599	.70	.0323	3.28	2.1275	.70
+18.50	2.0898	.70	.0272	3.56	2.0626	.70
+20.50	1.9122	.71	.0191	4.23	1.8930	.71
+24.50	1.3535	.76	.0102	5.78	1.3433	.76
+28.50	.6661	.91	.0043	8.89	.6618	.92
+29.50	.4863	1.01	.0035	9.87	.4828	1.01
+30.50	.3369	1.15	.0030	10.55	.3338	1.16

four positions described above versus normal core configuration was measured. As before, with the boron rod at the interface in P-16, edge core drawers were added to bring the system critical. Then axial reaction-rate traverses with ^{235}U, ^{238}U, and ^{10}B were measured in the adjacent matrix location (P-15). The results of the reaction-rate traverses are tabulated in Tables I.A.17 and I.A.18.

The results of the boron rod worth measurements in P-12 and P-16 are given in Table I.A.19. The subcritical measurements were performed using two methods. Under the listing "Inverse Kinetics" in Table I.A.19, all negative values were obtained by the standard rod-drop technique using the power-history data. The errors quoted are those derived from the rod-drop analysis and multiple measurements. All positive k_{ex} data in both columns were either obtained by the standard subcritical count-rate method, in which the control-rod calibration is assumed to remain constant, or the position of the control rod at critical was interpreted as a measurement of excess reactivity. The errors quoted in these data are those attributed to the count rates only and do not include the uncertainties in control-rod calibration.

(iii) Doppler Experiments (R. E. Kaiser)

Last Reported: ANL-7742, p. 21 (Sept 1970).

Preparations are being made for a shakedown run of the ZPPR reactivity Doppler system after completion of the control-element experiment program.

The PuO_2 Doppler expansion effects in ZPR-3 have been analyzed, but the results indicate the need for further work on this aspect of the problem. The small, positive Doppler effect was more than counterbalanced by the large, negative expansion effect as expected, but the overall result compares poorly with experiment, as shown in Table I.A.20.

The technique used to determine the expansion correction is described by Till,* and is based on a collision-probability analysis. Two approaches were used, one using flat-source collision probabilities in a cylinder, and the other employing the rational approximation. The results for both cases are included in Table I.A.20.

Possible sources of error are the known discrepancies in ^{239}Pu cross sections in ENDF/B-68, uncertainty in the expansion coefficient for sintered pellets of 70% theoretical density PuO_2, and the somewhat approximate methods of calculating the expansion effect.

*C. E. Till, "Fissile Doppler Effect Measurement and the Effects of Thermal Expansion," Reactor Physics Division Annual Report, July 1, 1966 to June 30, 1967, ANL-7310, pp. 143-151 (Jan 1968).

TABLE I.A.17. Assembly 62, Second Step, Axial ^{235}U and ^{238}U Counter Traverses Adjacent to Simulated Boron Rod in P-16. Simulated rod inserted to reactor interface.

	U-235		U-238	
Position (in.)	Rel. Count	Error	Rel. Count	Error
24.56	.5632	.99	--	--
23.56	--	--	.0084	2.72
22.56	.6915	.93	--	--
21.56	.7368	.91	.0148	2.05
-20.56	.7851	.90	--	--
-19.56	.8128	.89	.0290	1.47
-18.56	.8367	.88	--	--
-17.56	.8640	.88	.0553	1.08
-16.56	.8795	.87	--	--
-15.56	.8993	.87	.0751	1.32
-14.56	.9265	.86	--	--
-13.56	.9493	.85	.1261	1.04
-12.56	.9678	.85	.1536	.96
-11.56	.9819	.85	.1878	.88
-10.56	.9687	.85	.2293	.81
- 9.56	.9616	.85	.2785	1.06
- 8.56	.9574	.85	.3497	.97
- 7.56	.9310	.86	.4471	.89
- 6.56	.9159	.86	.5877	.81
- 5.56	.9040	.86	.7497	.75
- 4.56	.9228	.86	.8524	.73
- 3.56	.9589	.85	.9219	.71
- 2.56	.9803	.85	.9698	.70
- 1.56	.9994	.84	.9988	.70
- 0.53	.9907	.84	1.0011	.70
0	1.0000	--	1.0000	--
+ 0.50	1.0003	.84	1.0004	.70
+ 1.50	.9846	.85	.9815	.70
+ 2.50	.9626	.85	.9415	.71
+ 3.50	.9211	.86	.8850	.72
+ 4.50	.8815	.87	.8053	.74
+ 5.50	.8374	.88	.7065	.77
+ 6.50	.8444	.88	.5522	.83
+ 7.50	.8772	.87	.4087	.92
+ 8.50	.8900	.87	.3154	1.01
+ 9.50	.9072	.86	.2436	1.12
+10.50	.9191	.86	.1905	.87
+11.50	.9441	.85	.1542	.96
+12.50	.9764	.85	.1219	1.06
+13.50	1.0208	.84	.0963	.83
+14.50	1.0402	.83	.0749	.94
+15.50	1.0513	.83	--	--
+16.50	1.0288	.84	.0453	1.19
+17.50	1.0026	.84	--	--
+18.50	.9468	.85	.0277	1.51
+20.50	.8566	.88	.0165	1.94
+24.50	.6074	.97	.0063	3.13
+28.50	.3041	1.24	.0025	4.96
+22.50	.7429	.91	--	--
+26.50	.4495	1.07	--	--
+30.50	.1501	1.65	--	--

TABLE I.A.18. Assembly 62, Second Step, Axial ^{10}B Counter Traverse Adjacent to Simulated Boron Rod in P-16. Simulated rod inserted to reactor interface.

Position (in.)	B-10 (N + G) Rel. Count	Error	B-10 (G) Rel. Count	Error	B-10 (N+ G - G) Rel. Count	Error
-24.56	1.8896	.95	.0178	5.85	1.8717	.95
-22.56	2.2159	.93	.0223	5.24	2.2957	.92
-21.56	2.3733	.92	.0274	4.74	2.3459	.92
-20.56	2.4626	.91	.0326	4.36	2.4300	.92
-19.56	2.5053	.91	.0396	3.97	2.4657	.91
-18.56	2.5288	.91	.0480	3.61	2.4807	.91
-17.56	2.5505	.91	.0632	3.17	2.4872	.91
-16.56	2.5301	.91	.0647	3.14	2.4653	.91
-15.56	2.5322	.91	.0886	2.71	2.4435	.91
-14.56	2.5228	.91	.1024	2.54	2.4202	.92
-13.56	2.5107	.91	.1160	2.40	2.3946	.92
-12.56	2.4786	.91	.1440	2.18	2.3344	.92
-11.56	2.3918	.92	.1574	2.10	2.2342	.93
-10.56	2.2748	.92	.1844	1.96	2.0902	.94
- 9.56	2.1682	.93	.2211	1.82	1.9469	.95
- 8.56	2.0371	.94	.2613	1.70	1.7756	.96
- 7.56	1.8818	.95	.3215	1.57	1.5600	.99
- 6.56	1.6896	.97	.3701	1.49	1.3192	1.02
- 5.56	1.5415	.99	.4261	1.41	1.1151	1.06
- 4.56	1.5254	.99	.4776	1.36	1.0476	1.08
- 3.56	1.5260	.99	.5158	1.32	1.0098	1.09
- 2.56	1.5482	.99	.5420	1.30	1.0059	1.09
- 1.56	1.5778	.99	.5681	1.28	1.0093	1.09
- 0.53	1.5881	.98	.5605	1.29	1.0273	1.08
0	1.5700	--	.5700	--	1.0000	--
+ 0.50	1.5615	.99	.5486	1.30	1.0126	1.09
+ 1.50	1.5472	.99	.5469	1.30	1.0001	1.09
+ 2.50	1.5028	.99	.5281	1.31	.9744	1.10
+ 3.50	1.4838	1.00	.4981	1.34	.9854	1.09
+ 4.50	1.4598	1.00	.4486	1.39	1.0109	1.09
+ 5.50	1.4656	1.00	.3883	1.46	1.0770	1.07
+ 6.50	1.5770	.99	.3262	1.56	1.2506	1.03
+ 7.50	1.7455	.97	.2722	1.67	1.4730	1.00
+ 8.50	1.8973	.95	.2210	1.82	1.6761	.97
+ 9.50	2.0618	.94	.1952	1.91	1.8664	.96
+10.50	2.2169	.93	.1609	2.08	2.0558	.94
+11.50	2.3723	.92	.1318	2.26	2.2403	.93
+12.50	2.5813	.91	.1177	2.38	2.4634	.91
+13.50	2.7574	.90	.1000	2.56	2.6575	.90
+14.50	2.8010	.90	.0920	2.66	2.7096	.90
+15.50	2.9602	.89	.0797	2.85	2.8804	.89
+16.50	3.0469	.89	.0654	3.12	2.9814	.89
+17.50	3.0517	.89	.0547	3.40	2.9970	.89
+18.50	3.0122	.89	.0485	3.60	2.9636	.89
+20.50	2.8224	.90	.0375	4.07	2.7848	.90
+24.50	2.1667	.93	.0185	5.74	2.1482	.93
+28.50	1.1982	1.04	.0089	8.22	1.1892	1.05
+19.50	2.9646	.89	.0388	4.01	2.9258	.89
+22.50	2.5349	.91	.0283	4.66	2.5065	.91
+26.50	1.7037	.97	.0113	7.33	1.6924	.97

TABLE I.A.19. Assembly 62, Second Step, Simulated Boron-rod Study

Step	Matrix Location	Loading	% k_{ex} of the Assembly		Δ % k_{ex}[a]
			Inverse Kinetics	Inverse Count Rate	
1	P-12	Normal Fuel Composition	+.137[b] ± .002	--	Reference Steps 2 and 3
2	P-12	Boron Rod Full Up	+.074[b] ± .001	--	-.063 ±.003
3	P-12	Boron Rod at Interface	-.388 ± .020	-.400 ± .014	-.525 ±.020
4	P-12	Boron Rod at Interface[c] (reactor returned to critical)	+.135 ± .002	--	--
5	P-16	Normal Fuel Composition	+.140[b] ± .002	--	Reference Step 6
6	P-16	Boron Rod Full Up	+.047 ± .001	--	-.093 ±.003
7	P-16	Normal Fuel Composition	+.138 ± .002	--	Reference steps 8 and 9
8	P-16	Boron Rod In Core 2"	-.343 ± .014	-.358 ± .014	-.481 ± .014
9	P-16	Boron Rod at Interface	-.793 ± .025	-.783 ± .035	-.931 ± .025
10	P-16	Boron Rod at Interface[d] (reactor returned to critical)	+.076[b] ± .001	--	Reference Step 11
11	P-16	Boron Rod Fully Inserted	-.196 ± .003	-.194 ± .002	-.272 ± .003

[a]From inverse kinetics data, relative to reference as noted.

[b]Reactor critical. k_{ex} determined by control rod position at critical.

[c]Reactor returned to critical by adding half drawers at 1&2-L-12, 1&2-T-12, 1&2-J-14, 1&2-V-14, 1&2-J-18, and 1&2-V-18.

[d]Reactor returned to critical by adding half drawers at 1&2-L-12, 1&2-T-12, 1&2-J-15 & 17, 1&2-V-15 & 17, 1&2-J-14 & 18 and 1&2-V-14 & 18.

TABLE I.A.20. Comparison of Experimental and Calculational Results for the PuO_2 Doppler Experiment in ZPR-3 Assembly 53

ΔT, °K	Δρ, Ih/kg of ^{239}Pu			
	Experiment	Calc. (No. Expansion)	Calc. (Cyl. Exp)	Calc. (Rat. Approx)[a]
300-500	-2.47 ± 0.05	+1.30	-6.82	-5.04
300-800	-6.03 ± 0.05	+2.76	-17.55	-13.08
300-1100	-8.52 ± 0.05	+3.54	-29.11	-21.93
Total sample at 300°K	+661.8 ± 1.7	998.1	-	-

[a]Expansion calculation based on the rational approximation.

(iv) Measurement of Shielding and Neutron Streaming (G. G. Simons)

Last Reported: ANL-7688, p. 27 (April-May 1970).

Auxiliary support data were obtained for the thermoluminescent dosimeter (TLD) studies performed in ZPR-3 Assemblies 60, 61, and 62. (See April-May 1970 Progress Report, ANL-7688, pp. 35-42, and Sect. I.A.4.a(ii)(b)(1) on p. 23 of this report.) Measurements in Assembly 62 included determination of the gamma-ray exposure in the TLD rods before and after the designated reactor-induced exposure and the TLD response variance as a function of encasement material and sleeve thickness.

A mock run was made to measure the fraction of the total TLD exposure from residual gamma rays from the time of insertion into the reactor matrix until startup. This consisted of loading the TLD rods throughout the reactor, driving the halves together, and then separating the halves. This exposure was found to be less than 0.075%, the total exposure during a typical 100-W-hr run.

The second auxiliary experiment involved measuring the TLD exposure from the instant of reactor shutdown until the TLD rods were removed from the reactor. This involved installing the ZPR-3 radial traverse tube which extended from the reactor control room into the reactor cell and through the ZPR-3 matrix. Following insertion of reference TLD rods in 1-Q-16, ZPR-3 was run at 100 W for 1 hr; then a special stainless steel tube loaded with both TLD-700 and TLD-100 rods was rapidly inserted radially into the reactor; then the reactor was shut down normally. Ten minutes after shutdown, the TLD rods were extracted. The maximum exposure was less than 1%, the exposure received at the same matrix positions during a previous 100-W-hr run in this assembly.

The effect of TLD rod encasement was studied by exposing both TLD-700 and TLD-100 rods to an equivalent in-core gamma-ray flux

while inside different thicknesses of steel, aluminum, and Teflon sleeves. (This exposure was made during the 100-W-hr run discussed above.) The encased TLD rods received a nominal 3000 rads in core positions 1-O-15, 1-O-17, 1-Q-15, and 1-Q-17. A 0.035-in. sleeve was used in both 1-O-17 and 1-O-15 to monitor the relative gamma-ray dose between the two positions. The doses at these two positions were the same at equivalent drawer locations. All the doses were then normalized to the doses in the 0.035-in. sleeves (see Table I.A.21). The normalized TLD-700 doses for the five different stainless steel sleeves are shown in Fig. I.A.17 along with the core materials present in the reactor drawer.

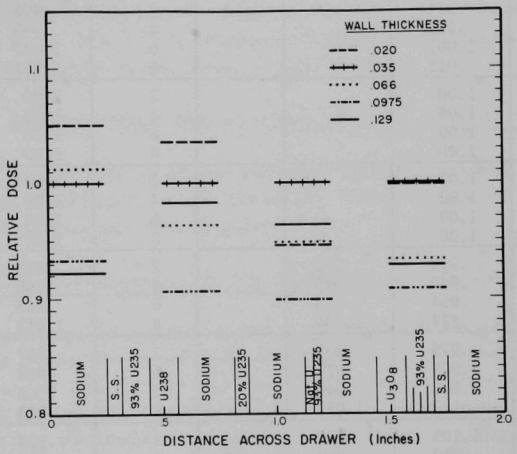

Fig. I.A.17. Gamma-ray Dose Variation as a Function of Encasement Material Measured in the ZPR-3 Assembly 62 Core. ANL Neg. No. ID-103-A11503.

TABLE I.A.21. TLD-100 and TLD-700 Readout Variations as a Function of Encasement Materials Following a 100 W-hr Exposure in ZPR-3 Assembly 62

Sleeve Wall Thickness (in.)	Position Across Drawer	Ratio of Dose: TLD / Reference TLD[b] — [a]TLD-100 Sleeve Materials: Stainless	Aluminum	Teflon	Position Across Drawer	TLD-700 Sleeve Materials: Stainless	Aluminum	Teflon
.020	1	#[c] .974			2	# .998		
	3	.939			4	.945		
	5	1.005			6	1.037		
	7	.911			8	1.051		
.035	1	* 1.00			2	* 1.00		
	3	1.00			4	1.00		
	5	1.00			6	1.00		
	7	1.00			8	1.00		
.035	1	+ 1.00			2	+ 1.00		
	3	1.00			4	1.00		
	5	1.00			6	1.00		
	7	1.00			8	1.00		
.066	1	+ .972	+ .995		2	+ .933	+ 1.104	
	3	.960	.995		4	.960	1.011	
	5	.954	1.023		6	.963	.972	
	7	.877	1.034		8	1.013	1.051	
.0975	1	* .978	* .962		2	* .907	* .949	
	3	.904	.911		4	.898	.961	
	5	.896	.949		6	.906	1.003	
	7	.887	1.017		8	.933	.940	
.129	1	@ 1.103	@ .977	@ 1.085	2	@ .928	@ .964	@ 1.003
	3	.909	.868	.870	4	.964	.885	.889
	5	.908	.930	.935	6	.983	.962	.976
	7	.958	.991	1.075	8	.922	.909	.959
.160	1			# .937	2			# .924
	3			.894	4			.884
	5			.992	6			.973
	7			.890	8			.971
.223	1		# .927		2		# .877	
	3		.936		4		.881	
	5		1.041		6		.917	
	7		.786		8		.949	

[a] Eight TLD rods were inserted into each sleeve starting with TLD 700 rod and alternating 700, 100, etc. These rod positions across the core cells were labeled 8, 7, 6, ---, 1.

[b] Reference TLD refers to the TLD encased in 0.035-in. stainless steel.

[c] Matrix Drawer Locations

* 1-O-15
@ 1-Q-15
\+ 1-O-17
\# 1-Q-17

B. Component Development

1. Instrumentation and Control

a. Instrumentation Development for Instrumented Subassembly (T. P. Mulcahey)(189a 02-024)

Instruments for in-core measurement of flow, fuel and coolant temperatures, and fuel-pin pressure are being developed consistent with requirements defined by the EBR-II Instrumented Subassembly test program. Development encompasses instrument design, performance analysis, fabrication, and tests leading to specifications and quality-assurance procedures for procurement from commercial vendors.

(i) Instrumented Subassembly (ISA) Flowmeters (G. A. Forster)

Calibrations of one commercially procured Mark III flowmeter in the Sodium Flowmeter Calibration Facility are in progress and should be completed by the end of November.

b. FFTF Instrumentation Development (R. A. Jaross)(189a 02-025)

Prototypes of permanent-magnet and eddy-current probe-type flowsensors are being designed, fabricated, and flowtested to establish detailed specifications and design for the FFTF permanent-magnet probe-type flowsensor, and to provide technical guidance to ensure competence in commercial fabrication of probe-type flowsensors. Supporting tests are conducted to determine radiation and long-term thermal effects on permanent-magnet materials of interest, and to study the effects of simulated fission-gas release on flowsensor response.

Flowtests and certain supporting tests are conducted in existing facilities (CCTL or CAMEL); new specialized facilities are designed and constructed, as required.

(i) In-core Flowsensors (T. P. Mulcahey)

(a) Permanent Magnet Probe-type Flowsensors (F. Verber)

Last Reported: ANL-7742, pp. 23-25 (Sept 1970).

As of October 19, 1970, the Type A-$4\frac{1}{4}$ Flowsensor (No. 1) has accumulated 2590 hr of testing in the CCTL in sodium at 1100°F and 16.4 ft/sec. During this time, the flowsensor output signal has decreased from the original value of 10.5 to 9.2 mV. The test will be continued for two weeks to determine a leveling-off point of the signal output. Meanwhile, the demagnetizing effect of CCTL electrical heaters located near the flowsensor is being investigated as a possible cause for the decrease in signal output.

As mentioned in ANL-7742, a sample of the magnetic particles found on Flowsensor A-4 was forwarded to an independent laboratory for chemical analysis. The results of this analysis are listed below.

Qualitative Analysis

Base	Fe
Major constituents	Cr, Ni, Na
Minor constituents	Mo, Mn, W
Traces	Si, Al, Cu, Ca

Quantitative Analysis

Fe	75.91%
Mn	0.29%
Ni	4.38%
Cr	1.79%
Na	1.06%

Notes:

1. Due to the small amount of sample available (0.0137 g), quantitative analysis for some of the minor and trace elements was not possible.
2. It may be assumed that some elements were present as oxides, based on total percentages of metallics found.

The quantitative analysis accounts for 83.43% of the 0.0137-g sample furnished. We were advised that a sample weighing at least 0.2 g and with ~5% oxides present would be required to permit identification of the oxides and their amounts. It is apparent that the high percentages of iron and nickel present as free elements or oxides, or both, account for the ferromagnetic properties of the particles.

During the FFTF Instrumentation Review Meeting in Richland, Washington, on September 2-4, 1970, ANL was requested to investigate the feasibility of an electromagnet, probe-type flowsensor.

Preliminary calculations for an electromagnet that would approximate the magnetic field produced by the permanent magnet of an A-$4\frac{1}{4}$ flowsensor indicate that approximately 1000 ampere-turns would be required and that the coil I^2R losses would be prohibitive.

A model electromagnet, which will be somewhat better than an air-core magnet, is under construction. It will be tested to determine whether the coil I^2R losses can be reduced to an acceptable value and still meet the minimum sensitivity requirement (2.2 mV at 220 gpm) of the flowsensor.

(b) Eddy-current Probe-type Flowsensors (J. Brewer)

Last Reported: ANL-7742, pp. 25-28 (Sept 1970).

A test was performed in the oscillating rig to determine the suitability of eddy-current probes for use in a dry thimble, as has been suggested for the FFTF. The test assembly consisted of a coil and bobbin (2X-4) with a 1-in.-OD, Type 304 stainless steel sheath, all enclosed in a Type 304 "thimble" (1.25 in. OD, 1.125 in. ID, 0.0625-in. wall thickness).

This assembly was oscillated laterally inside an aluminum sleeve (1.25-in. ID x 2-in. OD) that simulates flowing sodium. The results indicated almost 50% loss in probe sensitivity as compared to tests without the "thimble."

Eddy-current Probe No. 11 is being assembled for test in the CCTL. In preliminary tests in the oscillating rig, it exhibited the same sensitivity as Probe No. 10; however, the unbalance signal was approximately four times that of Probe No. 10. This is probably due to the uneven coating of alumina on the bobbin. Probe No. 11 will be ready for installation in the CCTL in about two weeks.

(c) Magnetometer Probe-type Flowsensors (D. Wiegand)

Following guidance generated at the FFTF Instrumentation Review Meeting at Richland, Washington, a feasibility study of a magnetometer-type flowsensor was initiated. Experimental work is pending fabrication of the flux-gate coils; however, theoretical work was done to show that the device can use either permanent magnets or electromagnets.

A computer program (MAGMOM) was written to calculate the magnetic moment of magnetic-spool-type electromagnets of any proportions operating under selected conditions.

Initial calculations were made for a conceptual design that uses two Alnico V magnets of 0.250-in. diameter and 1.125-in. length. These proportions are near those providing maximum external energy for full-strength Alnico V. A magnetic moment of 775 cgs units was estimated for the full-strength condition, and 155 cgs units for the temperature-stabilized condition.

The results showed that duplication of the full-strength value in electromagnets having the same overall size as the Alnico V magnets would require a prohibitive amount of excitation power. However, provision of the 155-unit stabilized value would require only 5 W at 1200°F.

c. Neutron-detector Channel Development (T. P. Mulcahey and G. F. Popper) (189a 02-138)

(i) Out-of-Core Detectors, Cables, and Circuits (A. Hirsch)

Last Reported: ANL-7737, pp. 44-46 (Aug 1970).

One of the two neutron detectors that were rebuilt by Reuter-Stokes (RSN-286) was shipped with readout instrumentation to EBR-II on October 16, 1970. The test assembly will be installed in the EBR-II before the next startup.

An apparent repair has been made to the second detector (RSN-286) by discharging a capacitor through the detector assembly while it was at 600°C. Temperature testing has been resumed.

d. Plant Dynamics and Control Analysis (W. C. Lipinski) (189a 02-528)

(i) Simplified Complete-plant Model

Last Reported: ANL-7742, p. 29 (Sept 1970).

In compliance with a work-plan milestone commitment, representatives from ANL and AEC-RDT met to discuss the simplified analytical model developed by ANL for the LMFBR complete-plant dynamics and control analysis. It was agreed that the model is acceptable as a basis for the next phase of the study, which will concentrate primarily on the characteristics of control of small perturbations about a fixed operating power level.

(ii) Simulation of Simplified Plant Model on Hybrid Computer

Not previously reported.

Included in the simplified plant model are pure time delays for the coolant temperatures introduced by transport lags through the piping connecting the major plant components. These time delays are to be simulated digitally on the hybrid computer; necessary programs are being written. For constant flow velocities, the variables are sampled and stored in the computer and become output after a fixed number of time delays. However, for the variable flow velocities to be used in the simulation, the time delay becomes a variable, dependent on the flow velocity history. The procedure being used to simulate variable time delay is to sample both temperature and flow velocity and store values for temperature variables that are averaged over fixed mass increments flowing in the piping. This is opposed to averaging over fixed time increments, as in the procedure for fixed flow velocity. The temperature stored in the computer becomes output after an additional number of mass increments, fixed at a constant value by the total pipe volume, have been sampled.

Signal flow diagrams for the analog simulation of the steam generator are also being completed.

2. Fuel Handling, Vessels, and Internals

a. Core Component Test Loop (CCTL) (R. A. Jaross) (189a 02-026)

The CCTL is operated, maintained, and modified to facilitate long-term tests of prototype FFTF fuel assemblies and in-core instrumentation in sodium under conditions established by the FFTF and LMFBR Programs. Technologies pertinent to sodium-loop operation--e.g., surveillance of sodium and cover-gas quality, and material compatibility, including the Type 304 loop structure--are developed and improved concurrently.

(i) Operation of Loop to Test Second FFTF Subassembly (F. A. Smith)

Last Reported: ANL-7742, pp. 48-49 (Sept 1970).

As of October 23, 1970, the CCTL has completed a total of 2893 hr of flowtesting at 1100°F and ~525 gpm. On October 9, the main sodium pump was arbitrarily shut down for a short period to investigate an extraneous building noise. The noise was traced to vibration of a loose mounting bolt on a building ventilator fan located 40 ft above the pump. Full-flow conditions were reestablished in less than 5 min from the time of pump shutdown.

On September 29, 1970, the CCTL sodium sample tube indicated a small leak in the region of a butt weld at one end of the tube. The tube was isolated and replaced without reducing loop operating conditions, including cold trapping. Details of this incident are described in Incident Report CCTL No. 3/ETD-IR-2 dated October 12, 1970.

In summary, the CCTL has accumulated 725 hr of flowtesting during the reporting period. The total downtime of about 0.07 hr results in an operating factor of 99.99+% at 1100°F, 525 gpm, and a pressure of 54 psig at the fuel assembly inlet.

A sodium sample removed for analysis on October 1, 1970, yielded an oxygen content of 6 ppm and a carbon content of 0.6 ppm. The plugging meter valve has been operated in the "closed" position with a plugging valve temperature range of 250-270°F with no decrease of flow, indicating a plugging temperature (for all impurities) of less than 250°F.

There has been no deviation, drift, or anomaly in the fuel assembly pressure or flow readings. The constant record of flow variables attest that the mechanical integrity of the FFTF fuel assembly has been maintained.

C. Experimental Breeder Reactor No. II--Research and Development

1. Equipment--Fuel Related (E. Hutter) (189a 02-045)

a. Handling Subassemblies Containing Failed Fuel

(i) Failed-fuel Transfer System (O. S. Seim, C. J. Divona, and R. Batch)

Last Reported: ANL-7679, pp. 34-36 (Mar 1970).

The failed-fuel transfer system (FFTS) was developed to provide a means of handling subassemblies containing fuel failures too severe for safe removal with the standard fuel-handling procedures. The basic requirements of the system are that it: (1) retrieve a failed-fuel subassembly from the transfer arm; (2) store the subassembly in the primary tank during its cooling period; (3) remove the subassembly from the primary tank; and (4) transfer the subassembly from the reactor building to the argon cell of the Fuels and Examination Facility (FEF).

The FFTS consists of three separate assemblies: the "X"-nozzle assembly, which seals and aligns the dipper; the dipper assembly, which extends through the "X" nozzle into the primary tank to retrieve and store a failed-fuel subassembly; and the assembly of a sealed container and a radiation shield, into which the dipper and subassembly are raised after being removed from the primary tank.

The "X"-nozzle assembly (see Fig. I.C.1) consists of a shield plug, extension tube, gate valve, and packing gland. The shield plug is inserted into the "X" nozzle and extends downward into the primary-tank sodium. The plug provides a $5\frac{1}{2}$-in. opening for the dipper and handling extension. Since the shield plug extends below the level of the primary-tank sodium, the dipper opening remains isolated from the primary-tank blanket gas. The shield plug has provisions for aligning the dipper with the transfer arm. An adjustable ring seal prevents leakage of blanket gas between the shield plug and the "X" nozzle.

The extension tube, gate valve (6 in.), and packing gland are fastened to the top of the shield plug. The extension tube is long enough to prevent the surfaces of the dipper assembly, which are exposed to sodium in the retrieval position, from leaving the inert atmosphere of the plug when the dipper is brought to the storage position. The gate valve seals the plug when the dipper is removed. Split, annular lead shields around the extension tube provide radiation protection.

The dipper (see Fig. I.C.1) is a closed-bottom tube $4\frac{1}{2}$ in. in diameter and slightly shorter than a fuel subassembly. To enhance

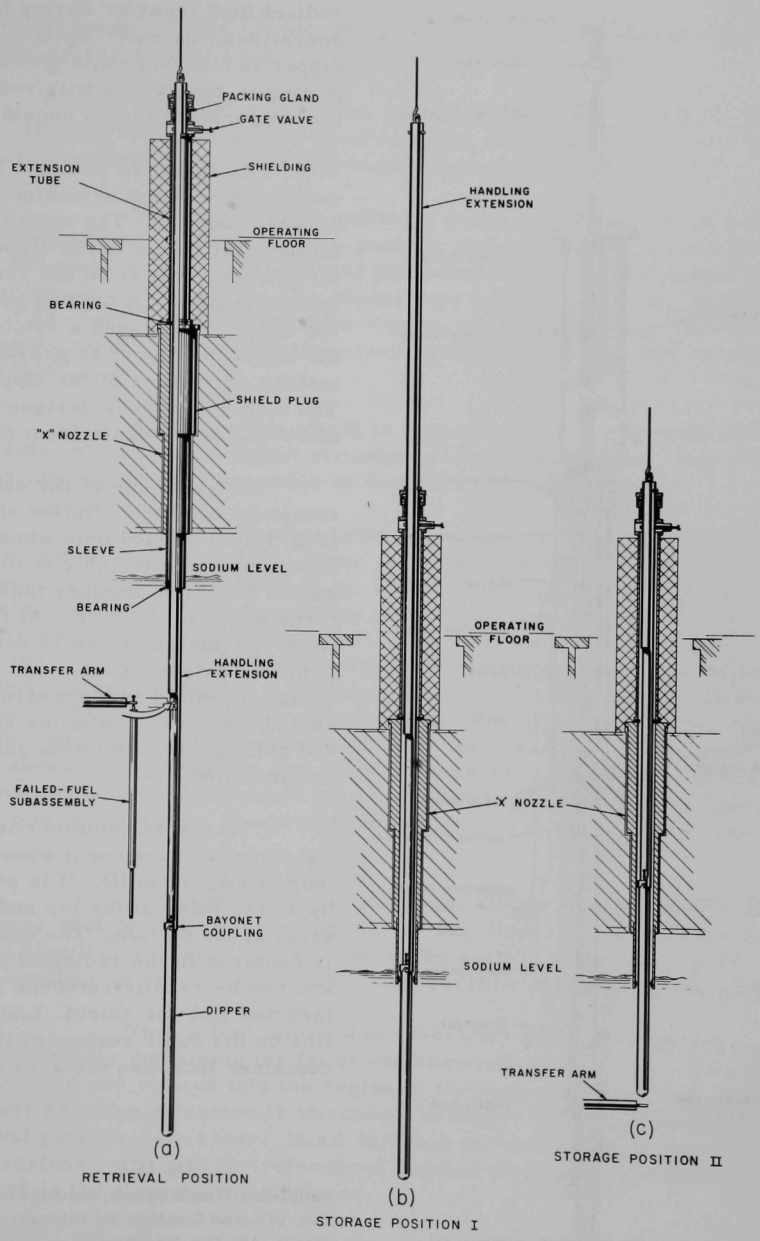

Fig. I.C.1. Failed-fuel Transfer System, Showing Dipper Positions. ANL Neg. No. 104-174.

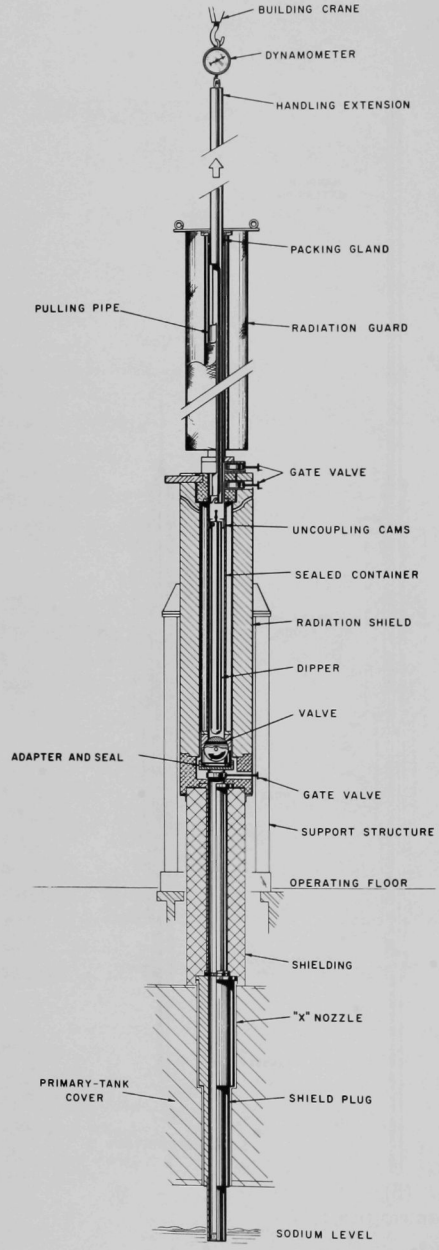

radiant heat transfer during handling operations, the outer surface of the dipper is black-chrome plated. The plating is compatible with sodium at the temperatures under consideration.

The dipper is attached to a two-piece handling extension by a bayonet coupling. The extension allows positioning of the dipper in the primary tank from the reactor operating floor. A locking pawl in the extension engages a cutout at the top of the dipper to prevent premature uncoupling of the dipper. The coupling joint is designed to allow sodium to drain from it.

The assembly of the sealed container and the radiation shield (Fig. I.C.2) is used only when the failed-fuel subassembly is to be removed from the primary tank and transferred to the FEF. At that time, the packing gland is removed from the extension tube, and the radiation-shield support structure, sealed container, radiation shield, and pulling-pipe radiation guard are installed.

The sealed container is a gas-tight tubular component about 9 ft long and $5\frac{1}{2}$ in. in ID. It is sealed by a gate valve at the top and a plug valve at the bottom. The container is centered in the radiation shield and can be readily removed from or inserted into the shield. Longitudinal fins on the outer surface of the sealed container increase the area exposed

Fig. I.C.2
Failed-fuel Transfer System, Showing Placement of Sealed Container and Radiation Shield. ANL Neg. No. 104-173.

for heat removal. Cams for unlocking and uncoupling the dipper from the handling extension are inside the top of the sealed container.

The radiation shield, which weighs about 15 tons, is a 12-in.-ID tube surrounded by 9 in. of lead and an outer steel jacket. It is compatible with existing carts and handling procedures.

The pulling-pipe radiation guard is fastened to the radiation shield above the gate valve. A packing gland at the top of the pipe seals the system; the guard protects personnel from possible radiation streaming above the shield. The pulling pipe holds the handling extension after it has been uncoupled from the dipper, and prevents any surfaces previously exposed to sodium from leaving the inert atmosphere beneath the packing gland.

The radiation shield is supported by a rectangular structure fastened to the top support structure of the primary tank. The structure is jointed for easy assembly or disassembly and removal.

When the system is installed, the "X"-nozzle shield plug is first installed in the nozzle. Next, the extension tube with the gate valve attached is bolted to the shield plug. Finally, the dipper and the handling-extension assembly, with the packing gland in position, are lowered through the gate valve into the primary tank. Owing to bowing of the primary-tank cover, the "X" nozzle must be tilted from the vertical and the shield plug adjusted to align the dipper vertically. The plug is adjusted with the aid of the transfer arm and a dummy subassembly. The dipper-alignment tests include disengagement and reengagement of the transfer arm and removal of the subassembly from the dipper by the transfer arm. When the desired alignment is attained, the shield plug is locked in place, and reference levels on the plug are zeroed. The levels indicate future misalignments that may occur.

The angular orientation of the dipper is also referenced, and the dipper seating ring is locked in place. The dipper is then raised to storage position II (c in Fig. I.C.1) to rest on the seating ring until needed. The upper handling extension is removed for clearance on the operating floor.

When a fuel failure too severe for standard handling occurs, the subassembly containing the failure is removed from the core by the transfer arm and rotated into the region of the fuel-transfer port. After the upper handling extension is attached, the dipper is lowered into the retrieval position by a crane. In all handling operations, the dipper and its extensions remain in the referenced angular orientation initially determined in the alignment procedures.

In the retrieval position (a in Fig. I.C.1), the dipper opening is 1.765 in. below the lowest point of the subassembly hanging from the

transfer arm. The transfer arm is rotated until the subassembly is over the mouth of the dipper. The dipper is then raised until it contains the subassembly. If a "wiggle" test assures that the subassembly is within the dipper, the transfer arm is disengaged and rotated away.

The dipper and subassembly can then be raised and held at the selected elevation in the primary tank. In storage position I (b in Fig. I.C.1), the mouth of the dipper is about 2 in. above the level of sodium in the primary tank. In this position, most of the dipper is submerged in the primary-tank sodium, but the dipper sodium is isolated from the primary-tank sodium and blanket gas. In storage position II (c in Fig. I.C.1), the lower 50 in. of the dipper is submerged in the primary-tank sodium, and there is a $1\frac{7}{8}$-in. clearance between the bottom of the dipper and the top of a subassembly hanging on the transfer arm. The dipper sodium is also isolated from the primary-tank environment in this position. With the dipper in this position, standard fuel-handling procedures can be followed without interference from the dipper.

When the subassembly has cooled sufficiently for removal to the FEF, the radiation-shield support structure is erected above the "X" nozzle. The "X" nozzle is then purged with fresh argon, and the nozzle packing gland is removed to allow the sealed container and radiation shield to be brought into place. The bottom of the sealed container slips into an adapter on the nozzle gate valve to form a gastight seal with the nozzle. The pulling-pipe radiation guard is then fastened to the radiation shield, and the building crane, with a dynamometer attached, is coupled to the handling extension, which protrudes from the pulling-pipe packing gland. The dipper is raised by the crane out of the primary tank, through the "X"-nozzle shield plug, and into the sealed container. The "X"-nozzle gate valve and the sealed-container plug valve are closed before the dipper is uncoupled.

Further lifting of the dipper uncouples it from the handling extension. The extension is withdrawn into the pulling pipe, leaving the dipper suspended from two protrusions in the container wall. When the container's top gate valve is closed, the handling extension, along with the pulling-pipe radiation guard, can be removed, and a shielding plate on the radiation shield is slid into position above the gate valve.

The radiation shield with the subassembly inside can now be transferred to the basement beneath the air cell following the route normally taken by the interbuilding coffin. The dipper and its sodium are disposable, but the sealed container can be decontaminated and reused.

2. New Subassemblies and Experimental Support (E. Hutter) (189a 02-046)

a. Experimental-irradiation Subassemblies

(i) Design Characteristics of the Mark-E19D and Mark E19E Irradiation Subassemblies (O. S. Seim and W. R. Ware)

Not previously reported.

The Mark-E19D and Mark-E19E irradiation subassemblies are designed for experimental studies of oxide fuel elements. In common with other subassemblies of the Mark-E series, both are designed for irradiating unencapsulated fuel elements to burnups higher than those achieved safely in other types of subassemblies. (See Progress Report for September 1970, ANL-7742, p. 35.) The Mark E19D accommodates 19 test elements that are 60.9 in. long, 0.250 in. in diameter, and wrapped with a 0.062-in.-dia spacer wire. The Mark E19E accommodates 19 test elements that are 40 in. long, 0.250 in. in diameter, and wrapped with 0.040-in.-dia spacer wire.

Both subassemblies meet the basic requirements for all EBR-II irradiation subassemblies (see ANL-7742). They were also designed to: (1) accept the possibility of a rupture of the cladding of oxide test elements; (2) prevent sizable pieces of debris from leaving the subassembly; (3) prevent failure propagation to adjacent subassemblies; (4) accommodate fuel elements swollen in previous irradiations; (5) accommodate additional irradiation swelling of elements; and (6) provide protection to the outer hexagonal tube from an internal pressure pulse that may occur with failure of the cladding of an element.

Both the Mark E19D and the Mark E19E have an upper and a lower collector. The upper collector, constructed of perforated sheet, prevents particles larger than 0.045 in. in diameter from leaving the top of the subassembly. The lower collector, a cup form, collects any particles that may settle to the bottom of the subassembly. The lower collector for the Mark E19D contains the base of the test elements. The unencapsulated test elements are surrounded by an inner hexagonal liner (or tube) made in six radial sections so that it expands to accommodate oversize elements and irradiation swelling. A cylindrical tube with a 0.094-in. wall surrounds the hexagonal liner. The liner and the tube protect the outer hexagonal tube from molten fuel and pressure pulses that may be caused by rupture of element cladding.

The largest possible outside diameter (2.062 in.) of standard 3/32-in.-wall cylindrical tube that would fit inside the outer hexagonal tube was used for the inner protective cylinder of the subassembly. The cylinder is much more resistant to internal pressure than the hexagonal tube. Tests

have shown that, without the protective cylinder in place, pressure bursts representative of those accompanying cladding rupture could bulge the outer hexagonal tube enough to cause problems when removing the subassembly from the reactor.

Both subassemblies are designed to hold the maximum number (19) of 0.250-in.-OD elements that can be contained with a protective cylinder and hexagonal liner in an outer hexagonal tube of standard EBR-II dimensions. The Mark E19D is designed to accept 60.9-in.-long elements reconstituted from the Mark-F37 and Mark-F37A irradiation subassemblies. These full-length elements require a complex lower-collector arrangement. The Mark E19E is designed to accept 40-in.-long elements from the Mark-N37 irradiation subassembly. The element in the Mark E19E extends $7\frac{5}{8}$ in. below the core to allow space for a platform or reflector in the bottom of the element. The lower collector in the Mark E19E is a simple cup in the top of the lower reflector. The lower axial reflector (below the test elements) serves as a radiation shield to protect the permanently installed reactor-vessel structure.

Figures I.C.3 and I.C.4 show the features of the final design of the subassemblies. The outer structure of each uses standard hardware consisting of a lower adapter, an outer hexagonal tube, and a top end fixture. All internal and external hardware is Type 304 stainless steel. The 19 test elements are fastened in place at their bases by a standard design of element-support grid. The bottom tips of the elements are T-slotted to fit over the T-shaped grid bars. The holes in the orifice plate must be sized for the particular experiment to be irradiated.

The Mark E19D does not use a lower axial reflector; instead, it relies on material within the long elements for shielding. The lower collector in that subassembly has a thick base just below the element-support grid. Sodium is drained from two 1/16-in. holes in the center of this base and from four 1/16-in. slots in the heavy cylinder forming the walls of the cup.

The Mark E19E uses a $14\frac{29}{32}$-in.-long lower axial reflector that is welded to the lower adapter. The lower collector, located within this lower reflector, is a $1\frac{3}{8}$-in.-dia cup extending about 3 in. below the six 0.594-in.-dia upper flow holes. The cup has a 1/8-in. hole at the bottom for sodium drainage during fuel handling. This unusually large drain hole was selected to provide rapid drainage during normal fuel handling.

The velocity of sodium flow through the large inlet holes in the lower collector of both subassemblies should prevent debris from leaving these holes during operation. The volume of the collector is sufficient to contain debris resulting from element failure.

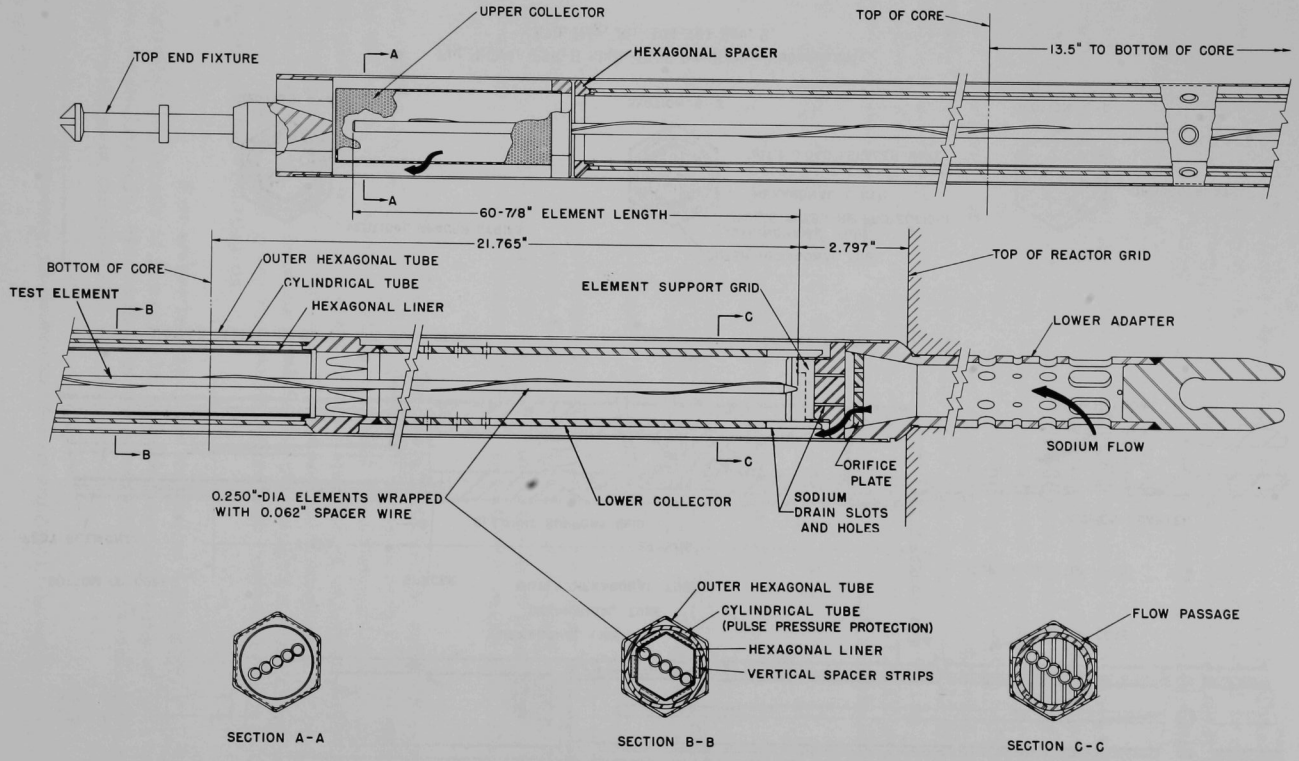

Fig. I.C.3. EBR-II Mark-E19D Irradiation Subassembly.
ANL Neg. No. 104-160 Rev. 2.

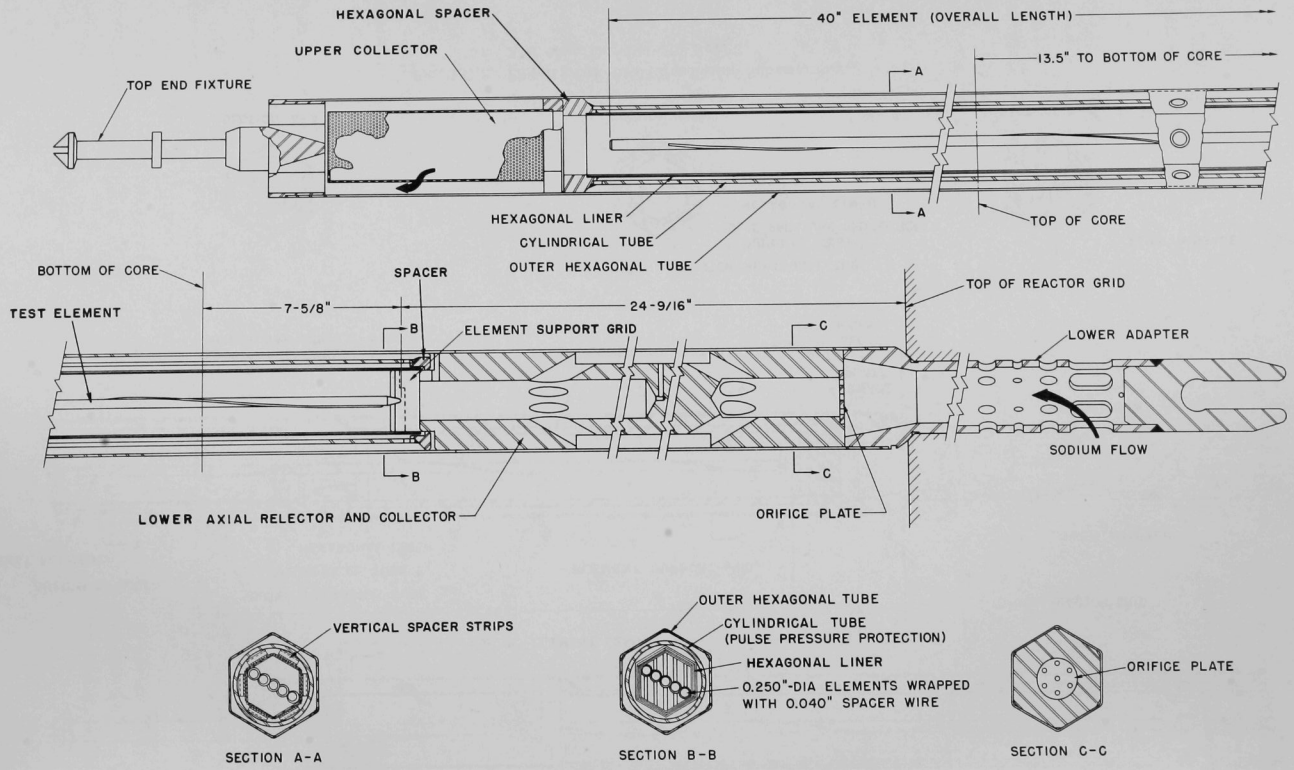

Fig. I.C.4. EBR-II Mark-E19E Irradiation Subassembly.
ANL Neg. No. 104-161 Rev. 2.

The top of the protective cylinder in both subassemblies is fastened to a hexagonal spacer. This spacer is plug-welded to the outer hexagonal tube. The cylinder is welded to a bottom spacer that floats inside the outer hexagonal tube. This design accommodates differential expansion and slight bowing of the cylinder.

The inner hexagonal tube, which is fairly fluid tight, is made of six 120°-angle segments, each overlapped one flat. The laps are closed by very light pressure from six vertical spacers, one of which is located between each flat of the inner hexagonal tube and the protective cylinder. A flow of sodium coolant is admitted to the space between the inner hexagonal tube and the cylinder through a slot at the supporting spacer below the core. The pressure of this coolant tends to press the walls of the inner hexagonal tube against the test elements and to accommodate swelling variations along the element length. This arrangement helps to maintain a favorable flow distribution through the element bundle.

3. Coolant Chemistry (D. W. Cissel) (189a 02-051)

a. Monitoring of Sodium-Coolant Quality

(i) Improved Methods for Detecting Water-to-Sodium Leaks in the EBR-II Secondary System (S. Greenberg)

Not previously reported.

A system that provides improved sensitivity and response time for detection of water-to-sodium leaks is desirable. Oxygen and hydrogen meters suitable for direct immersion in sodium, now under development in the ANL Sodium Technology activity, make this objective feasible.

Calculations to determine sensitivity and response time for different deployments of oxygen and hydrogen meters have been made. On the basis of economic and operational requirements and the fact that the systems are still in a state of development, it is tentatively recommended that one detector module* be installed downstream of the EBR-II superheaters. A calibration module for the oxygen meter will also be required. Table I.C.1 gives the sensitivities and response times for the recommended installation.

For water leakage, the minimum detectable rates result in negligible (in terms of reasonable shutdown times) rates of tube wastage. For steam leakage, extrapolation of recent APDA data indicates rates of tube wastage of the order of 3 mils/min.

*To achieve desired redundancy, the recommended detector module will consist of an oxygen meter and a hydrogen meter.

TABLE I.C.1. Sensitivities and Response Times for Combination of Oxygen Meter and Hydrogen Meter Downstream of EBR-II Superheaters[a]

	Min Leak Rate, lb/sec		Response Time, sec	
	Oxygen Detector	Hydrogen Detector	Oxygen Detector	Hydrogen Detector
Leak in superheaters	2.42×10^{-5}	1.29×10^{-5}	5	15
Leak in evaporators	2.42×10^{-5}	1.29×10^{-5}	~120	~120

[a]The assumptions upon which this table are based are: (a) power level, 62.5 MWt; limit of oxygen detection, 30 ppb; limit of hydrogen detection, 2 ppb; lag time of oxygen meter, nil; lag time of hydrogen meter, ~10 sec.

Development and specification of the improved system will continue in cooperation with the ANL Sodium Technology activity.

(ii) Analytical Cold Trap (W. H. Olson, E. R. Ebersole, and T. P. Ramachandran)

The prototype of the analytical cold trap, described in the Progress Report for April-May 1970 (ANL-7688, pp. 91-93), was disassembled in an inert-atmosphere glovebox, and the sample sections were analyzed for metals. Significant amounts of calcium, magnesium, and copper were found. Calcium and magnesium are impurities in the titanium-mesh packing of the cold trap. Copper came from a sample placed upstream of the trap during the operational test. The copper sample lost 290 mg during the operational test, and 197 mg of copper were found in the trap. Figure I.C.5 shows the distribution of copper in the trap as a function of temperature. The cold end of the prototype was not packed with mesh, so there

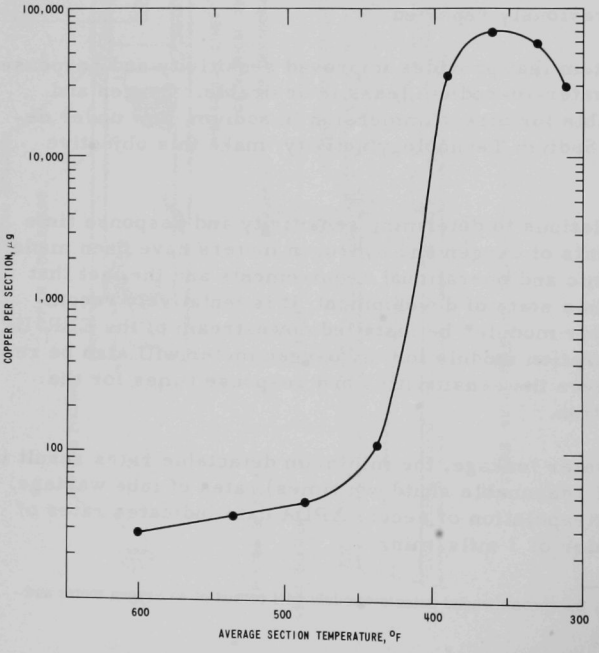

Fig. I.C.5
Distribution of Copper in Prototype of Analytical Cold Trap.
ANL Neg. No. IF-103-N5403.

are no data below about 300°F. In future traps, the cold end will be sectioned and packed with mesh as are the other sections of the trap.

4. Experimental Irradiation and Testing (R. Neidner) (189a 02-053)

a. Experimental Irradiations

Last Reported: ANL-7742, p. 48 (Sept 1970).

Table I.C.2 shows the status of the experimental irradiations in EBR-II on October 15.

TABLE I.C.2. Status of Experimental Irradiations in EBR-II as of October 15, 1970 (Run 46B in Progress)

Subassembly No. and (Position)	Date Charged	Capsule Content and (Number of Capsules)		Experimenter	Accumulated Exposure, MWd	Estimated Goal Exposure, MWd	Burnup[a]
XX02 (5F3)	4/13/70	UO_2-25 wt % PuO_2	(36)	HEDL	6,495	8,000	2.5
XG03A (8D2)	9/14/70	UO_2-20 wt % PuO_2	(2)	GE	1,100	5,000	0.3 + 8.0[b] = 8.3
XG04A (8A7)	9/15/70	UO_2-20 wt % PuO_2	(2)	GE	1,100	11,000	0.3 + 8.5[b] = 8.8
X058 (6F1)	4/24/69	UO_2-25 wt % PuO_2	(37)	GE	15,681	16,000	5.7
X061 (7A5)	4/23/69	Structural	(7)	INC	16,451	18,000	3.5
X062 (6F3)	5/23/69	UO_2-25 wt % PuO_2	(37)	GE	13,778	13,400	5.8
X073 (6C3)	12/12/69	UO_2-25 wt % PuO_2	(37)	HEDL	10,351	29,600	2.4
X076 (7D3)	3/27/70	UO_2-25 wt % PuO_2	(19)	WARD	6,652	15,000	2.4
X079 (4B2)	4/17/70	$(U_{0.85}$-$Pu_{0.15})C$	(19)	UNC	6,495	6,300	3.4
X080 (6E5)	9/11/70	UO_2-20 wt % PuO_2 Structural Structural	(12) (1) (4)	NUMEC/ANL GE GE	1,100	2,900	0.4 + 11.0[b] = 11.4 0.2 + 8.2[b] = 8.4 0.2 + 1.0[b] = 1.2
X081 (7C5)	5/24/70	UO_2-25 wt % PuO_2	(9)	GE	5,151	16,000	1.8 + 6.7[b] = 8.5
X083 (5E2)	9/15/70	Mark IA	(61)	ANL	1,100	10,000	0.4
X086 (4D3)	8/7/70	$(U_{0.8}$-$Pu_{0.2})N$ $(U_{0.8}$-$Pu_{0.2})C$ $(U_{0.8}$-$Pu_{0.2})C$	(10) (5) (4)	BMI LASL WARD	2,450	6,000	1.3 1.3 1.2
X088 (6F4)	5/24/70	UO_2-25 wt % PuO_2	(19)	WARD	5,151	12,500	1.4
X089 (2F1)	9/15/70	Structural	(7)	HEDL	1,100	7,800	0.4
X090 (7D5)	9/15/70	Structural Structural Structural Structural	(4) (1) (1) (1)	BMI INC ORNL HEDL	1,100	6,700	0.2 0.2 0.2 0.2
X091 (4E3)	9/11/70	Structural	(7)	HEDL	1,100	16,000	0.3
X092 (7B3)	9/15/70	Structural	(1)	LASL	1,100	2,700	0.2
X095 (7A5)	9/18/70	Structural	(1)	NRL	1,100	11,000	0.2
X100 (2D1)	10/7/70	Structural	(7)	ORNL	350	10,000	0.1
X103 (2F1)	10/7/70	Structural	(1)	HEDL	350	800	0.1

[a]Estimated accumulated center burnup on peak rod, based on unperturbed flux, but considering depletion effects (fuels, at. %; nonfuels, nvt x 10^{-22}).
[b]Previous exposure from another subassembly.

During the shutdown between Runs 46A and 46B, experimental subassembly X055 was removed from the grid. This subassembly contained 19 UNC mixed-carbide capsules. The average burnup of the lead capsule was approximately 4.3 at. %, and the midplane fluence for the subassembly was approximately 4.4×10^{22} nvt (total flux). Subassemblies X100 and X103 (see Table I.C.2) were loaded during the same shutdown.

b. Operational In-cell Handling and Examination Equipment (M. J. Feldman)

Last Reported: ANL-7377, pp. 50-52 (Aug 1970).

(i) Examination Equipment (J. P. Bacca and D. B. Hagmann)

(a) Profilometer (M. D. Carnes)

The contact profilometer for making continuous diameter surveys of capsules or elements (see ANL-7737) has been remotely tested in the air cell and is being routinely used for postirradiation diameter measurements. It can accommodate capsules and elements with spiral spacer wires. The diameter profiles of 107 irradiated capsules have been measured successfully with the instrument.

The uncertainty of the profilometer was determined by comparing its traces against values obtained with the Bausch & Lomb DR-25B optical gauge. The average uncertainty of the profilometer is less than ±100 μin. The profilometer has a random zero shift (average value is 30 μin.) whose magnitude is identified on each profile trace. The total uncertainty is the summation average uncertainty plus the zero shift for each individual profile.

(b) Milling Machine (D. M. Paige)

A small bench mill has been modified for remote operation and installed in the air cell. With outrigger support, it can machine items up to the size of a subassembly. Various standard mill cutters up to about 4 in. in diameter and small end mills can be used. The table has a longitudinal travel of 12 in., a cross feed of $5\frac{1}{2}$ in., and a vertical travel of $9\frac{1}{2}$ in. Vises and holding jigs are available.

c. Experimental Support (M. J. Feldman, J. P. Bacca, N. R. Grant, R. V. Strain, R. D. Phipps, S. T. Zegler, J. W. Rizzie, A. K. Chakraborty, D. B. Hagmann, H. A. Taylor, and G. C. McClellan)

Last Reported: ANL-7742, pp. 48-53 (Sept 1970).

(i) Subassembly Examinations. Table I.C.3 summarizes the status of examinations being made on the subassemblies listed.

TABLE I.C.3. Status of Examinations in the FEF

Subassembly No. and (Type)	Contents	Status
X018B (B7)	Structural (GE, ANL, WADCO); peak total fluence, 9.52 x 10^{22} n/cm^2.	Terminal postirradiation examinations are being made. Subassembly-straightness test and hexagonal-can measurements were completed. The can was removed by slitting axially after normal dismantling procedures failed, apparently because of swelling of the capsules. Visual examination and length and bow measurements of all seven capsules were completed. Diameter measurements (with the DR-25) of two capsules were completed.
X036 (A19)	Mixed-oxide fuel (GE); peak burnup of lead element, 5.3 at. %.	Visual examinations and neutron radiography showed no capsules defective. Diameter, length, bow, and weight measurements of all capsules were completed. This testing completes the interim examination of this subassembly.
X042 (B7)	Structural (PNL); peak total fluence for lead capsule, 3.5 x 10^{22} nvt.	In progress are visual examination; weight, bow, and length measurements; and neutron radiography. Reconstitution and continued irradiation of the experiment will depend on review of the neutron radiographs.
X043 (F37)	Unencapsulated mixed-oxide fuel elements (GE); peak burnup, 6.2 at. %.	The FEF standard procedure for washing sodium from experimental subassemblies was used for this multiple-hexagonal-tube subassembly; no abnormalities were noted. Interim examination of the unencapsulated elements was started. Examinations completed are visual examination of all 37 elements; profilometry and overall-length determination of 21 elements; and neutron radiography of 20 elements. The 20 elements neutron-radiographed (and possibly additional ones) will have their diameters measured and will be visually inspected and photographed. Reconstitution in a new subassembly for additional irradiation starting with Run 47 is planned.
X056 (F37)	Unencapsulated mixed-oxide fuel (GE); peak burnup, 6.3 at. %.	No problems were encountered when washing this multiple-hexagonal-tube subassembly with the FEF standard washing procedure for experimental subassemblies. Interim examination of the unencapsulated fuel elements was begun. Fifteen elements were diameter-surveyed and neutron-radiographed. Visual examination of all elements was completed. Additional examinations will include profilometry measurements, overall-length measurements, and visual and photographic inspection, all before reconstitution into a new subassembly for additional irradiation starting with Run 47.
X057 (B7)	Structural (WADCO); peak total fluence, 6.99 x 10^{22} n/cm^2.	Terminal postirradiation examination is being made. Subassembly-straightness test and hexagonal-can measurements were completed. The can was removed by slitting axially after normal dismantling procedures failed, apparently because of swelling of the capsules. Visual examination, length and bow measurements, and diameter measurements (with the DR-25) of all seven capsules were completed.
X064 (A19)	Mixed-oxide fuel (GE); peak burnup for lead element, 6.3 at. %.	Neutron radiographs of all 19 capsules showed no defects that might preclude continued irradiation. Diameter measurements and weight determinations of all 19 capsules were completed. Profilometer diameter measurements of five capsules were made. This testing completes the interim examination of this subassembly.
X065E (B37)	Helium-pressurized structural elements (ANL).	Reconstitution of this subassembly is planned so that the sixth cycle of irradiation for the pressurized test elements can begin at the start of Run 47. This subassembly is being irradiated as a part of the ANL/EBR-II in-reactor creep testing of stainless steel tubing.
X068 (B61A)	Encapsulated driver elements of Mark-IA fuel (ANL); peak burnup, 2.4 at. %.	Visual examination of three capsules has been completed. Interim examination of the remaining 58 capsules is in progress. One element will be destructively examined. The subassembly will be reconstituted for additional irradiation.
X070 (A19)	Mixed-oxide fuel (GE, NUMEC), mixed-carbide fuel (LASL, Westinghouse), mixed-nitride fuel (BMI); burnup values reported in September 1970 Progress Report, ANL-7742, p. 51.	Interim examination was concluded with completion of diameter surveys of all 19 capsules and diameter profilometry of 10 capsules. Ten capsules have been returned to the experimenters (GE, LASL, and BMI); the remainder are being considered for reconstitution in new subassemblies for additional irradiation.
X072 (A19)	Mixed-oxide fuel (ANL); lead-element peak burnup, 3.8 at. %.	Interim examination of the encapsulated elements was started.
X077 (B7A)	Structural (ORNL, PNL); peak total fluence, 0.8 x 10^{22} nvt.	Interim examination was completed. Visual examination of all capsules showed nothing abnormal. All capsules are being returned to the experimenters.
X078 (E61)	Unencapsulated Mark-IA driver elements (ANL); peak burnup on center element BF-11, 4.3 at. %.	Element BF-11 has been given visual and photographic examination, diameter survey, weight determination, and sodium-bond test. Neutron radiography of the element will complete the interim examination. The element will be reconstituted in a new subassembly for additional irradiation in an experiment of irradiation to cladding failure.
X087 (B61A)	Unencapsulated mixed-oxide fuel (WADCO); peak burnup, 1.1 at. %.	Subassembly was received from the reactor for a minimal interim examination and for reconstitution of the elements into a new subassembly (X087A) for additional irradiation.

(ii) Subassembly Fabrications. The following subassemblies were made up with new elements:

Subassembly No.	Type of Irradiation Subassembly	Content (and Number) of Capsules or Elements
X093	Mark B61A	WADCO unencapsulated mixed-oxide fuel elements (61)
X100	Mark B7A	ORNL encapsulated structural elements (7)
X103	Mark B7A	HEDL encapsulated structural element (1); dummy elements (6)

(iii) Removal of Sodium from Multiwall Prototypal Experimental Subassemblies (R. D. Phipps)

Experimental subassemblies with multiple hexagonal tubes could cause a problem while they are being washed with water in the inter-building coffin (IBC). Tests with models simulating various channel spacings between hexagonal tubes indicated that a sodium-water reaction could occur if the sodium is not drained completely from the annulus between the tubes before washing.

In recently completed tests, three prototypal multiple-wall subassemblies (Mark H37A, Mark F37, and Mark E61) were given a normal experimental-subassembly wash in the IBC after they had resided for about three days in the 700°F sodium of the reactor storage basket. Comparison of flat-to-flat measurements of the outer hexagonal tubes (the hexagonal cans) of each subassembly before and after the wash cycle showed no significant distortion of the cans that would indicate a violent sodium-water reaction had occurred between the tubes during washing. No unusual temperature increases in the IBC during the wash cycle were recorded. These results are, however, not conclusive, because visual examination of the inner tubes did not reveal any residual sodium products or any clear evidence that sodium had actually wet the surfaces between the walls of the tubes. The subassemblies had rinsed clean, as indicated by water conductivity and chemical analysis, in the usual amount of time. The rinse cycle would have been somewhat longer if sodium had been retained between the walls.

Washing of irradiated Mark-E61 subassembly X078 has been completed, and another Mark-E61 subassembly (X082) is scheduled to be washed soon. The results of these washings should provide additional information on this possible problem.

(iv) Summary of Capsule and Element Examinations. Table I.C.4 summarizes the various FEF examinations performed on experimental capsules and driver-fuel elements for September 1970 and fiscal year 1971.

TABLE I.C.4. Summary of FEF Examinations of Experimental Capsules and Driver-fuel Elements

	September 1970			Total for FY 1971		
	Driver-fuel Elements	Experimental Capsules	Other	Driver-fuel Elements	Experimental Capsules	Other
Weight	0	29	0	0	97	0
Periscope inspection	2	11	1	16	29	5
Stereomacroscope inspection	0	0	0	0	1	1
Diameter measurement						
With DR-25	48	74	4	176	139	4
With profilometer	0	9	0	0	23	0
Gamma scan	5	0	6	10	0	13
Length and bowing measurement	0	56	0	0	83	0
Balance point	0	0	0	0	0	0
Bonding and/or bond test	122	0	0	391	0	0
Neutron radiography	0	31	4	39	128	11
Plenum-gas sampling	0	0	0	8	2	0
Deencapsulation or decanning	5	0	0	13	2	4
Metallographic sampling	8	1	8	27	1	12
Metallographic examination	6	0	4	15	0	5
Shipped to experimenters	0	22	0	25	49	7

5. Materials-Coolant Compatibility (D. W. Cissel) (189a 02-063)

a. Evaluation and Surveillance of EBR-II Materials

(i) Evaluation of Reaction between Sodium and Mixed-oxide Fuel (S. Greenberg and W. E. Ruther)

Last Reported: ANL-7737, pp. 54-55 (Aug 1970).

The program described in ANL-7737 is in progress. A deliberately defected section of Element X007 from Subassembly X040A is being tested in 700°F flowing sodium with the cold trap held at 110°C, a temperature at which oxygen concentration is ~1-2 ppm. Element X007 contains 20 wt % plutonium mixed oxide (O/M = 1.98) with a smear density of 76.5% of theoretical and is clad with 20-mil-thick Type 304L stainless steel. Burnup is 5.8 at. %. The sample is 1.959 in. long. An axial defect approximately 0.8 in. long at the surface was made through the cladding by a 15-mil-thick abrasive wheel to a maximum depth of slightly greater than 0.015 in. into the fuel.

The defected element has been exposed for about seven days and has been inspected twice during this period. There have been noticeable but not catastrophic changes. The defect has widened and the cladding has bulged slightly. Measurements indicate a maximum increase in diameter of approximately 2 mils at the center of the defect. The rate of diameter increase appears to be decreasing with time.

(ii) Maximum-temperature Indicators for In-reactor Experiments (W. E. Ruther, S. Greenberg, and D. J. Dorman)

Last Reported: ANL-7742, pp. 53-55 (Sept 1970).

A series of experiments has been performed in an attempt to determine why the temperatures determined in in-reactor tests with maximum-temperature indicators (MTI's) did not correlate with actual temperatures.

Seven MTI inner capsules used in several experiments were refilled with sodium at 150°C. (It had been determined by weighing that three of the seven had not been completely filled previously by the standard procedure.) All capsules have been filled, weighed, reheated, and refilled until their filled weight is constant.

Three sets of experiments were conducted to determine the relative importance of time, temperature cycle, and gas-versus-vacuum fill of the annulus between the inner and outer capsule. The results, shown in Table I.C.5, indicate that (1) the gas-filled units were adequate for short exposure times, but indicated erroneously high temperatures with longer exposure; (2) the vacuum-filled unit suffered this loss of accuracy to a much greater extent that the gas-filled units; and (3) cycling the gas-filled units destroyed their usefulness as temperature indicators.

TABLE I.C.5. Response of MTI Capsules

Duration of Test, hr	Number of Temp Cycles	Low Temp of Cycle, °C	Fill between Capsules	Maximum Temp, °C	
				Actual	Calculated from MTI Weighings
2	1	RT	Gas	494 ± 2	506
2	1	RT	Gas		496
335	1	RT	Gas	494 ± 2	537
335	1	RT	Gas		526
335	1	RT	Vacuum		730
7	10	403	Gas	494 ± 2	631
7	10	403	Gas		>750

Since temperature cycles can occur in EBR-II during startup, sensitivity of the MTI's to temperature cycling must be eliminated. To gain an understanding of this sensitivity, two sets of MTI inner capsules were cycled at 150-370°C in a helium dry box while their behavior was observed as a function of ejection-tubing size. In both experiments, capsules fitted with hypodermic tubing (20 gauge in one experiment, 18 gauge in the other) operated smoothly for the first cycle. On subsequent reheatings, however, relatively large amounts of additional sodium were expelled, thereby leading to erroneously high calculated maximum temperatures (>650°C) after five complete cycles. It is postulated that the excessive expulsion of sodium is caused by a globule of sodium hanging at the base of the tube inside the capsule during cooling, while the entering gas bubbles passed the globule. On reheating, the sodium in the globule is forced up the hypodermic tubing and expelled by the expanding gas. MTI capsules fitted with tubing of 1/16-in. ID x 3/32-in. OD did not show this effect when cycled. The maximum temperature calculated from their weight change was within 4°C of the observed maximum temperature.

Six capsules with the larger ejection tubes are being prepared. They will be tested for accuracy, refilled, and supplied for the gamma-heating measurements proposed for EBR-II.

6. Reactor Analysis, Testing, and Methods Development (189a 02-144)

a. Nuclear, Thermal, and Hydraulic Surveillance

Last Reported: ANL-7742, pp. 57-69 (Sept 1970).

(i) Increasing the Power Level of EBR-II from 50 to 62.5 MWt. Various nuclear, thermal, and hydraulic tests were made in conjunction with the increase in power of EBR-II from 50 to 62.5 MWt effective with Run 46A. Summarized below are the most significant results of these tests.

(a) Rod-drop Studies (H. A. Larson, I. A. Engen, R. W. Hyndman, and M. R. Tuck)

The reactor was started up and brought to a power level of 50 MWt on September 21. After a series of rod drops at 50 MWt, the power level was reduced to 500 kWt to calibrate the reactivity worth of the drop rod. Additional rod drops were made, and the power level again was increased to 50 MWt. Rod drops were repeated at 50 MWt, and the resulting feedback data were used to predict the feedback at 56 MWt. Then, the power level was increased to 56 MWt, additional rod drops were made, and the resulting feedback data were used to predict the feedback at 62.5 MWt. The power level was increased to the goal of 62.5 MWt on September 25, and rod-drop measurements were repeated at this power level.

Typical rod-drop data are shown in Figs. I.C.6 and I.C.7, which give the power and computed feedback recovery at 50 and 62.5 MWt, respectively. At both powers, the feedback is negative and is prompt in the time interval 0-2 sec after the drop. Similar data sets (not illustrated) were taken over the power range from 62.5 to 40.0 MWt at the end of Run 46A.

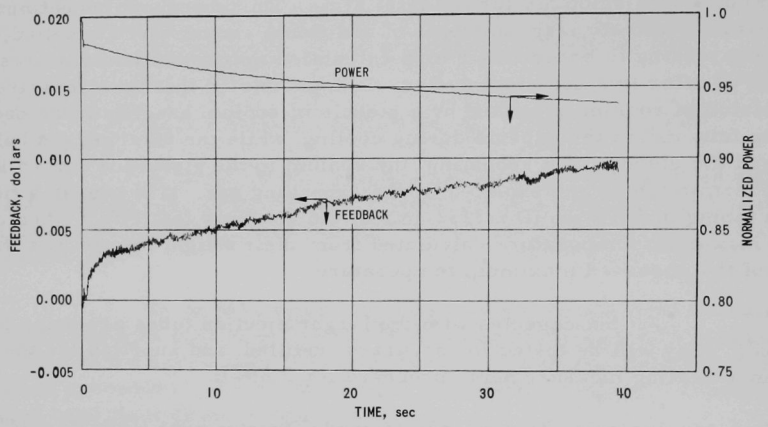

Fig. I.C.6. Power and Negative Feedback at 50 MWt at Start of Run 46A (average from five rod drops)

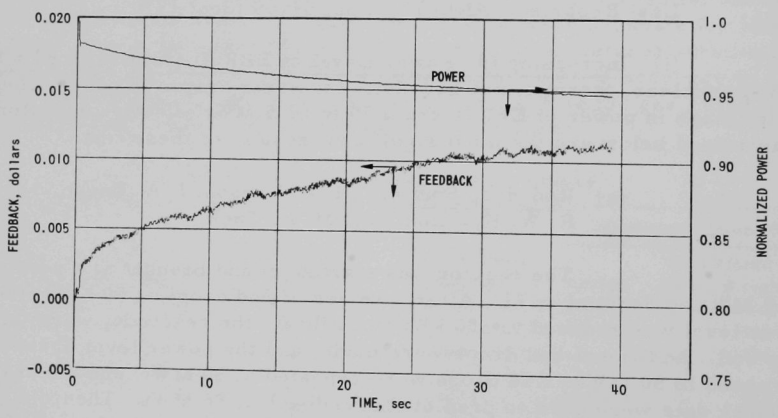

Fig. I.C.7. Power and Negative Feedback at 62.5 MWt at Start of Run 46A (average from four rod drops)

(b) Feedback-model Studies (H. A. Larson, I. A. Engen, R. W. Hyndman, and M. R. Tuck)

As cited in the preceding section, the feedback measured at 50 MWt was used to predict the feedback at 56 MWt. Similarly, the feedback measured at 56 MWt was used to predict that at 62.5 MWt. The method involved the fitting of feedback data to a mathematical model in the manner described by Hyndman and Nicholson.* Then, the coefficients (amplitudes) of each feedback term in the model were increased by the ratio of the power increase, and the feedback-recovery function was recomputed. Power was increased to the next level, and the measured feedback was compared with the predicted feedback.

The models, which incorporate the best-fit values for amplitudes and time constants, were as follows:

Power Level, MWt	Feedback Model
50	$-H(S) = \frac{0.1}{1 + 0.2S} + \frac{0.048}{1 + 0.4S} - \frac{0.018}{1 + 2.0S}$
56	$-H(S) = \frac{0.085}{1 + 0.2S} + \frac{0.0312}{1 + 0.4S} + \frac{0.037}{1 + 2.0S} + \frac{0.0341e^{-5.0S}}{1 + 5.4S}$
62.5	$-H(S) = \frac{0.095}{1 + 0.2S} + \frac{0.0335}{1 + 0.4S} + \frac{0.051}{1 + 2.0S} + \frac{0.020e^{-5.0S}}{1 + 5.4S}$

The amplitudes in these models are expressed in units of dollars of reactivity and are defined as the product of the power level (in megawatts) and the differential power coefficient of reactivity (in dollars of reactivity per megawatt). The feedback, -H, is a complex number and is expressed in dollars of reactivity. S is the complex operator, $i\omega$, where ω is oscillation frequency in radians/sec. Hence, when S = 0 (i.e., when the reactor is operating under steady-state conditions), -H defines the PRD (power-reactivity decrement), which is the amount of reactivity required to bring the system from hot critical to the power level at which the measurements were made.

In the models, a positive amplitude defines a negative feedback effect. Similarly, a negative amplitude indicates a positive feedback effect.

If feedback effects in the range of 50-62.5 MWt were truly linear, a simple multiplication of the amplitude for the 50-MWt model by the factor 62.5/50 should give the amplitudes measured at 62.5 MWt.

*R. W. Hyndman and R. B. Nicholson, The EBR-II Feedback Function, ANL-7478 (July 1968).

An inspection of the values in the models, however, shows that the feedback over the range of 50-62.5 MWt is not strictly linear. On the other hand, multiplication of the amplitudes for the 56-MWt model by the factor 62.5/56 does give reasonable predictions of the 62.5-MWt feedback function. Figure I.C.8 compares the measured data with those calculated from the model given in the figure.

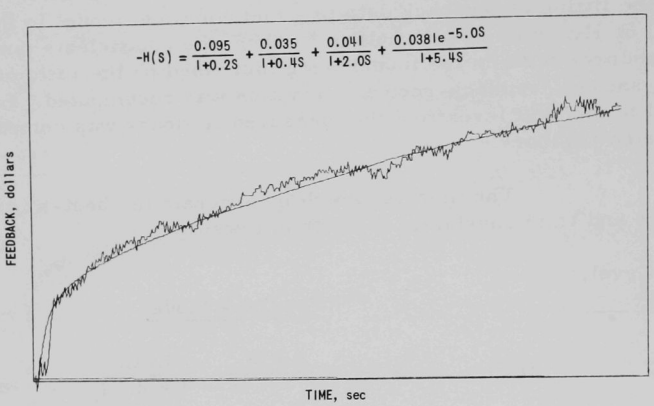

Fig. I.C.8. Comparison of Measured 62.5-MWt Feedback with Feedback-reactivity Curve Calculated from 56-MWt Data; Start of Run 46A

(c) Processing Rod-drop Data with the Sigma-5 On-line Computer (R. W. Hyndman, I. A. Engen, and M. R. Tuck)

Two methods were used for processing rod-drop data during Run 46A. One was the conventional method, which uses the IBM-1620 and IBM-360/75 computers. The other method used the recently installed Sigma-5 data-processing system, otherwise known as the digital data-acquisition system (DAS),* supplied by Xerox Data Systems.

Figure I.C.9 compares rod-drop feedback data processed by the two methods. The continuous curve for feedback was derived from an analysis made in the conventional manner. The open circles are values derived from the Sigma-5 analysis. The agreement is excellent, as it was with all other rod-drop data processed by the two methods during Run 46A. This excellent agreement indicates that the Sigma-5 system is operational for on-line processing of rod-drop data. (The data presented in Figs. I.C.6 and I.C.7 were processed with the Sigma-5 system.)

*R. W. Hyndman, R. O. Haroldsen, and J. R. Karvinen, EBR-II Digital Data Acquisition System Study, ANL/EBR-001 (May 1969).

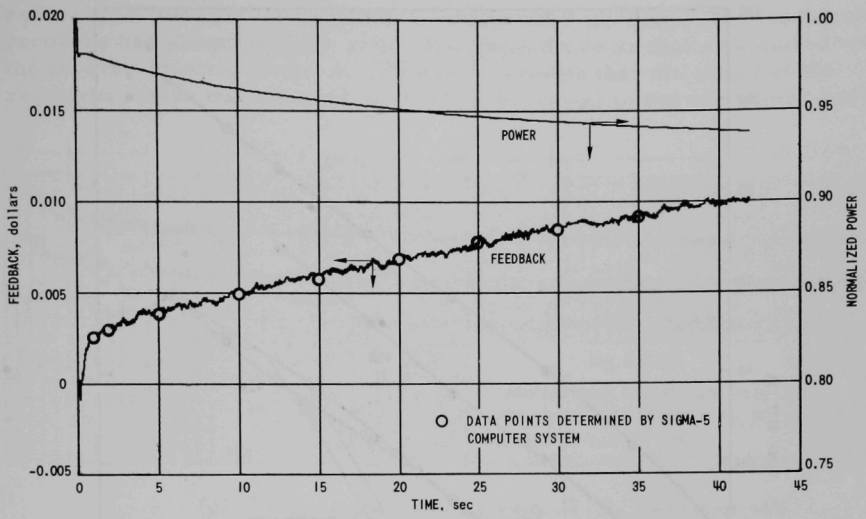

Fig. I.C.9. Comparison of Feedback Function as Measured by Conventional and Sigma-5 Methods

(d) Correction of Programming Errors in the Inverse-kinetics Codes (H. A. Larson and I. A. Engen)

Since the development of the inverse-kinetics program, the plots of feedback recovery have been characterized consistently by what appeared to be strong, negative "spikes" (positive feedback components) during the time (approximately 250 msec) the drop rod was falling. (See, for example, Fig. 1 of ANL-7476.) An examination of the computer program revealed an indexing error in the code relating the computed reactivity to the zero-power reactivity; i.e., there was a one-time-step error in the synchronization. Consequently, the feedback function, which is the difference between computed and zero-power reactivity, was in error. The effects of the error were reflected primarily when the reactor power level was changing the most rapidly, i.e., during the rod drop. After the drop, when power changes much more slowly, the effect of the indexing error is insignificant. All inverse-kinetics codes have been corrected.

(e) Power-Reactivity Decrement (PRD) for Run 46A (J. K. Long)

Power-coefficient measurements were made at approximate 10-MWt increments during the ascent to 62.5 MWt at the start of Run 46A and during the shutdown at the end of Run 46A. Figure I.C.10 compares the data from these measurements with data taken during Runs 45A and 38A. (Run 38A was made at 62.5 MWt, without irradiation experiments, in September 1969.)

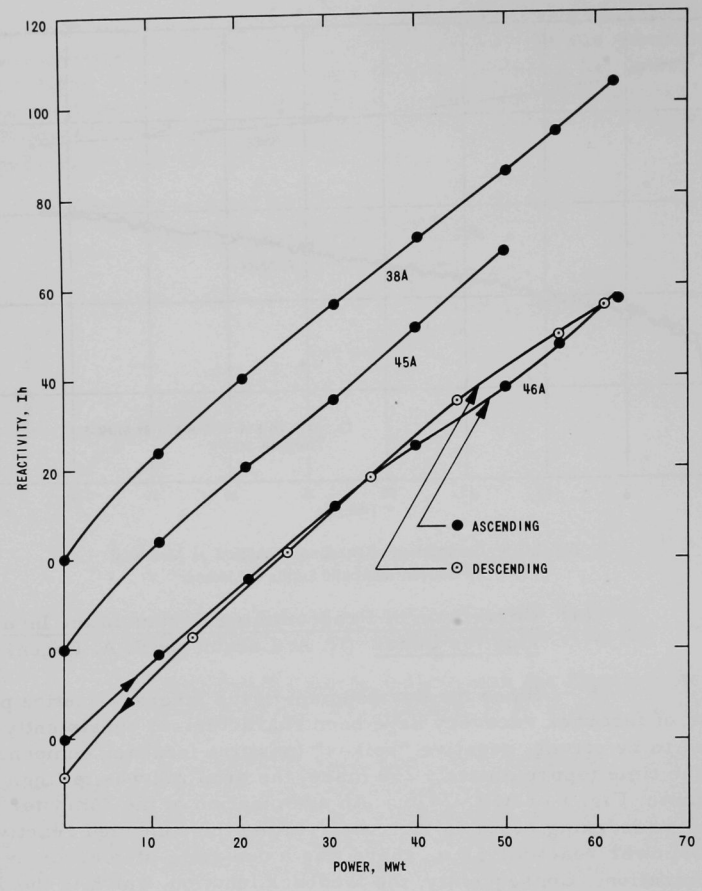

Fig. I.C.10. Power-Reactivity Decrement (PRD) for Runs 38A, 45A, and 46A (curves offset for separate viewing)

The slight upward bend between 50 and 62.5 MWt in the PRD curve for Run 38A is also apparent in the curve for Run 46A. This effect is believed to have originated from an increase in the fraction of fuel material entering the gamma phase at the higher temperatures associated with 62.5-MWt operation.

(f) On-line Reactivity Meter (J. R. Karvinen and C. C. Price)

Figure I.C.11 shows reactivity-meter recordings for rod drops at 50, 56, and 62.5 MWt. Apparent is the negative-feedback

recovery in the first few tenths of a second after the drop. The feedback recovery had essentially the same time dependence as that established with the inverse-kinetics program. This fact suggests that the output of the reactivity meter may be used for rapid assessment of the operative feedback.

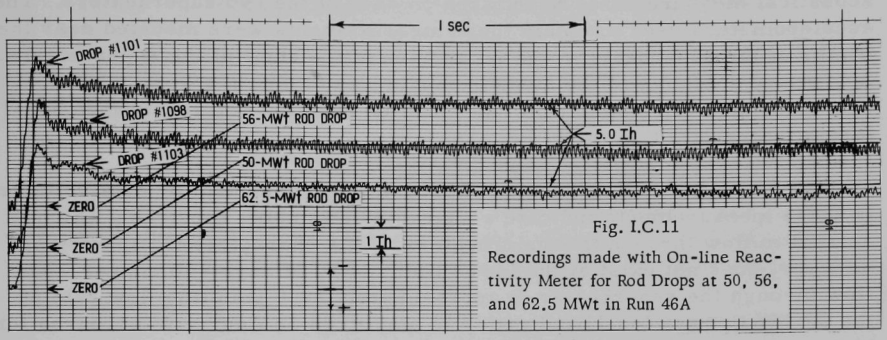

Fig. I.C.11
Recordings made with On-line Reactivity Meter for Rod Drops at 50, 56, and 62.5 MWt in Run 46A

(g) Noise-signature Analysis (J. R. Karvinen and C. C. Price)

Noise patterns were established for the neutron level and the two primary-sodium pumps at each steady-state power step in the ascent to 62.5 MWt. Figure I.C.11 shows that a considerable 10-Hz noise component existed, particularly at 50 and 56 MWt. Also apparent in the figure is the indication that the amplitude of the 10-Hz noise decreased after the power level was raised to 62.5 MWt. As Run 46A progressed, the amplitude continued to decrease and reached a level approximately 10-fold lower at the end of the run. During the shutdown at the end of Run 46A, noise measurements were taken at 56, 50, and 40 MWt and at 500 kW. For all these, the amplitude remained small. On startup of Run 46B, however, the amplitude of the 10-Hz noise returned to approximately the same level as for the Run-46A startup.

Noise patterns for the two primary pumps at 50 MWt at the startup of Run 46A were essentially the same as those established from earlier 50-MWt operation. Although no earlier pump-noise data for 62.5 MWt exist, the patterns established at 62.5 MWt during Run 46A were consistent with data taken at 50 MWt.

The potential of using noise analysis for monitoring performance of the primary pumps was illustrated on September 29. On that date, the power demand for pump No. 1 gradually increased by 5 kW, but no change in primary flow rate was indicated. Shortly thereafter, the audible noise from pump No. 1 was louder than usual. Noise recordings were taken and showed a change in the normal noise pattern. Over a period of about an hour, the noise pattern reverted to its usual form. Concurrently, audible noise and power demand returned to normal.

(h) Acoustic Monitoring of EBR-II Superheaters
(R. N. Curran and V. N. Thompson)

During the increase of power to 62.5 MWt in Run 46A, acoustical measurements were taken on each of the two superheaters. The accelerometers used to obtain these measurements were mounted near the center of the superheaters, on the surface of the shell of the superheaters. A primary objective of the measurements was to obtain a flow-related characteristic noise spectrum that could be used for reference when analyzing future data that might be taken.

The results of previous analyses and the data collected in these measurements indicate a characteristic noise spectrum, which is related to flow through the superheaters. This characteristic spectrum, however, does not exist at the lower flow rates. It begins to appear when flow through the superheater is approximately 1750 gpm (the flow rate at the 30-MWt power level) and grows in amplitude as flow rate increases for higher-power operation. The frequency range of this noise is approximately 1-2 kHz. The same general spectrum was seen on both superheaters. Above approximately 2 kHz, no such characteristic noise was detected. Below approximately 1 kHz, no noise was detected that could be correlated with flow through the superheaters.

Analysis of the data is not yet complete; however, no correlation is apparent so far between the data collected during the increase to power in Run 46A and the data collected during Run 38A, the previous 62.5-MWt run in September 1969. One reason for this lack of correlation is related to a change in the bandwidth of frequency response of the measuring systems. During September 1969, the frequency response was limited to about 500 Hz; during Run 46, however, the frequency response was increased to 4 kHz.

(i) Instrument Probe (W. R. Wallin)

During Run 46A, the temperature distribution of the coolant in the reactor outlet plenum was measured at a radius corresponding to a Row-14 blanket position. Average temperatures recorded (beginning with the lowest thermocouple) were 882, 878, 871, 910, 925, 902, and 896°F. During Run 38A in September 1969, corresponding temperatures were 853, 854, 858, 878, 881, 880, and 880°F. The small differences are believed caused by a change in the flow pattern in the plenum, which was caused by differences in the core loadings. The relationship between the pressure in the upper plenum (as indicated by pressure-sensing equipment on the probe) and flow rate did not change.

(j) Instrumented Subassembly XX02 (W. R. Wallin)

Flow-rate and temperature data from XX02 were consistent with all other system parameters. The indicated flow rate through

XX02 decreased from 49.2 to 47.2 gpm (relative to Run 45B) because of a decrease in the pressure drop in the core. Temperature increases were consistent with the power increase and the flow decrease.

(k) Intermediate Heat Exchanger (W. R. Wallin)

Monitoring of thermocouples of the intermediate heat exchanger did not reveal any significant change in the normal temperature distribution.

(l) Subassembly-outlet Temperatures (W. R. Wallin)

Subassembly-outlet temperatures increased linearly with power during the power increase. Small deviations from expected values were noted, but these were of the same order as those usually noted.

(ii) Analysis of Flow Coastdown in the Primary Cooling System of EBR-II (R. K. Lo and D. Mohr)

A dynamic model for coastdown of flow of primary coolant after cessation of pumping power has been derived and used to calculate values for the coastdown.

In the analysis used to derive the model, it was assumed that (1) both pumps fail simultaneously; (2) the power is interrupted at the output of the generator of the motor-generator (MG) set driving each pump; (3) the pressure drop of sodium through the piping, reactor core, reactor blanket, and intermediate heat exchanger is proportional to the 1.85 power of the flow rate; (4) the primary auxiliary pump is not operating; (5) the equations for steady-state pump head and torque hold during the transient; and (6) both pump-motor units behave identically.

The system dynamics can be described by the following equations:

$$\Delta H_p = 184.9\, n^2 - 5.709\, nw - 26.35\, w^2,$$

$$T_p = 1.94\, \Delta H_p + 798.6\, nw,$$

$$\Delta H_T = 151\, w^{1.85},$$

$$\frac{dw}{dt} = (\Delta H_p - \Delta H_T)/21.23,$$

and

$$\frac{dn}{dt} = -T_p/2780.6,$$

where

ΔH_p = pump discharge head in ft,

n = pump speed in rpm, normalized to a rated speed of 900 rpm,

w = flow rate in gpm, normalized to a rated flow of 4670 gpm/pump,

T_p = pump-load torque in lb-ft,

and

ΔH_T = pressure drop in ft.

The equations were programmed on an IBM computer code, Continuous System Modeling Program (CSMP).* Figure I.C.12 shows the calculated results along with the flow decay that would be measured if there is a 1.15-sec time lag in flow measurement.

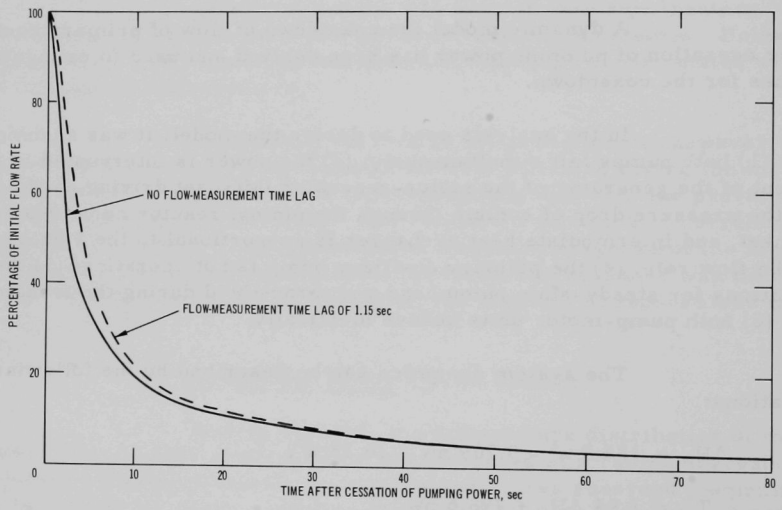

Fig. I.C.12. Calculated Coastdown in Flow of EBR-II Primary Coolant after Cessation of All Pumping Power

When the power is interrupted from the generator output to the pump-motor unit, as illustrated here, the flow decreases to 50% of the full flow in ~2.4 sec. When the power input to the motor of the MG set is

*System/360 Continuous System Modeling Program, Application Description, H20-0240-2, 3rd Ed., IBM (Aug 1968).

interrupted or when the clutch field current is cut off, however, the flow, as indicated by measurements of coastdown on EBR-II, decreases 50% in ~8-9 sec.* In this case, the generator continues to supply power to the pump-motor unit during the coastdown.

(iii) Increased Radiation Exposure of the EBR-II Reactor Cover due to Neutron Streaming (L. B. Miller and R. E. Jarka)

Some experimental subassemblies contain less stainless steel in the region above the core than EBR-II driver subassemblies. These experimental subassemblies provide a channel for neutrons to leak from the core region into the upper plenum, which is relatively transparent to neutrons. Neutronics analysis was performed to determine the increase in neutron flux at the reactor cover due to this neutron streaming through experimental subassemblies.

The increase in the high-energy flux above an experimental subassembly containing only sodium above the core region was 6%.

Figure I.C.13 shows the mathematical model of the EBR-II core and reflector used in the analysis. The four cases shown in Table I.C.6 were considered.

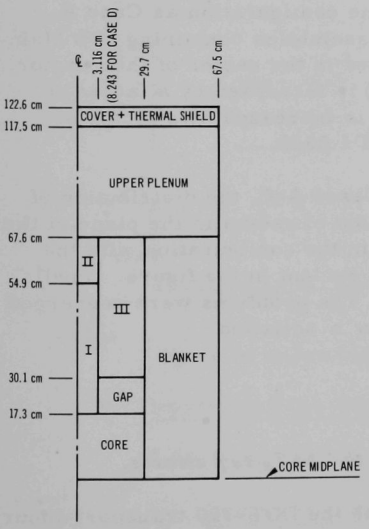

Fig. I.C.13. Mathematical Model of EBR-II for Determining Increase of Radiation Exposure of Reactor Cover due to Neutron Streaming

Case A represents the EBR-II reactor with the stainless steel axial reflector in Rows 2-6 and a fueled experimental subassembly containing 50% stainless steel above the core in Row 1. Case B represents the same EBR-II configuration except that a fueled experimental subassembly containing no stainless steel above the core region has replaced the experimental subassembly of Case A. The predicted change in criticality is $\Delta k = -0.0004$. The high-energy flux ($E > 3.68$ MeV) incident on the center of the thermal shield and the reactor cover is increased by a factor of 1.064. Lower-energy fluxes change less. The fluxes in Group 3 ($1.35 < E < 2.23$ MeV) and in Group 7 ($0.183 < E < 0.302$ MeV) near the peak of the flux spectrum are increased by a factor of 1.028 at the reactor cover. The low-energy flux (Group 22, $29 < E < 101$ eV) is increased by only a factor of 1.007.

*R. Wallin to D. Mohr, private communication (Aug 1970).

TABLE I.C.6. Parameters Used with Reactor Model for Calculating Effect of Neutron Streaming

Case	Regional Composition I	Regional Composition II	Regional Composition III	Size of Regions I and II	k_{eff}
A	50% sodium, 50% SS	50% sodium, 50% SS	SS reflector	1 row	1.00000
B	100% sodium	50% sodium, 50% SS	SS reflector	1 row	0.99963
C	50% sodium, 50% SS	50% sodium, 50% SS	Depleted-U blanket	1 row	0.99529
D	50% sodium, 50% SS	50% sodium, 50% SS	SS reflector	2 rows	0.99995

Case C represents the same configuration as Case A, except that the stainless steel reflector is replaced by a depleted-uranium blanket. This configuration causes much more severe irradiation of the reactor cover than Cases A and B. The high-energy flux (Group 1) is 2.6 times as high at the reactor cover in Case C as in Case A. The lower-energy fluxes, however, are smaller with the uranium blanket. The Group-7 flux is reduced by a factor of 0.69, and the Group-22 flux by a factor of 0.23.

Case D represents the same configuration as Case A, except that seven fueled experimental subassemblies containing 50% stainless steel above the core region are inserted in the center of the reactor. In this case, the high-energy flux (Group 1) is increased by a factor of 1.46 relative to Case A. The Group-7 flux is increased by a factor of 1.0064, and the Group-22 flux by a factor of 1.0026.

Figure I.C.14 shows, for Cases A-C, the distribution of high-energy ($E > 3.68$ MeV) flux as a function of radius in the plane of the top of the subassemblies. The higher flux in the configuration with the depleted-uranium axial blanket (Case C) is evident in the figure. Small distortions of the curves are also evident. The problems were converged until, for every point $\bar{r}$, the flux at iteration n satisfied

$$\frac{\phi^n(\bar{r}) - \phi^{n-1}(r)}{\phi^n(r)} \leq 10^{-4}.$$

The small distortions, therefore, are ascribed to S_4 ray effects.

The analysis was made with the DOT-380 transport-theory code. The mesh-point density was increased in the regions of interest and reduced to a minimum elsewhere. Fourteen mesh points were used in the radial direction, and 19 in the axial direction.

The 22-group cross-section set 238 was used. This set was prepared by averaging point cross section data for the spectra of the

EBR-II core, blanket, and stainless steel reflector. This cross-section set and its reduced-group counterpart, 23806, yielded results in good agreement with measured control-rod worths and ^{235}U fission rates in cores blanketed with depleted uranium and cores reflected with stainless steel. These sets, however, do not yield reliable results for a nickel-reflected core, because they do not contain appropriately averaged cross sections for a nickel reflector region. Fission rates for ^{238}U predicted with this set agree reasonably well with measurements in the core region, but diverge rapidly from the measured ^{238}U fission rates in the blanket region. (A discrepancy of the same magnitude is found in the ENDF/B cross sections.) The six-group set 23806 was not used for this work, because not enough confidence has yet been justified in the use of this set in regions far from the core boundaries.

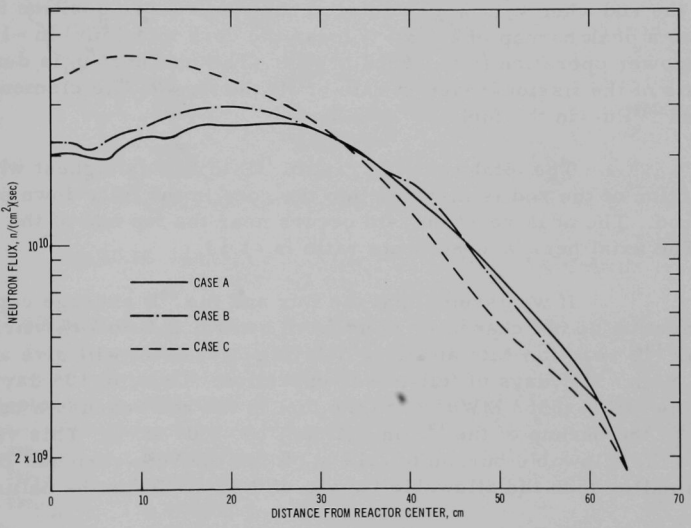

Fig. I.C.14. Group-1 Neutron Flux along Lower Edge of Upper Plenum

b. Improved Experimental-irradiation Capability

Last Reported: ANL-7742, pp. 69-74 (Sept 1970).

(i) Comparison of Burnups of ^{10}B and Fuel in the EBR-II High-worth Control Rod (B. R. Sehgal)

Calculations (unpublished) have been made by R. K. Lo to determine allowable burnups of ^{10}B atoms in the natural, 50%-enriched (in ^{10}B), and 90%-enriched B_4C of the high-worth control rod. Those calculations were based on an allowable hoop stress of 9400 psi in the gas-plenum

tube and a release of 100% and of 30% of ^{4}He from the ^{10}B(n,α) reaction. For 30% gas release, the allowable burnups of ^{10}B are 9.83, 3.87, and 2.14 at. %, respectively, for the natural, 50%-enriched, and 90%-enriched B_4C.

Additional calculations have been made by this author to determine the burnup of ^{10}B in B_4C when the burnup of the fuel in the rod reaches 1.5 at. %. The results are reported here.

From the calculations reported for the high-worth control rod in the Progress Report for August 1970 (ANL-7737, pp. 82-87) and the procedure of normalization detailed in the Progress Report for March 1970 (ANL-7679, pp. 53-58), it was found that, at the 62.5-MWt power level, the fuel in the rod when it is in control-rod position 5 (core position 5F1) achieves a peak burnup of 1.5 at. % (near the core midplane) in ~105 days of full-power operation (i.e., ~6562 MWd). (The fuel burnup is defined on the basis of the fission-reaction rate of all the fissionable elements--^{235}U, ^{238}U, and ^{239}Pu--in the fuel.)

The total reaction rate of ^{10}B in B_4C is highest when the B_4C section of the rod is inserted into the core in the fully down position of the rod. The peak reaction rate occurs near the top end of the B_4C section. The axial peak/average rate ratio is ~1.13.

If we assume that the flux and the ^{10}B average capture cross section do not change in going from natural B_4C to 90%-enriched B_4C, the peak ^{10}B reaction rate at the 62.5-MWt power level will give a ^{10}B burnup of 1 at. % in ~51.5 days of full-power operation. Thus, in 105 days of full-power operation (6562 MWd) when the fuel in the rod reaches a burnup of 1.5 at. %, the burnup of the ^{10}B in B_4C will be ~2.04 at. %. This value is close to the allowable burnup of 2.14 at. % for the 90%-enriched B_4C, but is much smaller than the allowable burnup of 9.83 at. % for the natural B_4C.

(ii) DOT XY, S_4 Calculations for an EBR-II Core with Depleted-uranium, Stainless Steel, and Nickel Reflectors
(B. R. Sehgal and R. H. Rempert)

DOT XY calculations* in the S_4 approximation have been completed for the EBR-II core for extended operation at 62.5 MWt (see Fig. I.C.15) reflected with depleted uranium, with four rows of stainless steel, and with four rows of nickel. Reported here are the calculated powers generated by individual subassemblies. The calculations were made with the 26-group, BENDF cross-section set, which is derived from the ENDF/B Category-1 data averaged with the MC^2 code** over the spectra in the various

*F. R. Mynatt, DOT, A Two-dimensional Discrete-ordinate Code, Report K-1694, Radiation Shielding Information Center, Oak Ridge National Laboratory. Also see Progress Report for October 1968, ANL-7513, p. 50.

**B. J. Toppel, A. L. Rago, and D. M. O'Shea, MC^2, A Code to Calculate Multigroup Cross Sections, ANL-7318 (June 1967).

composition regions of the reactor. Table I.C.7 lists the atom densities for each element that were used for the depleted-uranium, stainless steel, and nickel reflectors.

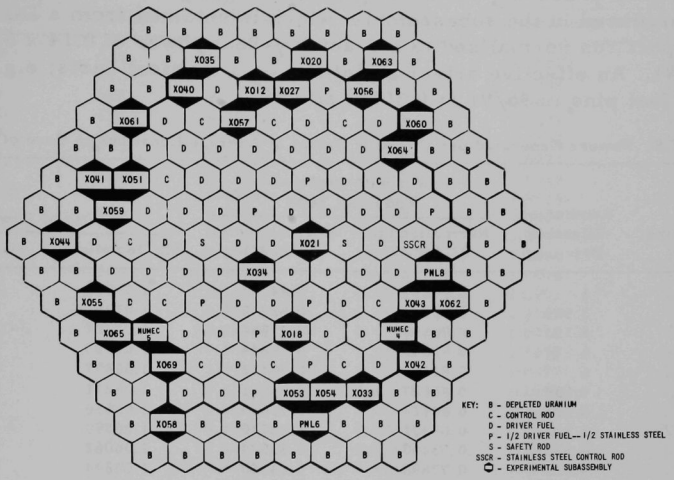

Fig. I.C.15. Typical Core Loading for Extended Operation of EBR-II at 62.5 MWt. ANL Neg. No. ID-103-L5455 Rev. 2.

TABLE I.C.7. Atom Densities, in atoms/(b)(cm), of Reflector Compositions for Core Shown in Fig. I.C.15

Isotope	Depleted U	Stainless Steel	Nickel
^{235}U	0.00006042	-	-
^{238}U	0.028156	-	-
^{239}Pu	0.0000206	-	-
Fe	0.0105924	0.0485322	0.0049455
Cr	0.00296894	0.0138683	0.0011389
Ni	0.00145027	0.0061446	0.0703897
Na	0.00567874	0.0043224	0.0031553

It was shown in the Progress Report for March 1970 (ANL-7679, pp. 53-58) that power generated in individual subassemblies at the 62.5-MWt power level of the reactor can be calculated from the fission rates of ^{235}U, ^{238}U, and ^{239}Pu in a subassembly and normalization factors for each reactor row. This procedure was used in the calculations reported here.

The calculated powers produced per effective driver at average core positions for the depleted-uranium reflector are shown in

Table I.C.8. Two sets of values are given: (1) normalized to a total reactor power of 62.5 MWt and (2) normalized to a power of 62.5 x 0.86 = 53.75 MWt, which is the power produced by the fission fragments and β rays generated in the fission process. To the second set of values must be added the γ-heat power produced in the subassembly, which is obtained from a DOT XY γ-transport run normalized to a reactor γ-heat power of 0.14 x 62.5 = 8.75 MWt. An effective driver is defined on a physical basis; e.g., a driver with 46 fuel pins is 46/91 (= 0.5055) effective.

TABLE I.C.8. Powers Generated per Effective Driver at Average Locations in Core of Fig. I.C.15

Average Core Location	Number of Effective Drivers	Power with Depleted-U Reflector, MWt		Ratio of Powers	
		Normalized to 62.5 MWt	Normalized to 53.75 MWt	SS/Depleted U	Ni/Depleted U
1A1	1	0.97857	0.84157	1.07338	1.03580
2N1	3.505	0.96244	0.82770	1.07051	1.03510
3N1	4.352	0.90679	0.77984	1.07127	1.04132
3N2	6	0.92842	0.79844	1.07055	1.03870
4N1	6	0.81525	0.70112	1.06697	1.04820
4N2	4.505	0.85627	0.73811	1.06271	1.04067
4N3	5.505	0.84919	0.73030	1.06550	1.04270
5N1	3.352	0.68301	0.58740	1.06390	1.06479
5N2	4.505	0.73260	0.63004	1.06062	1.05069
5N3	4.022	0.73896	0.63550	1.05894	1.05025
5N4	6	0.73193	0.62950	1.05891	1.05104
6N1	3	0.54112	0.46540	1.09214	1.14445
6N2	2	0.58559	0.50361	1.04434	1.09185
6N4	3.505	0.631669	0.54323	1.06347	1.08645
6N5	5.011	0.59391	0.51076	1.06930	1.10160

The ratios of powers generated per effective driver at average core positions for the stainless steel reflector and the nickel reflector to those generated for the depleted-uranium reflector are also shown in Table I.C.8. The ratios for the stainless steel reflector range from ~1.04 to ~1.09 and do not vary much over the core. The ratios for the nickel reflector range from ~1.04 to ~1.14 and increase toward the outer rows of the core.

Table I.C.9 shows the powers generated by the fueled experimental subassemblies in Rows 6 and 7 for the depleted-uranium blanket. Again two sets of values are shown--one normalized to a power of 62.5 MWt the other to 53.75 MWt--and the γ-heat powers produced in the subassemblies must be added to the last set. The ratios of powers produced for the stainless steel reflector and the nickel reflector to those for the depleted-uranium blanket are also shown in Table I.C.9. Except for a few subassemblies in Row 7, these ratios for the stainless steel reflector are generally less than 1.10. Many of the power ratios for the nickel reflector are larger than 1.10, and in Row 7, they range from 1.14 to 1.45.

TABLE I.C.9. Powers Generated in Fueled Experimental Subassemblies in Core of Fig. I.C.15

Subassembly Designation	Position	Power with Depleted-U Reflector, MWt		Ratio of Powers	
		Normalized to 62.5 MWt	Normalized to 53.75 MWt	SS/Depleted U	Ni/Depleted U
X059	6A2	0.22951	0.28338	1.08610	1.1206
X051	6A3	0.32288	0.27768	1.0782	1.1152
X040	6B1	0.49315	0.42411	1.0873	1.1717
X012	6B3	0.25098	0.21584	1.0577	1.1503
X027	6B4	0.21287	0.18307	1.0472	1.1226
X056	6C1	0.43538	0.37443	1.0377	1.0861
X064	6C3	0.25377	0.21824	1.0315	1.0616
PNL-8	6D2	0.49664	0.42711	1.0513	1.0752
X043	6D3	0.53240	0.45786	1.0500	1.0652
NUMEC 4	6D4	0.77352	0.66523	1.0579	1.0747
X033	6E1	0.33779	0.29050	1.1084	1.1939
X054	6E2	0.46699	0.40161	1.0804	1.1066
X053	6E3	0.31355	0.26965	1.0792	1.1047
X069	6F2	0.52673	0.45300	1.0782	1.1085
NUMEC 5	6F3	0.82846	0.71248	1.0716	1.0787
X020	7B5	0.15366	0.13215	1.1338	1.4521
X060	7C3	0.49315	0.42411	1.0677	1.1787
X062	7D3	0.41393	0.35598	1.1010	1.2162
X042	7D5	0.06270	0.05392	1.1446	1.1433
PNL-6	7E3	0.39561	0.34022	1.1431	1.2725
X058	7F1	0.32881	0.28278	1.1716	1.3496
X065	7F4	0.47004	0.40423	1.1042	1.1836
X055	7F5	0.45609	0.39224	1.1091	1.1887

The values of the power ratio in Row 7 for both the stainless steel and nickel reflectors are averages of the values obtained using the group cross sections for ^{235}U, ^{238}U, and ^{239}Pu weighted with the core spectrum and the reflector spectrum.

It is seen from Table I.C.9 that, with the stainless steel reflector, most of the fueled experimental subassemblies may be accommodated without reconstitution. Subassemblies X020, X042, PNL-6, and X058, which have power ratios of ~1.14 to ~1.17, could be moved into different locations.

With four rows of nickel reflector, it is perhaps not possible to use Rows 7 and 8 for irradiating currently constituted fueled experimental subassemblies.

(iii) DOT XY, S_2 Calculations for Two EBR-II Cores with Stainless Steel Reflectors (B. R. Sehgal and R. H. Rempert)

Reported here are the results of DOT XY calculations for two EBR-II cores: Core 1--the core for extended operation of EBR-II at 62.5 MWt (shown in Fig. I.C.15); and Core 2--a version (see Fig. I.C.16) of Core 1 that has been modified by substituting partial-fuel subassemblies for some driver subassemblies in Rows 3 and 4 to obtain a k_{eff} close to 1.0. Both cores were assumed to be reflected by stainless steel in Rows 7 to 10

and depleted uranium in Rows 11 to 16. The DOT calculations were made in the S_2 approximation. The cross-section set used was the 26-group set BENDF, which was derived from the ENDF/B, Category-1 data through the MC^2 code, using proper averaging for the various regional compositions of the reactor.

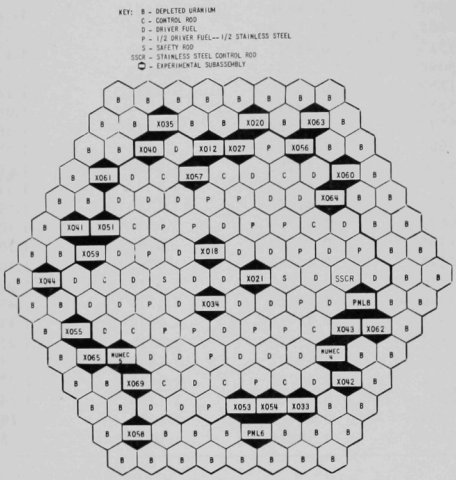

Fig. I.C.16

Modified Version of Core for Extended Operation of EBR-II at 62.5 MWt. ANL Neg. No. ID-103-L5455 Rev. 3.

The values of k_{eff} obtained for Cores 1 and 2 were 1.05595 and 1.00766, respectively. Table I.C.10 lists the powers generated by an effective driver at average subassembly positions in Cores 1 and 2, based on a total power of 62.5 MWt generated in the reactor. Table I.C.11 lists

TABLE I.C.10. Powers Generated by an Effective Driver at Average Positions in Cores 1 and 2[a]

Average Position of Subassembly	Number of Effective Drivers		Power/Effective Driver, MWt		Ratio of Powers, Core 2/Core 1
	Core 1	Core 2	Core 1	Core 2	
1A1	1	1	1.0416	1.0933	1.0496
2N1	3.505	3.0	1.0193	1.0759	1.0556
3N1	4.352	3.363	0.9606	1.003	1.0441
3N2	6	6	0.9739	1.0325	1.0601
4N1	6	6	0.8624	0.9310	1.0795
4N2	4.505	3.033	0.9121	0.9389	1.0294
4N3	5.505	3.033	0.9016	0.9463	1.0496
5N1	3.352	3.352	0.7239	0.8037	1.1102
5N2	4.505	4.505	0.7629	0.8451	1.1077
5N3	4.022	4.022	0.8107	0.8851	1.0917
5N4	6	6	0.7976	0.8384	1.0511
6N1	3	3	0.5923	0.6634	1.1202
6N2	2	2	0.6373	0.6783	1.0644
6N4	3.505	3.505	0.6785	0.7189	1.0595
6N5	5.011	5.011	0.6442	0.7241	1.1239
Total number of effective drivers	62.26	56.82			

[a]Based on total power of 62.5 MWt.

TABLE I.C.11. Powers Generated in Fueled Experimental Subassemblies in Cores 1 and 2

Subassembly Designation	Position	Power Generated, MWt		Ratio of Powers, Core 2/Core 1
		Core 1	Core 2	
X059	6A2	0.3539	0.3884	1.0976
X051	6A3	0.3418	0.3704	1.0836
X040	6B1	0.5384	0.5730	1.0643
X012	6B3	0.3739	0.3956	1.0580
X027	6B4	0.6002	0.6335	1.0555
X056	6C1	0.4806	0.5154	1.0723
PNL-8	6D2	0.5204	0.5836	1.1214
X043	6D3	0.5532	0.6541	1.1823
NUMEC 4	6D4	0.8043	0.9187	1.1422
X033	6E1	0.3631	0.4295	1.1829
X054	6E2	0.5004	0.5899	1.1797
X053	6E3	0.3318	0.3915	1.1798
X069	6F2	0.5536	0.6428	1.1612
NUMEC 5	6F3	0.8671	0.9968	1.1496
X020	7B5	0.2508	0.2694	1.0742
X060	7C3	0.5001	0.5431	1.0859
X062	7D3	0.4548	0.5144	1.1312
X042	7D5	0.0696	0.0801	1.1504
PNL-6	7E3	0.4556	0.5405	1.1864
X058	7F1	0.3942	0.4658	1.1817
X065	7F4	0.5089	0.5820	1.1436
X055	7F5	0.5015	0.5724	1.1414

the powers generated by the fueled experimental subassemblies in Rows 6 and 7 of Cores 1 and 2. The two tables also show the ratios of subassembly powers generated in Core 2 to those generated in Core 1.

The ratios of powers generated per effective driver in Core 2 to those in Core 1 vary from ~1.03 to ~1.12, the larger values being in Rows 5 and 6. This proportionately larger increase in the power generated by the outer rows of the core when fuel is removed from the middle rows of the core is due to the fact that the neutrons entering the outer rows are relatively soft. If the removal of the fuel is distributed uniformly over the core (e.g., by decreasing the volume fraction of fuel in the driver and experimental subassemblies), the ratio of power densities in Core 2 to those in Core 1 should be

$$\frac{\text{Power density in Core 2}}{\text{Power density in Core 1}} \simeq \frac{\left(\sum_j \eta_j M_j\right)_{\text{Core 1}}}{\left(\sum_j \eta_j M_j\right)_{\text{Core 2}}},$$

where $\eta_j = (\overline{\nu\Sigma_f/\Sigma_a})_j$ = the average number of neutrons generated per absorption in isotope j over the core, and M_j is the mass of isotope j. Calculations using the masses of ^{235}U, ^{238}U, and ^{239}Pu in Cores 1 and 2 and

the values of η_j from the output of a run of a MACH code* show the ratio of power density in Core 2 to that in Core 1 is ~1.08.

The ratios of power generated by the fueled experimental subassemblies in Core 2 to those in Core 1 range from ~1.06 to ~1.19 and depend upon the contents of a subassembly as well as the position of the subassembly relative to the partial-fuel subassemblies in Row 4.

7. Metal Driver Fuel Development and Application (C. M. Walter) (189a 02-145)

a. Mark-IA Fuel (A. K. Chakraborty and G. C. McClellan)

Last Reported: ANL-7742, p. 75 (Sept 1970).

(i) Postirradiation Examination of Vendor-produced, Impact-bonded Fuel. The vendor centrifugally bonded U-5 wt % Fs driver-fuel elements at 480-500°C for a time sufficient to transform the retained γ-phase in the fuel alloy to the equilibrium anisotropic phases. Stresses imposed during this transformation produced undesirable textures in the pins, which caused dimensional instability and shortening of the pins during irradiation. These centrifugally bonded fuel pins shortened in the axial direction and grew radially in the lower (spade) regions of the elements. The radial growth of the pins is roughly proportional to the applied stress resulting from the bonding operation.

An alternative to centrifugal bonding is impact bonding, which is used by ANL for producing their driver-fuel elements.

Eight subassemblies containing driver-fuel elements cast by the vendor and impact-bonded by ANL were assembled as part of a qualification program intended to verify satisfactory irradiation performance of these elements at 50-MWt reactor operation in EBR-II. These (qualification) subassemblies were irradiated in the burnup range of 0.85-1.79 at. %. One of them was a controlled-flow subassembly (C-2267), which was irradiated under conditions simulating 62.5-MWt operation.

Table I.C.12 summarizes the data for fuel swelling and diameter increase of the elements in the eight subassemblies. Postirradiation eddy-current testing of the bond of the elements revealed that none of the fuel pins shortened axially.

Figure I.C.17 compares the fuel swelling of impact-bonded vendor fuel with that of ANL-produced fuel as a function of burnup. Swelling of the vendor fuel in the qualification subassemblies is similar to that of

*D. A. Meneley, L. C. Kvitek, and D. M. O'Shea, MACH 1, A One-dimensional Diffusion-theory Package, ANL-7223 (June 1966).

ANL-produced fuel having similar silicon content and comparable burnup. Also, swelling of vendor fuel in controlled-flow subassembly C-2267 is similar to that of ANL-produced fuel in controlled-flow subassemblies following similar burnup.

TABLE I.C.12. Postirradiation-examination Data for the Eight Subassemblies in Program for Qualifying Impact-bonded Vendor Fuel

Subassembly Number	Maximum Burnup, at. %	Number of Elements Examined for Fuel Swelling[a]	Average Volume Swelling of Fuel, %	Range of Volume Swelling of Fuel, %	Number of Elements Diameter Surveyed	Range of ΔD/D of Elements, %
C-2261	0.85	30	3.0	2.2-3.8	-	-
C-2260	1.50	30	6.2	4.6-9.5	12	0.19-0.34
C-2263	1.69	29	9.3	5.2-13.4	6	0.37-0.56
C-2264	1.70	29	9.8	5.6-14.1	10	0.23-0.45
C-2265	1.73	31	9.5	5.2-13.7	12	0.25-0.51
C-2259	1.73	31	8.3	4.6-12.1	12	0.16-0.48
C-2266	1.79	29	12.1	6.8-15.9	10	0.37-0.53
C-2267[b]	1.79	85	16.5	13.7-18.3	9	0.42-0.76

[a]No axial shortening of fuel was observed in any element.
[b]Controlled-flow subassembly.

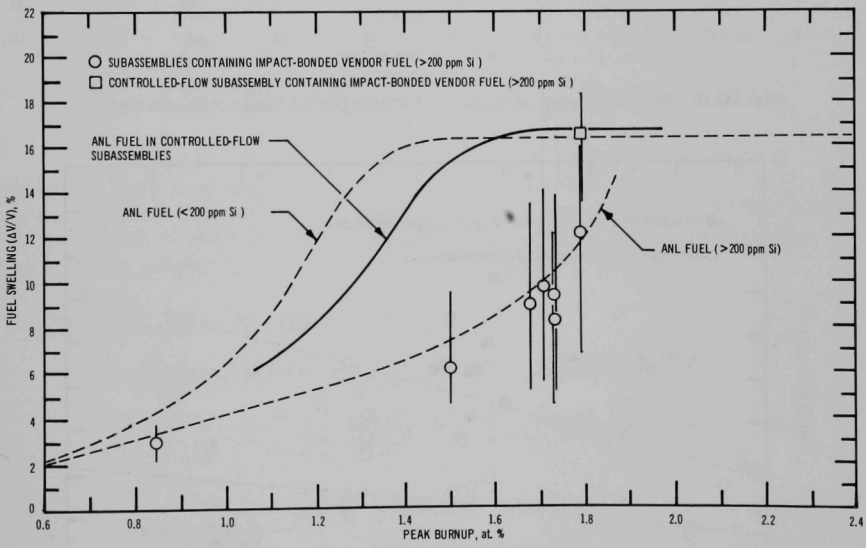

Fig. I.C.17. Swelling of Impact-bonded Vendor Fuel with Burnup

Figures I.C.18 and I.C.19 show the change in diameter of cladding of impact-bonded vendor elements as a function of burnup. In both figures, the solid lines represent the fluence-dependent swelling of stainless

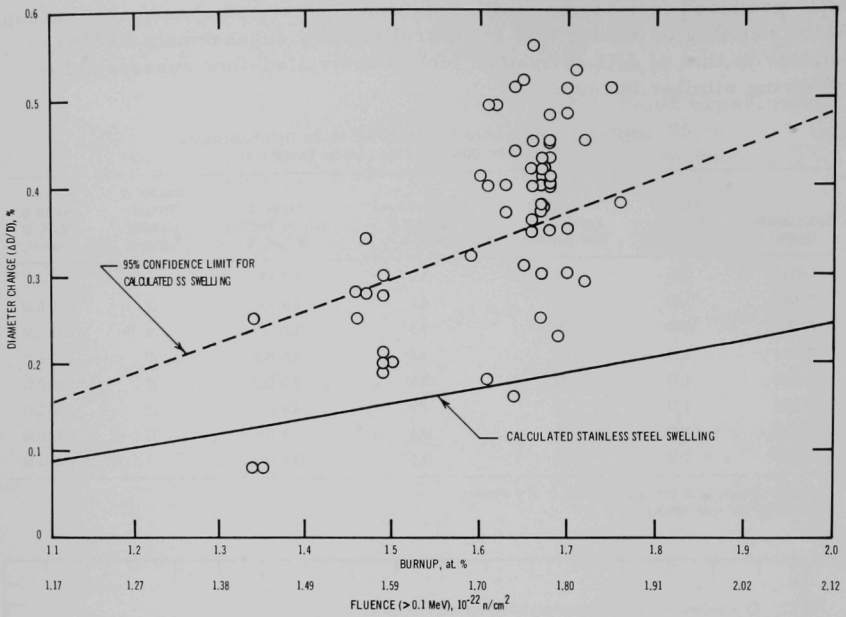

Fig. I.C.18. Diameter Change of Cladding of Impact-bonded Vendor Fuel with Burnup

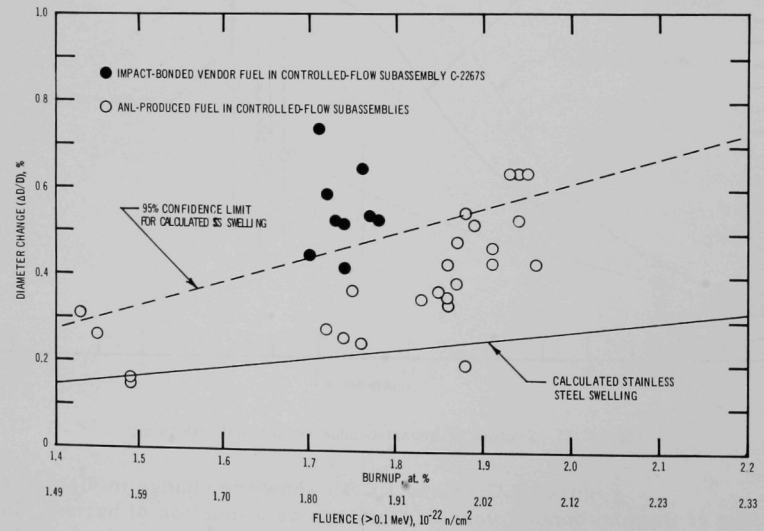

Fig. I.C.19. Diameter Change of Cladding of Impact-bonded Vendor Fuel and ANL-produced Fuel in Controlled-flow Subassemblies, as a Function of Burnup

steel as calculated using the PNL-Westinghouse equation with uncorrected EBR-II fluxes and fluence, and the broken lines are the upper 95% confidence limits for the calculated swelling. The $\Delta D/D$ values for impact-bonded vendor fuel elements (Fig. I.C.18) are somewhat higher than those measured for impact-bonded ANL-produced elements. This observation also holds true for the controlled-flow elements (Fig. I.C.19). Reasons for these observed differences are being sought.

b. Surveillance Support (J. P. Bacca, N. R. Grant, A. K. Chakraborty, and G. C. McClellan)

Last Reported: ANL-7742, p. 80 (Sept 1970).

Summarized below is the postirradiation surveillance performed on four subassemblies irradiated under various programs of this task.

Subassembly Number	Program	Maximum Burnup, at. %	Surveillance Performed
A-897	Study of depleted-uranium blanket	0.34	Element-diameter surveys; gamma scan; neutron radiography
C-2265	Impact-bonded vendor fuel	1.73	Diameter measurements with DR-25 optical gauge
C-2267S	Impact-bonded vendor fuel (controlled flow)	1.79	Fuel-volume and diameter measurements
C-2282	Heat-treated vendor fuel	1.76	Fuel-volume and diameter measurements

Ten driver subassemblies were assembled with vendor-produced fuel elements that had been heat-treated (see Sect. I.D.1.a). These subassemblies are intended to qualify the heat-treated Mark-IA driver fuel for use in 62.5-MWt operation of EBR-II. Three of the subassemblies began their irradiation at the start of EBR-II Run 46.

8. Operation with Failed Fuel (189a 02-148)

a. Experiments in EBR-II

(i) Irradiation of Oxide Fuel to Cladding Failure (J. F. Koenig)

Not previously reported.

A series of tests is planned in which unencapsulated mixed-oxide fuel elements will be irradiated to cladding failure in EBR-II. The primary objective of the tests is determination of the response of the various fission-product-monitoring systems to an actual failure of the cladding of such an element. Secondary objectives include: a better definition of how cladding fails; location of the failure along the element; determination of

whether or not propagation effects exist; and a practical evaluation of possible problems associated with postfailure fuel-handling procedures.

The first subassembly, Test A, will contain an element with a contrived cladding defect programmed to open 100-200 hr after immersion in the bulk sodium. The subassembly for Test B will contain an element with a peak burnup of 11 at. % and will be irradiated until the cladding ultimately fails. In Test C, a cluster of seven mixed-oxide elements having a peak burnup of 6 at. % will be irradiated until the cladding of one of the elements fails. Test D, now in the planning stage, will be irradiation of 19 mixed-oxide elements previously irradiated to burnups of the order of 5-6 at. %. Further details on Tests A-C follow.

(a) Test A, Predefected Element. The test specimen is a prototypal mixed-oxide element with a 0.005-in.-dia hole drilled through the cladding about 1/2 in. above the bottom of the fuel column. (The test specimen and environmental elements were supplied by WADCO at the HEDL site. All developmental and testing work on the test specimen was also performed by WADCO personnel.) The hole was filled with silver solder, and the surface of the defect was covered with a thin layer of nickel. Tests conducted under simulated environmental conditions indicated that the defect should open after a minimum exposure of 100 hr. The element will be irradiated in Subassembly X085, a Mark-E37A irradiation subassembly, at the center of two rows of environmental elements. The outer row of the subassembly will be solid stainless steel elements. Except for the defect in the test specimen, all elements in the inner 19-element cluster are identical.

The fuel is a mixed oxide with a wt % composition of 75 UO_2-25 PuO_2. The cladding, made of 20% cold-worked Type 316 stainless steel, is 0.230 in. in OD and has a 0.015-in. wall. The fuel has an 85% smear density and is separated from the cladding by an initial gas annulus of 0.003 in. The ratio of the fuel volume to the gas-plenum volume is 1.1.

Table I.C.13 summarizes the environmental conditions for the test.

TABLE I.C.13. Environmental Conditions for Test A of Program for Irradiating Mixed-oxide Fuel to Cladding Failure

Reactor power, MWt	62.5
Core position	4N3
Peak heat rating, kW/ft	
Test specimen	12.1
Hottest environmental element	12.3
Coldest environmental element	11.7
Maximum coolant temperature, °F	1100
Temperature of mixed coolant at subassembly outlet, °F	850
Maximum fuel temperature,[a] °F	
Test specimen	4120
Hottest environmental element	4130
Flow through subassembly, gpm	40.2

[a]Based on a fuel/cladding gap conductance of 1000 Btu/(hr)(ft²)(°F).

(b) Test B, Single High-burnup Element. The test specimen will be Element D-5 (NUMEC) from irradiation subassembly X012A. The capsule containing D-5 was opened, and the element was removed, inspected, and refitted with a new end fitting for accommodation in the irradiation subassembly. The element, having a peak burnup of 11 at. %, will be irradiated at the center of Subassembly X084, a Mark-E19E irradiation subassembly completely filled with fresh counterpart oxide elements. The test specimen is fueled with an 80 UO_2-20 PuO_2 (wt %) mixture. The cladding, made of Type 316L stainless steel, is 0.250 in. in OD and has a 0.015-in. wall. The fuel has a smear density of 88% and is separated from the cladding by an initial annular gas gap of 0.0015 in. The ratio of the fuel volume to the gas-plenum volume is 1.1.

Table I.C.14 summarizes the environmental conditions for Test B. Figure I.C.20 shows pertinent temperature profiles of the test specimen for the original irradiation environment and for the test. The calculated peak fluence for the test specimen is 8.5×10^{22} nvt. Swelling data were reported in the Progress Report for July 1970 (ANL-7726, pp. 49-51). Maximum growth of the cladding was 4.5%. The PNL swelling equation* indicates that 2% of the growth originated from stainless steel swelling.

The environmental elements, fabricated by WADCO, are fueled with mixed oxide of wt % composition 75 UO_2-25 PuO_2. The cladding of these elements, 20% cold-worked Type 316 stainless steel, is 0.25 in. in OD and has a 0.016-in. wall. The smear density of the fuel is 88%, and the initial gas annulus is 0.003 in. wide. The ratio of the fuel volume to the gas-plenum volume is 1.2.

(c) Test C, Seven High-burnup Elements. Seven elements previously irradiated in Subassembly X040A have been chosen for this test. These unencapsulated elements, now having a peak burnup of 6 at. %, are mixed oxides with wt % composition 80 UO_2-20 PuO_2. The Type 304L stainless steel cladding is 0.29 in. in OD and has a 0.020-in. wall. The smear density of the pellets is 81%, the initial gas annulus is 0.002 in. wide, and the fuel column is 11 in. long. The ratio of the fuel volume to the gas-plenum volume is 1.9. This higher-than-usual ratio will result in a higher plenum pressure for a given burnup, which may produce an earlier failure. This consideration was the main factor in choosing these elements for the first high-burnup cluster irradiation.

Table I.C.15 summarizes the environmental conditions for Test C. Figure I.C.21 shows the temperature profiles of the center element (ANL-024) in the subassembly for the test and for the terminal environment in X040A, when the peak heat rating was 15.7 kW/ft. The maximum growth

*T. T. Claudson, R. W. Barker, and R. L. Fish, The Effects of Fast Flux on the Mechanical Properties and Dimensional Stability of Stainless Steel, Nucl. Appl. Tech. 9(1), 10 (1970).

TABLE I.C.14. Environmental Conditions for Test B of Program for Irradiating Mixed-oxide Fuel to Cladding Failure

Reactor power, MWt	62.5
Core position	5N2
Peak heat rating, kW/ft	
Original irradiation in X012A	13.8
Test specimen (11 at. % burnup)	14.6
Hottest environmental element	13.4
Coldest environmental element	12.4
Maximum coolant temperature, °F	1100
Temperature of mixed coolant at subassembly outlet, °F	987
Maximum fuel temperature, °F	
Test specimen[a]	4530
Environmental element[b]	4340
Flow through subassembly, gpm	24.2

[a]Gap conductance of test specimen, 1200 Btu/(hr)(ft^2)(°F).
[b]Gap conductance of environmental element, 1000 Btu/(hr)(ft^2)(°F).

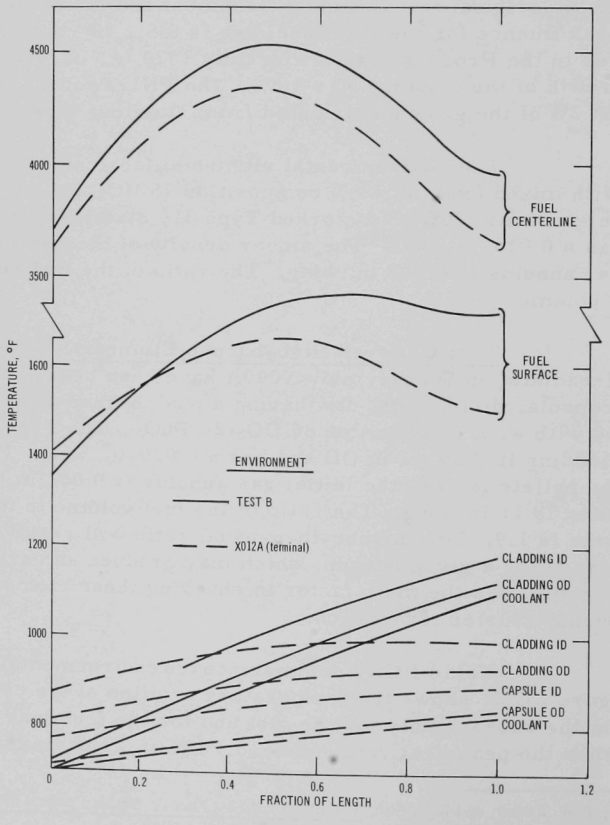

Fig. I.C.20. Temperature Profiles of Test Element NUMEC D-5

TABLE I.C.15. Environmental Conditions for Test C of Program for Irradiating Mixed-oxide Fuel to Cladding Failure

Reactor power, MWt	62.5
Core position	6N2 or 6N5
Peak heat rating, kW/ft	
Maximum	16.1
Center	15.9
Minimum	14.8
Maximum coolant temperature, °F	1020
Temperature of mixed coolant at subassembly outlet, °F	866
Maximum fuel temperature,[a] °F	4600
Flow through subassembly, gpm	15.7

[a]Fuel/cladding gap conductance of 1200 Btu/(hr)(ft^2)(°F).

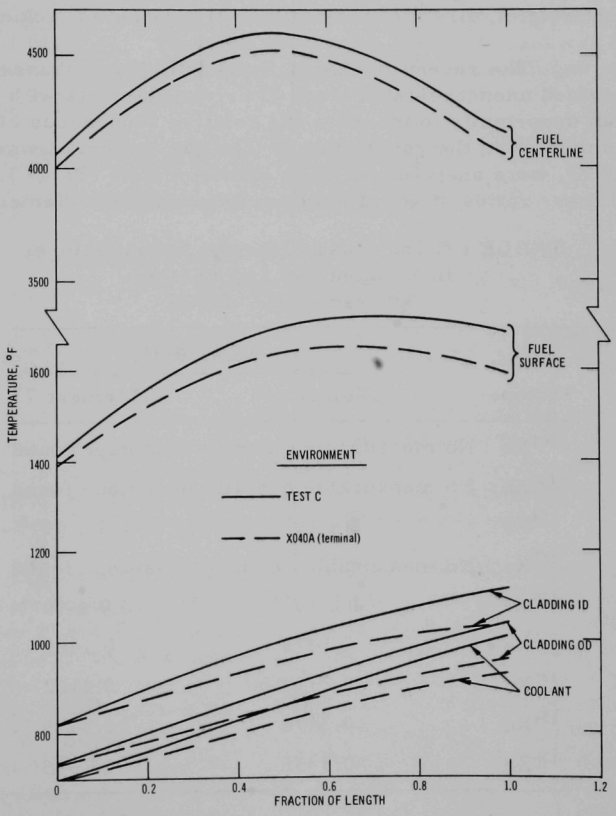

Fig. I.C.21. Temperature Profiles of Test Element ANL-024

of the cladding of this element at a burnup of 6 at. % was 1.4%. Of this, 0.7% was calculated with the PNL swelling equation to be due to stainless steel swelling.

b. Xenon-tag Technique

Last Reported: ANL-7742, pp. 82-86 (Sept 1970).

(i) Effective Yield Fractions for Low-mass Xenon Isotopes (E. R. Ebersole and M. T. Laug)

The successful application of the xenon-tag method for identifying defective experimental fuel elements has been predicted on the assumption that the effective yields of ^{124}Xe, ^{126}Xe, ^{128}Xe, ^{129}Xe, and ^{130}Xe are negligible. Although all available information indicates that this assumption is valid, direct experimental verification is lacking.

The recent discharge from EBR-II of Subassembly C-2203S, which contained unencapsulated Mark-II driver elements with high burnup, provided an opportunity to measure the relative abundances of xenon isotopes accumulated in the gas plenums. The gas contents from two elements, No. 46 and 73, were analyzed by mass spectrometer. Table I.C.16 lists the measured mass ratios of xenon isotopes found in these elements.

TABLE I.C.16. Mass Ratios of Xenon Isotopes in Elements 46 and 73 from Subassembly C-2203S

Isotope	Mass Ratio	
	Element 46	Element 73
^{124}Xe	No measurable quantity of isotope found	
^{126}Xe	No measurable quantity of isotope found	
^{128}Xe	2×10^{-5}	1.8×10^{-5}
^{129}Xe	No measurable quantity of isotope found	
^{130}Xe	1×10^{-4}	0.9×10^{-4}
^{131}Xe	0.1478	0.1467
^{132}Xe	0.2119	0.2122
^{134}Xe	0.3476	0.3475
^{136}Xe	0.2935	0.2935

Based on a value of 7.09% for the fast-fission yield of ^{134}Xe* and the information given in Table I.C.16, the effective yields for each of the remaining isotopes were established (see Table I.C.17).

TABLE I.C.17. Effective Yields of Xenon Isotopes in Elements 46 and 73 from Subassembly C-2203S

Isotope	Yield	Isotope	Yield
^{128}Xe	4.1×10^{-4}	^{132}Xe	4.33
^{130}Xe	2×10^{-3}	^{134}Xe	7.09[a]
^{131}Xe	3.02	^{136}Xe	5.96

[a]Yield for ^{134}Xe was used as the basis for yield normalization.

The fact that neither ^{124}Xe, ^{126}Xe, nor ^{129}Xe was found tends to rule out the possibility that any of these species is a fission product. The fact that ^{128}Xe and ^{130}Xe were found does not indicate that either of these species is necessarily a fission product. Xenon-128 could have originated from neutron capture in ^{127}I, a fission product that is radioactively stable. Similarly, ^{130}Xe could have been generated from neutron capture in ^{129}I, a fission product. The generation of ^{128}Xe and ^{130}Xe from the successive beta-decay of fission products seems unlikely. Both species are effectively blocked by their stable tellurium precursors.

9. Characterization of Irradiation Environment (189a 02-151)

Last Reported: ANL-7742, pp. 86-88 (Sept 1970).

(Experimental results for the ZPR-3 assemblies discussed here are reported in Sect. I.A.4, "ZPPR and ZPR-3 Operations and Analysis.")

a. Radial Reaction-rate Traverses in ZPR-3 Assembly 62 (D. Meneghetti, K. E. Phillips, and D. G. Stenstrom)

Radial reaction-rate traverses for ^{239}Pu fission and ^{10}B capture in ZPR-3 Assembly 62 have been calculated based on the flux solutions of a two-dimensional, RZ-geometry, S_4 approximation. A 29-group cross-section set having detector-cross-section values corresponding to MC^2 averagings of the various regional compositions was used.

Figures I.C.22 and I.C.23 compare the calculated traverses for ^{239}Pu fission and ^{10}B capture, respectively, with corresponding experimental values reported by the ZPR-3 experimental group in ANL-7742, pp. 17-20. The calculated values for ^{239}Pu fission response in the stainless steel-reflector region are less than the experimental values, a situation also noted for ^{235}U fission (see ANL-7742, p. 87). This discrepancy is also evident in the ^{10}B capture traverses. These discrepancies, which were not observed for either the blanketed or the nickel-reflected Assemblies 60 and 61, respectively, are probably caused by the poor energy resolution of the cross-section data for iron in the ENDF/B, Version-I compilation.

*F. L. Lisman et al., Burnup Determination of Nuclear Fuels, Project Report for the Quarter Apr 1 to June 30, 1968, and Final Report, IN-1277.

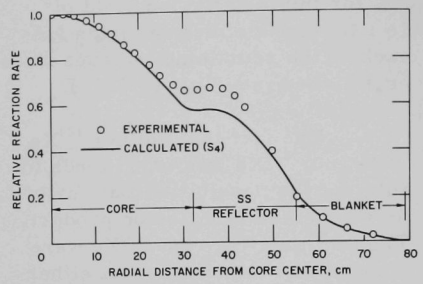

Fig. I.C.22. $^{239}Pu_f$ Radial Traverse at Axial Midplane of ZPR-3 Final Assembly 62

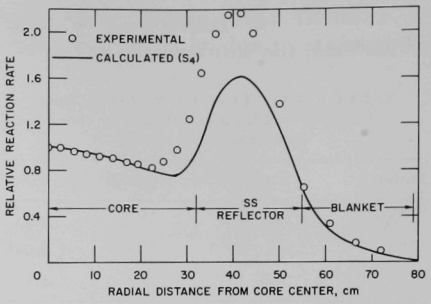

Fig. I.C.23. $^{10}B_C$ Radial Traverse at Axial Midplane of ZPR-3 Final Assembly 62

b. Calculated Gamma-deposition Profiles for ZPR-3 Assembly 60 (D. Meneghetti and D. G. Stenstrom)

Two-dimensional, RZ-geometry neutronics and gamma calculations for ZPR-3 Assembly 60 have been made with the DOT transport code. The gamma calculations used 20 energy groups with an S_6P_3 approximation. Figure I.C.24 shows the calculated radial profiles, in the midplane, for gamma deposition in a unit mass of iron and in a unit volume of regional core and blanket material. The experimental data shown with the profiles were obtained with thermoluminescent dosimeters (TLD's) by the ZPR-3 experimental group and were reported in the April-May 1970 Progress Report (ANL-7688, pp. 35-42). Both the experimental data and the calculated curves in the figure are set at unity at the core center. Since the TLD's were surrounded by a steel sleeve and placed near steel material whenever possible in the assembly, the calculated profile of deposition in iron should be compared with the experimental data. The experimental dose traverse does not drop off as rapidly as the calculated traverse in the radial-blanket region.

c. Comparison of 29-group Calculated Spectra with Experimental Spectra in ZPR-3 Assembly 61 (D. Meneghetti and K. E. Phillips)

Figure I.C.25 compares the calculated neutron-flux spectra at the core center, at the core edge near the nickel radial reflector, and in the nickel reflector of Assembly 61 with the experimental spectra. (The experimental data were reported in the Progress Report for June 1970, ANL-7705, p. 35.) The calculated spectra were obtained using RZ-geometry, 29-energy-group, DOT transport in the S_4 approximation. The 29-group cross-section set was derived from the ENDF/B (Version-I) compilation, using MC^2 averagings.

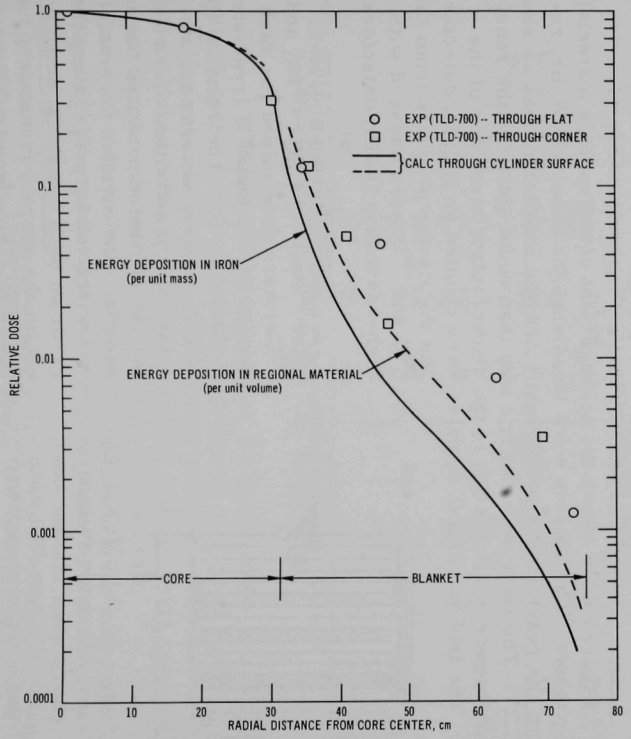

Fig. I.C.24. Calculated Radial Gamma-deposition Profile Compared with Experimental Values Obtained with Thermoluminescent Dosimeters (TLD's): ZPR-3 Assembly 60

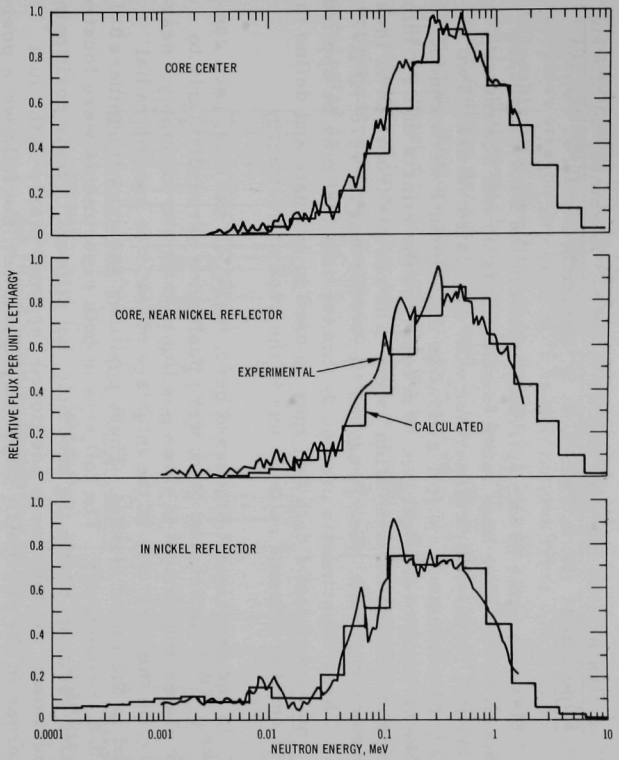

Fig. I.C.25. Comparison of Calculated Spectra with Experimental (proton-recoil) Spectra at Various Positions in ZPR-3 Assembly 61

d. Activation-rate Measurements in ZPR-3 Assembly 60 Mockup Experiment (N. D. Dudey, R. R. Heinrich, and R. J. Popek)

Measurements of foil-activation rates in the EBR-II mockup experiments in ZPR-3 have been made to obtain data on foil dosimetry, using the critical facility, for comparison with calculated values. Two independent, but complementary, foil-activation experiments were conducted in Assembly 60. Both were designed to account for the effects of ZPR thin-plate heterogeneities on the activation rates. The results from one of these were previously reported. (See Progress Report for August 1970, ANL-7737, pp. 27-33.) These experiments provide dosimetry data that may be applied to EBR-II and experimental data that may be used to evaluate and define the accuracy of reactor-physics calculations in the area of dosimetry.

In the experiment discussed here, three foil packets, each consisting of ^{235}U, ^{238}U, nickel, and gold, were positioned perpendicularly to the drawer plates and located in three positions within the assembly: near core center, on the core side of the interface of the core and the radial blanket, and in the radial blanket. These positions are drawer numbers 0-15, 0-11, and 0-8, respectively. The foil sets in both experiments were located in symmetric positions within the assembly, but differed in their positioning. In this experiment, the foils were positioned perpendicularly to the fuel plates, whereas in the previously reported experiment, the foils were positioned between and were parallel to the fuel plates.

Figure I.C.26 shows the arrangement of the various materials in the foil packets. The packets were irradiated for about 600 W-hr, removed from the reactor, and subsequently cut into smaller pieces as shown in Fig. I.C.27. The foils were cut in a way that would optimize the sensitivity to heterogeneity effects due to the drawer-plate structure of the assembly. The fold and nickel samples were counted on NaI(Tl) detectors, and the fission products from the ^{235}U and ^{238}U were assayed with high-resolution Ge(Li) detectors.

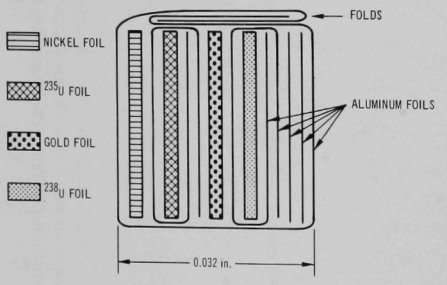

Fig. I.C.26. Expanded Side View of Foil-packet Arrangement in ZPR-3 Assembly 60 (foil thicknesses, in inches: nickel, 0.010; ^{235}U, 0.006; ^{238}U, 0.010; gold, 0.0002; aluminum, 0.0005)

Seven fission products (^{95}Zr, ^{97}Zr, ^{103}Ru, ^{131}I, ^{132}Te, ^{140}Ba, and ^{143}Ce) were determined for each sample of ^{238}U and ^{235}U irradiated in Assembly 60. The relative fission rates were determined by summing the activities of the seven individual fission products for each sample. The relative uncertainty was evaluated by propagating the error on each individual activity to obtain the overall uncertainty for the sum. The absolute fission rate

of a particular fission product is determined by dividing the activation rate by the appropriate fission yield. Ultimately, very accurate fission yields for these fission products will be determined from a third experiment in Assembly 60. (See Progress Report for March 1970, ANL-7679, pp. 113-114.) At present, however, neither the ^{235}U nor the ^{238}U yields for the seven fission products are well known. Meek and Rider* have summarized numerous fission-product yields for ^{235}U and ^{238}U in both a thermal and a fission spectrum of neutrons. We have used their recommended yields as a guide in estimating a set of fission-product yields that are relatively self-consistent with our measured fission-product activities. These yields are presented in Table I.C.18.

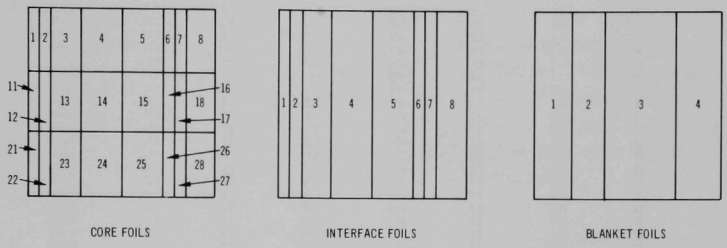

Fig. I.C.27. Foil-cutting Diagram (foils are 2 in. square)

TABLE I.C.18. Summary of Fission-yield Information

Reaction	Fission Product	Inferred Fission Yield,[a] %	Meek and Rider[b] Thermal, %	Meek and Rider[b] Fission Spectrum, %	Reaction	Fission Product	Inferred Fission Yield,[a] %	Meek and Rider[b] Thermal, %	Meek and Rider[b] Fission Spectrum, %
$^{235}U(n,f)$	^{95}Zr	6.7	6.2	6.7	$^{238}U(n,f)$	^{95}Zr	5.9		5.8
	^{97}Zr	6.3	5.9	6.77		^{97}Zr	6.1		4.9
	^{140}Ba	5.8	6.30	5.6		^{140}Ba	6.0		6.0
	^{132}Te	4.7	4.33	5.5		^{132}Te	5.3		4.4
	^{143}Ce	5.3	5.91	5.4		^{143}Ce	4.0		4.3
	^{131}I	3.4	2.91	3.7		^{131}I	3.3		3.2
	^{103}Ru	3.1	3.0	3.5		^{103}Ru	6.2		5.8
	Total	35.3	34.5	37.2		Total	36.8		34.4

[a]The inferred fission yields are self-consistent with foils irradiated near the core of ZPR-3 Assembly 60.
[b]Recommended fission-yield values from M. E. Meek and B. F. Rider, APED-5398 (Mar 1968).

The absolute fission rates for each sample were determined by dividing the sum of the seven individually measured fission-product activation rates by the sum of the seven self-consistent (inferred) fission yields. Although the uncertainties for the fission yields can only be estimated, they are thought to be accurate to ±5 to ±15%. The results of the fission-rate measurements are presented in Table I.C.19. Table I.C.20 summarizes the results for the absolute reaction rates for three of the

*M. E. Meek and B. F. Rider, Summary of Fission Product Yields for U-235, U-238, Pu-239, and Pu-241 at Thermal, Fission Spectrum and 14-MeV Neutron Energies, APED-5398 (Mar 1968).

TABLE I.C.19. Fission Rates for ^{235}U and ^{238}U Samples in ZPR-3 Assembly 60

Sample	^{235}U Relative Fission Rate x 10^{15}, sec^{-1}	^{235}U Relative Error, %	^{235}U Absolute Fission Rate x 10^{15}, sec^{-1}	^{238}U Relative Fission Rate x 10^{15}, sec^{-1}	^{238}U Relative Error, %	^{238}U Absolute Fission Rate x 10^{15}, sec^{-1}	$^{238}U/^{235}U$
Blanket							
1	4.10	2.2	11.6	0.073	4.2	0.200	0.0172
2	5.05	1.9	14.3	0.090	2.8	0.243	0.0170
3	5.19	3.0	14.7	0.110	2.9	0.300	0.0204
4	5.89	2.1	16.7	0.132	2.5	0.360	0.0216
Interface							
1	8.97	2.5	25.4	0.475	4.0	1.29	0.0508
2	9.23	2.5	26.1	0.490	2.7	1.33	0.0510
3	9.64	2.5	27.3	0.596	2.6	1.62	0.0593
4	9.84	2.6	27.9	0.620	2.8	1.68	0.0602
5	9.96	2.0	28.2	0.702	2.1	1.91	0.0677
6	10.1	2.9	28.8	0.735	2.7	2.00	0.0699
7	10.9	2.3	30.9	0.744	2.0	2.02	0.0654
8	11.0	2.2	31.2	0.746	2.6	2.03	0.0651
Core							
1	15.1	2.3	42.8	1.12	3.2	3.04	0.0710
2	15.4	2.5	43.6	1.12	3.2	3.05	0.0700
3	15.8	3.0	44.8	1.18	3.7	3.22	0.0729
4	15.3	2.3	43.3	1.11	3.9	3.03	0.0700
5	15.5	2.4	43.9	1.09	4.8	2.97	0.0677
6	15.9	2.4	45.0	1.17	3.1	3.19	0.0709
7	16.1	3.6	45.6	1.25	2.7	3.41	0.0748
8	16.3	2.9	46.2	1.19	3.5	3.24	0.0701
11	15.9	2.3	45.0	1.13	2.6	3.08	0.0684
12	15.3	2.7	43.3	1.09	3.2	2.97	0.0686
13	15.9	2.1	45.0	1.25	3.7	3.41	0.0758
14	15.3	2.2	43.3	1.18	2.7	3.22	0.0744
15	15.7	2.3	44.5	1.19	2.6	3.24	0.0728
16	16.0	2.1	45.3	1.20	3.1	3.27	0.0722
17	16.1	2.1	45.6	1.28	3.0	3.49	0.0765
18	16.0	2.2	45.3	1.20	3.2	3.27	0.0722
21	15.9	2.9	45.0	1.14	3.6	3.11	0.0691
22	15.7	2.6	44.5	1.14	2.4	3.11	0.0699
23	15.8	2.1	44.8	1.21	2.9	3.30	0.0737
24	15.4	2.5	43.6	1.14	2.6	3.11	0.0713
25	15.5	2.3	43.9	1.16	2.8	3.16	0.0720
26	16.3	2.2	46.2	1.21	2.8	3.30	0.0714
27	16.2	2.2	45.9	1.27	3.1	3.46	0.0754
28	16.2	2.1	45.9	1.19	3.1	3.24	0.0706

TABLE I.C.20. Absolute Reaction Rates in ZPR-3 Assembly 60

Sample	$^{197}Au(n,\gamma)^{198}Au$ Reaction Rate x 10^{16}, sec^{-1}	$^{197}Au(n,\gamma)^{198}Au$ Relative Error, %	$^{197}Au(n,\gamma)^{198}Au$ Absolute Error, %	$^{58}Ni(n,p)^{58}Co$ Reaction Rate x 10^{16}, sec^{-1}	$^{58}Ni(n,p)^{58}Co$ Relative Error, %	$^{58}Ni(n,p)^{58}Co$ Absolute Error, %	$^{238}U(n,\gamma)^{239}Np$ Reaction Rate x 10^{16}, sec^{-1}	$^{238}U(n,\gamma)^{239}Np$ Relative Error, %	$^{238}U(n,\gamma)^{239}Np$ Absolute Error, %
Blanket									
1	32.2	1.6	8.2	0.470	0.7	5.9	16.1	3.8	7.7
2	35.4	2.1	8.3	0.561	0.7	5.9	18.8	4.8	8.2
3	37.9	0.6	8.1	0.670	0.5	5.9	21.7	4.2	7.9
4	39.6	0.6	8.1	0.868	1.2	6.0	21.2	4.4	8.0
Interface									
1	54.1	0.6	8.1	3.42	0.9	5.9	29.3	2.2	7.0
2	50.6	1.2	8.2	3.60	1.0	5.9	28.3	2.7	7.2
3	50.7	0.7	8.1	4.05	0.5	5.9	30.5	4.4	8.0
4	53.1	0.6	8.1	4.27	0.4	5.8	32.6	3.8	7.6
5	54.0	0.7	8.1	4.81	0.2	5.8	33.6	4.1	7.8
6	53.7	0.2	8.1	5.32	0.4	5.8	33.3	2.6	7.1
7	54.3	0.7	8.1	5.55	0.5	5.9	32.4	2.8	7.2
8	55.2	0.5	8.1	5.18	0.3	5.8	35.9	5.1	8.3
Core									
1	74.5	1.0	8.1	8.31	0.2	5.8	46.2	4.2	7.2
2	76.0	0.8	8.1	8.40	0.1	5.8	46.0	1.5	6.1
3	73.0	0.3	8.1	8.74	0.2	5.8	47.5	2.1	6.3
4	75.1	0.4	8.1	8.48	0.1	5.8	49.8	7.2	9.3
5	75.4	0.2	8.1	8.73	0.4	5.8	47.9	7.3	9.4
6	74.5	1.1	8.1	9.10	0.9	5.9	47.6	2.4	6.4
7	74.2	0.5	8.1	9.27	0.7	5.9	46.4	2.0	6.3
8	75.3	0.6	8.1	8.60	0.6	5.9	45.9	3.7	7.0
11	73.2	0.4	8.1	8.47	1.4	6.0	47.0	2.7	6.5
12	75.3	0.3	8.1	8.60	0.5	5.9	45.3	3.6	6.9
13	75.8	0.2	8.1	8.97	0.9	5.9	48.8	6.5	8.8
14	76.1	0.3	8.1	8.75	1.6	6.0	47.6	2.4	6.4
15	76.4	1.2	8.2	8.92	0.3	5.8	47.9	3.2	6.7
16	75.7	0.4	8.1	9.39	0.6	5.9	49.3	5.8	8.3
17	76.7	0.2	8.1	9.54	0.5	5.9	48.8	5.7	8.2
18	76.5	0.2	8.1	8.81	0.5	5.9	49.5	4.8	7.6
21	72.2	1.0	8.1	8.58	0.8	5.9	46.9	1.8	6.2
22	75.6	0.4	8.1	8.62	0.7	5.9	47.6	4.7	7.6
23	73.7	4.4	9.2	8.97	0.1	5.8	47.5	2.3	6.3
24	77.1	0.3	8.1	8.66	0.2	5.8	46.4	2.2	6.3
25	77.3	0.1	8.1	8.92	0.8	5.9	49.9	3.3	6.8
26	74.5	0.7	8.1	9.37	0.4	5.8	47.2	1.8	6.2
27	78.1	0.5	8.1	9.53	0.4	5.8	49.0	1.7	6.2
28	77.9	0.5	8.1	8.85	0.6	5.9	49.5	1.5	6.1

reactions measured: $^{197}Au(n,\gamma)$, $^{58}Ni(n,p)$, and $^{238}U(n,\gamma)$. These three reaction rates, together with the two fission rates, will provide a means for characterizing the neutron-energy distributions.

10. Operation of Data Acquisition System (DAS) (189a 02-530)

Last Reported: ANL-7742, p. 89 (Sept 1970).

a. Acceptance Tests (R. W. Hyndman)

The digital data-acquisition system (DAS) passed its acceptance test of 30 days at 90% reliability. Operating time for the system during the 30-day test period was 96.6%. The 3.4% downtime was caused by failure of a card reader and of the rapid access device (RAD). The acceptance tests were conducted on all equipment listed in the original purchase contract, except the graphic-display unit. Also under test, but not as part of the original purchase contract, were an additional RAD, two magnetic-tape systems, and an extra 8 k of magnetic core storage.

D. Experimental Breeder Reactor No. II--Fuel Fabrication

1. Fuel and Hardware Procurement (M. J. Feldman) (189a 02-073)

a. Reclamation of Vendor Fuel (D. L. Mitchell)

Last Reported: ANL-7742, p. 90 (Sept 1970).

During this reporting period, 1800 more vendor elements were processed. Of these, 1461 were "accept" elements and 339 were "reject" elements. Void size in the sodium bond* was the principal cause for rejection. A high percentage (30-46%) of elements from the last five fuel batches to be heat-treated was rejected for voids. The reason for formation of voids in these batches is being determined.

E. Experimental Breeder Reactor No. II--Operations

1. Reactor Operations (G. E. Deegan) (189a 02-075)

a. Operations

Last Reported: ANL-7742, pp. 90-91 (Sept 1970).

From September 16 through October 15, the reactor operated for 1136 MWd in Runs 46A and 46B. These runs were the first of regular operation at 62.5 MWt. The accumulated total of EBR-II operation is 40,427 MWd.

Fuel handling for Run 46A was completed without difficulty after the No. 1 control-rod thimble was replaced. Inspection of the thimble showed that three flats were scratched and the upper end of one flat was deformed. Swelling in the core region was also evident.

A flux-wire irradiation run of 1 hr at 50 kW was made, and the subassemblies containing the irradiated wires were transferred to the FEF. The reactor was then started up for Run 46A, and the control rods were calibrated. Because fewer than usual experimental subassemblies had been loaded in the reactor for initial operation at 62.5 MWt, control-rod worths had decreased significantly from the previous run. A reactivity adjustment was therefore necessary, so the reactor was shut down. After fuel handling for the adjustment had been completed, the reactor was restarted on September 22. During the subsequent operation in Run 46A, special monitoring and physics tests were performed in accordance with an approved test procedure. Operation at 62.5 MWt was attained on September 25, and the testing program associated with higher-power operation was successfully completed.

*The elements rejected for void size may be reclaimed by impact bonding. (See Progress Report for July 1970, ANL-7726, p. 76.)

There were three scrams during Run 46A. One was caused by failure of an ac voltage regulator, and one by a low setting of a scram set-point for the secondary-sodium pump. The cause of the third scram is unknown. At the end of Run 46A, on October 6, there was no remaining excess reactivity, and power had been permitted to drift down to 61 MWt to complete the scheduled 750 MWd of operation.

The reactor was started for Run 46B on October 8. Loading for this run included installation of the first high-worth control rod and temporary replacement of the stainless steel drop rod with a standard fueled control rod. Two spurious scrams of the reactor occurred during Run 46B.

The loading changes for Run 46A, in addition to those reported last month and those reported above, included installation of three surveillance subassemblies containing heat-treated vendor fuel and four reconstituted surveillance subassemblies containing Mark-II fuel. The loading changes for Run 46B included installation of one reconstituted surveillance subassembly containing Mark-II fuel. (See Sect. I.C.4.a for changes of experimental subassemblies.)

2. Fuel Cycle Facility Operations* (M. J. Feldman) (189a 02-076)

a. Fuel Assembly (D. L. Mitchell)

Last Reported: ANL-7742, p. 91 (Sept 1970).

Eight Mark-IA subassemblies containing vendor-fabricated elements were assembled in the cold line during this reporting period. The vendor-fabricated elements that had been accepted by ANL verification inspection are being heat-treated to reclaim them (see Sect. I.D.1.a).

Table I.E.1 summarizes the production activities for September 16 through October 15, 1970, and for fiscal year 1971.

b. Fuel Handling and Transfer (N. R. Grant, W. L. Sales, and K. DeCoria)

Last Reported: ANL-7742, p. 91 (Sept 1970).

Table I.E.2 summarizes the fuel-handling operations performed.

c. Reactor Support (J. P. Bacca and N. R. Grant)

Last Reported: ANL-7742, pp. 93-94 (Sept 1970).

*The Fuel Cycle Facility (FCF) is now called the Fuels and Examination Facility (FEF).

ANL 7455

TABLE I.E.1. Production Summary for FEF Cold Line

	9/16/70 through 10/15/70		Total for FY 1971
Subassemblies Fabricated with Mark-IA Fuel			
With cold-line elements	0		0
With vendor elements	8		40
Preirradiation Treatment of Vendor Mark-IA Fuel			
Heat-treating of as-fabricated elements (22,614[a])			
Heat-treated, inspected, and accepted	1461		2627
Heat-treated, inspected, and rejected[b]	339		581
Total Elements Available for Subassembly Fabrication as of 10/15/70			
Cold-line fuel			
Mark IA		250	
Mark II		223	
Vendor fuel (Mark IA)			
Impact-bonded[c]		2685	
Heat-treated		2465	

[a]These elements, cast and centrifugally bonded by the vendor, have been accepted by ANL verification inspection, but not yet approved for general use in the reactor. They are being heat-treated to reclaim them (see Sect. I.D.1.a).
[b]Void size in the sodium bond is the principal cause for rejection. Elements rejected for this reason may be reclaimed by impact-bonding (see Sect. I.D.1.a).
[c]Impact-bonding by ANL of 11,853 unbonded vendor fuel elements was completed in fiscal year 1970.

TABLE I.E.2. Summary of FEF Fuel Handling

	9/16/70 through 10/15/70	Totals for FY 1971
Subassembly Handling		
Subassemblies Received from Reactor		
Driver fuel (all types)	12	44
Experimental	12	22
Other (blanket)	11	24
Subassemblies Dismantled for Surveillance, Examination, or Shipment to Experimenter		
Driver fuel	8	28
Experimental	10	20
Other (blanket)	3	4
Driver-fuel Elements to Surveillance	143	1191
Number from subassemblies	2	18
Subassemblies Transferred to Reactor		
Driver fuel		
From air cell	1	6
From cold line[a]	16	47
Experimental	6	10
Fuel-alloy and Waste Shipments		
Cans to Burial Ground	2	6
Blanket Subassemblies to Burial Ground	0	11
Skull Oxide and Glass Scrap to ICPP	0	0
Recoverable Fuel Alloy to ICPP		
Fuel elements[b]	2 (34.85 kg of alloy)	6 (104.48 kg of alloy)
Subassemblies[b]	5 (23.42 kg of alloy)	18 (92.64 kg of alloy)
Nonspecification material	0	0

[a]Cold-line subassemblies, following fabrication and final tests, are transferred either to the reactor or to the special-materials vaults for interim storage until needed for use in the reactor.
[b]Figure outside parentheses is number of shipments made; figure inside is weight of alloy shipped.

(i) Examination of Guide Thimbles from Reactor Grid Positions 5A3, 3A1, and 5D1 (R. D. Phipps and R. V. Strain)

A third guide thimble was received from the reactor for examination at the FEF. This control-rod thimble had received an estimated total maximum fluence of 1.5×10^{23} nvt (39,291 MWd) in grid position 5D1. It too had been removed from the reactor grid because of fuel-loading difficulties experienced in an adjacent position of the reactor grid. Examination of the two guide thimbles received previously was continued. These were the control-rod thimble from grid position 5A3 [calculated total maximum fluence of 1.4×10^{23} nvt (36,785 MWd)] and the safety-rod thimble from grid position 3A1 [calculated total maximum fluence of 1.7×10^{23} nvt (37,490 MWd)].

The thimble from position 5D1 was visually inspected and photographed through the air-cell periscope. Photographs made with the thimble in front of a straightness grid show some bowing, the top end of the thimble being bowed in a direction corresponding to the direction away from the core center while the thimble was in EBR-II. Longitudinal scratches (similar to those observed earlier on the thimbles from positions 3A1 and 5A3) were seen on the three flats that faced the core center while the thimble was in the reactor. No scratches were seen on the opposite three flats, but a portion of the top edge of one of these flats is deformed outwardly about 1/8 in.

The thimbles from grid positions 3A1 and 5D1 were measured for total-indicated-runout (TIR) with the subassembly-straightness tester. (These measurements give some indication of the magnitude of bowing.) The maximum TIR reading was 0.015 in. for the thimble from grid position 5D1 and 0.055 in. for the thimble from grid position 3A1. The maximum allowable preirradiation bow (TIR) is 0.080 in.

Measurements of the length of the hexagonal tubing of the thimble from 5D1 showed an average increase of 3/16 in. over the length of $49\frac{1}{2}$ in. on fabrication drawings. The thimble was also gross gamma-scanned for ^{58}Co and ^{54}Mn gamma activities along its length in one azimuthal orientation (along one flat of the hexagonal tube).

Measurements made of each of the three thimbles with a recently fabricated, milled, flat-surface plate will give (1) an indication of the axial bow and the concavity or convexity of each flat to an estimated accuracy of ±0.005 in. and (2) an indication of the twist of the thimbles. The measurements are being analyzed.

Design work is being initiated for a device to measure the flat-to-flat dimension across the flats and the corner-to-opposite-corner dimensions of the hexagonal tubes.

(ii) Measurement of Subassembly Outlet Temperature. Five additional subassemblies containing temperature monitors have been received from the reactor, dismantled, and processed. Table I.E.3 lists these subassemblies, their grid positions, and the monitors they contained.

TABLE I.E.3. Irradiated Subassemblies with Temperature Monitors Received from EBR-II

Subassembly No.	Grid Position	Type of Monitor[a]		
		Melt Wire	SiC	Sodium
C-2212S	1A1	X	O	O
C-2216S	2C1	X	X	X
C-2221S	2E1	O	X	X
C-2224S	4C1	O	X	X
B-3076S	6D1	X	X	X

[a]X indicates monitor was used in subassembly; O indicates monitor was not used.

(iii) Reconstitution of Subassemblies for Higher-power Operation. The fifth of six driver subassemblies containing Mark-II fuel was reconstituted for 62.5-MWt operation. This subassembly (C-2235S) was reconstituted from elements removed from Subassembly C-2229S (peak burnup, 1.8 at. %) and visually examined in the air cell. It has been transferred to the reactor. Interim examination of the sixth subassembly, C-2203S (peak burnup, 3.3 at. %), is not complete. This subassembly will be reconstituted as Subassembly C-2232S and transferred to the reactor.

(iv) Flux-wire Subassemblies. Three subassemblies containing flux wires 12, 14, and 15 were received from the reactor and washed. The wires were removed, and the subassemblies were stored for use in future flux determinations.

PUBLICATIONS

Plutonium Fuel Fabrication Techniques
J. E. Ayer
Metalurgia (Brazil) 26(153), 615-620 (Aug 1970)

Suitability of Some Components of the EBR-II Sodium Systems for Operation at 62.5 MWt
N. Bulut
ANL/EBR-016 (July 1970)

Dynamic Simulation and Analysis of EBR-II Rod-drop Experiments
A. V. Campise
ANL-7664 (Mar 1970)

Intergranular Corrosion Cracking of Type 304 Stainless Steel in Water-Cooled Reactors
C. F. Cheng
Reactor Technol. 13(3), 310-319 (Summer 1970)

Passive Splitters for Fast Pulse Processing
W. C. Corwin and K. G. Porges
Nucl. Instr. Methods 85, 155 (1970)

Proposal for Operating EBR-II at 62.5 MWt
R. A. Cushman (Report Coordinator)
ANL/EBR-012 (Aug 1969)

Operation of EBR-II at 62.5 MWt: An Evaluation of Plant and Reactor Data from Run 38A
R. A. Cushman (Report Coordinator)
ANL/EBR-013 (Dec 1969)

A New Technique for Investigating Feedback and Stability of a Nuclear Reactor
Ivar A. Engen
ANL-7686 (June 1970)

Conditional Variances Pertinent to Doppler Effect Studies
R. N. Hwang and L. B. Miller
Nucl. Sci. Eng. 42, 179-190 (Nov 1970)

An Automated System for Internal Friction Measurements
D. L. Smith, A. L. Winiecki, and R. H. Lee
J. Sci. Instr. 3, 715-718 (1970)

II. GENERAL REACTOR TECHNOLOGY

A. Applied and Reactor Physics Development

1. Theoretical Reactor Physics

a. Theoretical Reactor Physics (189a 02-081)

(i) Cross-section Data Evaluation (E. M. Pennington)

Last Reported: ANL-7742, p. 96 (Sept 1970).

The MC^2 library of Version II ENDF/B neutron cross-section data has been used to run MC^2 problems for Godiva, Jezebel, and Zebra 3, three of the ten assemblies for ENDF/B data testing. Godiva and Jezebel are small, bare, very fast assemblies consisting mainly of ^{235}U and ^{239}Pu, respectively. Zebra 3 is a reflected assembly with considerable ^{239}Pu and ^{238}U in the core, and a rather soft spectrum. The MC^2 problems were followed by S_n transport-theory calculations using the one-dimensional transport path in the ARC system. The values of k_{eff} obtained for Godiva, Jezebel, and Zebra 3 were 1.0012, 0.9887, and 0.9319, respectively.

The values of k_{eff} for both ^{239}Pu-fueled assemblies are too low. Calculations* for a series of ^{239}Pu-fueled assemblies using preliminary Version II data also resulted in low k_{eff} values. Low values for some of the other data-testing assemblies were reported informally at the CSEWG meeting at Brookhaven National Laboratory on October 7 and 8. These low k_{eff} values led to plans for a task force to prepare new versions of ^{239}Pu, ^{238}U, and ^{235}U after the data testing has been completed.

There is a problem with Version II ENDF/B data concerning the nuclear radius used in calculating unresolved resonance cross sections. Briefly, there are two nuclear radii involved; one is given explicitly and is to be used in calculating potential scattering; the other is to be calculated from a formula and is used in calculating penetration factors. ETOE and MC^2 use only the radius given explicitly for both potential scattering and penetration factors. One cannot allow for this discrepancy by merely changing ETOE and MC^2, because some of the basic ENDF/B data are not consistent with the use of the two radii, and one cannot tell this fact by merely looking at a listing of the data. The differences between the two radii are important at energies where p-wave contributions to capture and fission are significant, because p-wave contributions are very roughly proportional to the square of the radius used in calculating penetration factors. To investigate the matter further, the unresolved resonance code,

*W. W. Little, et al., Analysis of Critical Experiments Using Version II of the Evaluated Nuclear Data File (ENDF/B), Trans. Am. Nucl. Soc. 13, 1, 304 (1970).

UR, has been modified to handle the Version II ENDF/B unresolved resonance formats, and to use either both radii or only the potential scattering radius in the calculations.

(ii) Neutronics Calculation Capability

Last Reported: ANL-7726, pp. 85-86 (July 1970).

(a) Applications of Space-Energy Factorization to the Solution of Static Fast-Reactor Neutronics Problems (W. M. Stacey, Jr., and H. Henryson)

An approximate method for solving the neutron-diffusion equation, based upon factorization of the neutron flux into a spectral function and a spatial shape function (with weak energy dependence), was developed recently. This factorization of the flux leads to coupled equations for the spectral and spatial functions which must be solved iteratively, thus effectively defining an iteration procedure between a broad-group calculation for the spatial function appropriate for a given energy interval and a fine-group calculation for the spectral function appropriate within that energy interval. Numerical tests indicated that space-energy factorization with four to six shape-function intervals (energy intervals over which a single shape function is used) agreed very well with the direct solution for typical one-dimensional fast-reactor models represented with 24-energy groups.

An extension of the method employing several spectral functions associated with the various regions of a reactor, but with overlapping domains, has been examined. In this case, the single equation for the spectral function in the original method is replaced by a coupled set of equations for all the spectral functions. (These equations are also coupled to the equation for the spatial function, as in the original method.) Allowing different spectral functions to be used in different parts of a reactor produced greater flexibility. Numerical tests, for typical one-dimensional fast-reactor models with 24 energy groups, indicate that the added flexibility obtainable with multiple spectral functions does improve the accuracy of the factorization method in the prediction of k_{eff}, power distribution, spectra, etc., as expected. However, comparable improvement could be obtained with less computational expenditure by using more shape-function intervals in the original method. For example, when two shape-function intervals were used in a typical problem with two core regions, two blanket regions, and a reflector, the error in k_{eff} was -0.0081 with a single spectral function and was reduced to 0.0031 with three spectral functions. When four shape-function intervals were employed, the error in k_{eff} was reduced to -0.0024 with a single spectral function and to 0.0015 with three spectral functions.

One potential use of space-energy factorization is to provide an economical means of solving 20-30 group, multidimensional diffusion equations for fast-reactor design application. The experience obtained with one-dimensional calculations indicates a high probability of success in this application. An iterative solution routine, based upon a variant of the ADI technique, has been developed for the space-energy factorization equations in multidimensional geometries. An experimental two-dimensional code has been written to aid in the evaluation and further development of these numerical procedures. As with the one-dimensional studies, the factorization method is being evaluated as a means of obtaining an approximate solution and as a means of accelerating the solution of the conventional multigroup equations.

Another potential application of space-energy factorization is to spatially-dependent ultrafine-group (~2000) spectrum calculations for cross-section averaging. As a first step towards this application, the one-dimensional code used in previous studies has been extended to accommodate approximately 200 groups. The space-energy factorization method has yielded excellent results for several typical fast-reactor problems with this type of group structure. For example, a calculation with 15 shape-function intervals, which required 2.1 min (IBM-360), had an error in k_{eff} of 0.0009 relative to the direct solution of the 165-group diffusion equations, which required 9.75 min. When the fission source from the factorization solution was used as an initial guess to accelerate the multigroup solution, the total time (factorization plus multigroup) was 5.38 min. Use of the fission source from the factorization solution reduced the number of iterations needed to converge the multigroup solution (Chebyshev accelerated, k_{eff} convergence criterion 10^{-6}) from 42 to 14. The power-distribution and reaction-rate traverses predicted by the factorization solution agreed quite well with the direct multigroup predictions, for a model consisting of two core regions separated by a blanket and with an outer blanket.

The results indicate that the space-energy factorization method has considerable potential, both as an approximate method and as a means of accelerating the convergence of a direct solution by providing a good source guess. In particular, the method may make feasible ultrafine (~2000)-group 1D codes and broad (20-30)-group 3D codes with reasonable computational times.

(b) Spatial Synthesis (V. Luco)

Testing of the flux synthesis capabilities of the SYN2D flux synthesis module has continued, using the same highly nonseparable fast-reactor configuration* (described in Progress Report for April-May 1970, ANL-7688, p. 156). As last reported, a high degree of accuracy

*The asymmetric configuration with cores imbedded in the upper left and lower right corners of a large rectangular reflector region.

in k_{eff} and satisfactory fluxes were obtained using as trial functions flux profiles from a 2D-diffusion calculation over the same configuration. Several calculations using trial functions obtained from one-dimensional diffusion calculations have recently been completed.

The trial functions used are:

Functions 1 and 1'. These are 1D fluxes calculated using either the top (1) or bottom (1') portions of the Merriman configuration; a slab with two regions (core and reflector).

Functions 2 and 2'. These are 1D fluxes obtained with an external source located in the reflector region with a strength proportional to the fission source in the other (top or bottom) region. These are source calculations with the fission cross section set to zero.

Functions 3 and 3'. Same as 2 and 2' except that here the fission cross section is only reduced in magnitude, rather than set to zero.

Function 4. This is a symmetric 1D flux with two outside core regions and a central reflector region obtained by averaging the top and bottom regions. The core compositions are now a mixture in equal proportions of core and reflector.

All the calculations reported here used the same trial functions throughout the reactor. Table II.A.1 summarizes some of the results obtained in these series of synthesis calculations.

TABLE II.A.1. Synthesis Results for Merriman Configuration

Case	Trial Functions	k_{eff}	Δk_{eff}
1	1, 1'	1.055753	0.052859
2	1, 1', 4	1.054683	0.053929
3	1, 1', 2, 2'	1.101779	0.006833
4	1, 1', 3, 3'	1.103428	0.005184
5	1, 1', 2, 2', 4	1.107937	0.000675
6	Two 2D trial functions	1.1084	0.0001

Case 1 is the equivalent of the case reported before, using 2D instead of 1D trial functions. The present results show that these two 1D trial functions above are quite unsatisfactory. As can be seen from Table II.A.1, the best approximation obtained, that of Case 5 with five 1D trial functions, is satisfactory but appreciably less accurate than the 2D trial function case (Case 6).

Given "good" trial functions, the synthesis method performs well, but the present results indicate that the task of finding "good" trial functions by 1D calculations for extreme configurations like the one described here is not an easy one. This configuration was specifically chosen because of the anticipated difficulty in synthesizing a solution, and is not typical.

(iii) Reactor Computation and Code Development

Last Reported: ANL-7726, pp. 91-101 (July 1970).

(a) Calculation of Elastic Scattering Matrices for MC^2-2
(B. J. Toppel and C. G. Stenberg)

The general approach for the calculation of elastic scattering matrices for MC^2-2 outlined in ANL-7726 was followed. A change in notation has been made to facilitate clarity. All capital letters refer to ultrafine group (ufg) characteristics and all lower-case letters refer to hyperfine group (hfg) characteristics.

Consider N_0 to be the number of hfg per ufg and $\sigma_s^{0m}(E_i \to k)$ the P_0 scattering from energy E_i at the top of hfg i within ufg J into hfg k within ufg K. E_1 corresponds to the energy at the top of the ufg J, and E_{N_0+1} corresponds to the energy at the bottom of ufg J. Accumulating the P_0 scattering over the receptor group K from the energy E_i gives

$$\sigma_s^{0m}(E_i \to K) = \sum_{k=1}^{k=N_0} \sigma_s^{0m}(E_i \to k). \qquad (1)$$

The P_0 elastic scattering cross section from ufg J to ufg K, based on a trapezoidal integration over the hfg's within the source ufg J, is then

$$\sigma_{el_{J\to K}}^{0m} = \frac{\sigma_s^{0m}(E_1 \to K) + \sigma_s^{0m}(E_{N_0+1} \to K) + 2\sum_{i=2}^{N_0} \sigma_s^{0m}(E_i \to K)}{2N_0}. \qquad (2)$$

For scattering into the last ufg receptor group K, Eq. 2 must be modified to correctly account for the partial contribution of the scattering from the highest energetically possible hfg ℓ in the ufg source group J. The P_0 elastic transfer for scattering into the last ufg receptor group K is then given by

$$\sigma^{0m}_{el_{J\to K}} = \frac{\sigma_s^{0m}\left(E_{N_0+1} \to K\right) + 2\sum_{i=\ell+1}^{N_0} \sigma_s^{0m}(E_i \to K) - \left(1 - \ln\frac{1}{1-\alpha^m} + \ln\frac{E_{\ell+1}}{E_{K-1}}\right)\sigma_s^{0m}(E_{\ell+1} \to K)}{2N_0}, \quad (3)$$

where E_{K-1} is the energy at the top of ufg K.

The P_1 elastic transfer cross section was evaluated in a similar manner. If energies $\bar{E}_i$ and $\bar{E}_k$ are the midpoint energies of the hfg intervals in the source and receptor group, respectively, then

$$\sigma_s^{1m}(E_i \to k) = \frac{3}{2}\left(\frac{\bar{E}_k}{\bar{E}_i}\right)^{1/2}\left[(A^m+1) - \frac{\bar{E}_i}{\bar{E}_k}(A^m-1)\right]\sigma_s^{0m}(E_i \to k) \quad (4)$$

was taken as the P_1 scattering from energy E_i at the top of hfg i within ufg J into hfg k within ufg K. The P_1 scattering is accumulated over the receptor group in a manner similar to the P_0 scattering given in Eq. 1. The P_1 elastic transfer integration over the ufg source group J is similar to that given in Eqs. 2 and 3.

Results of the P_0 and P_1 elastic scattering using this method were obtained for various masses and at various energies to display the influences of anisotropy and mass on the kinematics of the scattering. The main parameter of interest is the number of hfg per ufg. In the original MC^2 code,* there is one hfg per ufg.

When integrating the scattering probability across the source ufg J to obtain $\sigma^{0m}_{el_{J\to J+N}}$ and $\sigma^{1m}_{el_{J\to J+N}}$ for all possible ultrafine receptor groups N, one would like to minimize the number of hfg's per ufg in the integration in order to minimize computer time while at the same time accepting a certain magnitude of error.

In Table II.A.2, the percentage errors in the calculation of the elastic transfer cross sections as a function of hfg per ufg are displayed relative to 20 hfg's per ufg. The energy of the source ufg J was chosen to be 6.11 MeV in order to illustrate an extreme case (high degree of anisotropy). The percentage error shown in each case is the largest

*B. J. Toppel, A. L. Rago, and D. M. O'Shea, MC^2, A Code to Calculate Multigroup Cross Sections, ANL-7318 (June 1967).

TABLE II.A.2. Errors in Elastic Scattering Transfer Cross Sections

(E_J = 6.11 MeV)

Material m	Percentage error in $\sigma_{el}^{0^m}$	Percentage error in $\sigma_{el}^{1^m}$	Total number of hfg scattered	Number of hfg/ufg	Weighted error for P_0 scattering[a]	Weighted error for P_1 scattering[b]
Be^9	2.5	3.1	54	1	0.35	0.52
	1.1	1.2	108	2	0.09	0.13
	0.7	0.7	162	3	0.04	0.06
B^{10}	15.0	15.0	49	1	0.53	0.84
	0.5	0.6	98	2	0.09	0.15
	1.6	1.6	146	3	0.06	0.09
C^{12}	16.0	16.0	41	1	0.58	0.95
	2.5	2.6	81	2	0.13	0.20
	1.2	1.3	122	3	0.06	0.09
O^{16}	18.0	19.0	31	1	2.20	3.70
	5.0	5.3	61	2	0.57	0.96
	0.9	1.0	91	3	0.20	0.34
Na^{23}	8.5	10.0	22	1	3.00	4.50
	3.4	3.8	43	2	0.76	1.10
	1.9	2.1	64	3	0.34	0.51
Fe^{56}	20.0	25.0	9	1	17.00	22.00
	5.0	6.4	18	2	4.40	5.80
	2.2	2.8	27	3	1.90	2.60
	1.2	1.6	35	4	1.10	1.40
Cu^{63}	22.0	27.0	8	1	23.00	28.00
	9.2	10.0	16	2	5.10	6.40
	4.7	5.5	23	3	2.20	2.80
	2.4	3.0	31	4	1.30	1.60
Mo^{96}	98.0	100.0	6	1	45.00	54.00
	13.0	16.0	16	3	5.80	8.20
	7.2	9.2	21	4	3.20	4.60
	3.0	3.9	31	6	1.40	2.00
Pu^{239}	200.0	280.0	3	1	68.00	82.00
	4.5	12.0	21	10	1.50	2.60
	0.8	2.3	33	16	0.28	0.50
	0.3	0.9	37	18	0.12	0.21

[a] The weighted error in the P_0 scattering from source ufg J is

$$\frac{\sum_{N=0}^{N=N^m_{max}} \left| \left(\begin{array}{c} \text{\% error in} \\ \text{ufg N for} \\ P_0 \text{ scattering} \end{array} \right) \sigma_{el_{J\to J+N}}^{0^m} \right|}{\sum_{N=0}^{N=N^m_{max}} \sigma_{el_{J\to J+N}}^{0^m}}$$

[b] The weighted error in the P_1 scattering from source ufg J is

$$\frac{\sum_{N=0}^{N=N^m_{max}} \left| \left(\begin{array}{c} \text{\% error in} \\ \text{ufg N for} \\ P_1 \text{ scattering} \end{array} \right) \sigma_{el_{J\to J+N}}^{1^m} \right|}{\sum_{N=0}^{N=N^m_{max}} \left| \sigma_{el_{J\to J+N}}^{1^m} \right|}$$

error encountered for all possible ultrafine receptor groups. For ^{10}B, the scattering probability for the next to the last receptor group, when integrated across the ultrafine source group, produced converging oscillatory values as the number of hfg's per ufg increased. This occurrence was just due to the particular shape of the scattering probability across the source group. For the light elements (e.g., beryllium, boron, carbon, oxygen, and sodium) the maximum error in the elastic transfer cross sections always occurred with the scattering into the next to the last receptor group. The next largest error resulted from the in-group scattering, N = 0. All other receptor groups for these light elements (even for 1 hfg per ufg) had errors of less than 1%.

Table II.A.2 also displays a measure of the weighted error in the P_0 and P_1 transfer cross sections in scattering from the source ufg. The error for each receptor group was weighted by the fraction of its contribution (relative to 20 hfg's per ufg) to the total scattering from the ultrafine source group. The error displayed was obtained by summing the weighted error for each ultrafine receptor group. Note that in the footnotes of Table II.A.2, the total number of hfg's scattered for material m when there is one hfg per ufg is denoted by N^m_{max}. The weighted error gives a measure of the overall accuracy of the calculation. For example, the light materials have a large error in the next to last receptor group, but the weighted error for these materials is small because the contribution of the next to last receptor group is small.

For all materials at energies where the scattering is isotropic in the center-of-mass system, the calculation of the P_0 and P_1 elastic transfer cross sections, using one hfg per ufg, resulted in errors of less than 1% for almost all ultrafine receptor groups. The weighted error in scattering from the source ufg was always less than 1.5%.

For the new MC^2-2 code, the probable requirement for the number of hfg's per ufg for the calculation of the P_0 and P_1 elastic transfer cross sections for an accurate and comparably fast computer running time are: one hfg per ufg for all materials when scattering is isotropic in the center of mass system; one hfg per ufg for materials lighter than and including sodium when scattering is anisotropic; two to four hfg's per ufg for materials heavier than sodium but lighter than mass 161 amu when scattering is anisotropic. For masses greater than 161 amu, use the heavy mass approximation (see pp. 91-95 of Progress Report for July 1970, ANL-7726) for all scattering.

In the final analysis, the number of hfg's per ufg to be used for the different materials in the calculation of the elastic transfer matrices will depend on the testing of the new MC^2-2 code. How the number of hfg's per ufg affect the values of the cross sections and buckling will determine how relaxed this number can be without compromising the accuracy of this new code.

(b) Data Management Change in BPOINTER
(B. J. Toppel and H. Henryson II)

A new data-management strategy has been incorporated into the dynamic allocation routine BPOINTER* in the ARC system with regard to the purging of arrays. The automatic purging of arrays was too costly if a user chose to use a small main-core array and a large bulk-core array. The new strategy calls for the automatic purging of an array only after an attempt has been made to allocate storage in both main and bulk core. Before the change, purging took place directly after attempting to allocate the array in main core. Consequently, the change may degrade the efficiency of modules which relied on this attribute, since arrays previously allocated to main core may now be placed in bulk. If no bulk core is used by a module, the change would be transparent to the module.

A "bug" has been found and corrected in the 1-D transport module NUC003. The error affected problems run using a white external-boundary condition.

The cataloged procedures resident on the AMD procedure library used in the management of ARC system libraries have been corrected to eliminate an error. If a number of job steps were run concurrently, the failure of one compilation step could affect the load module produced in a later step. The error was corrected by incorporating a dummy step into the procedures which invoked the initiator to delete data sets related to the job step that had failed.

2. Nuclear Data

a. Burnup Analysis and Fission Yields for Fast Reactors
(C. E. Crouthamel and R. P. Larsen) (189a 02-083)

(i) Determination of Fast Fission Yields and Nonfission Nuclear Transformations in a Fast Reactor

Last Reported: ANL-7705, pp. 139-141 (June 1970).

(a) Long-term Irradiation in EBR-II. The long-term irradiation in EBR-II of encapsulated samples of ^{232}Th, ^{233}U, ^{235}U, ^{238}U, ^{237}Np, ^{239}Pu, and ^{240}Pu (see Progress Report for April-May 1969, ANL-7577, pp. 139-141) has been completed. This irradiation, which was carried out in Subassemblies X018, X018A, and X018B (consisting primarily of structural materials), began in December 1966, and the samples were removed from the reactor in September 1970. (This removal date is nearly a year sooner than originally expected.) The subassembly occupied a position in

*A. S. Kennedy, Pointr, A Dynamic Storage Allocation Program, TM-98 (Feb 1967).

Row 2 for the first half of the irradiation and a position in Row 4 for the second half. Two sets of samples were irradiated: one in the core at about the vertical centerline, and the other in the axial blanket. These samples will be chemically analyzed to establish (1) the fast-fission yields of burnup monitors for fast reactors as well as yields of other fission-product nuclides that are of interest to the fast-reactor program, e.g., the krypton and xenon isotopes, and (2) the isotopic abundances of nuclides formed by nonfission nuclear transformations. The estimated burnups of the fissile nuclides are 20-25% for the samples irradiated in the core and 10-15% for the samples irradiated in the axial blanket. Burnup values of these magnitudes will enable the number of fissions (from pre- and postirradiation actinide element analyses) to be determined with an accuracy of ±0.5%. It is expected that the analysis of these samples will be initiated about September 1971.

(b) Determination of Fast-Fission Yields. A new method for determining the number of fissions that occur in a fast-reactor fuel was described previously in ANL-7705. A low-power (10-kW) irradiation of mica fission track detectors (mica disks in contact with nanogram amounts of the fissile nuclide) and of gram amounts of the fissile nuclide is conducted to establish a factor relating the activity of a particular fission product (e.g., ^{95}Zr) to the number of fissions. The number of fissions occurring in a longer irradiation at full reactor power can then be determined from this factor and a measurement of the ^{95}Zr activity. This determination, along with analyses for long-lived or stable fission products, would provide the necessary data for calculating the yields of these fission products.

Low-power irradiations conducted in the EBR-II mock-up experiments in Assemblies 60 and 61 of ZPR-3 have been previously described (see ANL-7705). A major objective of these irradiations was to provide ^{95}Zr-to-fissions factors for 2- to 3-month irradiations of ^{235}U, ^{238}U, and ^{239}Pu to be carried out in EBR-II. The completion of the long-term irradiations in EBR-II (discussed above) nearly a year sooner than anticipated has obviated the need for the shorter irradiation in EBR-II. The fission yields obtained by the analysis of the long-term irradiations will be more accurate, and the acquisition of the data will not be appreciably delayed.

The irradiations in Assemblies 60 and 61 of ZPR-3 also offered the opportunity (1) to make direct measurements of the fission yields of short-lived fission products and (2) to determine the effect of neutron energy on fission yields in the neutron spectra of EBR-II. The direct measurement of these fission yields is of particular importance to (n, f) dosimetry measurements. Present practice is to measure the activity of a particular short-lived fission product, e.g., ^{140}Ba (13 d), and to calculate the number of fissions using the literature value for the yield of the

stable end-of-chain fission product, ^{140}Ce (stable). (The assumption that the two yields are the same is based on mass-charge distribution theory.) There are indications from the data obtained to date that these yields are not the same in several important cases, and it is therefore necessary to measure directly the yields of the fission products being used in the dosimetry programs.

Gamma-spectrometric measurements of the ^{235}U, ^{238}U, and ^{239}Pu foils irradiated in Assemblies 60 and 61 of ZPR-3 have now been completed, the foils have been weighed, and the activities per gram of fissile nuclide are being calculated. For Assembly 60, the activities of ^{95}Zr (65 d), ^{103}Ru (42 d), ^{131}I (8 d), ^{132}Te (77 h), and ^{140}Ba (13 d) were determined. For Assembly 61, the same activities, as well as the activities of ^{97}Zr (17 h), ^{105}Rh (36 h), ^{133}I (21 h), ^{135}I (6.7 h), and ^{143}Ce (33 h), were measured. These shorter-lived activities could not be measured for the Assembly 60 samples because of a malfunction of the multichannel analyzer system.

Absolute fission yields cannot be calculated until analysis of the fission-track detectors is completed; however, the calculation of relative fission yields for the ^{235}U samples from Assembly 60 has led to the tentative conclusion that the fission yields do not vary significantly with neutron energy in EBR-II. (The core, interface, and blanket positions of the Assembly 60 irradiations correspond approximately to Rows 2, 7, and 12 of the present loading of EBR-II.) These relative fission yields were calculated by dividing the number of atoms of a particular nuclide (at zero time out of the reactor as calculated by the computer program) by the value obtained for ^{140}Ba. Barium-140 was chosen as the reference nuclide for two reasons: (1) Previous measurements of the fission yield of its stable daughter, ^{140}Ce, had indicated that the difference between yields in a thermal spectrum and a fast spectrum (EBR-I) is minimal (less than 2%, relative), and (2) the precision of the ^{140}Ba data is superior to that obtained for any other nuclide. The calculation of the relative fission yields are summarized in Table II.A.3.

TABLE II.A.3. ^{235}U Fission Yields of ^{95}Zr, ^{103}Ru, ^{131}I, and ^{132}Te Relative to ^{140}Ba as a Function of Location in Assembly 60, ZPR-3

Location	^{95}Zr	^{103}Ru	^{131}I	^{132}Te
Core	1.117	0.553	0.561	0.760
Interface	1.101	0.551	0.548	0.765
Blanket	1.120	0.548	0.550	0.746
Error (1σ)	±0.010	±0.005	±0.006	±0.015

Within the limits of error given in Table II.A.3, the relative fission yields show no change in going from the neutron spectrum of the core to that of the blanket. Of particular importance is the close agreement of the ^{103}Ru and ^{131}I values. These nuclides are on descending and ascending portions of the mass-versus-yield curve, the yields of such nuclides are much more dependent on neutron energy than the nuclides on the peaks of the curve, e.g., ^{95}Zr.

The relative fast fission yield values reported in Table II.A.3 are now being compared with thermal yield values. Foils of ^{235}U and ^{239}Pu have been irradiated in a thermal flux, and these foils are now being assayed gamma-spectrometrically for the same fission-product nuclides.

b. Reactor Code Center (M. Butler) (189a 02-085)

Last Reported: ANL-7742, p. 98 (Sept 1970).

Eleven program packages were added to the library this month. Nine of these are prepared for the CDC 6600 machine, one is an IBM 360 program, and one a UNIVAC 1108 version.

In accession number order, the new program packages are:

ACC No. 358, TWOTRAN, a general geometry version of the two-dimensional multigroup discrete-ordinates program supplied by LASL. This CDC 6600 version uses the extended core storage to solve problems in x,y and cylindrical r,θ and r,z geometries.

ACC No. 368, FLANGE2, a UNIVAC 1108 version of the program that uses the ENDF/B scattering-law data to compute thermal cross sections and scattering matrices. Gulf General Atomic submitted this package.

ACC No. 427, FARED/RETAP, a one-dimensional fast-reactor design and analysis package prepared for the CDC 6600 by the Babcock and Wilcox Company.

ACC No. 428, DOGGY, designed to perform the more frequent desk-calculator functions with tabular or graphical output. Fifty arithmetic, trigonometric, and special functions are incorporated in this Knolls Atomic Power Laboratory program prepared for the CDC 6600.

ACC No. 429, ASPIS, computes gamma-ray buildup factors for multilaminar slab geometry from plane, monodirectional, and slant sources. This shielding program, written for the CDC 6600, was contributed by the Bettis Atomic Power Laboratory.

ACC No. 434, HEATMESH, a Sandia Corporation, Livermore, program used to generate the geometrical data required for heat-transfer studies in complex structures represented as surfaces of revolution. This code was written for the CDC 6600.

ACC No. 435, BURST1, a LOFT program package which calculates the spatial distributions of pressure, mass velocity, and enthalpy within a PWR primary-coolant system during subcooled blowdown. This IBM 360 version was developed by Phillips Petroleum Company.

The last four were all written at the Knolls Atomic Power Laboratory for the CDC 6600 computer. ACC No. 422, SIMPLE1, is an algebraic programming language developed for interactive time sharing; ACC No. 444, ROPE, calculates roots of polynomials; ACC No. 445, LIZARD4, solves nonlinear ordinary differential equations; and ACC No. 446, MOST, is a function minimization algorithm.

B. Reactor Fuels and Materials Development

1. Fuels and Claddings

a. Behavior of Reactor Materials (189a 02-086)

(i) Thermal Gradient Migration of Pores in UO_2 (R. O. Meyer and J. C. Voglewede)

Last Reported, ANL-7679 pp. 115-117 (Mar 1970).

The migration of the residual pores left after sintering was observed in two polycrystalline specimens after annealing. Specimen 120 was 95% of theoretical density and had a grain size of about 5 μ. It was annealed for about 20 min in a gradient of 1005°C/cm with a maximum specimen temperature of about 2100°C. However, several unrecorded temperature excursions occurred so that the effective time of the anneal may have been longer than 20 min. Gross restructuring occurred near the hot end of this specimen. Microstructures before the anneal and near the hot end of the specimen after the anneal are shown in Fig. II.B.1. The appearance of columnar-grain growth and the formation of large lenticular voids are apparent. This directionally restructured region is limited to the top 1 mm of the specimen, which was above 2000°C.

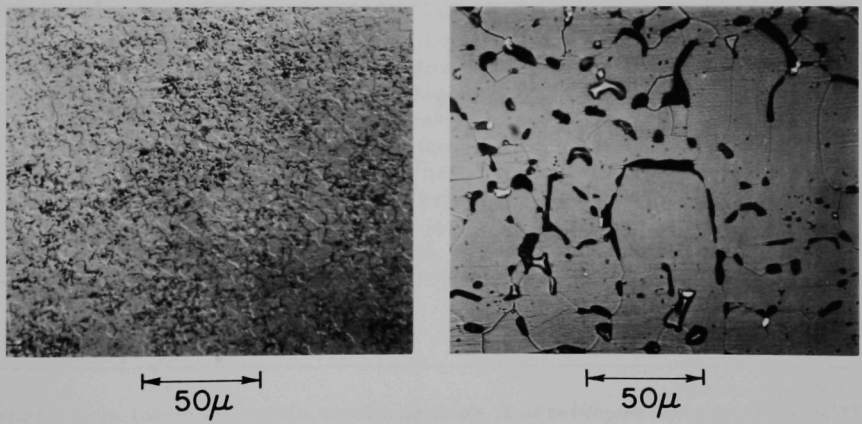

Before Annealing

After Annealing (High Temperature Is at Top in Photo)

Fig. II.B.1. Pore Migration and Restructuring in a UO_2 Sample Annealed in a Temperature Gradient. Neg. No. 53386.

Specimen 191 was 97.7% of theoretical density, had a grain size of about 30 μ, and was annealed for 1 hr in a gradient of 1041°C/cm with a maximum specimen temperature of 1935°C. Directional restructuring

occurred within the 100-μ region adjacent to the hot end of the specimen. In this zone elongated grains formed, and the pore content decreased considerably below the level remaining in the cooler regions.

The velocity of sinter pore migration can be predicted by assuming either a surface-diffusion or a vapor-transport mechanism. For surface diffusion,†

$$V_s = \frac{2\delta D_s^* Q_s^*}{rRT^2} \frac{dT}{dx}, \tag{1}$$

where T is the temperature, r is the radius of the pore, and R is the gas constant. For vapor transport,†

$$V_v = \frac{2p_v \Omega \Delta H_v}{3PS_{12}RT^2} \sqrt{\frac{2RT}{\pi}\left(\frac{1}{M_1} + \frac{1}{M_2}\right)} \frac{dT}{dx}, \tag{2}$$

where the expression for diffusion in a two-gas mixture was obtained from Jeans.†† The remaining symbols in Eqs. 1 and 2 are defined and assigned quantitative values in Table II.B.1. It is usually assumed that the total

TABLE II.B.1. Definition of Quantities Used in Calculations

Symbol	Definition	Value
δ	Depth of diffusing layer	3 Å[(a)]
D_s^*	Surface-diffusion coefficient	$5.7 \times 10^5 \exp(-108{,}000/RT)$ cm^2/sec[(b)]
Q_s^*	Surface heat of transport	100 kcal/mole-deg[(c)]
P_v	Equilibrium vapor pressure	$\exp(39.4/R) \exp(-143{,}100/RT)$ atm[(d)]
Ω	Molecular volume	4.09×10^{-23} cm^3[(e)]
ΔH_v	Heat of vaporization	143,100 cal/mole-deg[(d)]
S_{12}	Collision cross-section area	38.5×10^{-16} cm^2[(f)]
M_1	Molecular mass of gas in bubble	
M_2	Molecular mass of UO_2	270 g/mole
γ	Surface energy	600 erg/cm^2[(b)]

(a) Value assumed.
(b) P. S. Maiya, to be submitted to J. Nucl. Mater.
(c) Value assumed (see Progress Report for March 1970, ANL-7679, p. 115).
(d) M. Tetenbaum and P. D. Hunt, J. Nucl. Mater. 34, 86 (1970).
(e) Calculated from lattice parameter of 5.470 Å.
(f) Calculated from assumed impact parameter of 3.5 Å.

†F. A. Nichols, J. Nucl. Mater. 30, 143 (1969).
††James H. Jeans, An Introduction to the Kinetic Theory of Gases, MacMillan Co., New York (1940).

pressure P in a sealed pore is in equilibrium with the surface tension of the pore and is therefore equal to $2\gamma/r$ (γ is also listed in Table II.B.1). If a 10-μ-dia pore filled with hydrogen (the specimens were originally sintered in hydrogen) is assumed to be sealed, and if the pore is at 2000°C in a temperature gradient of 1000°C/cm, then Eqs. 1 and 2 predict a migration rate of 0.1 μ/hr for a surface-diffusion mechanism and 2.6 μ/hr for vapor transport. Since P is inversely proportional to r, and V_v is inversely proportional to P, vapor transport is likely to be the dominant migration mechanism for large pores; moreover, once this mechanism becomes dominant, a continued increase of velocity is possible as bubbles coalesce and grow. Nichols* has applied Eq. 2 to restructuring, and the equation has been incorporated in LIFE-1** for this purpose. The applicability of Eq. 2 to restructuring can be checked experimentally in the gradient furnace, which can also be used to verify the temperatures assumed to exist at the interface between the zones of columnar and equiaxed grains in a fuel element. To accomplish these goals, the specimens should be annealed in a temperature gradient for longer periods of time.

In addition to the textural changes shown in Fig. II.B.1, a zone of columnar grains formed on the cold side of the 0.3-mm-dia drill holes used as black-body cavities for temperature measurement. Such a restructuring suggests that these large cavities migrated in the temperature gradient, and it is possible to estimate a rate for the process. A theoretical value for the rate can also be calculated from Eq. 2 since vapor transport is certainly dominant in this case, and the equation applies equally well to spherical and cylindrical cavities. However, the cavity was open to the furnace atmosphere (assumed to be nitrogen), which had a pressure of about 10^{-5} Torr. This fixes P within the cavity at the same value, and, on this basis, the migration rate calculated from Eq. 2 for the hottest black-body cavity in specimen 191 is 45×10^5 μ/hr. This is 10^5 larger than the observed migration rate! Equation 2 obviously fails, and the faulty assumption is that diffusion in the gas (at a very low pressure) is the rate-limiting process. The sublimation rate is, in fact, the rate-limiting process. The sublimation rate is given by†

$$J_s = \frac{\alpha p_v}{\sqrt{2\pi mkT}}, \tag{3}$$

where α is the evaporation coefficient, m is the UO_2 molecular mass, and p_v is the same equilibrium vapor pressure used in Eq. 2. The migration velocity, as determined by the sublimation rate alone, is

$$V = J_s \Omega. \tag{4}$$

*F. A. Nichols, WAPD-TM-570 (Oct 1966).

**V. Z. Jankus and R. W. Weeks, ANL-7736, LIFE-I, a FORTRAN-IV Computer Code for the Prediction of Fast-reactor Fuel-element Behavior (to be published).

†J. P. Hirth and G. M. Pound, Progress in Mater. Sci. 11, 1 (1963).

Taking α = 1* in Eq. 3 gives a migration velocity of the same order of magnitude as the value derived from the width of the restructured zone adjacent to the cavity (see Table II.B.2). Sublimation as a rate-limiting step occurred because the total gas pressure P in the cavity was small. Sublimation will not be a rate-limiting process for small gas bubbles in a fuel element.

TABLE II.B.2. Migration of 0.3-mm-dia Cylindrical Cavities

Identification	Measured Migration	Calculated Migration (sublimation rate limited), μ/hr
Specimen 191 (1772°C cavity)	40 μ/1 hr	17.6
Specimen 120 (1834°C cavity)	60 μ/20+ min	30.5
Specimen 120 (1726°C cavity)	5 μ/20+ min	4.9

b. Chemistry of Irradiated Fuel Materials (C. E. Crouthamel and C. E. Johnson) (189a 02-087)

(i) Post-Irradiation Studies of Reactor Fuels and Cladding

Last Reported: ANL-7726, pp. 104-105 (July 1970).

Work is continuing on the electron-microprobe examination of a UO_2-20 wt % PuO_2 pellet fuel, F2R, obtained from the General Electric Laboratory at Vallecitos. This fuel had been irradiated to 6.5 at. % burnup at 16 kW/ft. Analyses have been made of metal inclusions located along radii extending from the void edge to the cool end of the columnar-grain region. Three different radial sections, approximately 120° apart, have been analyzed. The metal inclusions were of irregular shape and varied from 3 to 8 μm in size. The inclusions contained the noble-metal fission products molybdenum, technetium, ruthenium, rhodium, and palladium and small quantities of iron. The data are given in Tables II.B.3-II.B.5 where the elemental concentrations in weight percent are tabulated as a function of radial position.

*R. J. Ackermann, private communication.

TABLE II.B.3. Metal Inclusions in Mixed-oxide Fuel F2R, Section 1

Radial Distance, mm	Concentration, wt %					
	Mo	Tc	Ru	Rh	Pd	Fe
0.30	Void edge					
0.38	55.4	12.7	21.5	5.0	5.0	0.5
0.84	51.3	8.6	23.0	7.3	9.2	0.6
1.16	47.9	12.6	29.4	9.9	0.1	0.2
1.45	48.0	14.2	29.0	8.2	0.4	0.2
1.69	43.2	15.9	31.5	9.1	0.1	0.1
1.91	30.5	19.5	39.0	11.0	0.1	0.1
2.21	45.5	14.8	31.3	8.1	0.1	0.1
3.17	Cladding edge					

TABLE II.B.4. Metal Inclusions in Mixed-oxide Fuel F2R, Section 2

Radial Distance, mm	Concentration, wt %					
	Mo	Tc	Ru	Rh	Pd	Fe
0.24	Void edge					
0.62	58.6	9.2	21.7	5.6	4.3	0.5
0.94	56.8	10.3	19.0	5.4	7.7	0.7
0.95	54.3	11.2	21.6	6.0	6.5	0.5
1.20	49.2	13.0	28.2	8.2	1.1	0.3
1.42	50.4	13.8	26.9	8.2	0.6	0.2
1.65	38.0	18.3	34.2	9.3	0.1	0.1
2.01	30.1	19.8	39.0	11.0	0.1	0.1
3.12	Cladding edge					

TABLE II.B.5. Metal Inclusions in Mixed-oxide Fuel F2R, Section 3

Radial Distance, mm	Concentration, wt %					
	Mo	Tc	Ru	Rh	Pd	Fe
0.31	Void edge					
0.46	62.4	9.0	19.8	5.4	2.8	0.5
0.62	55.6	12.5	22.4	5.0	4.0	0.5
0.85	54.6	13.8	22.8	5.1	3.3	0.5
1.12	54.3	12.3	22.8	6.2	4.0	0.4
1.38	48.1	13.2	29.0	8.5	0.9	0.3
1.69	43.9	15.9	30.9	8.9	0.1	0.2
2.19	34.4	18.6	36.9	10.0	0.1	0.1
3.18	Cladding edge					

The data show that the concentrations of molybdenum, palladium, and iron decrease from the central void to the cladding, whereas the concentrations of ruthenium, technetium, and rhodium increase. A comparison of the experimental data with fission-yield data shows that the palladium concentrations are much lower in relation to the other noble-metal fission products than calculations predict. The ratios for Mo: Tc: Ru: Rh, calculated from fission yields, are 6.2: 1.5: 3.8: 1.0. The experimental results are in good agreement with the calculated ratios for Tc: Ru: Rh throughout the whole region; however, the concentration of molybdenum is higher at the void edge and lower at the cooler end of the columnar-grain region.

The distribution of palladium and iron throughout the columnar-grain region is expected to be governed by transport of elemental vapor species, since both palladium and iron have significant vapor pressures in the higher-temperature regions. The metallic inclusions nearest the void edge were observed to have the largest palladium and iron contents. This finding is somewhat unexpected; from a knowledge of the vapor pressures of palladium and iron, one might have expected these elements to condense in a cooler region. However, a similar increase in concentration near the void edge was observed for ^{85}Kr in F2R. (See Progress Report for April-May, 1970, ANL-7688, pp. 173-176.) Pore sweeping toward the hotter end of the thermal gradient occurs in this region of the fuel, and the thermal gradient diminishes at the void edge. Thus, this region is a potential location for the pileup of gas-filled pores sweeping toward the void edge. With cracks in the fuel providing a communication link to the central void, palladium, molybdenum, and iron vapor species found in the central void cavity may, upon slow cooling of the fuel, diffuse back into the fuel and condense as alloy inclusions near the void edge. The relatively small amounts of palladium and iron in the metal inclusions indicate that the transport of vapor back into the fuel has not been extensive.

Studies of vibra-packed fuels (see Progress Report for April-May, 1970, ANL-7688, p. 178) indicated that larger quantities of material were transported to the equiaxed-grain region through the porous unrestructured zone. However, in F2R, vapor transport was, we believe, largely blocked by the higher density (~95% TD) of the unrestructured region. Therefore, a shift in the distribution of all material transported by vapor-phase species toward the central void has resulted.

c. Thermodynamics of Carbide Fuel (A. D. Tevebaugh and P. E. Blackburn) (189a 02-088)

(i) Total Vapor Pressures and Carbon Potentials in the Ternary U-C-Pu System

Last Reported: ANL-7726, pp. 105-107 (July 1970).

The carbon potentials and total pressures of the U-Pu-C system are being investigated. Total pressure of actinide metal species as well as carbon activity are being measured by a transpiration technique. Activity measurements over a wide range of temperature and with well-defined composition are needed to establish reliable thermodynamic quantities and to define phase-boundary composition. In particular, carbon-activity data are important in predicting possible carbon embrittlement of cladding by carbide fuel, the chemical state of fission products, and effects of additives on the properties of fast-reactor fuels.

The study of the vaporization behavior of the uranium-carbon system is continuing. Current emphasis has been placed on the effects of oxygen contamination in uranium carbide on the system's uranium, carbon, and oxygen potentials. These studies are important in establishing allowable levels of oxygen impurity in carbide fuels. Little is known about the stability and phase relations of the uranium-carbon-oxygen system. The oxycarbide phase was generally investigated in the presence of other phases such as U, UO_2, U_2C_3, and UC_2.

Oxygen partial pressure, carbon activity, and total pressure of uranium-bearing species were measured at 2355°K with a carrier gas having a CO partial pressure of ~4 Torr (balance helium) and a CO/CO_2 ratio of $\sim 5 \times 10^4$. The composition of the uranium carbide charge (see ANL-7726, p. 106) was C/U = 0.96. The tentative results (Runs 101-1 and 101-2) are summarized in Table II.B.6. The lower oxygen content (~1 at. %) of the

TABLE II.B.6. Tentative Values of Carbon Activity, Oxygen Partial Pressure, and Total Pressure of Uranium-bearing Species for U-C-O System

	Run 100-1	Run 101-1	Run 101-2
Temperature, °K	2355	2355	2355
Time of run, hr	5.5	2.9	6.7
Flow rate, liters/min	1.10	1.08	1.08
Carrier gas	CO-He	$CO-CO_2$-He	$CO-CO_2$-He
Partial pressure CO in carrier gas, Torr	~10	4	4
CO/CO_2, input	3.2×10^4	5.4×10^4	5.7×10^4
CO/CO_2, output	2.2×10^4	4.6×10^4	4.7×10^4
-log $p(O_2)$ (based on input), atm	12.52	12.98	12.94
-log $p(O_2)$ (based on output), atm	12.20	12.70	12.78
Carbon activity (based on input)	2.0×10^{-3}	1.3×10^{-3}	1.4×10^{-3}
Carbon activity (based on output)	1.4×10^{-3}	1.0×10^{-3}	1.1×10^{-3}
-log p(U) total pressure of uranium-bearing species, atm	5.61	-	5.83
Composition	$UC_{1.00}O_{0.04}$	$UC_{1.00}O_{0.02}$	$UC_{1.00}O_{0.02}$
Metallographic examination	UO_2 not detected	UO_2 not detected	UO_2 not detected

oxycarbide residue, when compared with previous results (~2 at. %; Run 100-1 given in the table for comparison and previously reported in ANL-7726, p. 106), appears to be consistent with the lower oxygen partial pressure (higher CO/CO_2 ratio) of the carrier gas used in the present runs. The slightly lower values for the calculated carbon activity reflect the lower CO partial pressures used in the present runs. Consistent with previous results, the effect of a small addition of oxygen is a significant reduction in the activity of carbon.

A rough estimate of the free energy of formation of the oxycarbide composition $UC_{1.00}O_{0.02}$ at 2355°K was made from values for oxygen partial pressure, carbon activity, and total pressure of uranium-bearing species derived from our measurements. In the absence of species information, the uranium activity was roughly estimated based on the total pressure of uranium-bearing species, the assumption that the vapor is uranium gas, and the sublimation pressure of pure uranium. From the expression $\Delta G_f^\circ = R'T \log(N_i \Sigma a_i)$, a tentative value of $\Delta G_f^\circ \simeq 41.6$ kcal/mol was obtained.

d. Oxide Fuel Studies (189a 02-005)

(i) Fuel-element Performance* (L. A. Neimark and W. F. Murphy)

Last Reported: ANL-7742, p. 103 (Sept 1970).

Fuel elements C-11 and C-15 from the NUMEC Group C irradiation have been removed from their capsules, photographed, gamma-scanned, and dimensionally profiled. The elements contain UO_2-10 wt % PuO_2 pellets with an oxygen-to-metal (O/M) ratio of 1.99-2.00. The fuel smear density of Element C-11 is 88-89% of theoretical, and that of C-15 is 82-83% of theoretical. The cladding is Type 316L stainless steel with a 0.015-in. wall thickness. A 0.036-in.-dia spacer wire with a nominal 2-in. pitch was wrapped around the elements. The elements received a peak burnup of ~9.6 at. %.

The profilometry of the elements was performed after removal of the spiral wire wrap. Axial diametral profiles were made at angular orientations of 0.180°, 45-225°, and 90-270°. The plenum region of both fuel elements had essentially the same diameter (0.2530 ± 0.0003 in.) for all traces. The maximum measured diameters of fuel elements C-11 and C-15 were 0.2626 and 0.2628 in., respectively. These diameters occurred at the midlength of the fuel column, where the midwall cladding temperature was ~520°C and the fluence (above 0.1 MeV) was 7.3×10^{22} nvt. Based on the nominal diameter of the plenum region, these diameters correspond to diametral changes of ~3.9% in both elements.

*See also Sect. III.A.4, Nuclear Safety, Hot Laboratory Examinations.

All traces in the fuel-column region of both elements showed a small sine wave superimposed on the axial diametral profile. The period of the sine wave was 1 in., which corresponds to the half-pitch of the spacer wire, and the amplitude was as high as 3-4 mils. The circumferential diametral profile of Element C-15 was determined near the midplane of the fuel column by rotating the element in the profilometer. This procedure also generated a sine curve with an amplitude of 3.5 mils. These results indicate that the element has assumed an essentially oval shape under the spacer wire in the region of the fuel. The maximum ratio of the major-to-minor axis dimensions is 1.01, with the minor axis of the "oval" always under the spacer wire. The spacer wire had no effect on the diameter traces of the irradiation capsules. Both elements were easily removed from their capsules. The C-11 and C-15 fuel-element capsules had peak diametral increases of 6.5 and 5.6 mils, respectively. The capsule traces did show, however, shallow indentations at approximately 3-in. intervals. This interval corresponds to the dimples in the shroud tubes of the irradiation subassembly.

If the elements are assumed to have a circular profile with a diameter equal to the mean of the major and minor axes of the oval, only about 65% of the diametral increase can now be accounted for by cladding swelling.

(ii) Fabrication of Uranium Dioxide Helices for In-reactor Creep Studies (J. T. Dusek)

Last Reported: ANL-7742, pp. 105-106 (Sept 1970).

The special techniques involved in slip-casting UO_2 helices suitable for in-reactor creep testing were described in ANL-7742. Fabrication of these springs by extrusion has some advantage over slip casting by producing a "wire" that has a circular rather than a trapezoidal cross section and a lower porosity. A satisfactory extrusion procedure is summarized below.

A deflocculated UO_2 powder of submicron size range was prepared with 84.75% UO_2, 0.85% Superloid ammonium alginate, 0.85% Methocel 4000, 13.56% water, Mobilcer C (30 drops/100 g UO_2), and Darvan No. 7 (10 drops/100 g UO_2). The first three materials were dry-mixed; then the water, Mobilcer C, and Darvan were added in combination. Next, the mixture was plasticized on a water-cooled rolling mill and loaded into the extrusion die. The die was evacuated to a pressure of ~5 Torr, and a 5-12-ton load was applied. The plastic UO_2 mass was extruded through a nozzle, which is curved to match the diameter of the helix. The extruded product, a firm plastic "wire" ~2.5 mm in diameter, was formed on a sleeved mandrel, which was then covered and allowed to age overnight to allow the "wire" to set in the shape of a helix. The moist helix was transferred to a paper

sleeve for air drying. The air-dried helices were fired in flowing hydrogen with a slow, steady rise in temperature up to 1200°C over a period of 18 hr, then up to 1800°C for an additional 4 hr, and, finally, a soak at 1800°C for 2 hr. The furnace was then allowed to cool to room temperature before the helices were removed.

To permit a helix to be gripped by the creep-test fixture, the end turns must be slightly separated from the central turns. The separation is introduced by inserting a tungsten lock washer between the first and second turns at each end of a fired helix, and refiring at 1400°C.

These procedures have been instrumental in producing helices with up to 27 turns, outside diameters of 22.2-23.8 mm, and densities 94.0-96.5% of theoretical. The "wire" cross section is circular, which facilitates stress calculations, and has a fired diameter of ~1.8 mm.

2. Techniques of Fabrication and Testing

a. Nondestructive Testing Research and Development (189a 02-092)

(i) Neutron Radiography (J. P. Barton)

Last Reported: ANL-7742, pp. 109-111 (Sept 1970).

A transportable neutron-radiography facility has been constructed and is now available for use. The neutron source is ^{252}Cf with an intensity of ~2 x 10^8 n/sec 4π, but other isotopes and stronger intensities can be easily substituted if required.

Water has been selected for the bulk neutron moderator and shield because water is comparable with the best-known moderators for californium-based neutron radiography. The water (380 gal) may be emptied before moving the facility and replenished at the new site, thus considerably facilitating the shipment procedure. The use of water bulk moderator also allows versatility in operation; for example, small volumes of high-efficiency moderators or boosters can easily be placed around the source, and multiple collimated neutron beams can be extracted according to the requirements of the particular application.

The design of the facility has been kept as simple as possible. It is essentially a steel tank with a 1.24-m diameter, a 1.4-m height, and a 10-cm-dia lead source storage in the base center. The source may be raised from the storage position to any required exposure position along the central axis by a motorized drive, the source being held at the end of a horizontal plastic arm. Source movements are actuated from a control panel that may be several meters from the source container, thus allowing the facility to be used for high-intensity sources and for occasional fast-neutron radiography trials (for which the water level can be lowered about halfway).

With a ^{252}Cf source of 2 x 10^8 n/sec 4π in the central exposure positions, the radiation dose rate immediately at the surfaces of the facility is below 5 mrem/hr.

Provision is made for the use of either horizontal or vertical beam extraction, and the collimation ratio can be conveniently selected by interchangeable collimator sleeve inserts. The collimators are divergent in form. They are constructed with dense paraffin-wax packing for the innermost 12 cm and with paraffin-wax boron powder mixture (6:1 by volume) for the outer sleeve length. The size of the exposure field at the collimater exit is 15 cm in diameter. The total thickness of the water shield between the source and the exposure position can be varied between 38 and 75 cm by using a series of vertical collimators with different source positions.

Neutron radiographs of unit density with a collimation ratio of 1:15 and a LiF-ZnS scintillator-Royal Blue film direct-exposure technique require about 25-min exposure time. The facility will eliminate the use of a hot cell for further experimentation in small source, thermal-neutron and fast-neutron radiography techniques. In addition, a neutron beam will be readily available for studies of detection systems.

(ii) Laser Studies and Holography (N. Fernelius)

Last Reported: ANL-7726, pp. 118-119 (July 1970).

(a) Pulsed Laser Holography. A pulsed laser has short exposure times, which allows holograms to be made* without resorting to vibration-suppressing precautions. The greatest limitation to pulsed lasers is their short coherence length, which requires careful equalization of the optical path lengths of the reference and object beams. Many of the schemes** used to increase the coherence length tend to lower the output power of the laser, e.g., a pinhole in the resonant cavity to obtain single-mode operation† or a Fabry-Perot etalon filter on the output. To compensate for these power losses, a Q-switch type of operation can be used to increase output power and to obtain shorter pulse-length output, which lessens vibration suppression.

*R. E. Brooks, L. O. Heflinger, R. F. Wuerker, and R. A. Briones, Holographic Photography of High-Speed Phenomena with Conventional and Q Switched Ruby Lasers, Appl. Physics Letters 7, 92 (1965).

**R. E. Brooks, L. O. Heflinger, and R. F. Wuerker, Pulsed Laser Holograms, IEEE J. of Quantum Electronics QE-2, 275 (1966).

†F. J. McClung and D. Weiner, Longitudinal Mode Control in Giant Pulse Lasers, IEEE J. of Quantum Electronics QE-1, 94 (1965); A. D. Jacobson and F. J. McClung, Holograms Produced with Pulsed Laser Illumination, Appl. Optics 4, 1509 (1965); J. E. Bjorkholm and R. H. Stolen, A Simple Single-Mode Giant-Pulse Ruby Laser, J. Appl. Phys. 39, 4043 (1968); and W. Wetzels and A. Alfs, Double Giant Pulse Ruby Laser with Extended Coherence Length for Holography, Rev. Sci. Instr. 40, 1642 (1969).

Agfa-Gevaert Scientia emulsions 14C75, 10E75, and 8E75 are recommended for holograms, since the Kodak 649F emulsion, which is commonly used for He-Ne laser holograms, suffers a serious reciprocity failure at high intensities.*

Attempts have been made to adapt our Raytheon Model LH34 pulsed ruby laser to make holograms. A movable aperture, which allows single-mode operation, and a Q-switch were inserted. Q-switches are devices to hinder or delay the triggering of a laser pulse until a greater population inversion can be obtained in the active levels and thus a greater ultimate output. A bleachable chemical dye Q-switch was chosen because it was the least expensive.

An Eastman Liquid Q-switch Cell Model 609F was used for experimental tests on a variety of concentrations of Eastman Q-switch Solution 10220 and kryptocyanine dye (Konrad 82017) in methanol and acetonitrile solvents. The proper solution-to-solvent ratios to obtain Q-switching at a given excitor voltage level were difficult to ascertain since the solution deteriorates. Modifying the cell to hold larger liquid volumes and waiting for longer periods between flashes did not result in reproducible power outputs. In the future, the cell will be used mainly as a light power filter (i.e., opaque to light below a given power level) for the output of a laser, Q-switched by other means. To make pulsed holograms, some other Q-switching method is necessary, such as a slotted-wheel light chopper, a rotating prism, or a Pockels cell.

3. Engineering Properties of Reactor Materials

a. High-temperature Properties of Ceramic Fuels (189a 02-094)

(i) Plastic Yielding and Fracture of Mixed Oxides (J. T. A. Roberts and B. J. Wrona)

Last Reported: ANL-7742, pp. 112-114 (Sept 1970).

At a preliminary stage in a program designed to produce high-density test bars of UO_2-20 wt % PuO_2, several groups of bars were prepared with densities 87-96% of theoretical. Table II.B.7 shows how the density was affected by some of the main fabrication variables. These bars were used to determine the influence of porosity on the brittle-to-ductile transition T_c at a constant strain rate of 0.08 hr^{-1}. The sensitivity of T_c to changes in environment, composition, and microstructure is an important factor in fuel-element failure because cracking increases the effective fuel volume and therefore increases the swelling rate.

*M. Hercher and B. Ruff, High-Intensity Reciprocity Failure in Kodak 649-F Plates at 6943 Å, J. Opt. Soc. Am. 57, 103 (1967).

TABLE II.B.7. Fabrication Variables for UO_2-20 wt % PuO_2 Specimens

% TD by Immersion Method	Binder	Binder Addition Method	Pressing Pressure, psi	Sintering[a] Time, hr	Sintering[a] Temperature, °C
96.6 ± 0.36	Carbowax 4000	1% binder solution ball-milled with the powders	20,000	2-1/4[b]	1625
96.0 ± 0.1[c]	Carbowax 4000	1% binder	20,000	3	1700
95.7 ± 0.15	Carbowax 4000	0.5% binder solution mixed with ball-milled slurry before drying	20,000	4	1575
92.7 ± 0.9	Carbowax 4000	0.5% binder solution mixed with ball-milled slurry before drying	12,500	4	1575
91.2 ± 0.6	0.5% Acriloid 0.5% stearic acid	1% binder ball-milled with the powders	20,000	4	1625
89.5 ± 0.75	Carbowax 4000	0.5% binder solution added to the ball-milled slurry before drying	12,500	4	1575
87.9	Carbowax 4000	0.5% binder solution added to the ball-milled slurry before drying	12,500	4	1575

[a]He 6% H_2 atmosphere.
[b]Furnace shutdown resulted in unusual sintering time.
[c]New batch not yet tested.

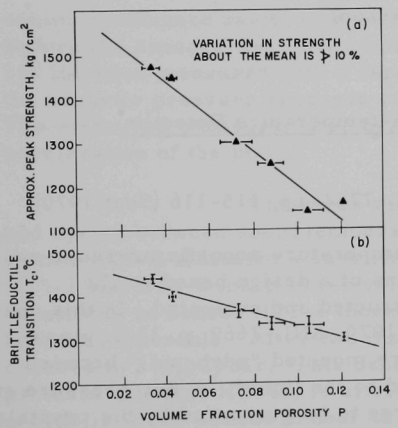

Fig. II.B.2. Dependence of Porosity on (a) Peak Strength and (b) Brittle-to-Ductile Transition in UO_2-20 wt % PuO_2

The brittle-to-ductile transition was defined as the temperature at which the load-deflection curve first deviates from linearity. To date, tests on UO_2-20 wt % PuO_2 bars have shown that T_c coincides with the temperature at which maximum strength is reached. (See Progress Report for August 1970, ANL-7737, pp. 129-130.) The dependence of both peak strength and T_c on volume fraction porosity (P = 1 - D/100, where P is the porosity, and D is the immersion density) is shown in Fig. II.B.2. The total reduction in T_c over the porosity range P = 0.044 to P = 0.12 is only ~150°C and can be described by the relation T_c = 1472 - 1408P°C. T_c is therefore, not sensitive to porosity and is equal to approximately half the melting temperature. The maximum strength, which occurs at T_c, is reduced by ~20% over the same range of porosity and is presumably related to a corresponding reduction in the area of the load-bearing surface.*

Certain characteristics of the mixed-oxide specimens prepared from mechanically blended powders are reproducible. The oxygen

*F. P. Knudsen, J. Am. Ceram. Soc. 42(8), 376-387 (1959).

content obtained from CO/CO_2 equilibration analyses always indicates an oxygen-to-metal ratio of 1.973 ± 0.007. X-ray powder patterns indicate a single-phase material, but microprobe traces reveal gross plutonium inhomogeneity (a factor of two between plutonium-rich and plutonium-depleted areas in some cases). Finally, grain size is very small, on the order of 1-2 μ, which is always smaller than the diameters of the largest pores, surface defects, or areas of locally high porosity present in the specimen.

C. Engineering Development

1. Instrumentation and Control (T. P. Mulcahey) (189a 02-096)

New and unique instrumentation is being developed to diagnose performance and detect abnormalities in LMFBR cores. Included are sensors and techniques for acoustical detection of sodium coolant boiling, monitoring of flow-rate-related phenomena that could detect imbalances between cooling and power, and the measurement of vibrations that might disturb overall reactor stability.

a. Boiling Detector (T. T. Anderson)

(i) Acoustic Method

(a) Development of High-temperature Detector (A. P. Gavin)

Last Reported: ANL-7742, pp. 115-116 (Sept 1970).

Two types of high-temperature acoustic pressure sensors (HT3 and HT5) that embody variations of a design based on the symmetric-drive concept are being constructed and evaluated. In this concept (see Progress Report for February 1970, ANL-7669, p. 124), piezoelectric crystals in the sensor housing are mounted "push-pull" between two opposing diaphragms that are exposed to the liquid. A net pressure at the diaphragms causes an electrical charge to be generated by the crystals.

Sensor Type HT3 features diaphragms of circularly embossed Type 304 stainless steel shim stock. The diaphragms in sensor Type HT5 consist of optically polished stainless steel disks with a machined circular groove for flexure. One unit of the first type (HT3-2) and two units of the second type (HT5-1 and HT5-2) have been fabricated and are being evaluated. Additional units are being fabricated.

Three piezoelectric pressure sensors rated to 1150°F have been received from a vendor. A check of pressure sensitivity shows them to be operational at room temperature.

(b) Tests of High-temperature Detectors in Water, Furnace, and Sodium (T. T. Anderson)

Last Reported: ANL-7737, p. 132 (Aug 1970).

Frequency responses of the three high-temperature acoustic pressure sensors (HT3-2, HT5-1, and HT5-2) in water have been determined, and the units are being calibrated in a high-temperature furnace.

The water tests were performed in a 1-m-dia tank, using wideband acoustic noise generated simultaneously by two sources: boiling generated by an electrically heated wire (1-30-kHz range), and a commercial hydrophone excited by a random-noise voltage source (20-100-kHz range). Of the three units tested, sensor HT3-2 had the highest acoustical output, and the frequency response equaled that of the hydrophone (0-100 kHz).

In the furnace tests, acoustic pressures are produced within the furnace cavity by a piston vibrating at the bottom of the cavity. Before the sensors were installed, pressures in the frequency range 100-500 Hz were measured with a capacitor-type microphone. At 350-450 Hz, the acoustic pressure response varied linearly with vibration amplitude. The measured pressures also agreed with values predicted from measured acceleration of the piston.

The three sensors were then installed in the furnace and cycled between room temperature and 1100°F. At room temperature, sensor HT3-2 indicated a sensitivity of 120 pC/bar at 400 Hz, and sensors HT5-1 and HT5-2 much lower values. After one temperature cycle, the sensitivity of sensor HT5-2 increased to 160 pC/bar, and sensor HT5-1 became inoperable. After two more cycles, the sensitivity of HT5-2 increased to 200 pC/bar. This behavior of HT5-2, also observed for the previously heated HT3-2, is attributed to better mechanical contact when gold foils in the sensor anneal at elevated temperature.

Electrical resistance of the sensors decreased with temperature reproducibly over several thermal cycles, and was unaffected by sensor internal pressures of 10-600 mm Hg abs.

After the furnace tests, the operable sensors will be recalibrated at high frequency in water before being tested in sodium.

2. Heat Transfer and Fluid Flow (M. Petrick and R. P. Stein) (189a 02-097)

Analytical and experimental investigations of liquid-metal heat transfer and fluid flow in components and systems are conducted to provide

information of immediate interest to the FFTF and LMFBR programs. Fundamental studies in heat transfer and fluid flow also are conducted to improve current, or to devise new, engineering prediction methods essential to the advancement of reactor technology in general.

a. LMFBR Flow Stability Studies (M. Petrick and R. Rohde)

This activity covers (1) the acquisition and analysis of experimental data on the vaporization and superheating of sodium in operating ranges (pressures, flow rates, temperatures, and equivalent diameters) and flow circuits of interest to the LMFBR program; and (2) the determination, by both experiment and analysis, of two-phase flow phenomena related to flow stability. An LMFBR Simulation Heat Transfer Loop is being constructed for the experiments.

(i) Preparation of Apparatus

Last Reported: ANL-7742, p. 117 (Sept 1970).

Installation of the leak detector system, insulation, and connection of thermocouples to junction boxes has been completed for the portion of the piping system between the heat exchanger and the preheater.

Final piping layout and piping design calculations for the oscillating plugging meter, hot trap, and sampling station have been completed.

Electrical power wiring of the loop was resumed with the installation of the 75-kVA transformer, the 115- and 230-V distribution panels, the heat-exchanger heater, and the vacuum pump for the test section.

b. Liquid-metal Heat Transfer in Pin Bundles (M. Petrick and T. Ginsberg)

Experiments are performed with simulated fuel-pin subassemblies fabricated with and without helical spacers to investigate the interchannel mixing mechanism and to develop a mathematical formulation that describes the mixing phenomenon in subassemblies typical of FFTF and LMFBR designs. The EBR-II Subassembly Water Test Loop at ANL is being modified to meet the experimental requirements.

(i) Modification of EBR-II Subassembly Water Test Loop (T. Ginsberg)

Not previously reported.

Design modifications are under way to convert the EBR-II Subassembly Water Test Loop from a closed-flow system to a once-through

flow system to meet the requirements of the subassembly interchannel mixing experiments. The initial series of experiments will be performed on a subassembly of seven, helically-spaced, 0.5-in.-dia stainless steel rods, having a pitch-to-diameter ratio of 1.2. This subassembly is being designed.

Figure II.C.1 shows schematically the essential features of the facility in which the mixing experiments will be performed. A tracer technique will be employed. In operation, water will be pumped from a supply vessel to the test assembly. To simulate the Reynolds-number characteristics of sodium systems, the water will be heated to 200°F by a 100-kW immersion heater in the vessel. An electrolyte solution will be injected into one subchannel of the test assembly at various axial positions.

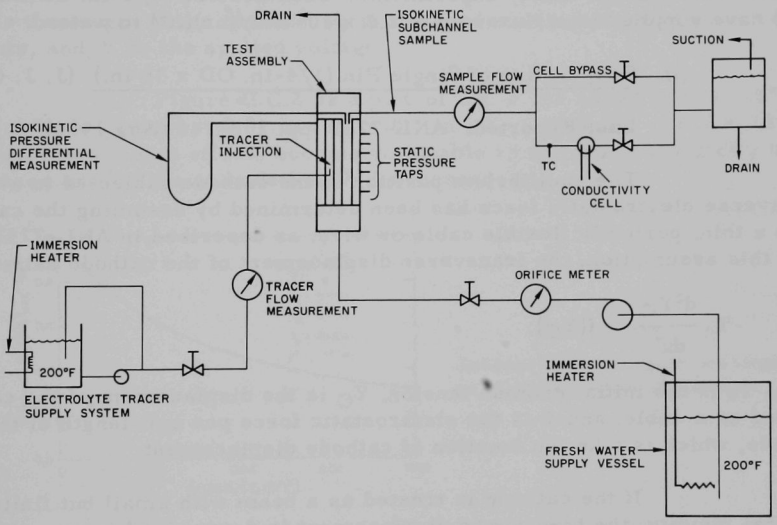

Fig. II.C.1. Schematic of Facility to Be Used for Subassembly Interchannel Mixing Experiments

Subchannel-averaged electrolyte concentrations will be measured at the exit plane of the subassembly. Here, the fluid in each subchannel will be isokinetically drawn out, thoroughly mixed, and passed through a conductivity cell where the electrolyte concentration will be measured. Both the isokinetic flow rate and the electrolyte concentration will be recorded.

The data obtained will be used to:

(1) Characterize the mixing mechanism resulting from the sweeping action of helical spacer wires.

(2) Develop a helical-flow-mixing correlation applicable to LMFBR and FFTF design geometries and flow characteristics.

(3) Evaluate the utility and accuracy of lumped-parameter calculational procedures.

c. Electron Bombardment Heater (EBH) Development (R. D. Carlson)

Electron-bombardment (EB) heaters are being developed to supply heat fluxes greater than 1.5×10^6 Btu/(hr)(ft^2) to liquid metals. Current effort is directed toward EB pin-type heaters that are prototypical of reactor fuel pins and that can be used to simulate these pins in various heat-transfer and reactor-safety experiments. Such heaters (1/4-in. OD x 24 in. long) have supplied heat fluxes up to 2.3×10^6 Btu/(hr)(ft^2) to water.

(i) Preparation of Single Pin (1/4-in. OD x 36 in.) (J. J. Carey)

Last Reported: ANL-7737, pp. 135-140 (Aug 1970).

The equilibrium position of the cathode subjected to a transverse electrostatic force has been determined by assuming the cathode to be a thin, perfectly flexible cable or wire, as described in ANL-7737. With this assumption, the transverse displacement of the cathode satisfies

$$-T_0 \frac{d^2 Y_C}{dx^2} = f(Y_C), \qquad (1)$$

where T_0 is the initial cathode tension, Y_C is the displacement of the cathode treated as a cable, and f is the electrostatic force per unit length of the cathode, which is a known function of cathode displacement.

If the cathode is treated as a beam with small but finite flexural rigidity, the transverse displacement is determined from

$$EI \frac{d^4 Y_B}{dx^4} - T_0 \frac{d^2 Y_B}{dx^2} = f(Y_B), \qquad (2)$$

where EI is the flexural rigidity of the cathode, and Y_B denotes the displacement of the cathode treated as a beam. Although the assumption that the cathode is perfectly flexible (EI = 0) appears reasonable and considerably simplifies the analysis, it is important to have a qualitative estimate of the effect of cathode bending resistance to transverse displacement.

Such an estimate has been obtained for a cathode with hinged ends by considering the solutions of Eqs. 1 and 2 in the form of a trigonometric series. The electrostatic force is approximated by the first two terms in a Taylor-series expansion about the uniform initial eccentricity Y_0; thus the analysis is restricted to small displacements.

A measure of the ratio of maximum beam displacement to maximum cable displacement is given by

$$\frac{(Y_B)_{MAX} - Y_0}{(Y_C)_{MAX} - Y_0} \simeq \left[1 + \frac{\phi_1 \pi^4}{\pi^2 - \phi_2 C_1} \right]^{-1}, \tag{3}$$

where

$$\left.\begin{aligned} \phi_1 &\equiv \frac{EI}{T_0(2\ell)^2}, \\ \phi_2 &\equiv \left(\frac{2\ell}{R_2}\right)^2 \frac{2\pi\epsilon V^2}{T_0}, \end{aligned}\right\} \tag{4}$$

2ℓ is the length of the cathode, R_2 is the anode radius, ϵ and C_1 are constants, and V is the applied voltage.

Figure II.C.2 is a plot of Eq. 3 for $(2\pi\epsilon V^2)/T_0 = 10^{-4}$, R_1 (cathode radius) = 0.01 in., R_2 = 0.1 in., Y_0 = 0.01 in., and ℓ = 18 in. As expected, beam effects become noticeable as the flexural rigidity increases and/or the cathode length decreases.

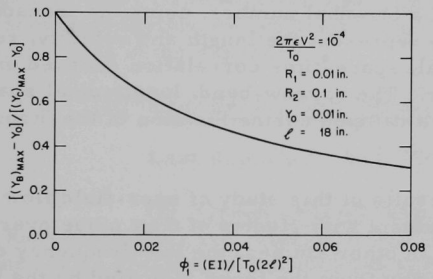

Fig. II.C.2
Influence of Flexural Rigidity and Length on Maximum Cathode Displacement

3. Engineering Mechanics (G. S. Rosenberg) (189a 02-099)

a. Structure-Fluid Dynamics (M. W. Wambsganss, Jr.)

(i) Near-field and Far-field Flow Noise

Last Reported: ANL-7726, pp. 134-136 (July 1970).

In ANL-7726, the mean-square spectral densities of near-field flow noise were presented for a range of axial flow velocities, and normalization of the spectra was discussed. Further analysis of the pressure-time histories has yielded information relating to the decay and convection of the flow noise.

Broad-band, space-time correlations, using differential pressure signals, were obtained from a variable-time-delay correlator. Convection velocity ratios, average eddy lifetimes, and longitudinal correlation lengths were computed from the correlation plots. Over the range of flow velocities tested, the convection velocity ratio and longitudinal correlation length had average values of 0.89 and 0.29 in., respectively; the average eddy lifetime decreased with increasing flow velocity. These results are in agreement with those of other investigators and also with those from a previous flowtest.

Broad-band results are of interest in obtaining a basic understanding of the characteristics of near-field noise. However, to calculate the response of structural components (e.g., fuel pins) to near-field excitation, it is necessary to have information relating to its narrow-band, statistical behavior, i.e., the frequency dependence of the characterizing properties. Narrow-band, space-time correlations were obtained using a constant filter bandwidth of 100 Hz.

For a given mean axial flow velocity, the convection velocity decreased with increasing frequency, indicating that the higher-frequency eddies are convected at a lower speed; this follows intuitively if the velocity distribution at a cross section of the flow channel is considered. The frequency was expressed in terms of a Strouhal number, using the transducer spacing and convection velocity to represent the length and velocity, respectively. The maximum, longitudinal, space-time correlation decayed exponentially with the Strouhal number. The narrow-band, longitudinal space correlation was representable as a damped cosine function of the Strouhal number.

In general, the results of this study of near-field flow noise in annular water flow are in agreement with studies of flow noise over flat plates and in pipes. However, as in other studies, the low-frequency data are difficult to analyze and often vary from the trend indicated by the higher-frequency results, or are erratic. Most likely, the low-frequency eddies are not as well defined as are the higher ones; in fact, if the width of the flow channel is taken to be the upper limit on eddy size, low-frequency eddies cannot exist. The low-frequency data are probably caused by slow variations in fluid flow, the statistical descriptions of which might be significantly different from those associated with turbulent-eddy flow. Since the low-frequency range is of primary interest (typical reactor components have relatively low fundamental frequencies at which they predominantly respond), additional study and development of analytical methods are required.

D. Chemistry and Chemical Separations

1. Fuel Cycle Technology

a. Molten Metal Decladding of LMFBR Fuels (D. S. Webster) (189a 02-173)

Laboratory and engineering work is being done to develop concepts for liquid-metal decladding of LMFBR fuel elements with a fuel-reduction step. The concepts are expected to be applicable also to the removal of Zircaloy cladding from light-water-reactor fuels.

(i) Engineering Concepts, Analysis, and Evaluation (R. D. Pierce)

Last Reported: ANL-7705, p. 162 (June 1970).

Major emphasis of our work on the head-end steps of LMFBR fuel reprocessing has shifted from molten-metal decladding and voloxidation to molten-metal decladding and liquid-metal reduction of the fuel oxides. The reduction step offers the advantage of completely removing iodine and other fission-product gases from the declad fuel. Since the decladding-reduction design has become the reference design for program planning, it is being expanded.

(ii) Engineering Development (R. D. Pierce)

Last Reported: ANL-7742, pp. 119-120 (Sept 1970)

(a) Gas-Release Experiments. An additional experiment was done simulating the release of fission gas under pressure upon the rupture of an irradiated fuel element partially immersed in molten zinc. In this experiment, the assembly, which was immersed to a depth of 3 in. in molten zinc, consisted of two simulated fuel elements contained in a 2-in.-dia steel tube representing a shroud. The tube had a 5/8-in. opening at the bottom and six 1/4-in. holes drilled around the circumference, 11 in. above the bottom. These holes provided a means of equalizing the pressure inside and outside the tube. The two simulated fuel elements were 0.25-in.-OD, 0.01-in.-wall, Type 304 stainless steel tubes containing close-fitting steel pins and argon at a pressure of 52-55 atm. The molten zinc was at 808°C.

The two immersed tubes ruptured after 1.5 and 1.75 min exposure. Examination of the tubes after the experiment revealed that the steel pins had remained inside. Splashing of zinc and salt occurred when the gas was released, and about 20 g remained on the walls of the shroud to a height of 37 in.; there was no evidence of splashing outside the shroud.

(b) Stainless Steel Dissolution in Zinc. An additional experiment (comprising several tests) was done to study the rate of attack on Type 304 stainless steel by zinc containing high loadings of nickel. Results were analyzed along with the results of earlier dissolution tests in which the melts contained various quantities of dissolved stainless steel.

In each test, a Type 304 stainless steel tube (3/4-in. OD, 5/8-in. ID, 4 in. long) was immersed vertically in a liquid Zn-Fe-Cr-Ni alloy. The liquid was stirred with an agitator having two blades 2 in. in diameter and 0.53 in. wide, and with a 45° pitch. The agitator speed was 0-500 rpm, but in most tests it was 100 rpm. After exposure for 1-30 min, a tube was removed from the zinc solution.

Some exposed tubes were placed in a vacuum retort to remove adhering zinc. The difference between the weight before immersion and the weight after retorting was the weight loss due to zinc attack.

All tubes were sectioned, polished, and etched. The thicknesses of the inner and outer reaction zones and of the unaffected steel were measured. The difference between the original and final thicknesses of unaffected steel was the depth of penetration of the zinc into the stainless steel.

The data for melts containing a wide range of stainless steel contents show an initial 5-min period of rapid penetration of the steel during which the thickness of the reaction layer increases and the penetration rate decreases. During this initial period, the iron, chromium, and nickel concentrations all influence the thickness of the reaction layer and thereby the penetration rates.

After about 5 min of immersion, the layer apparently reaches an equilibrium thickness and the penetration rate approaches a constant value. The steady-state penetration rates measured to date can be represented satisfactorily as a function of only the calculated nickel concentration in the melt, i.e., by

$$R_{ss} = \alpha(C_{Ni}^{*} - C_{Ni})^2,$$

where

R_{ss} = steady-state penetration rate, mm/min,

α = constant,

C_{Ni}^{*} = nickel concentration in bulk solution at zero penetration rate, weight fraction,

and

C_{Ni} = calculated nickel concentration in bulk solution, weight fraction; C_{Ni} is calculated by assuming (1) that the nickel charged is completely dissolved, (2) that the cosolubilities of iron and chromium in zinc at 800°C are 5.8 and 1.0 wt %, respectively, and (3) that the equilibrium Zn-Fe-Cr solid phase in the system contains 45 wt % zinc.

Since the reaction layer crumbles away from the fuel once the zinc penetrates the cladding completely, penetration-rate data are considered the most pertinent data obtained in decladding studies.

(iii) Process Demonstration Experiments (R. D. Pierce)

Last Reported: ANL-7726, p. 138 (July 1970).

(a) Semiworks Experiments. Following the zinc decladding step for LMFBR fuels, reduction of the UO_2-PuO_2 with Mg-40% Cu-5% Ca will cause nearly all the uranium to precipitate while the plutonium, also reduced to metal, will stay in metal solution. The plutonium-bearing alloys can then be fed to an acid-dissolution step in preparation for aqueous solvent-extraction processing.

Two reduction experiments (DR-8 and DR-9) were performed, using process conditions similar to those planned for reduction of highly irradiated fuel oxide. The objective was to demonstrate the feasibility of the process using equipment of similar design and the same size as that planned for the hot experiments. (Plutonium was absent in these scoping runs.)

In each run, 1000 g of $CaCl_2$-15 mol % CaF_2 and 100 g of pressed and sintered UO_2 pellets (1/4 in. diameter by 1/4 in. high) were charged into a $4\frac{1}{2}$-in.-ID tungsten crucible having four 3/8-in. baffles. In DR-8, 2000 g of Mg-42% Cu-5% Ca was also charged, while in DR-9 the metal charge was 1000 g of Mg-40% Cu-10% Ca. The reduction temperature was 820°C, and the reduction time 6 hr. Agitation was at 800-850 rpm with an agitator having two blades 2 in. in diameter, 3/4 in. wide, and with a 45° pitch.

The runs proceeded satisfactorily, with nearly all of the uranium oxide reduced to metal and precipitated. Because uranium is insoluble in the metal alloy, it is difficult to determine the degree of reduction accurately. After the run, the salt ingot was separated mechanically from the metal phase and the metal was carefully washed with acid. The quantity of uranium found by analysis in the salt and wash solutions was assumed to have been unreduced. Greater than 99% of the uranium was

reduced in DR-8 and greater than 96% in DR-9. Additional runs are under way with equipment identical to that to be used for the reduction of irradiated fuel oxide. Runs with plutonium-containing fuel are planned.

(iv) Behavior of Volatile Fission Products (M. J. Steindler)

Last Reported: ANL-7726, pp. 138-139 (July 1970).

During the decladding of irradiated fuel elements by use of liquid zinc, some of the iodine will be liberated from the annular and plenum regions of the fuel elements when the cladding is dissolved in liquid zinc at 800°C. A decontamination factor (DF) of 10^7-10^8 for iodine is expected to be required for the head-end steps of LMFBR fuel reprocessing. Zinc decladding is a promising procedure for achieving high iodine removal since iodine liberated in this process rapidly reacts with zinc to form zinc iodide that is quickly extracted into a cover salt layer on the molten zinc.

Experiments have been performed (1) to simulate the release of iodine fission gas during decladding and to investigate the degree of zinc-iodine interaction and (2) to study the use of a zinc pool as an off-gas scrubber. The experimental arrangement consisted of an iodine reservoir, a zinc pool held at 800°C and covered with a 2-cm-deep layer of molten LiCl-KCl, a safety trap, and an aqueous $Na_2S_2O_3$-NaOH scrubber. Argon was the carrier gas for the iodine, and the iodine was labeled with ^{131}I, the quantity being limited to the activity that could be safely handled in our apparatus.

In the first experiment, a mixture of 0.2 at. % I_2-Ar was bubbled through a 10-cm-deep zinc pool at a flow rate of 150 ml/min. After a known quantity of argon-iodine mixture was fed into the train, the cover salt was dissolved in water and aliquots from this solution and from the aqueous scrubber were counted. The counting rate of the salt solution was 1.23×10^6 counts per minute per aliquot, and the counting rate for the scrubber had not increased above background. A DF greater than 10^6 was thus achieved. The absence of activity in the scrubber indicates that possibly higher DF's can be reached in apparatus radiologically safe for handling iodine of higher specific activity.

In the second experiment, the pool depth was decreased and the gas flow rate increased to test the kinetic limitations of the method. Absorption of iodine from a stream of 0.2 at. % I_2-Ar passed through a shallow (3-cm-deep) zinc pool at flow rates of 150 and 300 ml/min was complete, indicating extremely rapid reaction.

Next, a blank run (with zinc absent) was performed. The iodine was accounted for in the salt and in the aqueous scrubber, verifying that the apparatus was functioning properly.

The two following experiments had the objective of briefly investigating the potential of zinc pools as off-gas scrubbers at a lower operating temperature of 500°C. Elemental iodine was used in these runs, although we are aware that iodine might exist in other chemical forms in plant off-gas. In one experiment with 0.2 at. % I_2-Ar bubbled through a 3-cm-deep zinc pool at 150, 300, and 500 ml/min, essentially complete iodine removal was effected (DF $> 10^4$). In the final experiment, a much lower iodine concentration in the gas stream simulated plant off-gas rather than gas from the fuel-element plenum. With 3×10^{-3} at. % I_2 in the argon, a zinc depth of 3 cm, and a gas flow rate of 300 ml/min, the DF was 10^5, indicating that good iodine decontamination could be expected at low concentrations of iodine.

b. LMFBR Fuel Fabrication--Analyses and Continuous Processing (A. A. Jonke and M. J. Steindler) (189a 02-158)

Last Reported: ANL-7726, pp. 141-142 (July 1970).

(i) U/Pu Ratio in Fuel

X-ray fluorescence is being evaluated as an in-line analytical method for determing the U/Pu ratio of UO_2-PuO_2 fuel during fabrication. Earlier work with ThO_2-UO_2 as a stand-in for UO_2-PuO_2 showed adequate resolution of the thorium and uranium peaks and improvement of counting statistics when the collimators used had 20-mil instead of 5-mil slit widths (ANL-7726, pp. 141-142).

The most recent experiments demonstrated a count rate of 7×10^3 cps for the ULα peak when the 20-mil collimators were used. To attain a counting precision of 0.5% at 95% confidence level for the uranium count would therefore require about 1/2 min. If the thorium peak and background were then counted sequentially, it is estimated that the total counting time (i.e., analysis time) for a pellet would be ~1 min.

Examination of sampling plans presently considered in batch processing of fuel shows that for this analysis rate, with a batch size of 500,000 pellets and a sample size of 800 pellets, each analytical instrument can accommodate a production rate of 1000 kg of oxide per day. For smaller batch sizes, more instruments would be needed.

2. General Chemistry and Chemical Engineering

a. Thermophysical Properties of Reactor Fuels (189a 02-162)

(i) Total Effusion of Pu-O and U-Pu-O Systems (C. E. Crouthamel and I. Johnson)

Last Reported: ANL-7705, pp. 165-166 (June 1970)

The chemistry of the U-Mo-O system is being investigated to provide a basis for understanding the extensive migration of molybdenum that has been observed in the postirradiation examination of oxide fuels. The migration of fission-product molybdenum is believed to be related to the local value of the oxygen potential during irradiation. The migration of molybdenum, as various gaseous oxide species, may also be an important mechanism for the redistribution of oxygen during irradiation. Therefore, the spatial distribution of molybdenum in irradiated fuel specimens may offer a means for the reconstruction of the oxygen-potential gradient that existed in the fuel during operation. Knowledge of the oxygen potential gradient in the fuel will be useful in predicting the extent of cladding attack (corrosion), solid fuel swelling, and, if a break in the cladding occurs, the extent of the reaction of coolant sodium with the fuel.

In the present investigation, the partial pressures of various gaseous molybdenum oxide species in equilibrium with UO_2-MoO_2 mixtures are being determined as a function of the oxygen-to-metal (O/M) ratio and the temperature. A combination of Knudsen effusion and mass-spectrometric techniques are being used for these studies.

In an initial scouting experiment a 1:1 (by weight) mixture of $UO_{2.1}$ and MoO_2 was heated in a Knudsen cell in a high vacuum at temperatures of 950-1420°C. Mass-spectrometric examination showed that the principal gaseous species were MoO_3, $(MoO_3)_2$, and $(MoO_3)_3$. Over the temperature range 1110-1380°C, the apparent partial pressures increased by factors of about 27 for MoO_3, 9 for $(MoO_3)_2$, and 5 for $(MoO_3)_3$. Since the composition of the sample changed (about 10% of the sample was vaporized) as the temperature was increased, meaningful enthalpies of vaporization cannot be obtained from these data.

A second experiment is under way in which the vapor species in equilibrium with a sample of MoO_2 are being examined under conditions similar to those used for the $UO_{2.1}$-MoO_2 sample. Initial results indicate that the following species are present at 1350°C: MoO_3, $(MoO_3)_2$, MoO_2, and MoO. The species MoO_2, which was not observed in the experiment with $UO_{2.1}$-MoO_2, was detected in the second experiment. The MoO may have resulted from decomposition of MoO_2 which deposited on the filament of the electron source. The partial pressure of MoO_3 over the $UO_{2.1}$-MoO_2 mixture was larger by a factor of about 50 than the partial pressure over MoO_2. The partial pressure of the polymeric species $(MoO_3)_2$ was significantly lower in the second experiment, and $(MoO_3)_3$ was not detected. These preliminary experiments indicate a definite interaction between UO_2 and MoO_2.

PUBLICATIONS

Survey and Status Report on Application of Acoustic-boiling-detection Techniques to Liquid-metal-cooled Reactors
T. T. Anderson, T. P. Mulcahey, and C. Hsu
ANL-7469 (Apr 1970)

Role of Accelerators in Neutron Radiography
J. P. Barton
Proc. 2nd Oak Ridge Conf. on the Use of Small Accelerators for Teaching and Research, Oak Ridge Associated Universities, Oak Ridge, Tennessee, 1970, CONF-700322, pp. 321-344

Method for Efficiency Gain in Neutron Radiography
J. P. Barton and M. F. Klozar
6th Intl. Conf. on Nondestructive Testing, Hannover, Germany, June 1-5, 1970. Deutsche Gesellschaft für Zerstorungsfreie Prüfverfahren e.V., Berlin, 1970, Vol. M, pp. 87-98

A Mass Spectrometric Investigation of the Volatilization Behavior of $(U_{0.8}Pu_{0.2})O_{2-x}$
J. E. Battles, W. A. Shinn, P. E. Blackburn, and R. K. Edwards
Plutonium 1970 and Other Actinides, Ed. W. N. Miner. Nuclear Metallurgy (Met. Soc. AIME, New York) 17(Part II), 733-742 (1970)

Neutron Radiography
H. Berger
Research Techniques in Nondestructive Testing, Ed. R. S. Sharpe. Academic Press, London, 1970, pp. 269-314

Radiography with Fast Neutrons
H. Berger
6th Intl. Conf. on Nondestructive Testing, Hannover, Germany, June 1-5, 1970. Deutsche Gesellschaft für Zerstorungsfreie Prüfverfahren e.V., Berlin, 1970, Vol. M, pp. 63-74

Forced Vibration of a Cantilevered Tube Conveying Fluid
S. S. Chen
J. Acoust. Soc. Am. 48, 773-775 (1970)

Aluminum Sorption Roughing Pump for Small Vacuum Systems
P. M. Danielson
J. Vacuum Sci. Technol. 7(5), 527-530 (Sept/Oct 1970)

Helium Production in EBR-II Irradiated Stainless Steel
N. D. Dudey, S. D. Harkness, and H. Farrar*
Nucl. Appl. Technol. 9, 700-710 (Nov 1970)

*Atomics International.

Effective Atomic Volume of Aluminum, Gallium, Germanium, and Silicon in Transition Element Intermetallic Compounds

A. E. Dwight

Abstract Bull. Met. Soc.-AIME Fall Mtg., Cleveland, Ohio, October 17-22, 1970, p. 194 Abstract

Argonne Code Center: Bibliographies of Computer Program Literature

C. Harrison, Jr., and Marianne Legan

ANL-7684 (June 1970)

Surface Relaxation of Uranium Dioxide

P. S. Maiya

Abstract Bull. Met. Soc.-AIME Fall Mtg., Cleveland, Ohio, October 17-22, 1970, p. 47 Abstract

The Uranium-Plutonium-Zirconium Ternary Alloy System

D. R. O'Boyle and A. E. Dwight

Plutonium 1970 and Other Actinides, Ed. W. N. Miner. Nuclear Metallurgy (Met. Soc. AIME, New York) 17(Part II), 720-732 (1970)

Service Routines for the Multigroup Cross-section Code MC^2

E. M. Pennington, J. C. Gajniak, A. B. Cohen, and W. Bohl

ANL-7654 (Apr 1970)

Fundamentals of Void Formation under Irradiation

P. G. Shewmon

Abstract Bull. Met. Soc.-AIME Fall Mtg., Cleveland, Ohio, October 17-22, 1970, p. 194 Abstract

Calculation of Heterogeneous Fluxes and Reactivity Worths

W. M. Stacey

Nucl. Sci. Eng. 42, 233-236 (Nov 1970) Note

Xenon-Induced Spatial Power Oscillations

W. M. Stacey

Reactor Technol. 13(3), 252-279 (Summer 1970)

Effect of Eccentricity on Effectiveness of a Sodium-to-Sodium Double-Pipe Heat Exchanger

R. P. Stein, M. J. Featherstone, E. L. Kimont, and T. R. Bump

Proc. 4th Int. Heat Transfer Conf., Versailles, September 1970, Vol. 1, HE1.1

Chemical Engineering Division Fuel Cycle Technology Quarterly Report, April, May, June 1970

D. S. Webster, A. A. Jonke, G. J. Bernstein, N. M. Levitz, R. D. Pierce, M. J. Steindler, and R. C. Vogel

ANL-7735

III. NUCLEAR SAFETY

A. LMFBR Safety

1. Accident Analysis and Safety Evaluation (G. J. Fischer) (189a 02-112)

a. Initiating Accident Code Development (F. E. Dunn)

Last Reported: ANL-7742, pp. 132-133 (Sept 1970).

(i) SAS2A Code. The initial coding has been completed for linking the VENUS disassembly code with SAS2A. The linkage is being tested. At every time step during a SAS2A run, the code will check the peak fuel temperature and the inverse power period. When either quantity exceeds a user-specified maximum, the code will link to the disassembly calculation by preparing a data file containing initial conditions for VENUS. The data file for VENUS either can be used immediately as input for a VENUS run in the same job, following SAS2A, or it can be punched onto cards for use in a later VENUS run.

The initial conditions for VENUS will be taken from the SAS2A results. SAS2A results will supply the densities and temperatures of the fuel, sodium, and steel, as well as the void fraction at every point in the core. SAS2A will also supply the initial reactivity and the initial rate of change of the reactivity.

In the process of coupling SAS2A and VENUS, some improvements have been made in the data storage in VENUS. These improvements reduce the total computer memory-storage requirements of the VENUS code by about 15% while increasing the number of regions that can be used in VENUS.

b. Analysis of Fuel Behavior (A. M. Judd)

(i) Analysis of Fuel Failure Propagation

Not previously reported.

Fault trees for the pin-to-pin stage of fuel failure propagation have been constructed. The purpose of these fault trees is to identify the most likely ways in which a local failure, affecting a small part of the subassembly (due, for example, to a blockage between the fuel pins, or failure of the cladding of one pin because of a manufacturing defect) might propagate to affect the whole subassembly. Another purpose is to identify the analytical problems.

The most likely routes to rapid voiding of the whole subassembly seem to be (1) by some form of cumulative blockage (where, for example, one pin fails, releasing fuel, which causes other pins to fail, releasing more fuel, which adds to the original blockage, causing further failures, etc., until the flow is restricted enough to cause bulk boiling), or (2) by a pressure pulse, due, for example, to release of high-pressure fission gas or to a small violent fuel-coolant interaction, which causes nearly simultaneous failure of many pins, which release gas rapidly at high pressure, voiding the subassembly long enough so that, when the coolant returns, violent boiling ensues.

The first of these is doubtful because it is hard to envisage how a blockage growing in this way can be tenacious enough to resist the coolant pressure gradient. The second might be impossible because the subassembly cannot be kept voided long enough for serious overheating.

Work is proceeding to calculate the flow and temperature transients due to gas release, and the effects of local overheating due to an overenriched fuel pellet or pin. An additional problem of great importance that presents serious analytical difficulties is the response of an irradiated embrittled fuel pin to an impulsive load, and whether failure results.

Future work will cover the effects of sodium logging of the fuel, and consequent chemical interaction between fuel and sodium causing pin swelling (which might be a means of very slow failure propagation, as opposed to the possibilities of rapid propagation outlined above), whole-subassembly accidents (such as inlet blockages), and subassembly-to-subassembly damage propagation.

2. Coolant Dynamics (H. K. Fauske) (189a 02-114)

a. Sodium Superheat (R. E. Henry, R. E. Holtz, and R. M. Singer)

Last Reported: ANL-7737, p. 153 (Aug 1970).

(i) Forced-convection Superheat Experiments with Annular Flow. Fabrication is under way on a single-pin heated test section that will measure incipient boiling superheats in a forced-convection system. The heater, of the ORNL design, is 36 in. long with a 0.250-in. OD; it is thermally partitioned to have 6 in. unheated, 22.5 in. heated, and 7.5 in. unheated. All tests will be run in the Fuel Element Failure Propagation Small Sodium Loop, which is operational. The volume fraction of entrained gas will be determined by the choked-nozzle technique described in ANL-7737. For the tests, test-section outlet temperatures will range from 1400 to 1600°F, and coolant velocities through the test section will range from 0 to 10 ft/sec.

(ii) Model of Incipient Boiling during Forced Convection. The pressure-temperature history model has been applied to reactor systems

to determine the incipient-boiling superheat for various postulated reactor accidents. The effect of the primary-coolant-system design (for example, EBR-II versus FFTF) on the incipient superheat has been demonstrated by considering its effect on gas entrainment in the coolant and/or partial pressure of inert gas in the surface cavities on the fuel elements. If inert-gas bubbles are present in the coolant (as a result of either mechanical entrainment at free surfaces and/or exiting from solution in the heat exchanger), nucleation will most likely occur from these bubbles. However, if gas bubbles are not present (as a result of location of the free surfaces), supersaturated coolant might pass through the core. This will result in nucleation occuring from the surface cavities.

For the EBR-II and FFTF reactor designs, the following conclusions can be drawn based on current state of understanding of nucleation in liquid metals: (1) The probability of inert-gas bubbles being present in EBR-II reactor is small, so nucleation most likely will take place from surface cavities; the partial pressure of inert gas in these cavities is calculated to be relatively small compared to the system pressure, which results in calculated superheats of about 100°F during various postulated accidents; (2) the probability of inert-gas bubbles being present in FFTF is considerably higher; however, if gas bubbles are not present, the partial pressure of inert gas in the surface cavities will be high (approximately equal to or greater than the cover-gas pressure); in either case, essentially no superheat is required to initiate boiling in the FTR reactor during various postulated accidents.

b. Sodium Expulsion and Reentry: In-pile (M. A. Grolmes and H. K. Fauske)

Last Reported: ANL-7742, pp. 133-134 (Sept 1970).

(i) Planning of In-pile Test Vehicles. Integrated in-pile (TREAT reactor) experiments are being planned to determine the overall consequences of coolant expulsion and reentry as they affect fuel failure and potential interactions of molten cladding, fuel, and coolant. For these tests, coolant expulsion will be specifically initiated by flow transients, such as a coastdown, and partial or complete blockage at steady power in a test vehicle that simulates current LMFBR design parameters. Near-term tests will be directed to simulation of FFTF conditions.

A conceptual design of a test vehicle has been proposed for this series of experiments. The test vehicle will accommodate seven active fuel pins of FFTF dimensions with once-through sodium flow providing the necessary inlet and exit pressure conditions. It has been established that the TREAT reactor can accommodate the length of the test vehicle and the associated sodium supply system. Detailed design of the system will be initiated, as will simultaneous consideration of the hazards and accident analysis.

3. Core Structural Safety (C. K. Youngdahl) (189a 02-115)

The objective is to develop analytical methods for predicting the plastic response of circular and hexagonal shells to internal impulsive loads.

a. Hexagonal-shell Analysis

Last Reported: ANL-7513, pp. 134-136 (Oct 1968).

The dynamic plastic deformation of a hexagonal shell loaded by an axisymmetric internal pressure is being analyzed. For the initial phase of the study, it is assumed that the pressure is uniform along the shell length, and the shell material is rigid, perfectly plastic, with a yield stress σ_y. A cross section of the shell and a free-body diagram of the half-side are shown in Fig. III.A.1, where H and L denote, respectively, the wall thickness and length of a side of the hexagon.

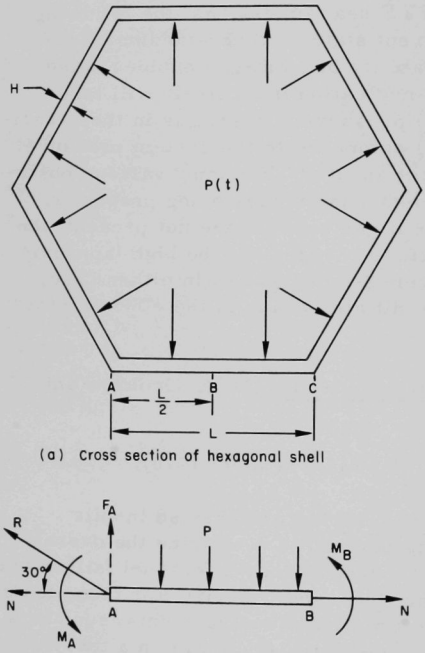

Fig. III.A.1. Loadings Used in Initial Study of Dynamic Plastic Deformation of a Hexagonal Shell

The yield condition of the shell wall is

$$(M/M_0) + (N/N_0)^2 = 1, \qquad (1)$$

where M is the circumferential bending moment, N the force per unit axial length, and M_0 and N_0 are defined by

$$M_0 = \tfrac{1}{4}\sigma_y H^2$$

and

$$N_0 = \sigma_y H. \qquad (2)$$

Plastic deformation of the shell wall is initiated at the yield pressure P_y when plastic hinges form at the corners and the midpoints of the sides of the hexagon. Through the use of limit-analysis procedures, P_y is found to be given by

$$P_y = \frac{(8H^2\sigma_y)}{L[L+(L^2+48H^2)^{1/2}]}. \qquad (3)$$

Applied peak pressures which exceed P_y produce dynamic plastic deformation of the shell. The equations of motion of the shell wall, the plastic flow rule, the yield condition of Eq. 1, and the geometric compatability conditions must be satisfied during the deformation process. A computer program is being written which solves the resulting sets of coupled nonlinear differential equations.

4. Fuel Dynamics Studies in TREAT (C. E. Dickerman) (189a 02-117)

a. Transient In-pile Tests with Ceramic Fuel (C. E. Dickerman)

Last Reported: ANL-7742, pp. 136-137 (Sept 1970).

(i) First Two Mark-II-loop Tests (H1 and H2) on Transient Failure Threshold of Mixed-oxide Fuel Element with Axial Heat Transport by Flowing Sodium. Exclusive of results from the fast-neutron hodoscope and analysis of the coolant behavior being performed using Cronenberg's fuel-coolant interaction model,* the analysis of the transient-test data from the H2 experiment has been completed. The latest conclusions from the SAS1A analyses are discussed in Sect. III.A.4.c below, Analytical Support.

Figure III.A.2 gives the transient-test data for the failure transient. The initial flow velocities both correspond to an average from the two flowmeters of 6.7 ± 0.5 m/sec in the test section. Failure is indicated by the initiation of flow and pressure anomalies at about 1.45 sec. [The transient thermal data have not been corrected for the typical response time (~20-25 m/sec) for our thermocouples.] With the assumption of this response, failure is also indicated at 1.45 sec from the rapid rise in the thermocouple closest the fuel, presumably by its contact with hot molten fuel resulting from cladding failure. This information was also substantiated by the posttest neutron radiographs of the test section, which indicated that the top 3 in. of the fuel column were missing. At 1.45 sec, the test data indicate that the coolant was significantly below 1013°C, the saturation temperature for the 2.91 atm pressure at the top of the fuel stack. Failure occurred at a sample energy of 1220 J/g (84% of the transient energy input) with about 30% of the fuel molten. At the time of failure, the maximum inner and outer cladding temperatures at the top of the fuel stack, which were calculated from SAS1A-ASH, were 1132 and 966°C, respectively. The calculated maximum coolant temperature at failure was 920°C, which was lower than the 1013°C saturation temperature at that location.

Figure III.A.3 shows the integrated sodium movement relative to steady state as a function of transient time. This relative movement is taken as the volume of sodium displaced at the given flowmeter as a result

*A. W. Cronenberg, H. K. Fauske, and S. G. Bankoff, A Mathematical Model for Fuel-Coolant Interaction, submitted for presentation at the ANS topical meeting on reactor mathematics and applications at Idaho Falls (Mar 1971).

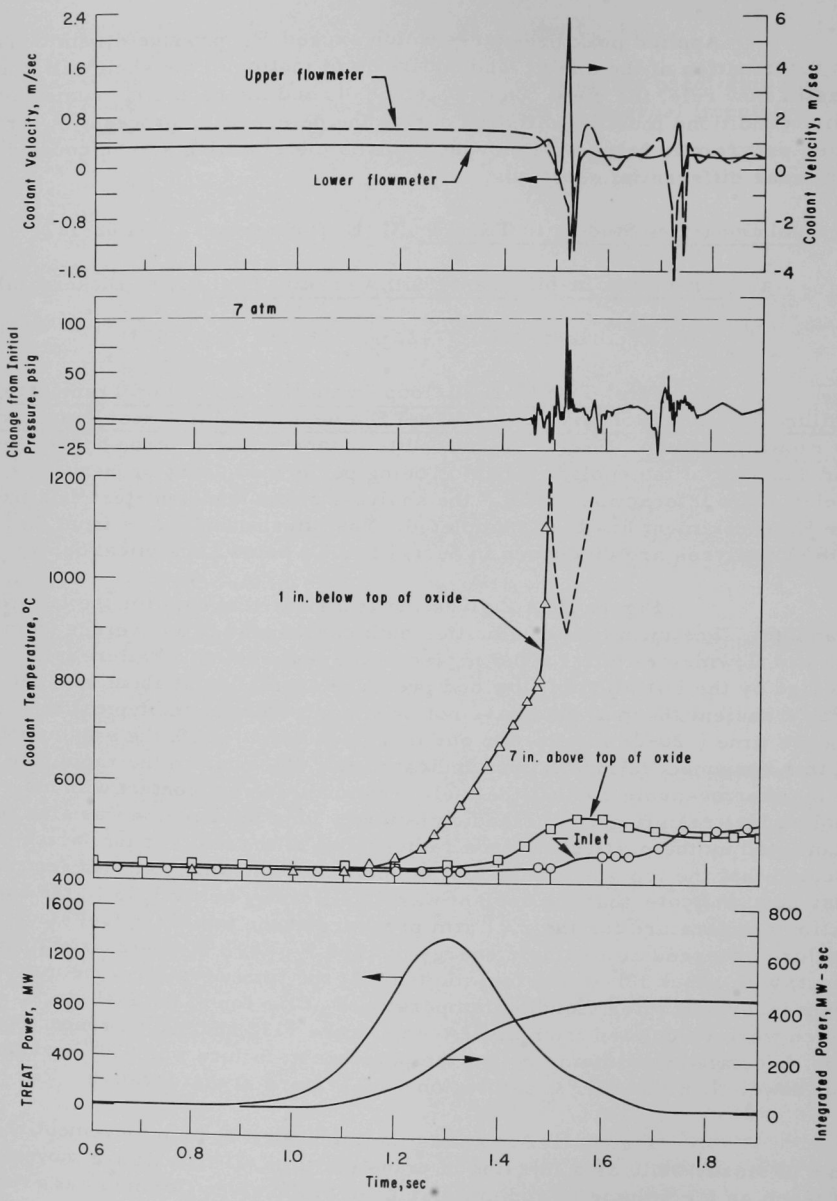

Fig. III.A.2. Test Data for Failure Transient 1317 in Test H2. ANL Neg. No. 900-409 Rev. 1.

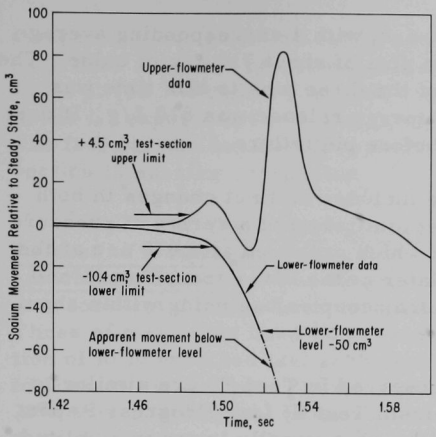

Fig. III.A.3. Integrated Sodium Movement Relative to Steady State as a Function of Transient Time in Test H2

of slug ejection from the test section. Under the assumption of an intact element and fuel holder, and the initiation of voiding at the top of the fuel column, the upper and lower volumetric limits of the test section also are displayed in Fig. III.A.3. Until analytical results from Cronenberg's model are available, voiding of the test section after cladding failure is assumed to be complete at 1.49 sec (see Fig. III.A.3). The expulsion is rather slow, probably as the result of a mild failure. After the initial vaporization of the small amount of liquid from the test section, probably followed by condensation above the test section, reentry is possible. Consequently, at 1.49 sec, reentry commences from the top of the test section, with void growth continuing at the bottom. The net effect is the expulsion of the void out the bottom of the test section. Then this reentry is followed by a much more vigorous expulsion, probably as a result of the interaction between the sodium and the hot fuel from the failed element.

A first approximation to the coolant superheat was obtained by taking the 1.33-atm initial pressure spike as the change in vapor pressure resulting from flashing of superheated coolant. For the saturation temperature corresponding to the pressure at the top of the fuel stack, before the inception of coolant bulk boiling, this pressure corresponds to a superheat of 54°C.

The H2 test section was removed from the Mark-II loop at the Fuel Examination Facility (FEF) and inserted into a liner, which was fabricated for the T-2 TREAT cask according to the specifications of General Electric Co. Drawing 693C267. According to U.W. Department of Transportation (DOT) Special Permit 5607, Drawing 693C267 describes a container suitable for shipping open or unclad material in the T-2 cask. The shipment of the H2 test section has been delayed at least 4-6 weeks for a clarification of the permit for shipping samples of the length of the H2 test section.

(ii) First Mark-II-loop Tests (E3) on Fuel-movement Failure of Irradiated Oxide Pin during a Power Excursion. Evaluation of the data from Test E3 is continuing. Failure of the fuel elements (half-length EBR-II-like UO_2 pins irradiated to 6% burnup in the MTR) apparently occurred about 0.668 sec after start of the transient. The reactor energy

release to this time was about 426 MW-sec, with a corresponding average fission-energy release in the three test pins of about 710 J/g of oxide. The average energy release in the hottest of the three pins to this time was about 765 J/g, and the maximum local energy release was 810 J/g. It does not appear that fuel melting occurred before pin failure.

Evidence of pin failure includes distinct changes in both inlet and outlet coolant flow at 0.668 sec, initiation of a series of pressure spikes at both transducers (the first of which occurred at 0.670 sec at the upper transducer and about 1-2 msec later at the lower transducer), and significant temperature rises on all thermocouples beginning within about 10 msec after postulated time of failure.

The pressure pulses observed in Test E3 are similar to the series of damped pressure pulses from Test S5 (see Progress Report for August 1970, ANL-7737, p. 177), although generally lower in amplitude.

The conversion of fission energy to work on the coolant is being calculated. As part of an effort to understanding the observed pressure pulses, a short computer code is being written to reduce flowmeter data from the loop instruments and to calculate the energy and momentum of the coolant in the complex geometry of the loop. Availability of this code should significantly simplify handling of data from future Mark-II-loop experiments.

(iii) First Mark-II-loop Experiments (E4 and E5) on Fuel-movement Failure of Mixed-oxide Fuel during a Power-excursion Accident. Test conditions have been established for the E4 transient experiment in TREAT. E4 is planned as a higher-energy follow-on to the H2 test and is intended to provide further data on the mode of failure and the characterization of fuel movement, as well as on coolant ejection and reentry. This will be the first test beyond the failure threshold for a prototype mixed-oxide FFTF fuel element and the last in the series of single-pin experiments.

Data from the H2 test indicated that failure occurred when about 30% of the fuel had melted. This corresponds to an input energy of approximately 1220 J/g of oxide. To get significantly beyond the threshold of failure, the energy input for the E4 test has been set at 1800 J/g. With the already established calibration factor of 3.3 J/g of oxide/MW-sec of TREAT energy, the required reactor energy is 545 MW-sec and the TREAT step input is 2.3% $\Delta k/k$. Calculations under these conditions using the SAS1A-ASH code indicate that the fuel-pin cladding will melt through at about 1540 J/g and sodium boiling will begin at about 1430 J/g. As for Test H2, the threshold of failure is expected when about 30-40% of the fuel is melted (~1200 J/g), with sodium expulsion at about 1500 J/g.

Because Test E4 is a power-excursion test simulating FFTF conditions, the B_6Si thermal-neutron filter will be used. Fuel-pin

comparison and expected radial power distributions during the transient have been reported previously. (See Progress Report for July 1970, ANL-7726, p. 155.) Preparations are being made to fit the Mark-II test loop used in the L1 experiment with the shield used in the H1 and H2 experiments. The fuel pin has been shipped to the TREAT Site, and outfitting of the test section is nearing completion.

(iv) First Mark-II-loop Experiments (D1 and D2) on Effects of Release of a Small Amount of Molten Fuel, Using Pins with Local High-enrichment Sections. The 12 prototypical (except for UO_2 fuel) FTR fuel pins for Test D1 have been completed and are in transit from WADCO. Three of these pins have UO_2 enrichment of 26%, with a 1.5-in.-long section of fully enriched fuel at the axial midplane. These pins are intended for use as central pins in seven-pin clusters. The remaining nine pins have 20%-enriched UO_2 fuel pellets and are to be used in the peripheral locations. A calibration run is planned, after which one central and two peripheral pins will be examined destructively. One central and six peripheral pins will be used for the test. The remaining two pins are spares. Complete quality-assurance documentation of the pin characteristics has been received.

Design of the fuel holder for the D1 and D2 experiments, which will accommodate a seven-pin cluster of prototypical FTR pins, is about 90% complete. The design incorporates provision for remote assembly of future test sections using preirradiated pins, although the details have not yet been worked out. Seven fuel pins are contained within a tube that simulates the adjacent pins of a cluster. Development work on the manufacturing technique for the tube has been completed. The technique developed consists of pressing the tubes onto an indented mandrel using a sheet-metal forming brake. The metal did not spring back to the degree anticipated, so it may be necessary to make a new mandrel for production tubes. A dummy cluster of pins is being made for use as a gauge to check fit-up and for use in development of remote assembly techniques.

b. Experimental Support (L. E. Robinson)

Last Reported: ANL-7737, pp. 169-170 (Aug 1970).

(i) Shipping-cask Procurement Documentation. The Chicago Operations Office certification of approval of the Mark-II-loop shipping cask has been received. RDT authorization to proceed with the procurement of two casks (one for the Nuclear Safety program, and one for general use) has been granted. The purchase requisition has been processed at ANL and is being considered by AEC-CH. Application for a Department of Transportation permit is pending.

(ii) Preparation of Last Six Mark-II Loops from FY 1970 Stocks

Last Reported: ANL-7737, p. 170 (Aug 1970).

The first two TREAT Mark-II integral sodium loops of the A version (A1 and A2) are being outfitted with trace heaters, pressure, temperature, and flow-rate instrumentation and other ancillary equipment in preparation for prooftesting. These loops are scheduled to be used for conducting the D1 and L2 tests, respectively. The other four loops (A3-A6) are being assembled primarily from the inventory of components manufactured earlier. The work is being performed in accordance with the manufacturing and quality-control plan developed for this project. In addition, an annular linear-induction pump (ALIP) stator, of the type used in the Mark-II loop, has been fabricated and is being used as the magnetic pressurization source in a coolant-dynamics experiment (189a No. 02-114) to investigate the superheat properties of sodium.

(iii) Adaptation of Cave Accessories for Minimal Usage of Cave for Mark-II Loops with Irradiated Mixed-oxide Fuels. Work has begun to supply equipment and equipment modifications for loading and unloading preirradiated mixed-oxide Mark-II-loop test sections using the FCF air cell. An existing cask will be modified, and auxiliary equipment will be supplied, consisting of an in-cell work table, a test-section receptacle, disassembly accessories, and miscellaneous fixtures and rigs. The schedule for engineering, fabrication, assembly, and checkout has been arranged to fit the schedule for the first Mark-II-loop experiment on irradiated mixed oxide (Test H3, planned for the last quarter of FY 1971).

c. Analytical Support (A. B. Rothman)

Last Reported: ANL-7742, pp. 138-140 (Sept 1970).

(i) Automated Handling of Hodoscope Data

Last Reported: ANL-7737, p. 171 (Aug 1970).

Development work continues toward providing an automated system for handling the TREAT hodoscope data of fuel motion during transient tests. This system was designed originally around the ANL CHLOE scanning device, which suffered continuing breakdowns last spring and was retired in favor of a new scanner, ALICE. ALICE, however, is not compatible with the software, films, and tape systems used for CHLOE. The hodoscope data were recorded originally on high-speed film in an analog representation, then reduced by manual operations in which relative film exposures were compared visually.* The automated system now being developed uses

*A. DeVolpi, C. E. Dickerman, and J. F. Boland, "Preliminary Performance Data from Fast Neutron Hodoscope at TREAT," Trans. Am. Nucl. Soc. 12(2) 868 (1969).

a binary representation of the hodoscope signals recorded on film. Film synchronization and reference marks are used to permit automatic extraction of numerical data from the film,* using CHLOE or ALICE.

Status of work under way to use ALICE is as follows:

(1) A 16-mm film capability being added to ALICE will permit the initial extraction of data from the film; all subsequent steps from translation of the raw ALICE data into numbers will be done using existing programming and the CDC-3600 computer.

(2) Modest reprogramming is under way so that the ALICE computer can do the preliminary processing of the raw scanning-system output; this reprogramming is expected to be complete by the time the ALICE system can handle the 16-mm TREAT film, which is imminent.

(3) Full use of ALICE capabilities will require extensive reprogramming, including generation of data plots; after this reprogramming is completed, the CDC-3600 will not be used. This step is required because availability of the CDC-3600 computer cannot be assured beyond the end of this fiscal year.

(4) The computer-produced digital data includes normalization; however, extensive man-controlled analysis is then required to select meaningful displays and characterization of fuel movements from the individual "picture" mosaic pieces (a maximum of 334 pieces, and minimum picture repetition time of 1.2 msec). This will use a display station, expected to be ready by the time the full CDC-3600 programming has been changed to the full ALICE-IBM-360 system. The PDP-11 computer for the display has been received, and also both magnetic-tape units; hardware and coupling stages are about 90% complete; software organization has begun.

A sizable backlog of TREAT transient film has been accumulated. For each transient experiment (including one for another contractor), we have determined and reported the specifications for hodoscope operating parameters, which depend on reactor power levels and transient duration as well as special data requirements of the experimenter.

Examination of the film from the latest experiment (L1) reveals some weak and missing display lamps. This indicates possibly poor synchronization, which would increase the work needed on L1 when ALICE is ready.

---

*A. DeVolpi, "Deciphering and Processing Digital Photographic Data," Ninth Intern. Conf. on High Speed Photography (1970).

(ii) Analysis of Transient In-pile Experiments

Last Reported: ANL-7742, pp. 138-140 (Sept 1970).

Detailed results of the SAS1A-ASH posttransient calculations for the H2 experiment are reported here for both the checkout transient (Tr-1316) and failure transient (Tr-1317). In these calculations, actual experimental flow and transient power data were used in conjunction with neutron-transport calculations for geometric power profiles and the calibration factor (3.30 J/MW-sec of TREAT per gram of oxide fuel).

Figure III.A.4 compares calculated coolant bulk temperatures with data from a thermocouple 1 in. below the top of oxide fuel for the checkout transient. The solid curve was obtained from the SAS1A-ASH code in which the effect of fuel cracking on gap conductance was included in a code modification described previously. (See Progress Report for August 1970, ANL-7737, pp. 171-173.) Values of parameters used were, in the notation described in ANL-7737, h_{gmax} = 2.0 W/cm^2-°C, c_1 = 0.002 W/cm-°C, c_2 = 0.004 W/cm-°C, and c_3 = 1.0 x 10^{-8}W/(cm^2-°C)/(dynes-cm^2). The agreement between calculation and experiment is considered satisfactory. The effect of including variations in gap conductance from fuel cracking is shown by the dashed curve in Fig. III.A.4; the dashed curve was obtained by setting c_1 = c_2 = 0.002 W/cm^2-°C, thus reducing SAS1A-ASH to SAS1A in the treatment of the gap-conductance equations. The two calculations are identical until the end of the power transient, because the fuel-cracking modification is initiated when the fuel begins to cool off. Furthermore, it is concluded that the fuel-cracking effect, although incorporated by a very simple technique, was quite noticeable in terms of outlet coolant bulk temperatures. These calculations also indicated that the fuel was never in contact with the cladding. Hence the pin should not have been deformed in the checkout experiment. This observation agrees with the minimal deformation found in the postmortem examination of the H1 pin, reported previously. (See Progress Report for June 1970, ANL-7705, p. 173.) Maximum fuel temperature for this checkout run was calculated to be 1890°C, well below the melting point.

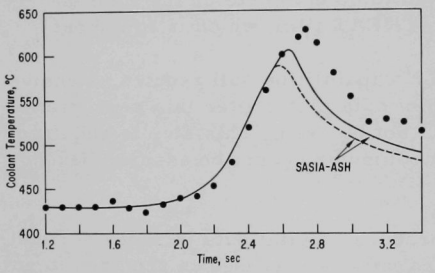

Fig. III.A.4. Comparison of Calculated Coolant Bulk Temperatures with Data from a Thermocouple 1 in. below Top of Oxide Fuel in Checkout Transient Tr-1316 before Test H2

Calculations of coolant temperature, pin deformation, etc., were performed for the actual failure run (Tr-1317), using the above-mentioned parameters specifying bond conductance and actual flow and

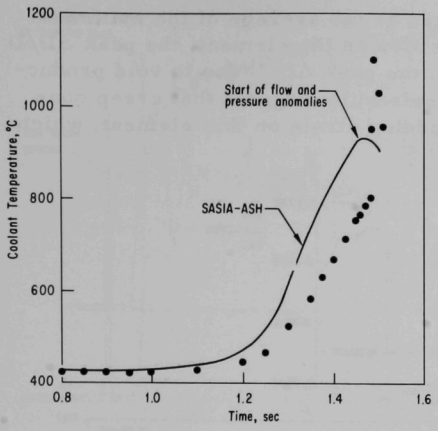

Fig. III.A.5. Comparison of Calculated Coolant Bulk Temperatures with Thermocouple Data from Test H2 (Tr-1317)

power-transient data. Figure III.A.5 shows the results with an expanded time scale. Note that this transient produced about 40% more energy than that required for full fuel melting under adiabatic conditions. Here again, the calculated coolant-temperature profile is seen to be in satisfactory agreement with the thermocouple data, except for a time lag of about 30-50 msec. The thermocouple time constant is estimated to be about 20-25 msec. At the time of pin failure (shown by arrow at 1.45 sec), about 30% of the oxide fuel was calculated to be in the molten state in an annulus with a 0.05-cm inner radius and a 0.20-cm outer radius, which is very close to an inner cladding radius of 0.259 cm. Some of the hot molten fuel, either from oozing up to or being pressed against the cladding by the pressure within the pin, could cause its melting, even though the cladding was calculated to be at 1080°C. Based on pressure and coolant-flow-rate data and on analytical calculations, it appears that cladding failure did not result from cladding vapor blanketing after coolant boiling, but possibly from molten fuel-cladding contact. However, coolant boiling can occur after failure because of hot fuel contacting the coolant directly. This hypothesis appears to be consistent with the test data. As much as 40-43% of mixed oxide could be molten towards the end of the transient.

d. Hot Laboratory Examinations (L. A. Neimark and J. D. B. Lambert)

Last Reported: ANL-7688, pp. 228-232 (Apr-May 1970).

(i) Examination of EBR-II-irradiated Fuel Elements. Element 007 from Subassembly X040A is being examined destructively. This wire-wrapped 0.290-in.-dia element, clad with 0.020-in.-thick Type 304L stainless steel, contained 76.5% smear density $(U_{0.8}Pu_{0.2})O_2$ and was irradiated to a mean burnup of approximately 5 at. % at a peak linear rating of 15.7 kW/ft in the first EBR-II assembly of unirradiated oxide pins.

Profilometry showed a cladding diametral strain of up to 1% with a superimposed "ripple" of up to ±0.2%. The period of the ripple corresponded with the 3-in. half-pitch of the wire wrap (see Fig. III.A.6). Angular profile scans indicated the element could be oval in section (see insert of Fig. III.A.6), with the minor axis of ovality in the plane of the

wire wrap. If the true diameter is taken as the average of the maximum and minimum diameters at a given position on the element, the peak $\Delta D/D$ was approximately 0.80%. In contrast, the peak $\Delta D/D$ due to void production was calculated to be 0.60%.* These results suggest that creep contributed significantly to the overall cladding strain on this element, which had a plenum-to-fuel volume ratio of 0.5.

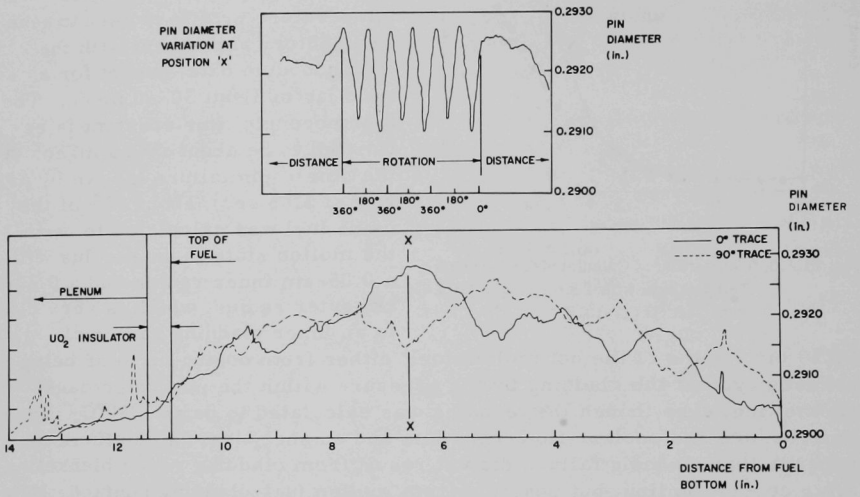

Fig. III.A.6. Diameter Traces on Element 007 at Two Orientations Showing the Effect of the Wire Wrap on the Shape of the Element Section

Neutron radiography showed an increase in the initial gaps between the fuel pellets after irradiation. Axial gamma scans also indicated concentrations of ^{137}Cs at these gaps and a high ^{137}Cs concentration at the top of the fuel column (see Fig. III.A.7). When the plenum was punctured, 56.21 cc (STP) of fission gas were collected. The fission gas released from the fuel was calculated as 74.7% for an assumed fuel mean burnup of 5 at. % and a generation rate of 0.246 rare-gas atoms per fission.

Longitudinal metallographic sections revealed that the fuel was continuous across the initial pellet gaps in the regions of equiaxed and columnar grain growth. The central void was larger than at other axial positions, and the boundaries of the fuel zones conformed to the temperature distribution that might be expected around a thermal discontinuity at the fuel surface. These features are identical to those observed previously in Element 012 at 3 at. % burnup.

*A. Boltax, P. Murray, and A. Biancheria, Fast Reactor Performance Model Development, Nucl. Appl. Tech. 9(2), 326-337 (1970).

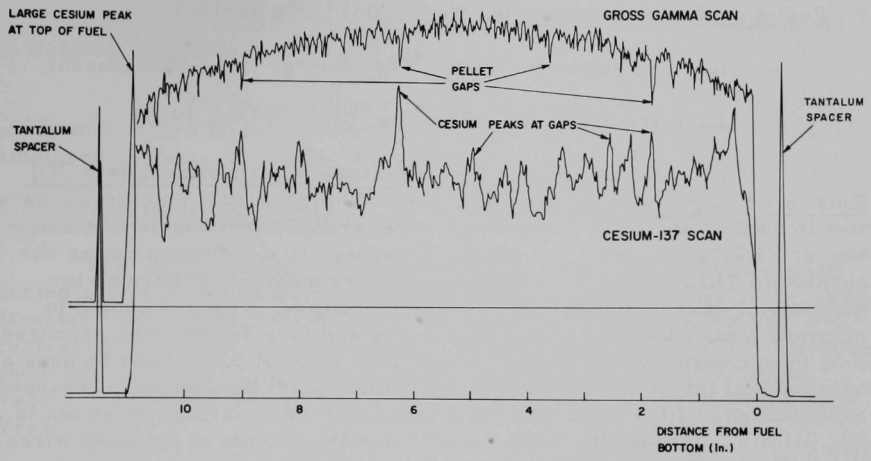

Fig. III.A.7. Longitudinal Gamma Scans on Element 007 for Gross Gamma Activity and for ^{137}Cs Activity, Showing Cesium Concentrations at Pellet Gaps

A gray phase, up to 0.002 in. thick, was observed in the fuel-cladding gap in the region of the cesium peak at the top of the fuel column. Electron-microprobe analysis identified this phase as almost pure cesium, with a uranium-plutonium content of less than 2%. Cesium penetration of the cladding was also clearly observed to a depth of 0.005 in. in this region (see Fig. III.A.8). Detailed examination continues to determine the extent of cesium penetration of the cladding as a function of temperature.

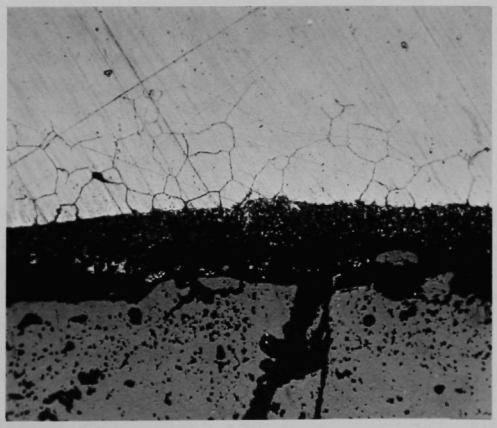

Fig. III.A.8. Transverse As-polished Section of the Fuel-cladding Gap in Element 007 at the Top of the Fuel Column, Showing Cesium Penetration into the Cladding to a Depth of 0.005 in.

5. Fuel-Coolant Interactions (R. W. Wright) (189a 02-164)

a. In-pile Simulation Tests: Work Energy (J. J. Barghusen)

Last Reported: ANL-7737, pp. 175-178 (Aug 1970).

(i) Medium-energy Power-excursion Experiment with UO_2 Pins in FFTF Simulation (Test S6). Test S6 is the initial piston-autoclave test in TREAT that uses a seven-pin wire-wrapped fuel bundle in simulation of FFTF geometry. The bundle is exposed to a meltdown power excursion in TREAT, and the resulting pressure pulses and thermal-to-mechanical-energy conversion ratios are obtained. The fuel bundle in previous tests consisted of five fueled pins and four dummy pins arranged in a square array with a sodium-to-pin area ratio of 1.24. Test S6 uses a hexagonal array of seven fuel pins (no dummy pins) that are wire wrapped and contained with a holder having a hexagonal inner surface as shown in Fig. III.A.9. Because the holder must clear the outside of the wrap wires, the sodium-to-pin area ratio of 0.94 (that includes thermocouple area) exceeds somewhat the FFTF value of 0.75. The change in pin geometry also results in a decrease in sodium mass, which is mostly within the array, from 200 g in previous tests to 115 g for Test S6.

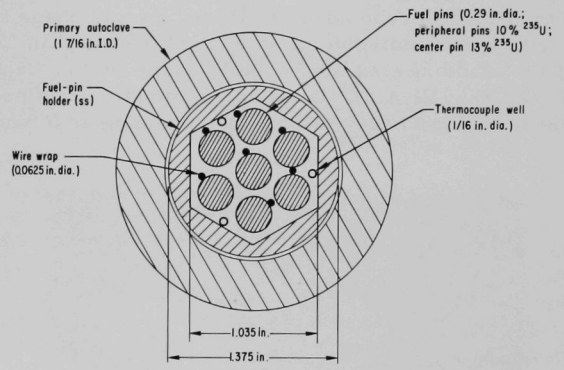

Fig. III.A.9. Fuel-pin Configuration for Piston-autoclave Test S6

The test uses the same type of fuel pins as previous tests; namely, stainless-steel-clad 0.29-in.-OD UO_2 pins having 41 g UO_2 per pin; the $5\frac{7}{8}$-in.-long fueled section of each pin is surmounted by a $6\frac{1}{8}$-in.-long blanket section; both sections contain helium at 15 psia. (The FFTF fuel has a 0.23-in. OD.) The seven-pin array contains about 287 g UO_2. The central pin contains UO_2 pellets enriched to 13% ^{235}U to compensate for flux depression; the peripheral pins contain 10%-enriched UO_2 pellets. A calibration test is determining the relative energy densities in the central and peripheral pins with these enrichments, and is obtaining the

calibration factor relating reactor integrated power to the average number of fissions per gram in the oxide fuel.

To provide a valid basis for comparison, Test S6 will be performed with a fission-energy input to the fuel nearly identical to that employed in Tests S3 and S5, 460 and 507 cal/g UO_2, respectively.

6. Post-accident Heat Removal (R. W. Wright) (189a 02-165)

The postaccident heat-removal work, in the past, has been conducted and reported under the headings "Engineering Analyses" and "Fuel-Structural Materials Interactions." However, the effort has become concentrated on specific FFTF problems; therefore the work has been reoriented under the headings "Core Debris Retention within the Reactor or Guard Vessel" and "Core Debris Retention within the Secondary Containment Vessel."

a. Core Debris Retention within the Reactor or Guard Vessel (J. C. Hesson and E. S. Sowa)

This work is to determine for specified FFTF accidents whether the core debris might breach the reactor and guard vessels during the post-accident period. The work includes: (1) analysis of the core meltdown process and of the nature and quantity of the core debris falling into the reactor-vessel bottom head, and analysis of whether this material might breach the vessel heads; and (2) experimental studies of heat removal from particulate beds under water and under sodium.

(i) Analytical Studies. Two hypothetical core-disruptive accidents are used for this analysis. The first is an overpower transient with a total heat-energy generation of 5000 MW in 2.6 sec. Since the heat removal into the coolant in the first 2.5 sec is 1000 MW, the net heat addition to the core is 4000 MW. The FFTF core contains 2860 kg of U-Pu oxide with a weight ratio of stainless steel (cladding and subassembly-can walls) to fuel oxide of approximately 0.6.

The temperatures of the sodium, cladding, and fuel (surface, center, and average) have been computed for positions throughout the core during normal operation. Also, the postaccident temperatures throughout the core have been computed by assigning the net heat generated to the fuel as one case, to the fuel and cladding as another case, and to the fuel, cladding, and can walls as a third case. These calculations indicate that some of the fuel is molten in all the fuel subassemblies at the end of the accident. These temperature distributions are used as starting points for the meltdown analysis.

Sodium natural convection (from the reactor vessel through the piping, pump, heat exchanger, bypass, and core) and cooling have been computed for several conditions of core blockage.

The quantity of steel below the fuel in the core that could act as a heat sink upon meltdown has been computed.

Analyses of core-meltdown processes are continuing.

(ii) Experiments. The experiments are to determine the maximum heat flux through beds of particles under liquid as a function of particle size, porosity, density, and bed thickness for use in estimating whether the fuel debris might penetrate the vessel head. Ideally, heat generation within the particles to simulate decay heat is desired, but this is difficult to achieve in out-of-pile work. As a substitute, bottom-heating of the bed is being used. Preliminary runs have been made with particulate beds under water, and further experiments will be made with UO_2 particulate beds under sodium. Both laboratory and in-pile experiments are planned with UO_2 beds under sodium.

The preliminary experiments in water used a 3.25-in.-dia steel container heated by a gas flame, with sand, limestone, and lead shot as bed materials. Among the factors controlling the heat flux are particle size, particle density, and settled-bed porosity. Heat flux, as measured by the rate of water evaporation, increased with particle size and bed porosity. In the tests, the heat flux increased slightly at the higher values of ΔT (near burnout), probably as a result of bed agitation by more violent movement of vapor through the bed. Heat fluxes between 40,000 and 80,000 Btu/hr-ft^2 were obtained with 2-3-in.-deep beds of sand and lead shot, and up to 100,000 Btu/hr-ft^2 were obtained with 3-in.-deep beds of limestone gravel.

Equipment is being designed for tests to measure heat fluxes through UO_2 particulate beds under sodium.

7. 1000-MWe Contract Management, Technical Review, and Evaluation (L. W. Fromm) (189a 02-186)

Not previously reported.

This program is being terminated by directive of AEC-RDT.

8. 1000-MWe Safety Analysis Study Subcontracts (L. W. Fromm) (189a 02-121)

Last Reported: ANL-7742, pp. 154-155 (Sept 1970).

This program is being terminated by directive of AEC-RDT. Subcontractors will issue final reports covering work completed to date as appropriate.

B. Operations

1. TREAT Operations (J. F. Boland) (189a 02-122)

Last Reported: ANL-7742, pp. 155-156 (Sept 1970).

a. Operations

Experiment GE-C4X was subjected to a transient designed to cause cladding failure. This experiment, which contained a fully enriched UO_2 sample, was a lead experiment for future TREAT experiments on GE fuel materials that have been irradiated in EBR-II.

A steady-state irradiation of a seven-pin cluster of stainless-steel-clad UO_2 fuel elements was conducted to determine the relationship between the fission rate in the experiment and the reactor power. The purpose was to establish test requirements for piston-autoclave experiment RAS S-6. This experiment will differ from previous S-series experiments in employing FTR fuel-element geometry and wire spacers to determine if pressure generation is strongly dependent on fuel-element configuration.

Neutron radiographs were made of EBR-II driver fuel, melt-wire temperature indicators, a self-powered neutron detector, and experimental capsules from Subassemblies X068, X072, X042, X043, and X056. Neutron radiographs were also made of TREAT experiment GE-C4X.

(i) Automatic Power Level Control System. Installation and testing of the hydraulic drive system were completed. Control rods were installed on one drive, and this drive is being used during normal steady-state and transient operations. Installation and testing of the automatic control system are still awaiting AEC approval to operate with digital-computer control.

C. Engineering Safety Features--Safety Features Technology

1. Reactor System and Containment Structural Dynamic Response (S. H. Fistedis) (189a 02-126)

a. Hydrodynamic Response of Primary Containment to High-energy Excursion (Y. W. Chang)

(i) Automatic Rezoning of Code to Extend Excursion Treatment into Sodium-momentum Domain (Y. W. Chang)

Last Reported: ANL-7679, p. 170 (Mar 1970).

Programming of the rezoning code has been completed. The preliminary version of the code was used in the FFTF Head-cavity Study.

Because zone distortions were eliminated through the rezoning process, the calculation was extended into the sodium-momentum domain. For the FFTF Head-cavity Study, the calculation continued until the sodium slug impinged on the top shield plug. To illustrate the result of rezoning, Fig. III.C.1 shows the configuration of a reactor before and after rezoning. (Because of axisymmetry, only half the reactor is shown.)

(ii) Parametric Studies of System Geometries and Excursion Magnitudes and Durations to Assist FFTF Accident Analysis (Y. W. Chang)

Last Reported: ANL-7726, pp. 168-171 (July 1970).

Recent studies indicate that the REXCO-H code works equally well for low-energy as for high-energy excursions. The problem used for one of these studies was a column of sodium slug contained in a cylindrical vessel and moving upward under the pressure of an expanding core vapor. The vessel was assumed to have only membrane strength and was allowed to move radially outward, but the top head was assumed to be fixed. When the sodium slug contacted the top head, the sodium slug was moving with a velocity of 150 ft/sec and had a total kinetic energy of 88.3 MW-sec. The pressure in the core vapor was only 200 psig at the time of impact, but had an internal energy of 58.2 MW-sec. The impact pressure and duration of impact obtained from REXCO-H are in good agreement with sodium-hammer calculations using acoustic-wave approximation. REXCO-H results also show excellent balance on energies, even when the pressure in the sodium slug is so low that the flow can be treated as an incompressible one. Table III.C.1 lists the energies at various time intervals, as calculated by the REXCO-H code. The deviation of energy at t = 6.204 msec is only 1.77%.

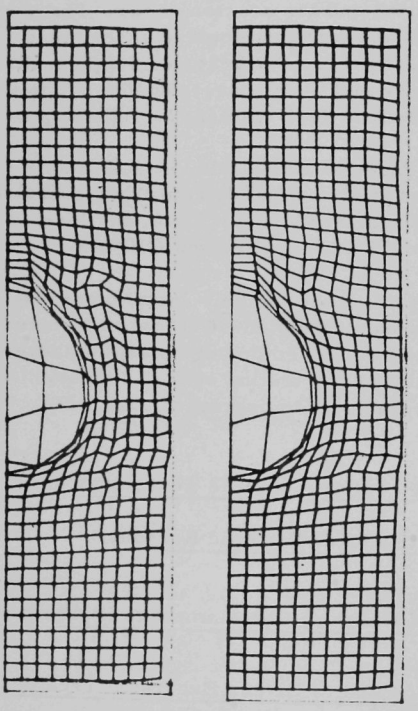

Fig. III.C.1. Two Reactor Configurations following Excursion: Before Rezoning (left) and after Rezoning (right)

TABLE III.C.1 Energy Balance

Time, msec	Internal Energy, MW-sec	Kinetic Energy, MW-sec	Vessel Strain Energy, MW-sec	Total Energy, MW-sec	Deviation of Energy, %
0	58.2	88.3	0	146.5	0
0.252	67.8	78.7	0	146.5	0
0.508	75.5	70.8	0.2	146.5	0
0.764	78.2	67.5	0.7	146.4	0.07
1.020	77.1	67.8	1.5	146.4	0.07
1.500	68.8	73.8	3.7	146.3	0.14
2.012	56.2	83.5	7.1	146.8	0.20
2.524	56.0	80.1	10.7	146.8	0.20
3.004	56.0	76.9	14.0	146.9	0.27
3.516	56.0	73.6	17.5	147.1	0.41
4.028	55.9	70.6	21.0	147.5	0.68
4.508	55.8	67.8	24.2	147.8	0.89
5.020	55.6	64.9	27.6	148.1	1.09
5.500	55.6	62.1	30.7	148.4	1.30
6.012	55.4	59.4	34.1	148.9	1.64
6.204	55.4	58.3	35.4	149.1	1.77

(iii) Comparison of Codes with Existing Experiments (J. E. Ash)

Last Reported: ANL-7679, pp. 171-175 (Mar 1970).

The REXCO-H computer code is being applied to four test cases to demonstrate its validity and applicability to containment problems involved in reactor safety. The test cases are model experiments in which the accident energy release is simulated by the detonation of chemical high-explosive charges.

The first test case treated was that of a bare 2-oz charge of RDX/TNT 60/40 in water performed by the United Kingdom Atomic Energy Authority. (The experimental configuration is shown on p. 173 of ANL-7679.) The peak shock pressure computed at the wall of the 2-ft-dia containment vessel was 2.0 kb; the peak pressure measured in the experiment was 1.6 kb. In investigating this discrepancy, we learned that unreported tests showed that the yield of the explosive charges used is about 20% lower than the conventional value we assumed. [Our assumption for the yield of the Composition B charge was based on Los Alamos report LA-3466 (June 1966).]

The computation was performed for both coarse- and fine-grid spacing and for cylindrical and spherical charge shapes. The computed peak pressure was independent of the charge shape, provided the shape was relatively compact. Subsequent computations were based on a spherical

shape, which has the computational advantages of spherical symmetry in the neighborhood of the charge and avoids the excessive cell distortion that occurs at the corners of a cylinder. The physical significance of this computational result is that the effects of the charge detonation adjust very rapidly in accordance with the configuration of the surroundings with little dependence on charge shape. The computation was performed with a coarse grid, in which the charge was covered by only two cells, and with a fine grid, in which the charge was partitioned into 26 cells. The peak pressure at the wall was about 10% higher for the fine grid, indicating that the coarse grid tends to spread out the shock more. The reasonably close agreement tends to confirm the convergence of the computational procedure.

The second test case considered, also performed by the UKAEA, involved the same bare charge and containment-tank configuration as discussed above, but the charge was confined in the structure shown in Fig. III.C.2. In the experiment, the pressure transmitted to the containment wall was considerably delayed and the peak was attenuated down to about 0.3 kb. The computed values depended critically on the equation of state assumed for the lead-shot region. If the interstices between the shot are permeated with water, little attenuation is achieved. If the gaps are assumed to be dry (i.e., filled with air), the material is effectively crushable, resulting in a reduction of the peak pressure reaching the containment wall from 1.9 kb for the water-saturated lead shot to about 0.8 kb for the dry lead shot. This peak pressure is still significantly higher than the measured pressure of 0.3 kb, indicating that the purely hydrodynamic assumption for the behavior of the lead shot (that it is undergoing significant deformations and absorbing energy) is inadequate and the inelastic equations should be employed.

The third test case under study is a series of scale-model experiments carried out jointly by the CEA-Euratom and the UKAEA at Cadarache, France. The experimental configuration is shown in Fig. III.C.3. Hexogene charges (15, 30, and 60 g) were introduced into a 25-cm-dia 42.4-cm-high steel simulated core vessel. The blankets are simulated by a mixture of uranium and steel rods (average density 12.7 g/cm^3); the neutron reflectors are represented by six concentric stainless-steel cylinders 0.25 cm thick, spaced 0.1 cm apart; the heat shield is represented by four longer 0.1-cm-thick cylinders, spaced 0.1 cm apart. Experimental data were obtained for three charge weights and for cold water and sodium heated to 150, 250, 400, and 550°C.

The experiments for the fourth test case, with the configuration shown in Fig. III.C.4, were run by the U.S. Naval Ordnance Laboratory. The shock pressures and times of arrival were not measured, but the much slower "blast pressure" following the rupture of the model reactor vessel and the release of the sodium vapor into the oxygen-depleted air chamber were measured. The effects of the explosives must be inferred from photographs of the deformed reactor-vessel model. The secondary shield simulant

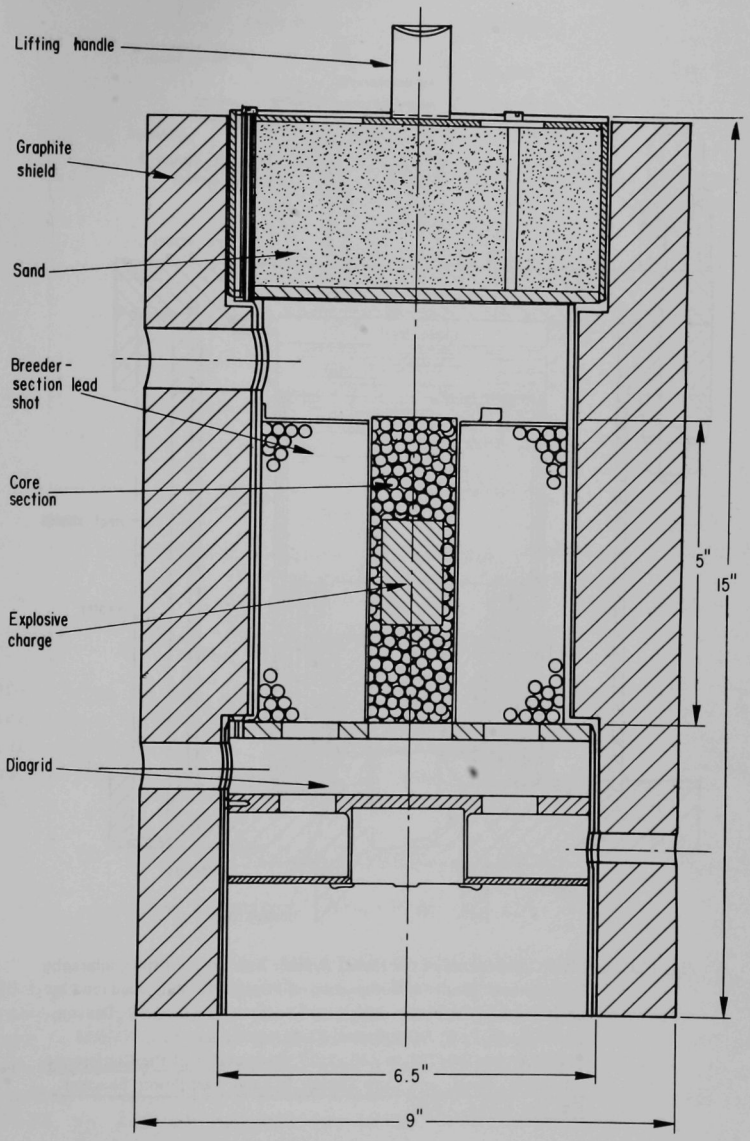

Fig. III.C.2. Cross Section of Model Core and Breeder Structure for UKAEA Experiments [from "A Model Investigation of Explosion Containment in Single Tank Fast Reactors," by N. J. M. Rees (UKAEA), pp. 692-719, in ANL-7120, Proceedings of the Conference on Safety, Fuels, and Core Design in Large Fast Power Reactors, October 11-14, 1965]

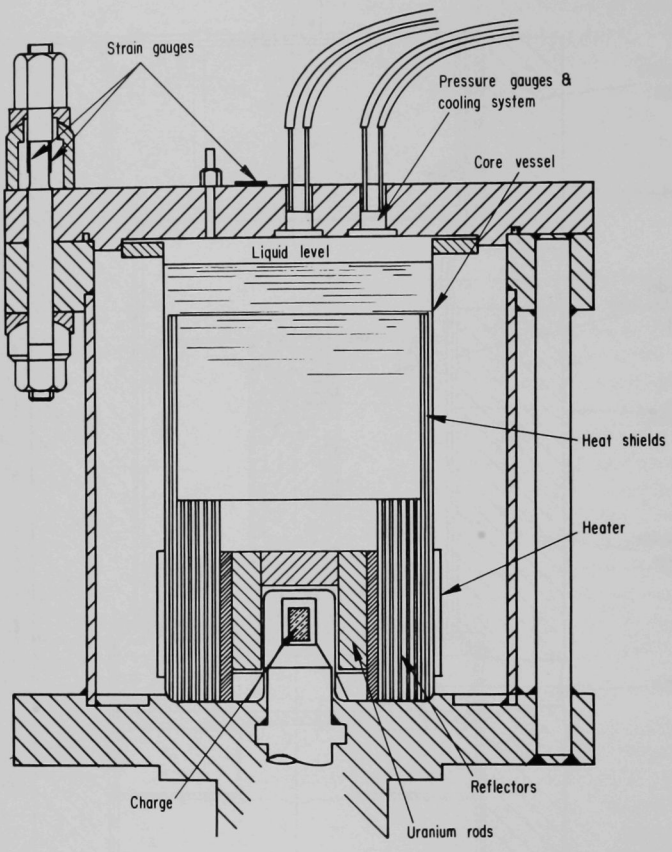

Fig. III.C.3. Main Components of the Model Reactor Assembly for the Cadarache Experiments [from "A Comparison of Pressure Loading Produced by Contained Explosions in Water and Sodium," by G. A. V. Drevon, (Saclay), M. F. G. Falgayrettes (Cadarache), and F. J. Walford (UKAEA), pp. 720-733, in ANL-7120, Proceedings of the Conference on Safety, Fuels, and Core Design in Large Fast Power Reactors, October 11-14, 1965]

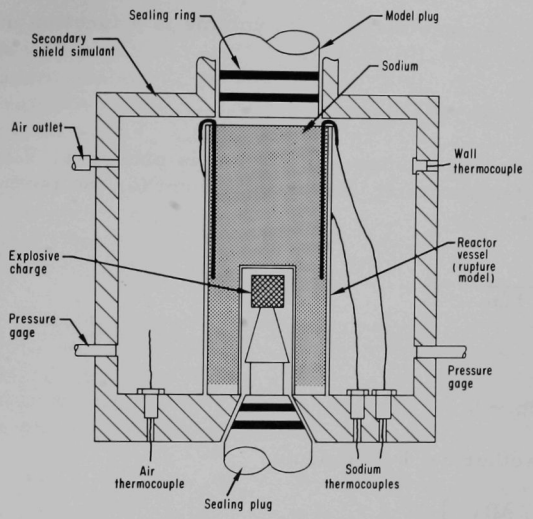

Fig. III.C.4. Rupture Model Assembled in Idealization of Model Secondary Shield for Naval Ordnance Laboratory Experiments [from Response of Enrico Fermi Reactor to TNT Simulated Nuclear Accidents, p. 29, NOLTR 62-207, November 1964]

is a 20-in.-dia, 18.4-in.-high cylindrical tank. The charge was 126.45 g of pressed pentolite PETN/TNT 50/50. A mass of 10,720 g of 850°F sodium filled the rupture model. The 430°F air in the surrounding chamber was almost pure nitrogen. The REXCO-H code is being applied to the rupture model.

(iv) Insertion of Heat Transfer into Codes (T. J. Marciniak)

Last Reported: ANL-7726, pp. 168-172 (July 1970).

Appropriate subroutines are being added to the REXCO-H code to handle sodium in postburst accident cases that include fuel-coolant interaction. The program includes the definition of a fuel-coolant interaction zone in which fuel and coolant volume fractions, densities, and temperatures plus the fuel-particle size are specified for each individual cell in the zone. Then, using a quasi-steady-state heat-transfer model (see ANL-7688, pp. 240-244, April-May 1970), the temperature of the coolant is calculated.

To be able to calculate the effect of the thermal expansion of the liquid sodium, an equation of state based on the work of Anderson*

*Orson L. Anderson, The Use of Ultrasonic Measurements under Modest Pressure to Estimate Compression at High Pressure, J. Phys. Chem. Solids, Pergamon Press, 1966, 27, pp. 547-565.

was developed. Because the specific volume is a function of pressure and temperature, i.e., $V = f(p,T)$, then

$$dV = -\beta V\, dp + \alpha V\, dT, \tag{1}$$

where β is isothermal compressibility, p is pressure, V is specific volume, and T is temperature. Anderson's form for the isothermal compressibility is

$$\beta = \frac{1}{B_0 + B_0' p} = \frac{1}{B}, \tag{2}$$

where

$B_0 = Bp \to 0$

B = isothermal bulk modulus

$$B_0' = \left\{\left(\frac{\partial B}{\partial p}\right)_T\right\}_{p\to 0} = (B')p \to 0.$$

Substitution of Eq. 2 into Eq. 1 and integrating yields

$$p = \frac{B_0}{B_0'}\left\{\left(\frac{V_0}{V}\right)^{B_0'} \exp\left[B_0' \int_{T_0}^{T} \alpha(T)\, dT\right] - 1\right\}, \tag{3}$$

where V_0 is initial specific volume, T_0 is initial temperature, V is present specific volume, and $\alpha(T)$ is the volumetric coefficient of thermal expansion. Neglect of thermal expansion, i.e., $\alpha = 0$, causes the reduction of Eq. 3 to Murnaghan's equation of state, which is currently an option in the basic REXCO-H code.

At present the code appears to have the capability of handling the fuel-coolant interaction up to the point of sodium evaporation. Some preliminary calculations indicate peak pressures of about 600 atm in an interaction zone 20 cm in diameter by 30 cm long under 60 cm of sodium. However, these results are quite preliminary and the code is still being debugged. Incorporation of subroutines to handle sodium vaporization is also continuing.

b. Dynamic Response of Core Subassemblies (J. M. Kennedy)

Not previously reported.

The objective of this work is to develop analyses and codes that will permit the evaluation of accidents that occur in a single subassembly

and that possibly propagate to the adjacent one or two rows of subassemblies. The code will give stresses, deformations, velocities, and possible extent of permanent damage to the accident subassembly and to the surrounding subassemblies, thus providing important input to the Fuel-element Failure Propagation work (189a No. 02-116) and possible input to the Accident Analysis work (189a No. 02-112) where changed core geometries are needed for recalculation of neutronics. The developed codes will be compared with experiments conducted with timely subassembly and cluster configurations and dimensions, and with controlled energy releases whose equation of state is reflected in the code inputs.

(i) Development of Mathematical Model. Due to symmetry, only one-twelfth of the total system will have to be analyzed, with each core subassembly having a hexagonal cross section, the core subassemblies packed in a hexagonal arrangement, and assuming that the transient loads are identical on each flat of the hexagon-shaped subassembly.

The core subassemblies will have as their structural representation a connected set of plate elements. The increased stiffness at the corners of the hexagon-shaped core subassemblies is included by employing available analysis.* The coolant in the channels between the core subassemblies and in the fuel bundles within the core subassemblies is being represented by means of an early model developed from published information.**

The displacement method is employed in the solution of the dynamic response of core subassemblies. A transient-response analysis is being performed using the direct method of problem formulation. The direct method has as its degrees of freedom the displacements at grid points.

The matrix properties of the dynamic system are assembled by the Direct Dynamic Matrix Assembler module, which assembles the mass, damping, and stiffness matrices from various sources in terms of displacements at grid points.

The differential equations of a linear structural problem, when written in the general matrix form, are expressed by

$$[p^2M + pC + K]\{u\} = \{P\},$$

where t is time, p is d/dt (the time derivative), M is mass matrix, C is damping matrix, K is stiffness matrix, u is displacement vector, and P is transient load vector.

*L. M. McWethy, An Analytical Evaluation of the Consequences of a Hypothetical Instantaneous Loss of Coolant Flow to a Fast Flux Test Facility Driver Fuel Assembly, GEAP-10059 (July 1969).

**G. H. Golden, and J. V. Tokar, Thermophysical Properties of Sodium, ANL-7323 (Aug 1967).

Numerical integration of the coupled equations is achieved by using the central-difference equivalent

$$\frac{1}{\Delta t^2}[M]\{u_{n+2} - 2u_{n+1} + u_n\} + \frac{1}{2\Delta t}[C]\{u_{n+2} - u_n\} + [K]\{au_{n+2} + (1 - 2a)u_{n+1} + au_n\} =$$

$$a\{P_{n+2}\} + (1 - 2a)\{P_{n+1}\} + a\{P_n\},$$

where Δt is time step, u_n is value of u at $t = t_n$, and a is an arbitrary coefficient selected on the basis of stability and accuracy.

With substitution of the value of $a = 1/3$ for a margin of stability and collecting like different time-step terms, the integration algorithm is

$$\left[\frac{1}{\Delta t^2}M + \frac{1}{2\Delta t}C + \frac{1}{3}K\right]\{u_{n+2}\} = \frac{1}{3}\{P_{n+2} + P_{n+1} + P_n\} + \left[\frac{2}{\Delta t^2}M - \frac{1}{3}K\right]\{u_{n+1}\}$$

$$+ \left[-\frac{1}{\Delta t^2}M + \frac{1}{2\Delta t}C - \frac{1}{3}K\right]\{u_n\}.$$

A measure of the error in this equation is calculated by the distortion of the frequency and damping of its normal modes from those of the exact dynamic equations.

The initial conditions needed are the values of $\{u_0\}$, $\{\dot{u}_0\}$, $\{u_{-1}\}$, $\{P_0\}$, and $\{P_1\}$. With the assumption that the acceleration is zero for $t \leq 0$, the initial conditions are

$$\{u_{-1}\} = \{u_0\} - \{\dot{u}_0\}\Delta t,$$

$$\{P_{-1}\} = [K]\{u_{-1}\} + [C]\{\dot{u}_0\},$$

and

$$\{P_0\} = [K]\{u_0\} + [C]\{\dot{u}_0\},$$

where $\{\dot{}\}$ indicates time derivative.

Velocities and accelerations along with displacements are outputs of the transient analysis. The expressions for the velocity and acceleration are

$$\{\dot{u}_n\} = \frac{1}{2\Delta t}\{u_{n+1} - u_{n-1}\}$$

and

$$\{\ddot{u}_n\} = \frac{1}{\Delta t^2}\{u_{n+1} - 2u_n + u_{n-1}\}.$$

This analysis considers various types of accidents with their particular response to be used as input in the code. Input is available for the molten fuel-coolant interaction accident in a single subassembly, which employs the REXCO-H code for analysis. (See Progress Report for July 1970, ANL-7726, pp. 168-172.)

(ii) Modification of Excursion Computer Code. The general-use code NASTRAN, Level 8.1.0, for structural analysis has been obtained. The executable module of NASTRAN has been moved onto a private disk pack. Attempts are being made to execute demonstration problems.

PUBLICATIONS

Emergency Core-Cooling Problem in LMFBR's
I. Charak
Reactor Technol. 13(3), 280-309 (Summer 1970)

An Experimental Study of Transient Free-Convection Heat Transfer with Mercury in a Vertical Rectangular Channel
R. P. Heinisch, R. Viskanta,* and R. M. Singer
Wärme- und Stoffübertragung 3(3), 127-130 (1970)

Physical (Hydraulic) Modeling of Heat Dispersion in Large Lakes: A Review of the State of the Art
Edward Silberman** and Heinz Stefan**
ANL/ES-2 (Aug 17, 1970)

Prediction of the Incipient Boiling Conditions Following a Blocked LMFBR Subassembly Accident
R. M. Singer and R. E. Holtz
Nucl. Appl. Technol. 9, 767-770 (Nov 1970)

Correlation Parameters for Eliminating the Effect of Pulse Shape on Dynamic Plastic Deformation
C. K. Youngdahl
J. Appl. Mech. 37(3), 744-752 (Sept 1970)

*Purdue University.

**University of Minnesota, St. Anthony Falls Hydraulic Laboratory.

X